Optimizing Photocatalytic Hydrogen Evolution Through Synergistic Charge Transfer in Donor Acceptor Based Hybrid Photocatalyst

A dissertation submitted in partial fulfilment of requirements

for the degree of

Doctor of Philosophy

Submitted by

Tamal Pal

Roll No. 186122041

Department of Chemistry

Indian Institute of Technology Guwahati

Guwahati-781039, Assam, India

Statement

I do hereby declare that the work incorporated in this thesis entitled, "**Optimizing Photocatalytic Hydrogen Evolution through Synergistic Charge Transfer in donor acceptor based hybrid Photocatalyst**" is the result of investigations carried out by me under the guidance of Prof. Chivukula V Sastri, at the Department of Chemistry, Indian Institute of Technology Guwahati, Guwahati, Assam, India.

In keeping with the general practice of reporting scientific observations, due acknowledgements have been made wherever the work described is based on the findings of other investigators. I further declare that this work has not been submitted in part or full to any other university or institute for award of any degree or diploma.

Tamal Pal

IIT Guwahati
June 2025

Tamal Pal

Prof. Chivukula V Sastri
Professor, Department of Chemistry
Indian Institute of Technology Guwahati
Guwahati-781039, Assam, India

Phone: +91-361-258-2323
Email: sastricv@iitg.ac.in

Certificate

This is to certify that the work included in this thesis entitled “**Optimizing Photocatalytic Hydrogen Evolution through Synergistic Charge Transfer in donor acceptor based hybrid Photocatalyst**” by Mr. Tamal Pal, Department of Chemistry, Indian Institute of Technology Guwahati has been carried out under my supervision. I further certify that this work has not been submitted to any other University or Institution in part or full for the award of any degree or diploma.

IIT Guwahati
June 2025

Prof. Chivukula V Sastri
Thesis supervisor
Department of Chemistry
Indian Institute of Technology Guwahati
Guwahati –781039, Assam, India

Acknowledgement

It feels overwhelmed writing this THESIS! I don't know if I have been successful or not but I know for certain is that, I have come across through so many hurdles and took lessons from that. For a research scholar failure is a part of their everyday life, it was also true for me. Learning from the failure, show up every day in lab at right time, working in odd hours, keep working when even nothing is working in your favour- all these odd situations have changed my perspective towards life and made me more persistent towards my goal. I have faced quite big challenges, might be more than everyone else. Be it personal, or professional and dangling constantly in between success and failure, somehow, I have managed to survive till now. But it would be very unfair if I don't mention the names of the people at the end here, who helped me anchor my ship to the shore. I am delighted to extend my deepest gratitude to everyone who played a role in bringing this journey to fruition. Your contributions have been truly meaningful, and I sincerely thank each one of you from the bottom of my heart.

I take this opportunity to show my gratitude to Prof. Parameswar Krishnan Iyer for granting me the opportunity to work in his well-equipped laboratory. His unwavering support, insightful suggestions, and scientific guidance consistently propelled my research forward. I also appreciate his assistance in securing financial support when my stipend was over. I extend my sincere thanks to my supervisor, Prof. Chivukula V Sastri, for his profound insights and continuous motivation. His trust in my capabilities and the freedom he provided in steering the direction of my research were instrumental in shaping my academic journey.

I express my sincere gratitude to my doctoral committee members, Prof. Mohammad Qureshi and Prof. Nageswara Rao Peela, for their thorough evaluation. Their insightful suggestions and critical feedback during the progress seminars significantly enhanced my research from multiple perspectives and contributed to the improvement of my thesis

I sincerely express my gratitude towards all my teachers especially Mr. Kishalay Ghosh, Dr. Pratyay Ghosh, Prof. Tridip Tripathy and all my teachers at Midnapore College as well as IIT Guwahati for imbibing good values and knowledge in me.

I am extremely beholden to Dr. Koushik Rout and Prof Pradeep C. Parameswaran from IIT Mandi, India for allowing us to use the XPS-UPS facility which were extremely essential for continue our research work.

Soumallya deserves a special mention since I would not be able to acquire the degree without the constant backing of him. I am indebted for his selfless support and advices that made this journey possible for me in spite of all the hitches. I had the best of the times working with him. We have built quite a strong bonding through these years and hope to work together in future. He commands the highest respect for his selfless dedication, unwavering diligence, and the invaluable contributions he has made to the research projects.

The most devoted gratitude of course goes to my parents, and to late dadu who always stand beside me to keep me going. My parents are undeniably the people for whom I can be what I am today. I can't repay those sleepless nights, those hard works and all the sacrifices they have done for me and my success, if any, are the fruits of their endurance.

I can't miss this opportunity to express my hearty admiration towards my go to person Sumana, my wife, with whom I shared the inmost connection. She has always supported me especially in the tough phases of my life. She always pushed me one step forward when I was going to quit altogether and encouraged me when I felt lost. knowing all my ups and downs, and tolerating those on a daily basis, she deserves a massive endorsement from my end. She braces each and every step I have taken till date. Even if I failed to achieve this, I know these people will still be on my side of the earth!

I would also like to acknowledge all my other lab mates including, Rahul Bhaiya, Ramesh Bhaiya Raman Bhaiya, Subrata Da, Ritwik, Raj, Priyam, Debika, Tapasi, Debashis, Kavita, Mayur, Himanshu, Ramkrishna, Deepak, Manab, Mrinalini, Dheeraj, Srinibas, Antim, Ananta for creating a pleasant and vibrant laboratory atmosphere and making my days memorable. I am blessed to have friends and well-wishers like Tanumoy, Mihir, Khadimul. I could always count on them when I needed help.

Tamal Pal

Dedicated to

my late grandfather, Sri Taraknath Pal

Thesis Abstract

The exponential increase of global population and the enduring dependence on fossil fuel resources causes huge challenges towards mankind. In terms of energy density, H_2 is unparalleled, possessing the highest energy density (approximately 142 kJ/mol) in comparison to all other fossil fuels and energy sources. it is noteworthy that nearly 65% of hydrogen's overall production is allocated for synthesis of NH_3 by Haber-Bosch process as well as polyester and resin production. The conventional sources from which hydrogen is produced encompass a variety of materials, notably including natural gas, various hydrocarbons, and water in its liquid form. At present, the production of hydrogen is predominantly attributed to natural gas, heavy oils, naphtha and coal, which creates enormous pollution. The substantial progress achieved in the field of photocatalytic H_2 production has effectively established photocatalysis as a promising intermediary technology that facilitates the conversion of solar energy into H_2 fuels, a development that has unfolded over the last forty years and highlights the increasing importance of such technologies in addressing global energy challenges.

The work embodied in the thesis entitled **"Optimizing Photocatalytic Hydrogen Evolution Through Synergistic Charge Transfer in Donor Acceptor Based Hybrid Photocatalyst"** focusses broadly in the four areas (1) Probing on the role of degree of chemical reduction in RGOs for improved photocatalytic activity of $MAPbI_3$/RGO heterostructures through appropriate band alignments. (2) Role of solvent assisted morphology dependent MAPI has been investigated for better photocatalytic and photoelectrochemical activities. Altercation in reaction medium from HI to DMF not only alter the surface morphology from cuboid to rod shape, it also influences various aspects of photocatalytic and photoelectrochemical activities. $MAPI_{DMF}$ exhibited superior performances in terms of HER activities by 28 times Compared to $MAPI_{HI}$. Alongside role of polyfluorene polymer in the encapsulation of $MAPbI_3$ microcrystal by through electrostatic interaction, which enhances both the structural integrity in ambient moisture abundant atmosphere as well as the photocatalytic H_2 evolution rates. (3) Rational design of heterostructures made of amorphous MoS_2 and environment friendly lead free MABI, where boosted HER performance was achieved through smooth transition from type I to type II heterojunction by atomic level alteration in chemical composition. (4) Formation of g-C_3N_4 based covalent heterostructure. Where carbon nitride was directly anchored with metal co-ordinated ligand centers through covalent bonding enabling improved millimole scale H_2 evolution rates.

The dissertation begins with a brief general introduction, **Chapter 1**, which serves as a background for this thesis and as a basis for the works that are presented in the following chapters.

In chapter 2, role of oxygen content dependent RGOs in MAPI/RGO heterostructures has been investigated for photochemical and photoelectrochemical activities. This chapter also summarizes the fact that variation in extent of chemical reduction not only controls the atomic percentage of oxygen content, but also governs the varied bandgaps as well as band edge positions for three variants of RGOs. Among all these variations, S2_RGO with bandgap of 2.59 eV and oxygen content of 24% was identified as the best performing co-catalyst with highest HER. On contrary MAPI/S3_RGO registered lowest photoelectrochemical and HER activities where S_3/RGO is the most chemically reduced variant of RGO with lowest oxygen content (18%) with a bandgap of 2.33 eV. For MAPI/S1_RGO composites the performance were slightly lesser than MAPI/S2_RGO. To rationalize the occurrence of disparities in photoelectrochemical and photocatalytic activities of all three MAPI/RGO composites, we have proposed an electron transfer mechanism, where depending upon the relative CBM positions of MAPI and respective RGO, dissimilar photogenerated electron transfer took place.

Chapter 3, summaries the role of solvent assisted morphology dependent MAPI has been investigated for photocatalytic and photoelectrochemical activities. Altercation in reaction medium from HI to DMF not only alter the surface morphology from cuboid to rod shape, it also influences various aspects of photocatalytic and photoelectrochemical activities. $MAPI_{DMF}$ exhibited superior performances in terms of HER activities by 28 times Compared to $MAPI_{HI}$. The superior HER performances of $MAPI_{DMF}$ were supported by quenched photoluminescence intensity, higher photocurrent, lower charge transfer resistance. The improved photocatalytic and photoelectrochemical activities might be attributed to larger surface area possessed by rod shape $MAPI_{DMF}$. A greater surface area provides more reaction sites, enabling the absorption of a higher number of photons resulting accelerated H_2 evolution. A stable $MAPbI_3$/polyfluorene composite was successfully prepared by an *in-situ* fabrication. The incorporation of polyfluorene on $MAPI_{DMF}$ surfaces not only broadens the light absorption range but also enhances charge segregation and transport at the $MAPI_{DMF}/PF_{10}$ interface, leading to improved photocatalytic and photoelectrochemical activities. Under optimized conditions, $MAPI_{DMF}/PF_{10}$ exhibited a maximum HER activity of 6200 μmol h^{-1} g^{-1}. The enhanced HER activity of $MAPI_{DMF}/PF_{10}$ may be attributed to the efficient interfacial charge transfer from $MAPI_{DMF}$ to the polyfluorene co-catalyst owing to proper alignment of CBM of $MAPI_{DMF}$ and the LUMO of polyfluorene.

Chapter 4 summarizes the influence of phosphorus doping on band gap and energy levels. This study elucidates that the band gap of MoS_2 declines from 1.39 eV for pristine MoS_2 to 1.28 eV for P50_MoS_2, and it further diminished to 1.07 eV for P100_MoS_2 upon doping with P. Concurrently, the VBM energy level of all the MoS_2 variants experienced a downward shift. Consequently, P50_MoS_2/MABI and P100_MoS_2/MABI composites have established a type II heterojunction, whereas MoS_2/MABI results in a type I heterojunction.

It is noteworthy that type II heterojunctions are typically more favorable for the separation and migration of photogenerated charges when compared to type I heterostructures,

P50_MoS_2/MABI demonstrated superior photocatalytic and photoelectrochemical efficiencies relative to the others. Even though P100_MoS_2/MABI possessed type II heterojunction still it exhibited the least reaction rates among three composites. The relative energy band positions of P100_MoS_2 and MABI might be attributed to the diminished HER activity. The CBM of P100_MoS_2 was located at significantly deeper energy level compared to $E(H^+/H_2)$, inhibiting its function as a photoelectron carrier, thereby resulting in the compromised photocatalytic HER activities of P100_MoS_2/MABI composites.

Chapter 5 summarizes the chemical functionalization of g-C_3N_4 via a covalent methodology employing cyano porphyrin has been demonstrated to serve as a significant tactic for augmenting and introducing novel properties to g-C_3N_4, thereby facilitating charge separation and enhancing visible light absorption in the tail region. This advancement enables the attainment of improved HER activities from ascorbic acid aqueous solutions. The covalent grafting of porphyrin moieties onto the g-CN sheet has provided coordination sites for transition metals such as Ni^{2+} and Co^{2+}. The Metal co-ordinated por_g-CN could further enhance the H_2 evolution rates. The presence of metalated porphyrin moieties on g-CN has been shown to alter the kinetics of photogenerated charge migration, as evidenced by photocurrent and impedance studies. Porphyrin-anchored g-CN has demonstrated hydrogen evolution of 3200 $\mu mol \cdot g^{-1}h^{-1}$. Notably, the maximum hydrogen evolution recorded was 4200 $\mu mol \cdot g^{-1}h^{-1}$, achieved by Co_por_g-CN. This accelerated HER performance was attained through covalent linkage, where the migration of photogenerated charge transfer was considerably more feasible in comparison to conventional heterostructures. Between the Ni and Co metalated photocatalysts, Co_por_g-CN exhibited a slight upper hand in terms of HER activities. In the case of transition metal-coordinated photocatalysts, prior to the formation of molecular hydrogen, metal hydride bonds are established. The cleavage of the metal hydride bond is regarded as the rate-determining step (RDS) that governs the rate of hydrogen evolution. The displacement of the H^- ion, which initiates the formation of molecular H_2, is considerably more facile for Co_por_g-CN.

Table of Contents

Chapter 1: Introduction

Chapter 2: Composites of Reduced Graphene Oxide and $MAPbI_3$ Crystals for Photocatalytic Hydrogen Generation

Chapter 3: Solvent assisted shape dependent $MAPbI_3$/polyfluorene heterostructures with larger surface area for improved photocatalytic H_2 evolution

Chapter 4: Transformation from type-I to type-II $MA_3Bi_2I_9$ based heterostructure photocatalyst via energy band engineering

Chapter 5: Molecularly Doped Porphyrin Covalent Heterojunction Carbon Nitride Instigating Cocatalyst-Free Solar Energy Harvesting via Water Splitting

Lists of Figures

Lists of Tables

Lists of abbreviation

MAPI	**Methylammonium Lead Iodide ($MAPbI_3$)**
GO	Graphene Oxide
RGO	Reduced Graphene Oxide
EIS	electrochemical impedance spectroscopy
E_{FB}	Flat band potential
PF	Polyfluorene polymer
$MAPI_{HI}$	HI assisted $MAPbI_3$
$MAPI_{DMF}$	DMF assisted $MAPbI_3$
$MAPI_{DMF}/PF_{10}$	Heterostructures made of $MAPI_{DMF}$ and polyfluorene (10 wt%)
BET	Brunauer, Emmett, and Teller
DMAP	4-Dimethylaminopyridine
MABI	$MA_3Bi_2I_9$
DAT	2,4-diamino-1,3,5-triazine
g-CN	graphitic carbon nitride ($g-C_3N_4$)
g-CN_Por	Porphyrin doped $g-C_3N_4$
E_f	Fermi energy level

Optimizing Photocatalytic Hydrogen Evolution Through Synergistic Charge Transfer in Donor Acceptor Based Hybrid Photocatalyst

A dissertation submitted in partial fulfilment of requirements
for the degree of
Doctor of Philosophy

Submitted by
Tamal Pal
Roll No. 186122041

Department of Chemistry
Indian Institute of Technology Guwahati
Guwahati-781039, Assam, India

Statement

I do hereby declare that the work incorporated in this thesis entitled, "**Optimizing Photocatalytic Hydrogen Evolution through Synergistic Charge Transfer in donor acceptor based hybrid Photocatalyst**" is the result of investigations carried out by me under the guidance of Prof. Chivukula V Sastri, at the Department of Chemistry, Indian Institute of Technology Guwahati, Guwahati, Assam, India.

In keeping with the general practice of reporting scientific observations, due acknowledgements have been made wherever the work described is based on the findings of other investigators. I further declare that this work has not been submitted in part or full to any other university or institute for award of any degree or diploma.

Tamal Pal

IIT Guwahati
June 2025

Tamal Pal

Prof. Chivukula V Sastri
Professor, Department of Chemistry
Indian Institute of Technology Guwahati
Guwahati-781039, Assam, India

Phone: +91-361-258-2323
Email: sastricv@iitg.ac.in

Certificate

This is to certify that the work included in this thesis entitled "**Optimizing Photocatalytic Hydrogen Evolution through Synergistic Charge Transfer in donor acceptor based hybrid Photocatalyst**" by Mr. Tamal Pal, Department of Chemistry, Indian Institute of Technology Guwahati has been carried out under my supervision. I further certify that this work has not been submitted to any other University or Institution in part or full for the award of any degree or diploma.

IIT Guwahati
June 2025

Prof. Chivukula V Sastri
Thesis supervisor
Department of Chemistry
Indian Institute of Technology Guwahati
Guwahati –781039, Assam, India

Acknowledgement

It feels overwhelmed writing this THESIS! I don't know if I have been successful or not but I know for certain is that, I have come across through so many hurdles and took lessons from that. For a research scholar failure is a part of their everyday life, it was also true for me. Learning from the failure, show up every day in lab at right time, working in odd hours, keep working when even nothing is working in your favour- all these odd situations have changed my perspective towards life and made me more persistent towards my goal. I have faced quite big challenges, might be more than everyone else. Be it personal, or professional and dangling constantly in between success and failure, somehow, I have managed to survive till now. But it would be very unfair if I don't mention the names of the people at the end here, who helped me anchor my ship to the shore. I am delighted to extend my deepest gratitude to everyone who played a role in bringing this journey to fruition. Your contributions have been truly meaningful, and I sincerely thank each one of you from the bottom of my heart.

I take this opportunity to show my gratitude to Prof. Parameswar Krishnan Iyer for granting me the opportunity to work in his well-equipped laboratory. His unwavering support, insightful suggestions, and scientific guidance consistently propelled my research forward. I also appreciate his assistance in securing financial support when my stipend was over. I extend my sincere thanks to my supervisor, Prof. Chivukula V Sastri, for his profound insights and continuous motivation. His trust in my capabilities and the freedom he provided in steering the direction of my research were instrumental in shaping my academic journey.

I express my sincere gratitude to my doctoral committee members, Prof. Mohammad Qureshi and Prof. Nageswara Rao Peela, for their thorough evaluation. Their insightful suggestions and critical feedback during the progress seminars significantly enhanced my research from multiple perspectives and contributed to the improvement of my thesis

I sincerely express my gratitude towards all my teachers especially Mr. Kishalay Ghosh, Dr. Pratyay Ghosh, Prof. Tridip Tripathy and all my teachers at Midnapore College as well as IIT Guwahati for imbibing good values and knowledge in me.

I am extremely beholden to Dr. Koushik Rout and Prof Pradeep C. Parameswaran from IIT Mandi, India for allowing us to use the XPS-UPS facility which were extremely essential for continue our research work.

Soumallya deserves a special mention since I would not be able to acquire the degree without the constant backing of him. I am indebted for his selfless support and advices that made this journey possible for me in spite of all the hitches. I had the best of the times working with him. We have built quite a strong bonding through these years and hope to work together in future. He commands the highest respect for his selfless dedication, unwavering diligence, and the invaluable contributions he has made to the research projects.

The most devoted gratitude of course goes to my parents, and to late dadu who always stand beside me to keep me going. My parents are undeniably the people for whom I can be what I am today. I can't repay those sleepless nights, those hard works and all the sacrifices they have done for me and my success, if any, are the fruits of their endurance.

I can't miss this opportunity to express my hearty admiration towards my go to person Sumana, my wife, with whom I shared the inmost connection. She has always supported me especially in the tough phases of my life. She always pushed me one step forward when I was going to quit altogether and encouraged me when I felt lost. knowing all my ups and downs, and tolerating those on a daily basis, she deserves a massive endorsement from my end. She braces each and every step I have taken till date. Even if I failed to achieve this, I know these people will still be on my side of the earth!

I would also like to acknowledge all my other lab mates including, Rahul Bhaiya, Ramesh Bhaiya Raman Bhaiya, Subrata Da, Ritwik, Raj, Priyam, Debika, Tapasi, Debashis, Kavita, Mayur, Himanshu, Ramkrishna, Deepak, Manab, Mrinalini, Dheeraj, Srinibas, Antim, Ananta for creating a pleasant and vibrant laboratory atmosphere and making my days memorable. I am blessed to have friends and well-wishers like Tanumoy, Mihir, Khadimul. I could always count on them when I needed help.

Tamal Pal

Dedicated to

my late grandfather, Sri Taraknath Pal

Thesis Abstract

The exponential increase of global population and the enduring dependence on fossil fuel resources causes huge challenges towards mankind. In terms of energy density, H_2 is unparalleled, possessing the highest energy density (approximately 142 kJ/mol) in comparison to all other fossil fuels and energy sources. it is noteworthy that nearly 65% of hydrogen's overall production is allocated for synthesis of NH_3 by Haber-Bosch process as well as polyester and resin production. The conventional sources from which hydrogen is produced encompass a variety of materials, notably including natural gas, various hydrocarbons, and water in its liquid form. At present, the production of hydrogen is predominantly attributed to natural gas, heavy oils, naphtha and coal, which creates enormous pollution. The substantial progress achieved in the field of photocatalytic H_2 production has effectively established photocatalysis as a promising intermediary technology that facilitates the conversion of solar energy into H_2 fuels, a development that has unfolded over the last forty years and highlights the increasing importance of such technologies in addressing global energy challenges.

The work embodied in the thesis entitled **"Optimizing Photocatalytic Hydrogen Evolution Through Synergistic Charge Transfer in Donor Acceptor Based Hybrid Photocatalyst"** focusses broadly in the four areas (1) Probing on the role of degree of chemical reduction in RGOs for improved photocatalytic activity of $MAPbI_3$/RGO heterostructures through appropriate band alignments. (2) Role of solvent assisted morphology dependent MAPI has been investigated for better photocatalytic and photoelectrochemical activities. Altercation in reaction medium from HI to DMF not only alter the surface morphology from cuboid to rod shape, it also influences various aspects of photocatalytic and photoelectrochemical activities. $MAPI_{DMF}$ exhibited superior performances in terms of HER activities by 28 times Compared to $MAPI_{HI}$. Alongside role of polyfluorene polymer in the encapsulation of $MAPbI_3$ microcrystal by through electrostatic interaction, which enhances both the structural integrity in ambient moisture abundant atmosphere as well as the photocatalytic H_2 evolution rates. (3) Rational design of heterostructures made of amorphous MoS_2 and environment friendly lead free MABI, where boosted HER performance was achieved through smooth transition from type I to type II heterojunction by atomic level alteration in chemical composition. (4) Formation of g-C_3N_4 based covalent heterostructure. Where carbon nitride was directly anchored with metal co-ordinated ligand centers through covalent bonding enabling improved millimole scale H_2 evolution rates.

The dissertation begins with a brief general introduction, **Chapter 1**, which serves as a background for this thesis and as a basis for the works that are presented in the following chapters.

In chapter 2, role of oxygen content dependent RGOs in MAPI/RGO heterostructures has been investigated for photochemical and photoelectrochemical activities. This chapter also summarizes the fact that variation in extent of chemical reduction not only controls the atomic percentage of oxygen content, but also governs the varied bandgaps as well as band edge positions for three variants of RGOs. Among all these variations, S2_RGO with bandgap of 2.59 eV and oxygen content of 24% was identified as the best performing co-catalyst with highest HER. On contrary MAPI/S3_RGO registered lowest photoelectrochemical and HER activities where S_3/RGO is the most chemically reduced variant of RGO with lowest oxygen content (18%) with a bandgap of 2.33 eV. For MAPI/S1_RGO composites the performance were slightly lesser than MAPI/S2_RGO. To rationalize the occurrence of disparities in photoelectrochemical and photocatalytic activities of all three MAPI/RGO composites, we have proposed an electron transfer mechanism, where depending upon the relative CBM positions of MAPI and respective RGO, dissimilar photogenerated electron transfer took place.

Chapter 3, summaries the role of solvent assisted morphology dependent MAPI has been investigated for photocatalytic and photoelectrochemical activities. Altercation in reaction medium from HI to DMF not only alter the surface morphology from cuboid to rod shape, it also influences various aspects of photocatalytic and photoelectrochemical activities. $MAPI_{DMF}$ exhibited superior performances in terms of HER activities by 28 times Compared to $MAPI_{HI}$. The superior HER performances of $MAPI_{DMF}$ were supported by quenched photoluminescence intensity, higher photocurrent, lower charge transfer resistance. The improved photocatalytic and photoelectrochemical activities might be attributed to larger surface area possessed by rod shape $MAPI_{DMF}$. A greater surface area provides more reaction sites, enabling the absorption of a higher number of photons resulting accelerated H_2 evolution. A stable $MAPbI_3$/polyfluorene composite was successfully prepared by an *in-situ* fabrication. The incorporation of polyfluorene on $MAPI_{DMF}$ surfaces not only broadens the light absorption range but also enhances charge segregation and transport at the $MAPI_{DMF}/PF_{10}$ interface, leading to improved photocatalytic and photoelectrochemical activities. Under optimized conditions, $MAPI_{DMF}/PF_{10}$ exhibited a maximum HER activity of 6200 μmol h^{-1} g^{-1}. The enhanced HER activity of $MAPI_{DMF}/PF_{10}$ may be attributed to the efficient interfacial charge transfer from $MAPI_{DMF}$ to the polyfluorene co-catalyst owing to proper alignment of CBM of $MAPI_{DMF}$ and the LUMO of polyfluorene.

Chapter 4 summarizes the influence of phosphorus doping on band gap and energy levels. This study elucidates that the band gap of MoS_2 declines from 1.39 eV for pristine MoS_2 to 1.28 eV for P50_MoS_2, and it further diminished to 1.07 eV for P100_MoS_2 upon doping with P. Concurrently, the VBM energy level of all the MoS_2 variants experienced a downward shift. Consequently, P50_MoS_2/MABI and P100_MoS_2/MABI composites have established a type II heterojunction, whereas MoS_2/MABI results in a type I heterojunction.

It is noteworthy that type II heterojunctions are typically more favorable for the separation and migration of photogenerated charges when compared to type I heterostructures,

P50_MoS$_2$/MABI demonstrated superior photocatalytic and photoelectrochemical efficiencies relative to the others. Even though P100_MoS$_2$/MABI possessed type II heterojunction still it exhibited the least reaction rates among three composites. The relative energy band positions of P100_MoS$_2$ and MABI might be attributed to the diminished HER activity. The CBM of P100_MoS$_2$ was located at significantly deeper energy level compared to E(H^+/H_2), inhibiting its function as a photoelectron carrier, thereby resulting in the compromised photocatalytic HER activities of P100_MoS$_2$/MABI composites.

Chapter 5 summarizes the chemical functionalization of g-C_3N_4 via a covalent methodology employing cyano porphyrin has been demonstrated to serve as a significant tactic for augmenting and introducing novel properties to g-C_3N_4, thereby facilitating charge separation and enhancing visible light absorption in the tail region. This advancement enables the attainment of improved HER activities from ascorbic acid aqueous solutions. The covalent grafting of porphyrin moieties onto the g-CN sheet has provided coordination sites for transition metals such as Ni^{2+} and Co^{2+}. The Metal co-ordinated por_g-CN could further enhance the H_2 evolution rates. The presence of metalated porphyrin moieties on g-CN has been shown to alter the kinetics of photogenerated charge migration, as evidenced by photocurrent and impedance studies. Porphyrin-anchored g-CN has demonstrated hydrogen evolution of 3200 $\mu mol \cdot g^{-1}h^{-1}$. Notably, the maximum hydrogen evolution recorded was 4200 $\mu mol \cdot g^{-1}h^{-1}$, achieved by Co_por_g-CN. This accelerated HER performance was attained through covalent linkage, where the migration of photogenerated charge transfer was considerably more feasible in comparison to conventional heterostructures. Between the Ni and Co metalated photocatalysts, Co_por_g-CN exhibited a slight upper hand in terms of HER activities. In the case of transition metal-coordinated photocatalysts, prior to the formation of molecular hydrogen, metal hydride bonds are established. The cleavage of the metal hydride bond is regarded as the rate-determining step (RDS) that governs the rate of hydrogen evolution. The displacement of the H^- ion, which initiates the formation of molecular H_2, is considerably more facile for Co_por_g-CN.

Table of Contents

Chapter 1: Introduction

Chapter 2: Composites of Reduced Graphene Oxide and $MAPbI_3$ Crystals for Photocatalytic Hydrogen Generation

Chapter 3: Solvent assisted shape dependent $MAPbI_3$/polyfluorene heterostructures with larger surface area for improved photocatalytic H_2 evolution

Chapter 4: Transformation from type-I to type-II $MA_3Bi_2I_9$ based heterostructure photocatalyst via energy band engineering

Chapter 5: Molecularly Doped Porphyrin Covalent Heterojunction Carbon Nitride Instigating Cocatalyst-Free Solar Energy Harvesting via Water Splitting

Lists of Figures

Lists of Tables

Lists of abbreviation

MAPI	**Methylammonium Lead Iodide ($MAPbI_3$)**
GO	Graphene Oxide
RGO	Reduced Graphene Oxide
EIS	electrochemical impedance spectroscopy
E_{FB}	Flat band potential
PF	Polyfluorene polymer
$MAPI_{HI}$	HI assisted $MAPbI_3$
$MAPI_{DMF}$	DMF assisted $MAPbI_3$
$MAPI_{DMF}/PF_{10}$	Heterostructures made of $MAPI_{DMF}$ and polyfluorene (10 wt%)
BET	Brunauer, Emmett, and Teller
DMAP	4-Dimethylaminopyridine
MABI	$MA_3Bi_2I_9$
DAT	2,4-diamino-1,3,5-triazine
g-CN	graphitic carbon nitride ($g-C_3N_4$)
g-CN_Por	Porphyrin doped $g-C_3N_4$
E_f	Fermi energy level

[This page was left empty intentionally]

CHAPTER 1

Introduction

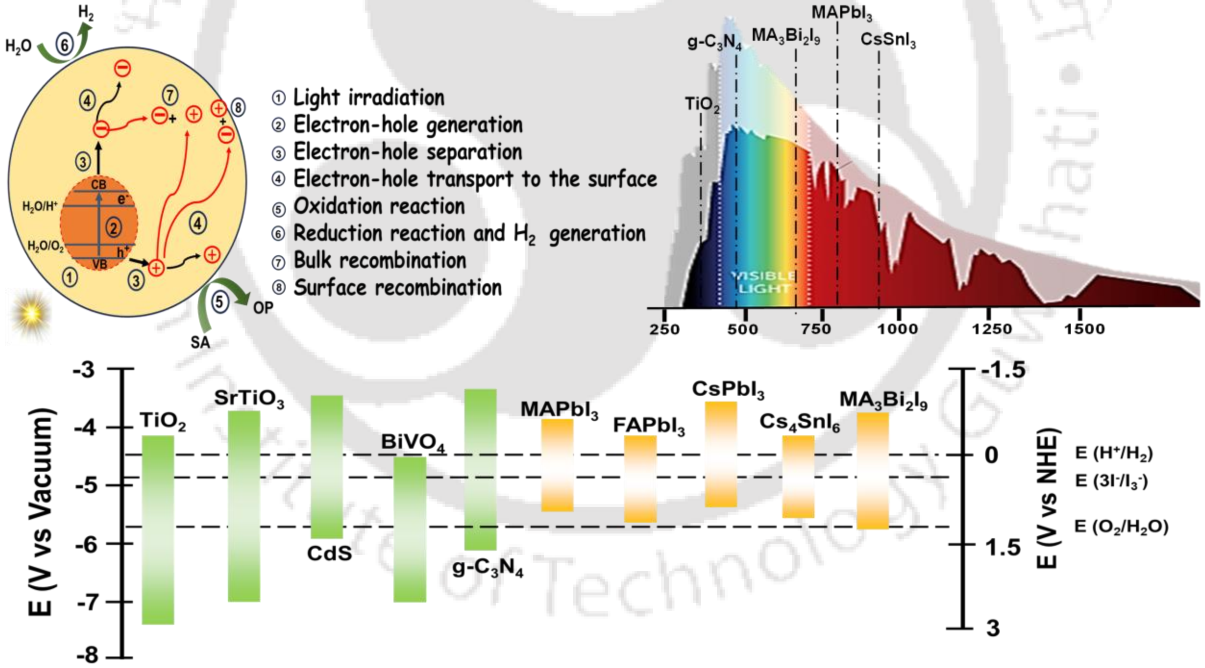


भारतीय प्रौद्योगिकी संस्थान गुवाहाटी
Indian Institute of Technology Guwahati

1.1 Energy crisis & environment friendly alternatives:

Humanity currently finds itself grappling with a multifaceted crisis that encompasses both energy shortages and environmental degradation, a predicament that can be largely attributed to two critical factors that are interrelated: the exponential increase of global population and the enduring dependence on fossil fuel resources. Forecasts suggest that the world population is poised to increase dramatically, with estimates indicating a rise of approximately 40-50% within the forthcoming five decades, culminating in a total exceeding 9 billion individuals by the mid of 21st century, 2050.[1, 2] This rapid and significant demographic growth presents two profound challenges that society must confront. Firstly, it will inevitably lead to a heightened demand for energy resources, creating an unprecedented necessity for energy production and consumption by the year 2050. Secondly, this burgeoning population will catalyse an accelerated depletion of the planet's finite fossil fuel reserves, with particular emphasis on the extraction and utilization of coal and natural gas reserves, which are already under substantial stress from existing consumption patterns.

In light of this situation, it is important to recognize that the prevailing economic paradigm, which governs societal interactions and resource management, exerts a profound influence on the life-cycle assessments and benchmarks that are pertinent to our society. The life-cycle paradigm, which encompasses the comprehensive and extensive consumption of modern commodities and goods, can trace its roots back to the era of the industrial revolution, a period characterized by the widespread embrace of an economy heavily reliant on fossil fuels. Within this particular economic framework, the utilization of petroleum began to proliferate, finding applications in both transportation systems and various industrial processes, thereby rapidly solidifying its position as the predominant energy source of choice. Despite the considerable advantages and conveniences provided by petroleum, as well as the remarkable innovations in transportation and product development that accompanied its rise, certain segments of the population remained sceptical and wary of its long-term viability and sustainability. It was only after the insightful and prescient warnings issued by M. King Hubbert, who forecasted the imminent depletion of the Earth's oil reserves,[3] that a broader societal concern began to crystallize regarding this pressing issue, a concern that was rooted in the understanding of the protracted geological processes required for the formation of these fossil fuels within the Earth's crust.[4, 5] This alarmingly accurate prediction gained validation during the initial oil crisis that transpired between the years 1973 and 1979, a pivotal moment that sparked widespread awareness and discussion about energy resources and their limitations. Since that critical juncture, CO_2 emissions have continued to ascend at an alarming rate,[6] contributing to a concerning trend that correlates with a significant increase in global surface temperatures, which has risen by approximately 0.9 °C by the year 2020,[7, 8] visually represented in **Figure 1**.

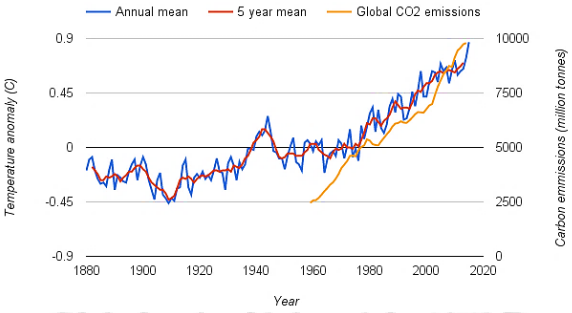

Figure 1.1: Temperature anomaly and carbon emission around the globe within 1980-2020. (ref. 8)

The global emissions of CO_2 can be attributed to consumption and utilization of solid or liquid fossil fuels, illustrated in **Figure 2**, that has emerged as the principal catalyst for the dramatic escalation observed in recent decades, thereby playing a pivotal role in the broader phenomenon of climate change.[9] **Figure 3** displayed the energy supply distribution confirming use of conventional non-renewable fuel such as coal (33%), natural gas (32.7%), nuclear (19.5 %), petroleum (0.7%).**[10]**

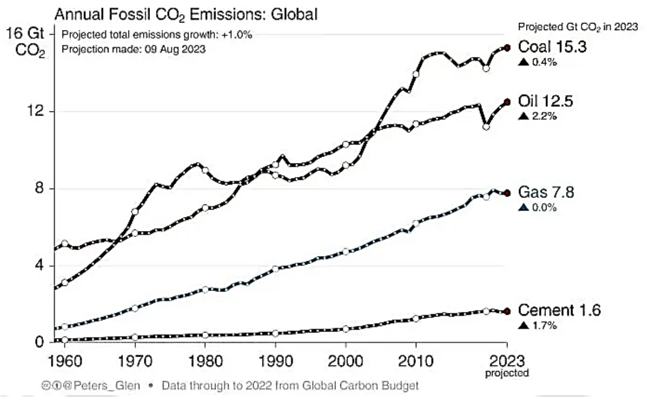

Figure 1.2: Global emissions of CO_2 due to consumption and utilization of fossil fuels and solid or liquid forms. (ref. 9)

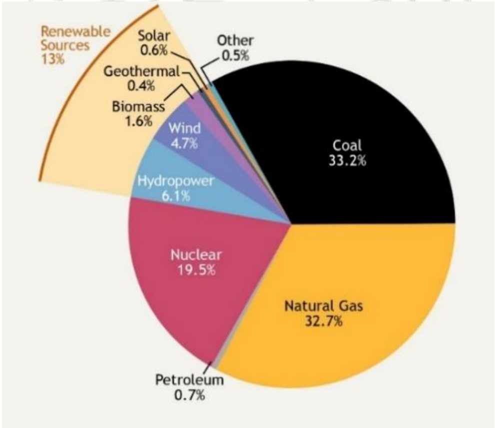

Figure 1.3: Different Energy sources used to generate electricity. (ref 10)

1.2 Renewable energy: an alternate solution:

The implementation of renewable energy sources is increasingly recognized as a feasible and sustainable solution for the gradual elimination and substitution of traditional fossil fuels,[11] which have long been associated with detrimental environmental effects and resource depletion. Among the established renewable energy forms available, which include tidal and ocean currents, wind energy, hydroelectric power, biomass, geothermal energy, and solar power, it is solar energy that stands out as the most promising and viable alternative, primarily due to its ability to harness the sun, an energy source that is both abundant and powerful.[12] A multitude of initiatives, research projects, and technological advancements have been actively pursued and realized across a broad array of solar energy systems, reflecting the growing interest and investment in this field. It can be convincingly asserted that photovoltaic technology, alongside concentrated solar power (CSP) methodologies, has attained unprecedented levels of sophistication and development to date, thereby achieving significant acceptance and integration within the broader energy sector. Furthermore, the increasing recognition of the potential of solar energy has mobilized ongoing research and innovation, aimed at enhancing efficiency and reducing costs, which could further bolster its adoption in various applications. Consequently, the journey toward a sustainable energy future appears to be increasingly reliant on the continued advancement and deployment of solar energy technologies, underscoring their essential role in a comprehensive strategy to transition away from fossil fuel dependency.

1.2.1 Hydrogen

Hydrogen stands as the most diminutive among all the elements that have been identified to date, and it simultaneously holds the distinction of being the most abundant chemical element throughout the vast expanse of the universe. The reason for its absence in a natural state on the surface of the Earth can be attributed to the fact that H_2, exhibits a density that is significantly lower than that of the surrounding air, which leads to its tendency to disperse into the atmosphere rather than remaining concentrated in one location. This element is not only noted for being exceedingly light, but it also boasts environmentally friendly characteristics that make it a desirable fuel option; however, it is important to recognize that hydrogen engages readily in a variety of chemical reactions with numerous other substances, which underscores its remarkable potential as an effective reactant in various chemical processes. [13] As a result of these properties, hydrogen can serve as a source of fuel, whether through direct combustion in traditional internal combustion engines or via utilization in hydrogen fuel cells, both of which yield water as the sole byproduct, thereby completely avoiding the emission of greenhouse gases such as carbon dioxide (CO_2), and firmly establishing hydrogen as a viable alternative fuel that is both clean and sustainable.[14]

In terms of energy density, H_2 is unparalleled, possessing the highest value in comparison to all other energy sources. This is primarily due to its substantial energy content, which is calculated to be approximately 142 kJ/mol; this value is notably two to three times greater than the energy content of traditional fossil fuel, like methane at 55 kJ/mol, propane at 50.3 kJ/mol, gasoline at 45.8 kJ/mol, and natural gas at 47.2 kJ/mol.[15]

The anticipated demand for hydrogen, along with its utilization, is expected to increase significantly, driven by its intrinsic qualities of being non-polluting, inexhaustible, efficient, and economically viable, characteristics that are pivotal in the context of the energetic transition from reliance on fossil fuels to the establishment of a hydrogen economy, a paradigm that has gained traction particularly after the political upheavals that occurred in the Middle East during the 1980s. Given this backdrop, there has been a notable surge in societal motivation to adopt hydrogen as a central component of an economic model.[16] An ideal system for the production of H_2 necessitates the adoption of the water electrolysis technique, which should be powered by a clean and renewable electricity source, thereby ensuring the establishment of an environmentally sustainable cycle that supports the broader goals of sustainable development and energy transition.[17]

1.2.2 Hydrogen production & consumption

The conventional sources from which hydrogen is produced encompass a variety of materials, notably including natural gas, various hydrocarbons, and water in its liquid form. At present, the production of hydrogen is predominantly attributed to natural gas, which accounts for approximately 48% of the total output, while heavy oils and naphtha contributed around 30%, and coal contributes about 18% to this energy sector.[18] Due to its diverse and multifaceted characteristics as a fuel, hydrogen finds extensive application across a range of industrial processes; for example, it is noteworthy that nearly 65% of hydrogen's overall production is allocated for synthesis of NH_3 by Haber-Bosch process as well as polyester and resin production as depicted in **Figure 4**. Furthermore, another significant domain of application for hydrogen is within the oil refining industry, where it is employed for a multitude of purposes, predominantly in the hydrocracking process, which facilitates the transformation of long-chain hydrocarbons into lighter, more usable hydrocarbons, as well as in the hydrodesulphurization process that effectively eliminates sulfur compounds from petroleum products, and in the de-aromatisation process that is aimed at the extraction of aromatic compounds from complex mixtures, particularly as a component of the broader oil refining procedure.[19] In addition to the aforementioned applications, hydrogen is also utilized in comparatively smaller quantities as a propellant in aerospace technology, specifically in rocket propulsion systems, where its unique properties are harnessed for efficient thrust generation in space exploration endeavours.

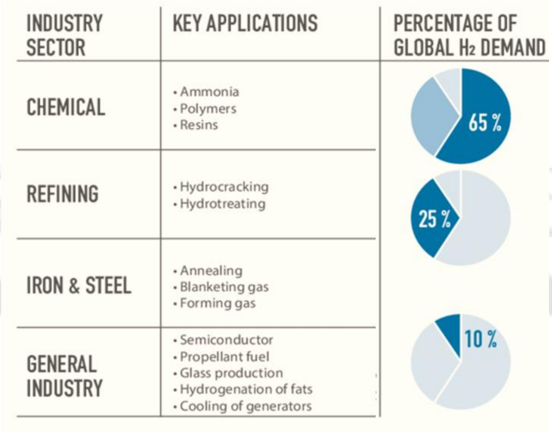

INDUSTRY SECTOR	KEY APPLICATIONS	PERCENTAGE OF GLOBAL H₂ DEMAND
CHEMICAL	• Ammonia • Polymers • Resins	65 %
REFINING	• Hydrocracking • Hydrotreating	25 %
IRON & STEEL	• Annealing • Blanketing gas • Forming gas	
GENERAL INDUSTRY	• Semiconductor • Propellant fuel • Glass production • Hydrogenation of fats • Cooling of generators	10 %

Figure. 1.4: Global hydrogen demand and production from various sources.

1.2.3 Solar driven H_2 production

The initial documented instance of ultraviolet (UV) light-induced photocatalytic hydrogen generation utilizing titanium dioxide (TiO_2) was reported in the year 1972,[20] a landmark event that has motivated an extensive and multifaceted range of scientific inquiry and technological advancement spanning several decades, ultimately culminating in a variety of applications that hold significant relevance for human society; these applications range from essential processes such as energy conversion, which includes techniques like water splitting and carbon dioxide (CO_2) reduction, to transformative chemical reactions and the remediation of organic pollutants that threaten environmental sustainability.[21] The substantial progress achieved in this field has effectively established photocatalysis as a promising intermediary technology that facilitates the conversion of solar energy into chemical fuels designed for storage, a development that has unfolded over the last forty years and highlights the increasing importance of such technologies in addressing global energy challenges. Among the various non-fossil-based fuels, hydrogen emerges as a particularly noteworthy candidate, widely acknowledged within the scientific community as a highly promising energy carrier for the future. However, the principal obstacle that hampers the widespread adoption of hydrogen gas as a viable fuel source resides in its natural scarcity, coupled with the lack of economically viable, environmentally friendly, and non-nuclear methods for its production, in addition to the complexities associated with its storage and transportation logistics, which further complicate its practical implementation in energy systems. Consequently, the process of converting solar energy into hydrogen, commonly referred to as the generation of solar fuels assumes critical significance in the context of the evolving energy landscape anticipated in the forthcoming decades.[22]

In the realm of photocatalysis, a photocatalyst operates by absorbing ultraviolet (UV) light and/or visible light irradiation emitted from either sun or an artificial illuminated light source, thereby initiating a series of intricate photophysical processes. During this absorption phase, electrons residing in the VB of the photocatalyst are elevated to the CB, resulting in the creation of holes within the VB; this phenomenon effectively generates pairs of negatively charged electrons (e^-) and positively charged holes (h^+). This particular phase is commonly referred to as the "photo-excited" state of the semiconductor material, where the energy differential separating the VB from the CB is termed the "band gap," which plays an exceedingly vital role in the absorption of sunlight and other forms of light. It is imperative that this energy gap corresponds suitably to wavelength of incident light to ensure effective absorption by photocatalyst material. Followed by the process of photoexcitation, the excited electrons and holes undergo a separation process and got transferred to the photocatalyst surface, where, in the context of the photocatalytic HER, they function as reductant and oxidant respectively, in the production of H_2 and O_2 gases, thus facilitating the generation of these essential energy carriers.

1.3 Basics and history of photocatalytic H_2 production

1.3.1 Genesis

The conceptual foundation of photo-assisted electrolytic water splitting is profoundly rooted in the groundbreaking research conducted by the esteemed scientists Fujishima and Honda in the year 1972, who ingeniously employed ultraviolet (UV) light to irradiate a titanium dioxide (TiO_2) anode that was systematically paired with a platinum cathode illustrated in **Figure 1.5**, thereby laying the groundwork for the inception of contemporary heterogeneous photocatalysis utilizing TiO_2 along with a variety of other compatible materials, ultimately igniting a plethora of extensive endeavours aimed at the meticulous design of highly efficient heterogeneous photocatalysts specifically for the purpose of water splitting.[20] Despite the monumental significance of this scientific breakthrough, which unequivocally paved the way for novel avenues in the production of solar fuels. The process of cleaving water into its molecular components of hydrogen and oxygen has remained an elusive goal that has yet to be fully realized in practice. When the surface of the TiO_2 electrode is subjected to irradiation by UV light, oxygen evolution is instigated at the TiO_2 electrode as a direct consequence of a water oxidation reaction. While concurrently, the reduction process facilitates the evolution of hydrogen at the platinum black electrode. A prominent limitation associated with the pioneering approach arises due to the intrinsic characteristics that are inherently linked to the electronic structure of TiO_2, which is characterized by an optical band gap that exceeds 3 eV, thereby necessitating the utilization of UV radiation, a form of light that constitutes a mere 5% of the total solar radiation that reaches the earth surface.[23] This innovative concept, which was fundamentally derived from the operational principles underlying photoelectrochemical cells that utilize semiconductor electrodes, was subsequently adapted and advanced by the distinguished researchers across the globe. They applied this foundational knowledge to the creation of a sophisticated system for photocatalysis that employs semiconductors in form of particles or powders as effective photocatalysts.

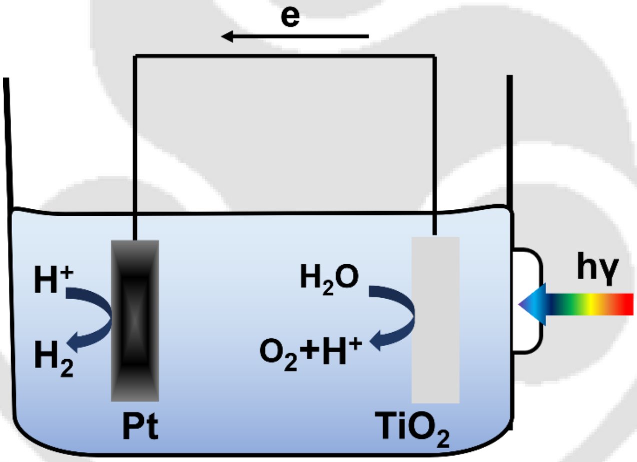

Figure 1.5: Diagram of a photoelectrochemical cell (PEC).

1.3.2 Fundamentals & factors effecting Photocatalytic water splitting

Reactions that are instigated by photocatalytic materials typically adhere to a series of sequential processes, which can be delineated as follows, also illustrated in **Figure 1.6.**[24]

(a) the initial step involves the absorption of photons, which subsequently leads to generation of charges that are crucial for the photocatalytic activity.

(b) Following this photon absorption, there occurs a migration of the photogenerated charge carriers, which are electrons and holes, towards the surface of the photocatalytic material, where they can engage in further reactions.

(c) It is important to note that a significant proportion of these charge carriers are often neutralised either within the bulk structure or at the surface of photocatalyst, primarily through interactions characterized by Coulomb forces, or they may be captured by traps such as structural defects present in the material.

(d) Consequently, only a limited fraction of the photogenerated charge carriers is able to ultimately engage in the redox reactions, which in turn leads to a suboptimal performance in terms of photocatalytic chemical oxidation and reduction activities, as well as a correspondingly low quantum yield, reflecting the inefficiencies inherent in the system.

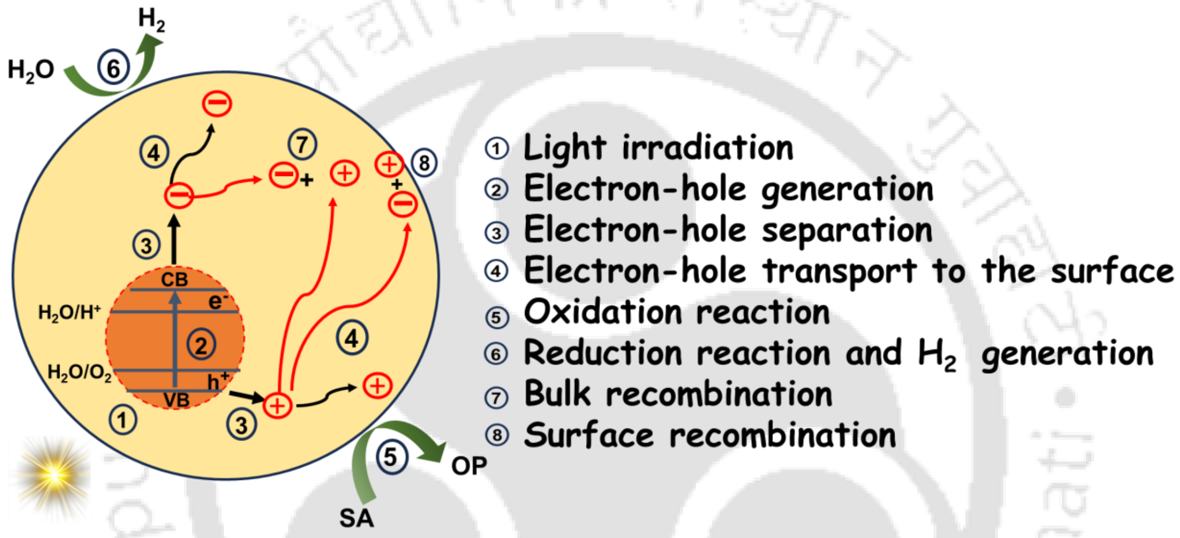

Figure 1.6: A Solar driven water splitting process containing the specific steps involved during solar activation of the photocatalyst. (Black arrows show favourable steps, while red arrows show unfavourable steps.)

1.3.3 Thermodynamic feasibility

In order to effectively facilitate the simultaneous processes of reduction and oxidation of H_2O, it is of paramount importance that the adherence to two specific thermodynamic prerequisites is achieved without compromise. These two indispensable factors consist of the precise matching of the band gap in conjunction with the impeccable alignment of the band position, which are both critical to the overall efficiency of the process. To successfully generate photoexcited electrons and holes, it is essential that the energy of incident photons is not only equal to but indeed exceeds the threshold defined by its band gap. The process of water splitting into H_2 and O_2 is inherently characterized as an uphill thermodynamic reaction, necessitating additional energy input as shown in **Figure 1.7.**[25] The standard Gibbs free energy change associated with this reaction, denoted as **ΔG^0**, is quantified as 237 kJ/mol, which equivalently translates to approximately 1.23 eV, as illustrated in **Equation 3**. Consequently, it follows that the band gap value (**E_g**) of the photocatalyst must have to be larger than 1.23 eV, corresponding to wavelengths of less than 1000 nm, in order to satisfy the thermodynamic requirements necessary for the achievement of effective water splitting depicted in **Figure 8**. Nevertheless, for the utilization of visible light within the spectrum, it is crucial that the band gap energy is maintained below 3.0 eV, which corresponds to wavelengths greater than 400 nm.[26] In this particular context, the electrons are observed to transition from the valence band to the conduction band, while concurrently, the holes remain localized within the valence band, thereby influencing the overall charge carrier dynamics.

$2H^+ + 2e^- = H_2, E_{redox} = 0$ V (**Equation 1**)
$2H_2O + 4h^+ = 4H^+ + O_2, E_{redox} = 1.23$ V (**Equation 2**)
$H_2O = H_2 + 1/2O_2, \Delta G = +237$kJ/mol (**Equation 3**)

The charges by photo irradiation possess the capability of H^+ reduction and H_2O oxidation, respectively, contingent upon the stipulation that both oxidation and reduction potentials of water must reside in the limit of photocatalyst band gap. Specifically, the lower energy level of CB must exhibit a potential of more -ve than that of the reduction potential of H^+/H_2 (0 V vs NHE at pH=0), the upper energy level of the VB must demonstrate a potential more +ve than that of the oxidation potential of O_2/H_2O (1.23 V vs NHE at pH=0), as depicted in **Figure. 1.8**. In order to enhance the solar-to-hydrogen (STH) efficiency, the band gap of the semiconductor should be minimized to facilitate the consumption of greater proportion of visible light from the solar spectrum. Nevertheless, the process of narrowing the band gap may result in a diminished driving force that offsets the threshold energy barrier connected with the redox reaction. The phenomena of charge separation, charge carrier mobility, transfer of charge carriers to active surface sites, devoid of recombination or trapping, are all critical processes that govern the efficacy of solar driven water splitting. Nonetheless, numerous factors including crystallinity, crystal structure, surface morphology, surface area and the presence of cocatalysts will also influence these aforementioned processes.[27] The band edges in the energy levels of the semiconductor photocatalyst typically fluctuate with variations in pH. Furthermore, the phase stability of photocatalyst across differing pH conditions also contributes significantly to its performance.

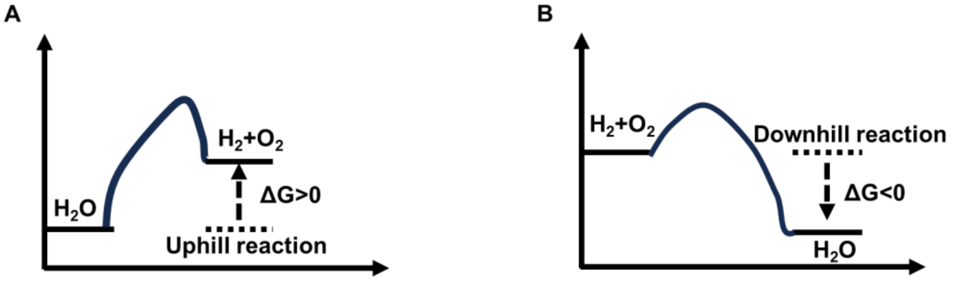

Figure 1.7: Gibbs free energy change for (A) water splitting and (B) the reaction between H_2 and O_2.

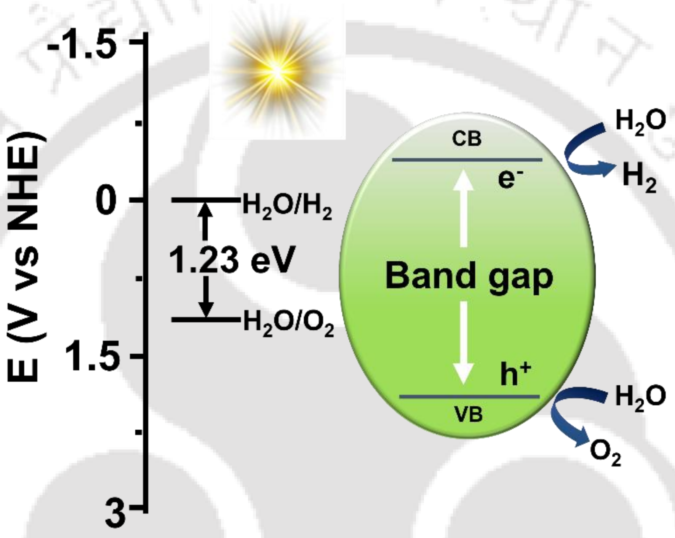

Figure 1.8: Fundamental principle of semiconductor-based photocatalytic water splitting for hydrogen generation.

1.3.4 Kinetic factors

In addition to the thermodynamic obstacles, the kinetics associated with water splitting also presents significant challenges. In the realm of photocatalysis, the processes involving the generation, separation, and migration of photogenerated charge carriers typically occur over a time scale ranging from femto- to nano-seconds. Conversely, the surface redox reactions necessitate a considerably longer duration (micro- to seconds) for completion and are frequently the rate-limiting factor.[28] Notably, the most sluggish phases in the photocatalytic water-splitting process were the surface reactions, which encompass the HER through proton reduction and the OER via oxidation. The HER results in the formation of H_2, while the OER perpetually supplies protons for the HER and depletes holes created by photo excitation.

Nonetheless, it is observed that the OER generally proceeds at a significantly slower rate than that of the HER.

1.3.5 Cocatalyst

photocatalysts devoid of co-catalysts frequently demonstrate notably diminished or even entirely absent HER activity. Co-catalysts boost the efficacy of semiconductor photocatalysts in photocatalytic hydrogen generation through various mechanisms.[29]

Firstly, these substances have the capacity to enhance light absorption. Cu_2O nanogranules that were subsequently coated with Pt and Au nanolayers (Au/Cu_2O/Pt), discovering that Au/Cu_2O/Pt photoelectrodes significantly improve light absorption by facilitating photoinduced electron transport attributable to the surface plasmon resonance (SPR) phenomenon and the resultant hot electrons generated from the electron collector layer (Pt).[30]

Secondly, co-catalysts can significantly bolster charge transport at their interfaces with semiconductors. The incorporation of co-catalysts onto semiconductors represents a promising strategy to enhance the separation and transport of photoexcited electron-hole pairs, mitigate charge recombination, and thereby elevate the photocatalytic efficacy of solar water splitting processes.[31, 32]

Thirdly, co-catalysts can provide highly active sites for photocatalytic reactions involving H^+ reduction and H_2O oxidation by reducing the corresponding activation energy barriers. Additionally, these materials can improve the stability of photocatalysts by inhibiting photo-corrosion. For instance, the long-term productivity of Cu_2O photocatalysts is typically low due to self-photodecomposition, which limits their overall performance. Consequently, the incorporation of co-catalysts could substantially enhance carrier transfer efficiency, and modifications in the charge transfer pathway contribute to the mitigation of self-decomposition.[33]

1.3.6 Sacrificial agents

The utilization of sacrificial agents (SA) represents one of the most efficacious strategies to enhance HER activity. In a conventional solar driven hydrogen generation procedure, the electrons generated by light exposure facilitate the reduction of protons (H^+) to H_2, whereas the photogenerated holes are utilized in the oxidation (such as the oxygen evolution reaction, OER). Specifically, the function of SA is to offer a straightforward pathway for interaction with the holes, typically through a one-electron transfer mechanism, thereby substituting the more complex four-electron OER.[34] The single-electron transfer pathway generally exhibits significantly lower overpotentials and accelerated reaction kinetics compared to OER. Moreover, SA-facilitated HER can circumvent the formation of diatomic oxygen from OER, maintaining an oxygen-free environment throughout the entirety of the photocatalytic reaction.[26] Ultimately, by capturing the excess holes, the incorporation of SA can substantially mitigate photo-corrosion effects as shown in **Figure 1.9.**

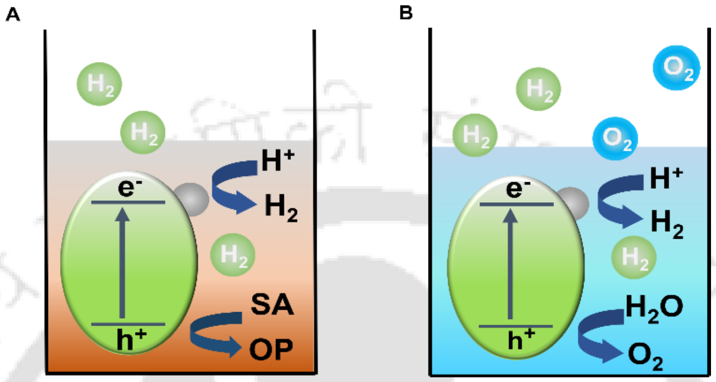

Figure 1.9: Photocatalytic sacrificial agent mediated HER and water splitting (A) Photocatalytic sacrificial agent-assisted HER. (B) Photocatalytic water splitting.

Abbreviations: SA, sacrificial agent; OP, oxidation product.

1.4 Metal halide perovskite based Photocatalytic H_2 evolution

The pursuit of an advanced semiconductor photocatalyst characterized by superior photoconversion efficiency has prompted researchers to explore a vast array of semiconducting substances. An optimal photocatalyst embodies a multitude of essential attributes, including a wide spectrum of light absorption, prolonged operational durability, effective charge separation, and appropriate redox potential for targeted photocatalytic reactions. Nevertheless, the photocatalysts identified to date fall significantly short of this ideal benchmark. Since its discovery, TiO_2 has garnered considerable attention among various photocatalytic materials due to its affordability, non-toxic nature, and enhanced photochemical resilience. However, its substantial bandgap serves as a constraining factor which hinder the effective harnessing of solar photons. Similar to TiO_2, the ABO_3 and AB_2O_4 structural materials are also semiconductors with large bandgap that operate exclusively in the UV range. Conversely, other oxide materials, such as ABO_4, ABO_2, aurivillius oxides, and ternary chalcogenides, are capable of absorbing visible light. Yet, their inappropriate band edge alignments render them unsuitable for catalysing photocatalytic reactions, thereby inherently restricting their applicability.[35] Consequently, the inadequate photoreduction potential of these substances, attributable to their extensive bandgap and rapid recombination of charge carriers, intensifies the motivation to engineer novel semiconductor-based photocatalyst systems with desirable photoactive properties through innovative materials discovery.

Since Miyasaka and associates initiated the development of hybrid halide-perovskite-based solar cell in 2009,[36] metal halide perovskite (MHP) semiconductors have captivated the attention of scholars globally due to their efficacious utilization in high-performance optoelectronic devices, which encompass efficient solar cells, light-emitting diodes (LEDs), photodetector and lasers apparatuses. MHPs are classified as ionic crystals characterized by ABX_3. In this formula, 'A' denotes as cation of mono valency (MA^+, FA^+ and Cs^+); 'B' signifies a bivalent ion such as Pb^{2+}, Sn^{2+}, or Cu^{2+}; while X represents ions like Cl^-, Br^-, or I^-. [37] The documented metal MHP photocatalysts can be categorized into several groups, including lead-based hybrid perovskites, perovskites made of all-inorganic precursor, two-Dimensional Dion–Jacobson hybrid perovskites, ruddlesden–Popper layered perovskites, as well as lead-free perovskites. The lead-free perovskite derivatives, represented by the formulas $A_2B(IV)X_6$ (e.g., Cs_2SnI_6), $A_2B(I)B(III)X_6$ (e.g., $Cs_2AgBiBr_6$), and $A_3B(III)_2X_9$ (e.g., $Cs_3Bi_2Br_9$), have recently been synthesized as photocatalysts as an environment friendly alternative to the toxic lead containing perovskites.[38]

The structural integrity of materials is significantly influenced by the interactions between the cations at A site and BX_6^{4-} octahedra. The general composition of ABX_3 encompasses BX_6^{4-} octahedra that share vertices, thereby constructing a three-dimensional network, wherein the A^+ cations reside within cavities, exhibiting a 12-fold coordination by halide to neutralize charge and reinforce the structural network. The Goldschmidt tolerance factor (t) is frequently employed as a parameter to anticipate the integrity of metal halide perovskites lattice. Typically, a stable perovskite architecture is feasible within the range of $0.8 \leq t \leq 1$.[39] t can be defined as,

$$t= r_A+r_B/(\sqrt{2}(r_A+r_B)) \quad \textbf{(Equation 4)}$$

where r_A, r_B, and r_X are the ionic radii of A^+, B^{2+}, and X^- ions, respectively. Configuration of Ideal symmetrical cubic (α phase) ABX_3 having robust crystal integrity are found only in specific instances, necessitating those approaches to value 1. When the ionic radii deviate excessively, whether being too small or large, the BX_6 unit undergo distortion or tilting, resulting tetragonal (β phase) or orthorhombic (γ phase) arrangements with in lower-symmetry. If $t < 0.8$, the construction of a perovskite structure is not achievable. conversely, when t significantly exceeds 1, the three-dimensional framework of BX_6 octahedra linked by shared vertices becomes unstable, prompting the development of 2D layered perovskite structures. Furthermore, alongside, octahedral parameters μ (defined as r_B/r_X) suggested as supplementary structural stability indicators.[40] When three-dimensional perovskite lattice are diminished to low-dimensional configurations, the constraints on size are alleviated. For instance, in two-dimensional layered perovskites, there exists no limitation on the dimensions of the A-site cations due to the role of A^+ cations as interlayer spacers. Additionally, novel tolerance factors were formulated to accommodate more intricate perovskite compositions.[41]

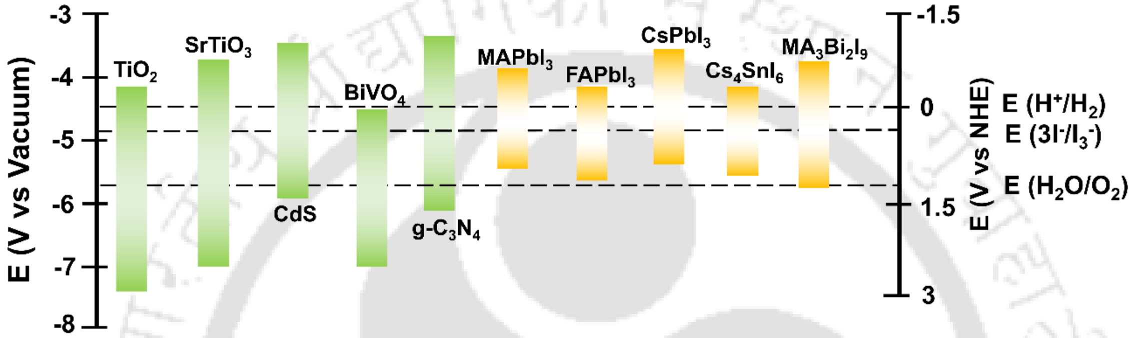

Figure 1.10: Band gap and band position of various photocatalytic semiconductors both conventional and halide perovskite photocatalysts against vacuum and normal hydrogen electrode (NHE).

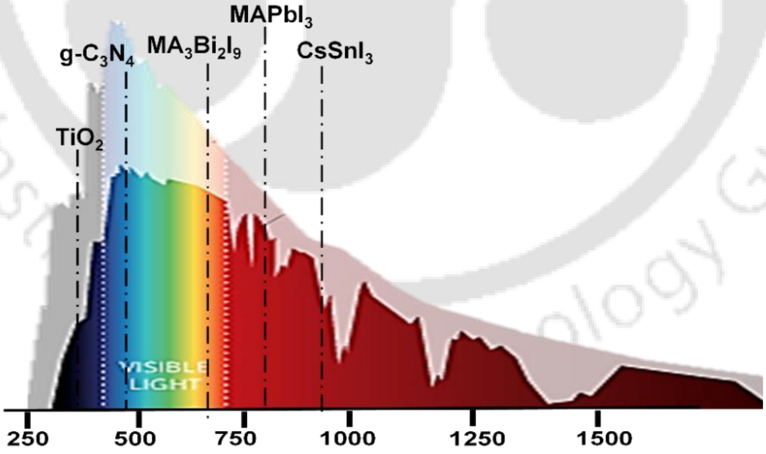

Figure 1.11: Solar spectrum and absorption range of various halide perovskite photocatalysts in comparison to those of TiO_2 and $g\text{-}C_3N_4$.

In comparison to traditional semiconductors, metal halide perovskites demonstrate an appropriate bandgap and exhibit exceptional light absorption efficiency across a broad spectrum. Attributes such as reduced production costs and straightforward solution processing;

adjustable and direct bandgap;[42] extended carrier diffusion lengths;[43] elevated carrier mobility[44] and remarkable defect tolerance have captivated the interest of research communities in perovskite materials.[45] In contrast to more traditional photocatalysts, metal halide perovskites (MHPs) have showcased comparatively smaller bandgap, as illustrated in **Figure 1.10**, facilitating the absorption of sun spectrum of full visible range. Due to such superior optoelectronic characteristics, halide perovskite semiconductors are regarded as optimal candidates for high-performance photocatalysis shown in **Figure 1.11.**[46]

Nevertheless, the inaugural report on halide-perovskite-based photocatalysts, published in 2016,[47] wherein Nam and colleagues delineated a methodology for photocatalytic-driven HI splitting to generate H_2 utilizing $MAPbI_3$, capitalizing on the dynamic equilibrium of dissolution and precipitation in saturated aqueous solution of HI depicted in **Figure 1.12**. They illustrated that when subjected to visible light irradiation (wavelength: $\lambda \geq 475$ nm; intensity: 100 mW cm^{-2}), the photocatalytic hydrogen generation efficacy of $MAPbI_3$ can be maintained for 160 hours without any discernible decrement in performance, and no degradation of the $MAPbI_3$ crystalline phase was noted following the prolonged photocatalytic activity. In the year 2020, Zhao and colleagues engineered a $MAPbI_3$ microcrystal/monolayer MoS_2 nanosheet ($MAPbI_3$-MC/ML-MoS_2) composite photocatalyst for photocatalytic hydrogen evolution reaction (HER) via HI splitting.[48] This photocatalyst demonstrated remarkable long-term stability, exhibiting nearly invariant hydrogen generation activity throughout the entire 208-hour evaluation period under simulated solar irradiation. This dynamic strategy for stabilizing interfacial equilibrium has also been validated as effective for the hydrogen generation catalyzed by lead-containing halide perovskites in various aqueous solutions containing haloid acids.

Despite the efficacy demonstrated by this methodology, the ionic lattice of metal halide perovskites (MHPs) exhibits considerable instability when subjected to conventional photocatalytic reaction conditions. MHPs are prone to rapid decomposition into PbX_2 (where X = I, Br, Cl) precipitates, Cs^+/MA^+/FA^+ cations, and halide ions upon contact with polar molecules. The volatility associated with amine salts which are hygroscopic in nature, particularly the MA^+ and FA^+ cations present in hybrid MHPs, exacerbates moisture-induced disintegration. [49] Additionally, water interacts with lattice via hydrogen bonding, leading to hydration of surfaces, which results in a polycrystalline non-perovskite coating and the formation of grain boundaries.[50] The absorbed water molecules readily permeate through the MHP lattice and produce intermediate hydrate forms through reactions with the $[PbX_6]^{4-}$

octahedral units.[51] The hydrogen bond established between the constituents of organic and inorganic nature plays a pivotal role in maintaining the perovskite structure's stability, which was compromised when water forms two distinct types of hydrogen bonds; first, the robust interaction with the lhalides and the another weaker interaction with the organic cations.[52] The aforementioned instability challenges have catalyzed the formulation of diverse strategies aimed at fostering stable photocatalytic conditions, which can be succinctly categorized as follows: (i) Providing passivation on perovskite surface, [53] (ii) reducing direct exposure by employing solvents and solutions of low polarity, [54] and (iii) encapsulating perovskite nanocrystals to protect them from moisture abundant environment.[55]

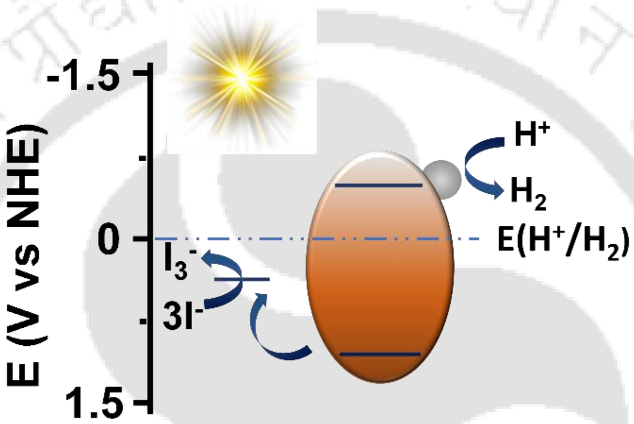

Figure 1.12: Energy diagram of perovskite for photocatalytic HI splitting.

1.5 Heterojunctions

In conventional photocatalytic processes, the redox reaction on surface transpires on a millisecond timescale, substantially slower than the generation of charge carriers (picoseconds), their migration (pico-/nanoseconds), and even their recombination (nano-/microseconds), consequently resulting in considerable amounts of undesirable recombination.[28, 56] Hence, to extend the lifetime of photoexcited carriers and enhance surface reactions, heterojunction photocatalysts are extensively engineered to attain superior photocatalytic efficacy.

A conventional heterojunction is generally characterized as the interface between two distinct semiconductors with differing band positions, potentially resulting into varied band alignments. It represents one of the most prevalently employed methodologies, utilizing a consolidation of two semiconductors within a single intimate framework to form a robust heterojunction.

Typically, heterojunctions in photocatalytic applications are categorized into three types based on the band energy alignment between two semiconductors: Type I (“straddling”), Type II (“staggered”), and Type III (“broken”), as depicted in **Figures 1.12.** Within the heterostructures, light excitation induces the formation of electron-hole pairs and their subsequent separation can occur in one or both parts of heterostructures.[57]

Targeted excitation of a singular semiconductor component and utilizing a wavelength sufficiently long to exclusively excite the component with the narrowest bandgap, can facilitate the migration of charge carriers through the interface, provided that the band alignment permits the system to progress downhill energetically.

1.5.1 Type I, Type II, Type III heterojunctions and efficiencies

In a conventional type-I heterojunction, the energy levels of the CB and VB of one semiconductor (P1) are positioned at elevated and reduced energy region, respectively, in comparison to the analogous bands of another semiconductor (P2) (as depicted in **Figure 1.13A**). Upon exposure to light, the photogenerated charge carriers accumulate within one semiconductor (P2). In this arrangement, effective segregation of electron-hole pairs is not achieved, which signifies the principal limitation of a straddling type junction. Additionally, the redox capability is considerably compromised as the reduction/oxidation reactions transpire in the semiconductor component possessing a lower redox potential (P2), thus substantially undermining the redox efficacy of the heterojunction photocatalyst.[58]

Conversely, within type-II heterojunction photocatalyst, the photogenerated charge carriers are capable of migrating to two discrete semiconductors, thereby facilitating efficient segregation of hole and electron pairs. In this context, the conduction band (CB) and valence band (VB) of one semiconductor (P1) are situated at higher energy levels than the corresponding bands of the other semiconductor (P2) (**Figure 1.13B**). Among the traditional heterostructures it is apparent that the type-II heterojunction represents the most efficient heterojunction for augmenting photocatalytic performance due to the advantageous architecture for the effective segregation of hole and electron pairs. [59]

Likewise, redox potential of a staggered type heterojunction catalyst is also likely to be attenuated, as the oxidation and reduction reactions were facilitated in distinct semiconductor component, each exhibiting diminished redox potentials. In a type-III heterojunction, the extreme staggered bandgap precludes any overlap of the bandgaps, as illustrated in **Figure 1.13C**.

In the context of type-II heterojunction photocatalysts (**Figure 1.13B**), the energy levels of semiconductor P1 are noted to be elevated relative to those of semiconductor P2. Consequently, the photoelectrons generated through photoexcitation will migrate towards semiconductor P2, while the resultant holes will transfer to semiconductor P1 when subjected to light irradiation, thereby promoting a spatial segregation of the hole and electron pairs.[50–52] likewise to the type-I heterojunction, the reductive and oxidative capabilities of the type-II heterojunction photocatalyst are reduced, as the reduction and oxidation reactions transpire on semiconductors characterized by lower reduction and oxidation potentials, respectively. As depicted in **Figure 1.13C**, the structural configuration of the type-III heterojunction photocatalyst resembles that of the type-II heterojunction photocatalyst, with the notable distinction that the staggered gap is sufficiently pronounced to prevent any overlap of the bandgaps.[60]

Type I and type III band alignments are regarded as suboptimal for photocatalytic applications due to the intrinsic recombination of charge carriers, exacerbated by a reduction in redox capacity in type I configurations and the absence of synergistic interactions in type III heterojunction. In type II heterojunctions, the CB and VB of P2 were positioned at lower than the corresponding bands of semiconductor P1, resulting in partially overlapping band gaps (**Figure 1.13B**). Metal halide perovskites typically function as semiconductor I in type II heterojunctions.

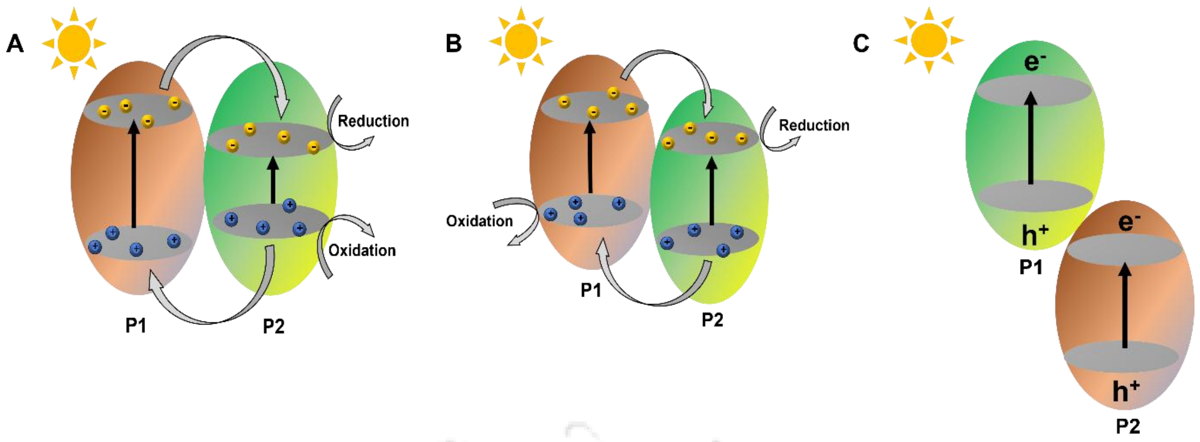

Figure 1.13: Band energy diagram of (A) type I, (B) type II and (C) type III heterostructures.

1.5.2 p-n junction

A p-n junction may be characterized as a distinctive type II interface, which engenders a pronounced internal electric field at its interface, facilitating acceleration of the spatial segregation of hole and electrons in divergent directions. This mechanism ultimately results in effective and expedited charge separation in comparison to a conventional type II junction. Notwithstanding, while the type-II heterojunction possesses the theoretical capacity to spatially segregate hole and electron pairs, the resultant acceleration in the hole and electrons segregation across such a heterojunction interface is inadequate to counteract the ultrafast hole and electron recombination phenomena occurring within the semiconductors. Consequently, the concept of a p–n junction heterostructure has been proposed, which possesses the capability to expedite the transportation of hole and electron pairs across the heterojunction, thereby ameliorating the efficacy through the provision of an additional electric field.[61] In particular, an efficacious p–n heterojunction photocatalyst can be synthesized through the amalgamation of p-type and n-type semiconductors. In the absence of light irradiation, electrons located in the n-type semiconductor adjacent to the p–n interface exhibit a propensity to diffuse into the p-type semiconductor, resulting in the formation of +ve charge species, as illustrated in **Figure 1.14**. Concurrently, holes generated by photo excitation situated in p-type component in proximity to p–n junction, are inclined to dissipate into the n-type component, thereby generating negative charges. This process of hole and electron diffusion persists until the equilibrium in Fermi level was established in the system. Consequently, the vicinity surrounding of p–n junction becomes charged, engendering a “charged” region called as internal electric field. [62] Upon exposure to incident solar irradiation having energy levels equal to or exceeding their bandgap values, both p-type and n-type semiconductors undergo excitation, resulting in the generation of holes and electrons pairs. The photogenerated holes and electrons within the p-type and n-type semiconductors will migrate under the influence of the internal electric field towards the conduction band of the n-type semiconductor and the valence band of the p-type semiconductor, respectively, culminating in the spatial segregation of hole and electron pairs. It is imperative to note that this process of hole and electron segregation is thermodynamically favourable, as the CB and VB of the p-type component are typically positioned at upper energy levels than that of n-type component within a photocatalyst of p–n heterojunction. Consequently, the efficiency of hole and electron segregation in p–n heterojunction surpasses that observed in photocatalysts with type-II heterojunction, attributable to the synergistic interaction of band alignment and internal electric field.

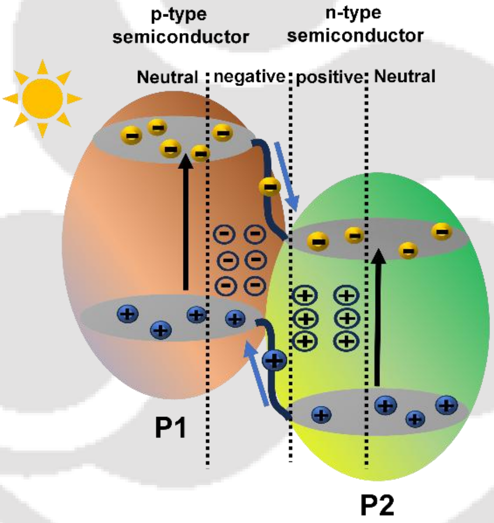

Figure 1.14: Band energy diagram of p-n junction.

1.5.3 Direct Z scheme

Addition to p–n junction, an alternative mechanism within heterostructure of type-II configuration, referred as Z scheme, involves migration of one singular charge. In this configuration, the light irradiation on the two semiconductor components and the consequent transfer of electrons lead to an efficient charge segregation, thereby retaining the holes and electrons within the semiconductor components that possess the maximum reduction potential and oxidation potentials, respectively. The charge transfer results in the allocation of CB electrons and VB holes in two distinct semiconductor components, incurring an energy cost that is nevertheless lower than that associated with the p–n junction. In this scenario, the resultant holes and electrons are positioned on the CB and VB of with most reducing and oxidizing capabilities respective pair. Such charge transfer may occur with or without a medium, which can include molecular species and metal ions in solution or a metallic contact with proper work function. spatial segregation of holes and electrons across different components at their junction considerably slows down recombination of charges, resulting in prolonged transients characterized by elevated chemical energy.[63]

A traditional Z-scheme photocatalyst is made of 2 semiconductor components, photocatalyst 1 (P1) and photocatalyst 2 (P2), and a donor (D) /acceptor (A) pair (**Figure 1.15**). P1 and P2 were not in direct contact. During the reaction, photo-electrons were transferred from the CB of P1 to the VB of the P2 mediated by A/D pair through the following redox reactions:

$$A + e^- = D \qquad \textbf{(Equation 5)}$$

$$D + h^+ = A \qquad \textbf{(Equation 6)}$$

Catagorically, the transition of species A to species D occurs through a reaction involving photogenerated electrons derived from the conduction band of Photosystem 1 (PI). Subsequently, species D undergoes oxidation back to species A via the action of photogenerated holes originating from the valence band. Given that electrons tend to accumulate at Photosystem 2 (P2), which possesses a higher reduction potential, while holes concentrate at Photosystem 1 (P1), characterized by a higher oxidation potential, it is feasible to attain a spatial segregation of hole and electron pairs, thereby optimizing redox capabilities. Nonetheless, traditional Z-scheme photocatalysts are constrained to construction in the liquid phase, which restricts their broader applicability in the domain of photocatalysis. [64]

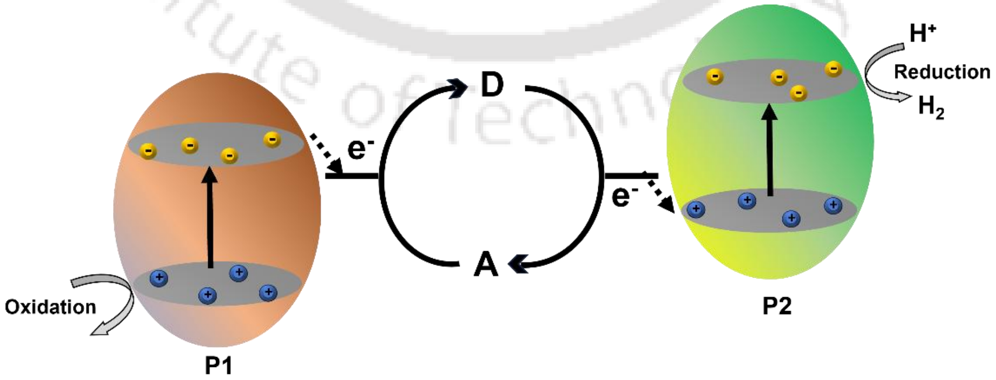

Figure 1.15: Band energy diagram of Z scheme heterostructure.

1.6 Measurements & characterization

The typical experimental research on semiconductor photocatalysts consists of three parts, namely, materials synthesis, characterization, and photocatalytic efficiency testing. Characterization of these semiconductor include chemical composition, physical properties, and determination of band structure as enlisted in **Figure1.16**. These properties are important for assessment of photocatalytic activities of semiconductor photocatalysts for specific applications. [65]

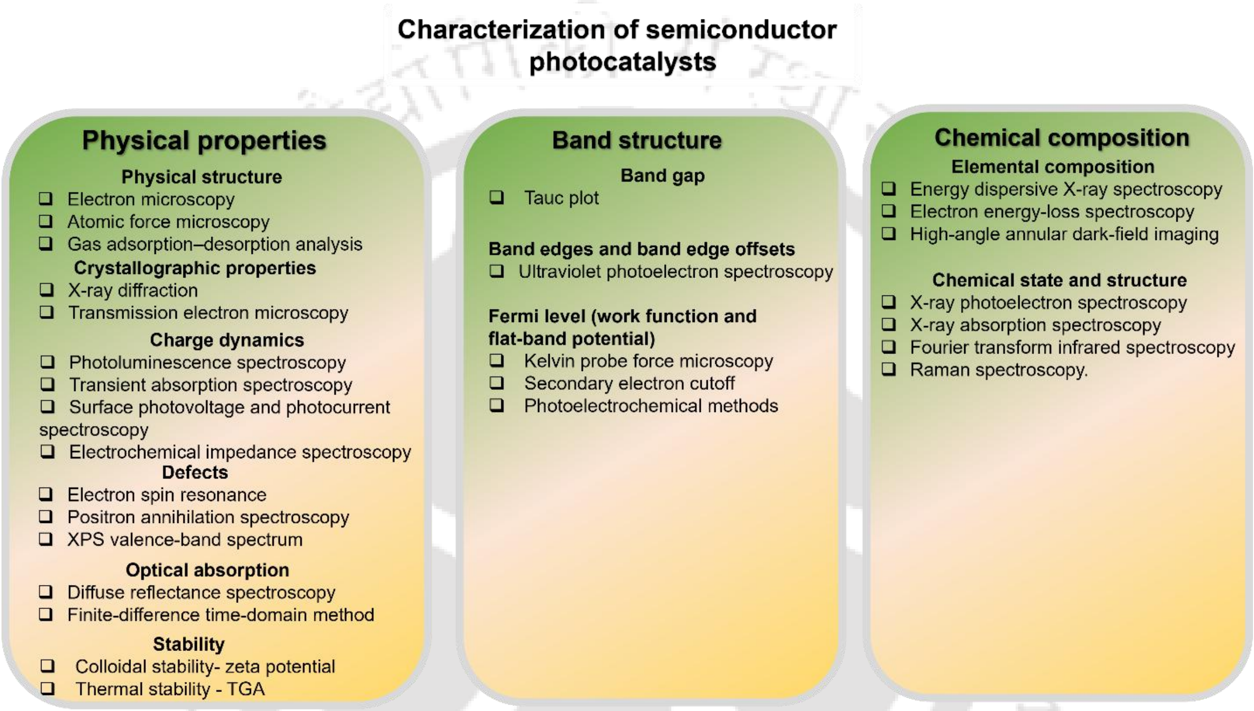

Characterization of semiconductor photocatalysts

Physical properties

Physical structure

☐ Electron microscopy
☐ Atomic force microscopy
☐ Gas adsorption–desorption analysis

Crystallographic properties

☐ X-ray diffraction
☐ Transmission electron microscopy

Charge dynamics

☐ Photoluminescence spectroscopy
☐ Transient absorption spectroscopy
☐ Surface photovoltage and photocurrent spectroscopy
☐ Electrochemical impedance spectroscopy

Defects

☐ Electron spin resonance
☐ Positron annihilation spectroscopy
☐ XPS valence-band spectrum

Optical absorption

☐ Diffuse reflectance spectroscopy
☐ Finite-difference time-domain method

Stability

☐ Colloidal stability- zeta potential
☐ Thermal stability - TGA

Band structure

Band gap

☐ Tauc plot

Band edges and band edge offsets

☐ Ultraviolet photoelectron spectroscopy

Fermi level (work function and flat-band potential)

☐ Kelvin probe force microscopy
☐ Secondary electron cutoff
☐ Photoelectrochemical methods

Chemical composition

Elemental composition

☐ Energy dispersive X-ray spectroscopy
☐ Electron energy-loss spectroscopy
☐ High-angle annular dark-field imaging

Chemical state and structure

☐ X-ray photoelectron spectroscopy
☐ X-ray absorption spectroscopy
☐ Fourier transform infrared spectroscopy
☐ Raman spectroscopy.

Figure1.16. Characterization techniques of photocatalytic semiconductor.

Utilizing these methodologies not only facilitates the correlation between characterization outcomes of a photocatalyst and its catalytic efficacy. It may also unveil novel phenomena.

(1) Advancement of photocatalysts were achieved through alterations in chemical composition, structural configuration, and crystallinity and other attributes. This can be confirmed using XPS, XAS, FTIR, Raman spectroscopy, FESEM, FETEM and XRD techniques.

(2) Investigation of charge migration phenomena in heterojunctions, as previously indicated, XPS and XAS possess the capability to elucidate charge transport between multiple components in a heterojunction by analysing the oxidation states of a particular element across individual constituents and the heterojunction itself. However, in situ XPS and TAS methodologies enable real-time observation of charge transport by documenting the variation

in oxidation states of a constituent element and transient absorption data following the irradiation of the heterojunction with light.

(3) Examination of defects, which may arise from light irradiation or interaction with water, oxygen, carbon dioxide, and various other prevalent molecules were observed through the application of in situ XPS, XAS, FTIR, and Raman spectroscopy.

1.7 Factors effecting Photocatalytic H_2 evolution

By analyzing the variances among the evaluation parameters, an initial assessment of catalytic performance from diverse angles can be conducted. Nevertheless, the experimental conditions are frequently inconsistent across different studies, presenting a significant obstacle in utilizing these methodologies and achieving a coherent and standardized comparison among various systems. Several critical indicators within the current evaluation techniques can be enhanced for improved assessment.

1.7.1 Light Source

The efficacy of the photocatalyst is intrinsically linked to the characteristics of the light source employed. Typically, xenon (Xe) lamps, mercury (Hg) lamps, AM1.5 G solar simulators, and light-emitting diodes (LEDs) are the predominant light sources utilized in laboratory settings. [66] Nonetheless, substantial discrepancies exist among these artificial light sources, complicating the establishment of standardized protocols across various research facilities. The spectral range and light intensity can differ markedly among different light sources. Variations in incident photon flux can yield disparate photocatalytic outcomes, even when utilizing the same photocatalyst. For diverse illumination sources, both the spectral range and light intensity display significant fluctuations. Varying incident photon fluxes can produce divergent photocatalytic efficiencies, even when investigating the same photocatalyst. The precise light intensity incident upon the reaction surface is heavily influenced by factors such as the reactor material, the distance separating the light source and the reactor, and the area exposed to irradiation. Even with an equivalent mass of photocatalyst, differing irradiation areas and suspension conditions can result in varied photocatalytic performances.

1.7.2 Reaction Temperature

The photoactivity of catalysis is significantly influenced by the reaction temperature. Elevated temperatures can enhance photocatalytic efficiency due to a synergistic photothermal effect. Extremely high temperatures may even surpass the kinetic constraints associated with visible-light irradiation, as demonstrated by Hu et al. through their examination of black Pt/TiO_2.[67] When temperatures exceed 200°C, the differential temperature can exert a more pronounced effect on photocatalytic performance. Unlike LEDs, the other artificial light sources (Xe lamps, Hg lamps, and AM1.5 G) exhibit substantial thermal effects. However, it is commonplace for the reaction temperature to fluctuate by 10 or 20 °C across different locations and seasons. Maintaining a rigorously consistent temperature before and after the photocatalytic reaction is challenging. Consequently, variations in temperature complicate the comparison of photocatalytic performances among different photocatalysts.

1.7.3 Photocatalyst Mass

The rate of photocatalytic hydrogen production is determined by the volume of gas evolved per unit reaction time and per unit mass of photocatalyst. The mass of the photocatalyst directly influences the calculation of the hydrogen production rate, AQY and the solar-to-hydrogen efficiency (STH).[68] Thus, it was closely associated with the quantity of photocatalyst employed, and variations in mass can result in differing rates even for the same photocatalyst. This phenomenon arises because the rate of hydrogen evolution is not often proportional to the mass of photocatalyst utilized, due to constraints related to light absorption and diffusion conditions.[69] When large quantity of photocatalyst is employed, a significant portion may be unable to effectively absorb sufficient light, resulting in diminished photocatalytic activity when normalized to the unit mass of photocatalyst. Clearly, under such conditions the hydrogen evolution rate fails to accurately interpret the intrinsic capabilities of the photocatalyst.

1.7.4 Catalyst photostability

The photostability of a photocatalyst is defined as its capability to preserve its catalytic function and structural coherence when subjected to extended durations of light exposure, specifically ultraviolet (UV) or visible light. In the realm of photocatalysis, substances such as semiconductors are energized by light to promote chemical reactions, including the degradation of contaminants or the splitting of water molecules. For photocatalysts to be viable and effective over extended periods, they must exhibit photostability, which indicates that they do not deteriorate or diminish in efficacy as a result of the light exposure that initiates their catalytic activities.[70] Certain photocatalysts may experience reduction or oxidation upon light exposure. For example, photocatalysts based on metals may undergo changes in their oxidation states, subsequently affecting their catalytic characteristics. These alterations can significantly influence their photostability. Over time, the surfaces of photocatalysts may develop passivation layers (such as oxide films) that can either reinforce the material's stability or, on the contrary, impede its catalytic efficiency.

1.8 Reference

(1) Taagepera, R. A World Population Growth Model: Interaction with Earth's Carrying Capacity and Technology in Limited Space. *Technol. Forecast. Soc. Change* **2014**, *82*, 34–41.

(2) Scirp.org.https://www.scirp.org/journal/paperinformation?paperid=118917.

(3) Hubbert, M. K. Energy from Fossil Fuels. *Science* **1949**, *109*, 103–109.

(4) P.J. McCabe, D.L. Gautier, M.D. Lewan, C. Turner, The future of energy gases, 1993. DOI:10.3133/CIR1115.

(5) The Origin of Petroleum. *Nature* **1923**, *112*, 627–628.

(6) Regional, and National Fossil-Fuel CO2 Emissions: 1751-2017. United States: N. p., 2020. Web. DOI:10.15485/1712447.

(7) Hansen, J.; Ruedy, R.; Sato, M.; Lo, K. Global Surface Temperature Change. *Rev. Geophys.* **2010**, *48*. DOI: 10.1029/2010rg000345.

(8) *Given the impact of fossil fuels on climate change; Is it wrong for graduate engineers to go into the Oil and Gas Industry?* PREMag. https://prestudentconversation.wordpress.com/2016/04/11/given-the-impact-of-fossil-fuels-on-climate-change-is-it-wrong-for-graduate-engineers-to-go-into-the-oil-and-gas-industry.

(9) Global fossil CO_2 emissions are projected to rise in 2023, https://cicero.oslo.no/en/articles/global-fossil-emissions-are-projected-to-rise-in-2023.

(10) Our energy sources, electricity — *the National Academies*. Nas.edu. http://needtoknow.nas.edu/energy/energy-sources/electricity.

(11) Jia, T.; Dai, Y.; Wang, R. Refining Energy Sources in Winemaking Industry by Using Solar Energy as Alternatives for Fossil Fuels: A Review and Perspective. *Renew. Sustain. Energy Rev.* **2018**, *88*, 278–296.

(12) Şen, Z. Solar Energy in Progress and Future Research Trends. *Prog. Energy Combust. Sci.* **2004**, *30*, 367–416.

(13) Nazir, H.; Muthuswamy, N.; Louis, C.; Jose, S.; Prakash, J.; Buan, M. E. M.; Flox, C.; Chavan, S.; Shi, X.; Kauranen, P.; Kallio, T.; Maia, G.; Tammeveski, K.; Lymperopoulos, N.; Carcadea, E.; Veziroglu, E.; Iranzo, A.; M. Kannan, A. Is the H_2 Economy Realizable in the Foreseeable Future? Part III: H2 Usage Technologies, Applications, and Challenges and Opportunities. Int. J. Hydrogen Energy 2020, 45, 28217–28239.

(14) Li, Z.; Fang, S.; Sun, H.; Chung, R.-J.; Fang, X.; He, J.-H. Solar Hydrogen. *Adv. Energy Mater.* **2023**, *13*. DOI: 10.1002/aenm.202203019.

(15) Ogden, J. M.; Steinbugler, M. M.; Kreutz, T. G. A Comparison of Hydrogen, Methanol and Gasoline as Fuels for Fuel Cell Vehicles: Implications for Vehicle Design and Infrastructure Development. *J. Power Sources* **1999**, *79* , 143–168.

(16) Barreto, L.; Makihira, A.; Riahi, K. The Hydrogen Economy in the 21st Century: A Sustainable Development Scenario. *Int. J. Hydrogen Energy* **2003**, *28*, 267–284.

(17) Ueckerdt, F.; Bauer, C.; Dirnaichner, A.; Everall, J.; Sacchi, R.; Luderer, G. Potential and Risks of Hydrogen-Based e-Fuels in Climate Change Mitigation. *Nat. Clim. Chang.* **2021**, *11*, 384–393.

(18) Hong, X.; Thaore, V. B.; Garud, S. S.; Karimi, I. A.; Farooq, S.; Wang, X.; Usadi, A. K.; Chapman, B. R. Decarbonizing Singapore via Local Production of H2 from Natural Gas. *Int. J. Hydrogen Energy* **2023**, *48*, 8743–8755.

(19) Liu, W.; Zuo, H.; Wang, J.; Xue, Q.; Ren, B.; Yang, F. The Production and Application of Hydrogen in Steel Industry. *Int. J. Hydrogen Energy* **2021**, *46*, 10548–10569.

(20) Fujishima, A.; Honda, K. Electrochemical Photolysis of Water at a Semiconductor Electrode. *Nature* **1972**, *238*, 37–38.

(21) Khaki, M. R. D.; Shafeeyan, M. S.; Raman, A. A. A.; Daud, W. M. A. W. Application of Doped Photocatalysts for Organic Pollutant Degradation - A Review. J. Environ. Manage. **2017**, *198*, 78–94.

(22) Shaner, M. R.; Atwater, H. A.; Lewis, N. S.; McFarland, E. W. A Comparative Technoeconomic Analysis of Renewable Hydrogen Production Using Solar Energy. *Energy Environ. Sci.* **2016**, 9, 2354–2371.

(23) Aldosari, O. F. Photocatalytic Water-Splitting for Hydrogen Production Using TiO_2 -Based Catalysts: Advances, Current Challenges, and Future Perspectives. *Catal. Rev. Sci. Eng.* **2025**, 1–38. DOI: 10.1080/01614940.2024.2446476.

(24) Samanta, B.; Morales-García, Á.; Illas, F.; Goga, N.; Anta, J. A.; Calero, S.; Bieberle-Hütter, A.; Libisch, F.; Muñoz-García, A. B.; Pavone, M.; Caspary Toroker, M. Challenges of Modeling Nanostructured Materials for Photocatalytic Water Splitting. *Chem. Soc. Rev.* **2022**, *51*, 3794–3818.

(25) Chen, X.; Shen, S.; Guo, L.; Mao, S. S. Semiconductor-Based Photocatalytic Hydrogen Generation. *Chem. Rev.* **2010**, *110*, 6503–6570.

(26) Bie, C.; Wang, L.; Yu, J. Challenges for Photocatalytic Overall Water Splitting. Chem **2022**, *8*, 1567–1574.

(27) Kranz, C.; Wächtler, M. Characterizing Photocatalysts for Water Splitting: From Atoms to Bulk and from Slow to Ultrafast Processes. Chem. Soc. Rev. **2021**, *50*, 1407–1437.

(28) Takanabe, K. Photocatalytic Water Splitting: Quantitative Approaches toward Photocatalyst by Design. *ACS Catal.* **2017**, *7*, 8006–8022.

(29) Rosman, N. N.; Yunus, R. M.; Shah, N. R. A. M.; Shah, R. M.; Arifin, K.; Minggu, L. J.; Ludin, N. A. An Overview of Co-catalysts on Metal Oxides for Photocatalytic Water Splitting. *Int. J. Energy Res.* **2022**, *46*, 11596–11619.

(30) Chen, D.; Liu, Z.; Guo, Z.; Yan, W.; Xin, Y. Enhancing Light Harvesting and Charge Separation of Cu_2O Photocathodes with Spatially Separated Noble-Metal Cocatalysts towards Highly Efficient Water Splitting. J. Mater. Chem. A Mater. Energy Sustain. **2018**, *6*, 20393–20401.

(31) Li, D.; Shi, J.; Li, C. Transition-metal-based Electrocatalysts as Cocatalysts for Photoelectrochemical Water Splitting: A Mini Review. *Small* **2018**, *14*. DOI: 10.1002/smll.201704179.

(32) Basu, M.; Zhang, Z.-W.; Chen, C.-J.; Lu, T.-H.; Hu, S.-F.; Liu, R.-S. CoSe2 Embedded in C3N4: An Efficient Photocathode for Photoelectrochemical Water Splitting. ACS Appl. Mater. Interfaces **2016**, *8*, 26690–26696.

(33) Cao, S.; Li, Y.; Zhu, B.; Jaroniec, M.; Yu, J. Facet Effect of Pd Cocatalyst on Photocatalytic CO_2 Reduction over g-C_3N_4. J. Catal. **2017**, *349*, 208–217.

(34) Kumaravel, V.; Imam, M.; Badreldin, A.; Chava, R.; Do, J.; Kang, M.; Abdel-Wahab, A. Photocatalytic Hydrogen Production: Role of Sacrificial Reagents on the Activity of Oxide, Carbon, and Sulfide Catalysts. Catalysts **2019**, 9, 276. DOI: 10.3390/catal9030276.

(35) Wang, W.; Xu, M.; Xu, X.; Zhou, W.; Shao, Z. Perovskite Oxide Based Electrodes for High-performance Photoelectrochemical Water Splitting. *Angew. Chem. Int. Edl.* **2020**, *59*, 136–152.

(36) Kojima, A.; Teshima, K.; Shirai, Y.; Miyasaka, T. Organometal Halide Perovskites as Visible-Light Sensitizers for Photovoltaic Cells. *J. Am. Chem. Soc.* **2009**, *131*, 6050–6051.

(37) Ha, S.-T.; Su, R.; Xing, J.; Zhang, Q.; Xiong, Q. Metal Halide Perovskite Nanomaterials: Synthesis and Applications. *Chem. Sci.* **2017**, *8*, 2522–2536.

(38) Xiao, Z.; Song, Z.; Yan, Y. From Lead Halide Perovskites to Lead-free Metal Halide Perovskites and Perovskite Derivatives. Adv. Mater. **2019**, *31*. DOI: 10.1002/adma.201803792.

(39) Travis, W.; Glover, E. N. K.; Bronstein, H.; Scanlon, D. O.; Palgrave, R. G. On the Application of the Tolerance Factor to Inorganic and Hybrid Halide Perovskites: A Revised System. Chem. Sci. 2016, 7, 4548–4556.

(40) Travis, W.; Glover, E. N. K.; Bronstein, H.; Scanlon, D. O.; Palgrave, R. G. On the Application of the Tolerance Factor to Inorganic and Hybrid Halide Perovskites: A Revised System. Chem. Sci. **2016**, *7*, 4548–4556.

(41) Wu, Y.; Lu, S.; Zhou, Q.; Ju, M.-G.; Zeng, X. C.; Wang, J. Two-dimensional Perovskites with Tunable Room-temperature Phosphorescence. *Adv. Funct. Mater.* **2022**, *32*. DOI: 10.1002/adfm.202204579.

(42) Hutter, E. M.; Gélvez-Rueda, M. C.; Osherov, A.; Bulović, V.; Grozema, F. C.; Stranks, S. D.; Savenije, T. J. Direct–Indirect Character of the Bandgap in Methylammonium Lead Iodide Perovskite. *Nat. Mater.* **2017**, *16*, 115–120.

(43) Chen, Y.; Yi, H. T.; Wu, X.; Haroldson, R.; Gartstein, Y. N.; Rodionov, Y. I.; Tikhonov, K. S.; Zakhidov, A.; Zhu, X.-Y.; Podzorov, V. Extended Carrier Lifetimes and Diffusion in Hybrid Perovskites Revealed by Hall Effect and Photoconductivity Measurements. *Nat. Commun.* **2016**, *7*, 1–9.

(44) Rehman, W.; Milot, R. L.; Eperon, G. E.; Wehrenfennig, C.; Boland, J. L.; Snaith, H. J.; Johnston, M. B.; Herz, L. M. Charge-carrier Dynamics and Mobilities in Formamidinium Lead mixed-Halide Perovskites. *Adv. Mater.* **2015**, *27*, 7938–7944.

(45) Kang, J.; Wang, L.-W. High Defect Tolerance in Lead Halide Perovskite $CsPbBr_3$. *J. Phys. Chem. Lett.* **2017**, *8*, 489–493.

(46) Wang, W.; Tadé, M. O.; Shao, Z. Research Progress of Perovskite Materials in Photocatalysis- and Photovoltaics-Related Energy Conversion and Environmental Treatment. *Chem. Soc. Rev.* **2015**, *44*, 5371–5408.

(47) Park, S.; Chang, W. J.; Lee, C. W.; Park, S.; Ahn, H.-Y.; Nam, K. T. Photocatalytic Hydrogen Generation from Hydriodic Acid Using Methylammonium Lead Iodide in Dynamic Equilibrium with Aqueous Solution. *Nat. Energy* **2016**, *2*, 1–8.

(48) Zhao, X.; Chen, S.; Yin, H.; Jiang, S.; Zhao, K.; Kang, J.; Liu, P. F.; Jiang, L.; Zhu, Z.; Cui, D.; Liu, P.; Han, X.; Yang, H. G.; Zhao, H. Perovskite Microcrystals with Intercalated Monolayer MoS2 Nanosheets as Advanced Photocatalyst for Solar-Powered Hydrogen Generation. *Matter* **2020**, *3*, 935–949.

(49) Christians, J. A.; Miranda Herrera, P. A.; Kamat, P. V. Transformation of the Excited State and Photovoltaic Efficiency of $CH_3NH_3PbI_3$ Perovskite upon Controlled Exposure to Humidified Air. *J. Am. Chem. Soc.* **2015**, *137*, 1530–1538.

(50) Murali, B.; Dey, S.; Abdelhady, A. L.; Peng, W.; Alarousu, E.; Kirmani, A. R.; Cho, N.; Sarmah, S. P.; Parida, M. R.; Saidaminov, M. I.; Zhumekenov, A. A.; Sun, J.; Alias, M. S.; Yengel, E.; Ooi, B. S.; Amassian, A.; Bakr, O. M.; Mohammed, O. F. Surface Restructuring of Hybrid Perovskite Crystals. *ACS Energy Lett.* **2016**, *1*, 1119–1126.

(51) Zhu, Z.; Hadjiev, V. G.; Rong, Y.; Guo, R.; Cao, B.; Tang, Z.; Qin, F.; Li, Y.; Wang, Y.; Hao, F.; Venkatesan, S.; Li, W.; Baldelli, S.; Guloy, A. M.; Fang, H.; Hu, Y.; Yao, Y.; Wang, Z.; Bao, J. Interaction of Organic Cation with Water Molecule in Perovskite $MAPbI_3$: From Dynamic Orientational Disorder to Hydrogen Bonding. *Chem. Mater.* **2016**, *28*, 7385–7393.

(52) Wang, R.; Mujahid, M.; Duan, Y.; Wang, Z.-K.; Xue, J.; Yang, Y. A Review of Perovskites Solar Cell Stability. *Adv. Funct. Mater.* **2019**, *29*. Doi:10.1002/adfm.201808843.

(53) Wu, Y.; Wang, P.; Zhu, X.; Zhang, Q.; Wang, Z.; Liu, Y.; Zou, G.; Dai, Y.; Whangbo, M.-H.; Huang, B. Composite of $CH_3NH_3PbI_3$ with Reduced Graphene Oxide as a Highly Efficient and Stable Visible-light Photocatalyst for Hydrogen Evolution in Aqueous HI Solution. *Adv. Mater.* **2018**, *30*. DOI: 10.1002/adma.201704342.

(54) Xu, Y.-F.; Yang, M.-Z.; Chen, B.-X.; Wang, X.-D.; Chen, H.-Y.; Kuang, D.-B.; Su, C.-Y. A $CsPbBr_3$ Perovskite Quantum Dot/Graphene Oxide Composite for Photocatalytic CO_2 Reduction. *J. Am. Chem. Soc.* **2017**, *139*, 5660–5663.

(55) Xu, Y.-F.; Wang, X.-D.; Liao, J.-F.; Chen, B.-X.; Chen, H.-Y.; Kuang, D.-B. Amorphous-TiO_2-encapsulated $CsPbBr_3$ Nanocrystal Composite Photocatalyst with Enhanced Charge Separation and CO_2 Fixation. *Adv. Mater. Interfaces* **2018**, *5*. DOI: /10.1002/admi.201801015.

(56) Jang, J. S.; Kim, H. G.; Lee, J. S. Heterojunction Semiconductors: A Strategy to Develop Efficient Photocatalytic Materials for Visible Light Water Splitting. *Catal. Today* **2012**, *185*, 270–277.

(57) Moniz, S. J. A.; Shevlin, S. A.; Martin, D. J.; Guo, Z.-X.; Tang, J. Visible-Light Driven Heterojunction Photocatalysts for Water Splitting – a Critical Review. Energy Environ. Sci. **2015**, *8*, 731–759.

(58) Low, J.; Yu, J.; Jaroniec, M.; Wageh, S.; Al-Ghamdi, A. A. Heterojunction Photocatalysts. *Adv. Mater.* **2017**, *29*. DOI: 10.1002/adma.201601694.

(59) Purohit, S.; Yadav, K. L.; Satapathi, S. Metal Halide Perovskite Heterojunction for Photocatalytic Hydrogen Generation: Progress and Future Opportunities. Adv. Mater. Interfaces **2022**, *9*. DOI: 10.1002/admi.202200058.

(60) Dhakshinamoorthy, A.; Li, Z.; Yang, S.; Garcia, H. Metal–Organic Framework Heterojunctions for Photocatalysis. Chem. Soc. Rev. **2024**, *53*, 3002–3035.

(61) Niu, J.; Albero, J.; Atienzar, P.; García, H. Porous Single-crystal-based Inorganic Semiconductor Photocatalysts for Energy Production and Environmental Remediation: Preparation, Modification, and Applications. *Adv. Funct. Mater.* **2020**, *30*. DOI: 10.1002/adfm.201908984.

(62) Che, L.; Pan, J.; Cai, K.; Cong, Y.; Lv, S.-W. The Construction of P-n Heterojunction for Enhancing Photocatalytic Performance in Environmental Application: A Review. *Sep. Purif. Technol.* **2023**, *315*, 123708. DOI: 10.1016/j.seppur.2023.123708.

(63) Wang, Z.; Li, C.; Domen, K. Recent Developments in Heterogeneous Photocatalysts for Solar-Driven Overall Water Splitting. Chem. Soc. Rev. **2019**, *48*, 2109–2125.

(64) Li, H.; Tu, W.; Zhou, Y.; Zou, Z. Z-scheme Photocatalytic Systems for Promoting Photocatalytic Performance: Recent Progress and Future Challenges. Adv. Sci. **2016**, *3*. DOI: 10.1002/advs.201500389.

(65) Zhang, L.; Ran, J.; Qiao, S.-Z.; Jaroniec, M. Characterization of Semiconductor Photocatalysts. Chem. Soc. Rev. **2019,** *48*, 5184–5206.

(66) Chen, X.; Liu, L.; Yu, P. Y.; Mao, S. S. Increasing Solar Absorption for Photocatalysis with Black Hydrogenated Titanium Dioxide Nanocrystals. *Science* **2011**, *331*, 746–750.

(67) Han, B.; Hu, Y. H. Highly Efficient Temperature-Induced Visible Light Photocatalytic Hydrogen Production from Water. J. Phys. Chem. C Nanomater. Interfaces **2015**, *119*, 18927–18934.

(68) Chen, S.; Takata, T.; Domen, K. Particulate Photocatalysts for Overall Water Splitting. Nat. Rev. Mater. **2017**, *2*, 1–17.

(69) Cheng, H.; Lv, X.-J.; Cao, S.; Zhao, Z.-Y.; Chen, Y.; Fu, W.-F. Robustly Photogenerating H2 in Water Using FeP/CdS Catalyst under Solar Irradiation. *Sci. Rep.* **2016**, *6*, 1–10.

(70) Xiao, M.; Wang, Z.; Maeda, K.; Liu, G.; Wang, L. Addressing the Stability Challenge of Photo (Electro)Catalysts towards Solar Water Splitting. Chem. Sci. **2023**, 14, 3415–3427.

[This page was left empty intentionally]

CHAPTER 2

Composites of Reduced Graphene Oxide and MAPbI3 Crystals for Photocatalytic Hydrogen Generation

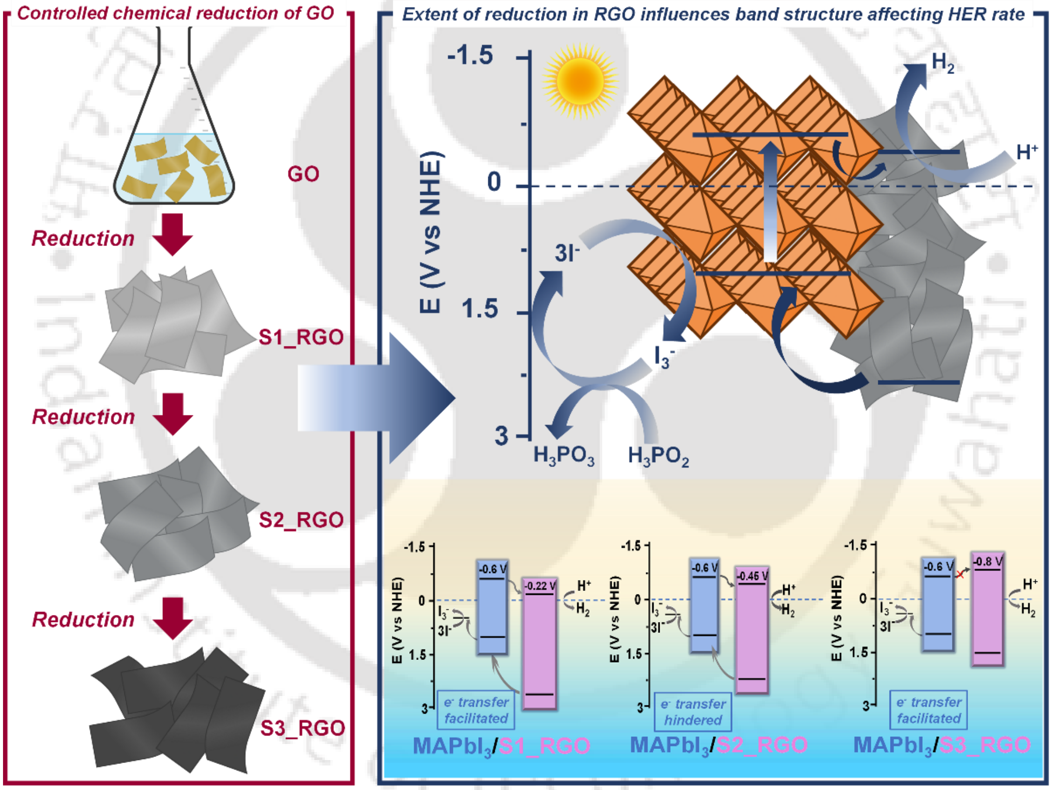

Article: Pal, T.; Bhowmik, S.; Suhail, A.; Sharma, S.; Peela, N. R.; Sastri, C. V.; Iyer, P. K. Composites of Reduced Graphene Oxide and $MAPbI_3$ Crystals for Photocatalytic Hydrogen Generation. *ACS Appl. Nano Mater.* **2024**, *7*, 12163–12170

Keywords: Varied reduction of RGO, Photocatalytic hydrogen evolution, Hybrid perovskite, Photogenerated electron transfer, effect of band alignment, in-situ crystallization.

2.1 Abstract

Lead halide perovskite has emerged as an alternate material for photocatalytic H_2 evolution owing to its excellent optoelectronic properties. However, designing an efficient and stable perovskite photocatalyst system still remains a challenging task. Pristine $MAPbI_3$ exhibited a lesser H_2 evolution activity due to lack of reactive sites and its faster degradation. Herein, reduced graphene oxides (RGOs) with varied chemical reduction were integrated with $MAPbI_3$ microcrystals by in-situ coupling to construct a robust and effective heterostructure resulting into a strong interconnection between $MAPbI_3$ and RGO. Careful selection of co-catalysts with appropriate bandgaps and proper alignment of band positions are the key steps for successful photocatalytic H_2 generation. This work highlights that facile and easy photogenerated charge separation and migration can be achieved for $MAPbI_3$/RGO heterostructures where chemically modified RGOs having favourable bandgap and band positions were incorporated with $MAPbI_3$ via unusual improved in-situ crystallization resulting into remarkable mmol scale photocatalytic H_2 evolution in aqueous HI medium under white light LED illumination. Under optimal reaction conditions, the H_2 evolution rate can reach up to 4493 μmol g^{-1} h^{-1}.

2.2 Introduction

Limited resources of conventional fossil fuel and its devastating negative impact on environment and human health causes a great challenge for mankind. It is well accepted that H_2 is one of the most promising energy resources because of its high energy density per unit mass and pollution free combustion.[1-3] Effective solar driven H_2 generation from splitting of water or other substances like hydrohalic acids HX (X= Cl, Br, I) holds the key to attain H_2 economy. H_2 is not only useful as a fuel for transportation but also a valuable feedstock in heavy industries like steel, fertilizers etc.[4,5] At present, H_2 is mostly being produced by reforming of natural gas which is expensive as well as a source of tremendous pollution.[6] On the contrary, greener approaches like photocatalytic water splitting or hydrogen halide splitting to produce green H_2 has emerged as an environmentally benign, carbon-neutral technique compared to traditional natural gas cracking.[7-9] In recent times, halide perovskites have emerged as breakthrough materials in a series of optoelectronic devices such as solar cells, LEDs, lasers, photo-detectors etc.[10-13] Halide perovskite materials have excellent properties like high absorption coefficient,[14] suitable bandgap to capture a large fraction of the solar photons, high carrier diffusion length[15] and low exciton binding energy[16] which facilitates easier separation of photogenerated charges. Because of all these fascinating properties, hybrid organic-inorganic halide perovskites are promising candidates for photocatalytic H_2 generation. In particular, the role of halide perovskite materials in photocatalytic H_2 generation from halogen acids splitting have drawn the attention of the research groups worldwide. After the first discovery of HI splitting using $MAPbI_3$ perovskite[17] by Nam et. al. in 2016, several reports have been published for the same.[18-28] In spite of this progress, there are some tedious hurdles like high moisture sensitivity, harsh acidic operational conditions, critical pH sensitivity and poor gas evolution rates which make the journey of perovskite photocatalysts little onerous as a catalyst for commercial use.

To enhance the rate of photocatalytic H_2 generation, a co-catalyst was tagged to the perovskite photocatalyst. The function of co-catalyst was to act as a bridge between the perovskite (photosensitizer) and the medium (e.g., H^+ for H_2 evolution reaction). Basically, tagging the co-catalyst to the photocatalyst creates a Schottky barrier that ensures the co-catalyst receives maximum number of photogenerated charges while preventing bulk charge recombination. Various materials like Pt, Ni3C, MoS_2, Black Phosphorus, PEDOT: PSS, TiO_2 etc. have been reported as co-catalysts for photocatalytic activities.[17,18,19,29-31] In context of RGO as a co-catalyst, gram scale synthesis of RGO (Reduced Graphene Oxide) is feasible in laboratory environment as well as economical. RGO is one of the few materials which is stable in strong acidic media,[32] rendering it as an excellent choice as co-catalyst in MAPbI$_3$/co-catalyst composites system for solar driven HI splitting. RGO is one of the few semiconductor materials where desired and improved outcome can be obtained by bandgap alteration which is possible by facile chemical reduction. RGO acts as an excellent electron reservoir[33] as well as a transporter leading towards enhanced photocatalytic performance of the composites by facilitating separation and migration of photogenerated electrons from MAPbI$_3$ to the H$^+$ ions in the reaction medium.

In this study, three chemically reduced RGOs were synthesized, namely S1_RGO, S2_RGO, and S3_RGO by altering the quantity of Na$_2$SO$_3$ utilized, specifically 50 mg, 100 mg, and 200 mg. The least reduced variant S1_RGO was prepared with 50 mg of Na$_2$SO$_3$. Conversely, S3_RGO with the highest degree of reduction, obtained through the use of 200 mg of Na2SO3. Herein, we have reported a facile and efficient method of developing methylammonium lead iodide (MAPI) based catalyst/co-catalyst heterostructures with as-prepared RGOs via in-situ crystallization.

MAPbI$_3$/RGO system for photocatalytic hydrogen evolution was reported earlier. However, in this article we have investigated the role of degree of chemical reduction in RGOs for photocatalytic activity of MAPbI$_3$/RGO heterostructures. Varied reduction of GO not only influence the bandgap of RGO but also affect the VBM positions of the specific RGO which further create an impact on charge transfer characteristics in photocatalytic HER. Even though all heterostructures exhibited improved H$_2$ evolution reaction (HER) activity as compared to pristine MAPI, the highest photocatalytic H$_2$ generation rates were delivered by MAPI/S2_RGO composites. Pristine MAPI microcrystal showed HER activity of 30 µmol g^{-1} h^{-1} under visible white light LED (**Figure S2.1**) whereas for MAPI/S2_RGO composites the registered maximum HER activity was 4493 µmol g^{-1} h^{-1} which is 150 times higher than pristine MAPI.

2.3 Results and discussion

The pristine MAPI is inherently crystalline in nature that was well described in X-ray diffraction as shown in **Figure 2.1**. The signature peaks of MAPI were observed at 14.14°, 28.48°, 31.92°, 40.71° and 43.25° corresponding to planes (110), (220), (222), (400) and (402) respectively; belonging to space group I4cm (108) (JCPDS no= 01-083-7582). As-prepared pristine MAPI displayed identical XRD patterns with standard reference, confirms successful single-phase product formation. The RGO is amorphous in nature and displayed broad peaks in the range between 18° to 32° that corresponds to (002) plane and a sharp peak around 42.6° (**Figure S2.2**). **Figure 2.1** depicts that MAPI/S2_RGO composites had retained all signature peaks of the pristine MAPI. No characteristic broad peaks of the amorphous RGO co-catalyst were observed in the diffractogram of MAPI/RGO composites due to the high crystalline nature of MAPI. Similar kinds of patterns were observed for MAPI/S1_RGO and MAPI/S3_RGO (**Figure S2.3**). It is worth mentioning that no change in XRD pattern of MAPI/S2_RGO was observed even after 100 hours of white light exposure in aqueous HI/H_3PO_2 solution which portrays that no structural degradation of perovskite crystal structures occurred even after 100 hours of H_2 evolution activity (**Figure S2.4**). The 3 variants of RGOs were further characterized with Raman spectroscopy as displayed in **Figure S2.5.**

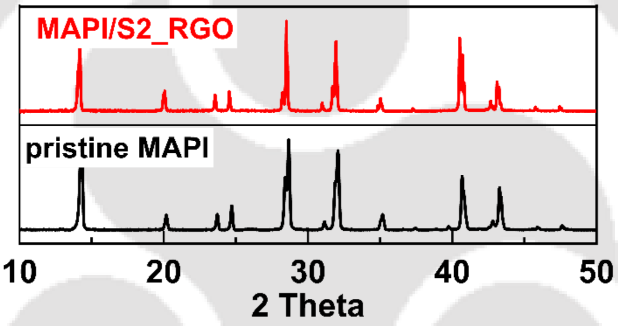

Figure 2.1: XRD patterns of the synthesized pristine MAPI, and MAPI/S2_RGO.

The absorption characteristics of three RGO co-catalysts were examined using UV-visible spectroscopy. The three RGO co-catalysts (S1_RGO, S2_RGO, S3_RGO) exhibited slightly shifted UV-visible spectra due to variations in the degree of reduction. **Figure 2.2 a** illustrates that these co-catalysts possessed different bandgaps (calculated from the Tauc's plot), which might be attributed to their distinct chemical compositions. The least reduced co-catalyst (S1_RGO) had a bandgap of 2.83 eV, while S2_RGO (moderately reduced) and S3_RGO (maximum reduced) had bandgaps of 2.59 eV and 2.33 eV, respectively (**Figure 2.2 b, c, d**). These findings established a direct correlation between the extent of chemical reduction and the measured bandgaps. As the degree of chemical reduction progressed from S1_RGO to S2_RGO to S3_RGO, there was a gradual decrease in the bandgap, with S1_RGO having the highest value of 2.83 eV and S3_RGO having the lowest value of 2.33 eV.

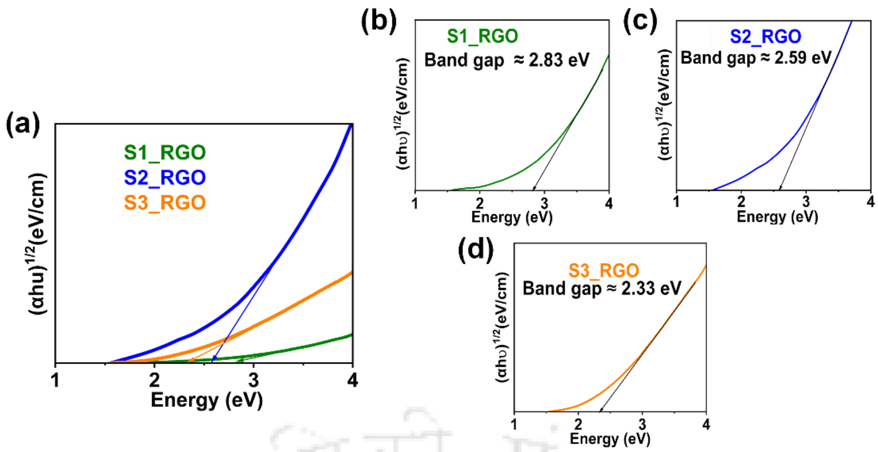

Figure 2.2: (a) comparative studies of bandgaps of RGOs. Bandgaps of (b) S3_RGO, (c) S1_RGO, (d) S2_RGO calculated from Tauc's plot

Solid state UV-visible spectroscopy was employed to examine the absorption properties of MAPI/RGO composites. Upon incorporating the co-catalysts, MAPI/S1_RGO and MAPI/S2_RGO composites exhibited a notable enhancement in their visible light absorption capabilities in comparison to the pristine MAPI, when subjected to equivalent sample quantities (**Figure 2.3**). In contrast, the pristine MAPI displayed the lowest absorption intensity within 400-800 nm region, with a bandgap of 1.55 eV determined from the Tauc's plot (**Figure. S2.6**). It is important to note that the absorption tail for the RGO loaded MAPI composites was extended beyond 800 nm. It signifies that MAPI/RGO composites can absorb a wider range of solar radiation than the pristine MAPI. This absorption phenomenon is commonly observed in composites with strong heterojunctions.[31]

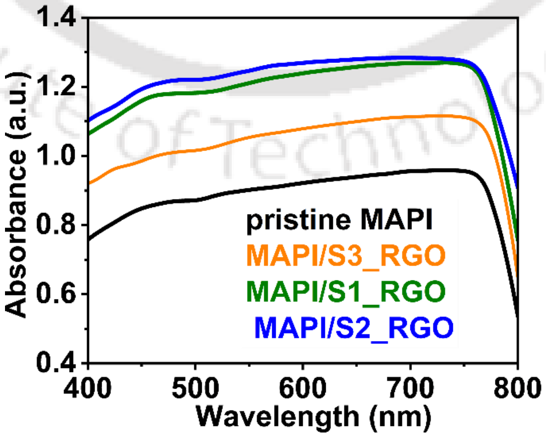

Figure 2.3: Solid state UV-visible spectra of pristine MAPI and its composites.

To understand the morphology, interaction between MAPI, RGO and the distribution of the elements in the photocatalyst composites, FESEM), FETEM and EDX analysis were performed. **Figure 2.4 a**, **b** represents the FESEM images of MAPI/S2_RGO composites and pristine MAPI respectively. The pristine MAPI microcrystals were highly crystalline in nature with a morphology corresponding to smooth surface. Furthermore, upon loading of RGO to MAPI, a microstructure was formed where tiny clusters of RGO were found to be firmly embedded on the MAPI surface indicating an intimate integration of MAPI and RGO. EDX was performed to understand the elemental distribution in the composites. Elemental mapping of the MAPI/S2_RGO photocatalyst composite (**Figure 2.4 d, e**) depicts that the Pb and I atoms (contributed by MAPI) were observed to be uniformly distributed throughout the crystal. As shown in **Figure 2.4 f, g** TEM and HRTEM images of MAPI/S2_RGO composites depict that MAPI and RGO have 2 distinct clear lattice fringes with d spacing of 0.231 nm and 0.356 nm for RGO and MAPI respectively. The robust heterojunction might be attributed to growth of MAPI microcrystal structures around the RGO clusters.

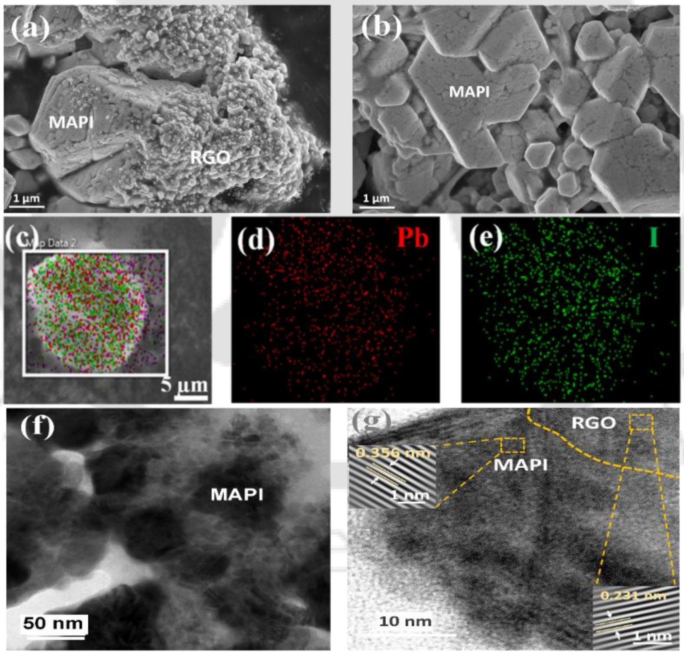

Figure 2.4: FESEM top view images of (a) pristine MAPI, (b) MAPI/S2_RGO composite. EDX elemental mapping of (c) all elements, (d) Pb, (e) I. TEM (f) and HRTEM (g) images of MAPI/S2_RGO. Inset of (g) showing the magnified images of MAPI and S2_RGO.

XPS, a surface-sensitive technique was performed for detailed elemental analysis of S1_RGO, S2_RGO and S3_RGO. As shown in **Figure 2.5 a,** two prominent peaks at 284.7

eV and 531.6 eV appeared in the survey scan of RGOs, corresponding to carbon and oxygen respectively. The atomic percentages calculated from the survey scan spectra, reveals that S1_RGO variant has carbon and oxygen contents of 70% and 30% respectively. For S2_RGO and S3_RGO the carbon and oxygen contents are 76%, 24% and 82%, 18%. respectively. The survey findings unequivocally demonstrate that the carbon-to -oxygen ratio for RGO exhibited a gradual increase as the extent of chemical reduction progressed from S1_RGO to S2_RGO to S3_RGO. On the other hand, as shown in Figure 5b, the deconvoluted C1s XPS spectra of three RGO variants revealed presence of 2 segments. First segment assigned at 284.7 eV originates from non-oxygenated carbons (C=C, C–C) of graphene structure. The 2nd segment assigned around 287 eV signifies the presence of oxygenated carbon atoms.[34] From **Figure 2.5 b**, it was clearly evident that 2nd segment got gradually diminished from S1_RGO towards S3_RGO as the extent of chemical reduction increases. These results strongly corelates with the relative carbon and oxygen content in RGOs as discussed earlier.

XPS was also employed to investigate the interplay between RGO and MAPI within composites. The survey spectrum of MAPI/RGO composites suggested the presence of Pb, I, C and O elements in composites depicted in **Figure 2.5 c**. whereas, **Figure 2.5 d** and **Figure 2.5 e** portray the electronic effect of S2_RGO on MAPI/S2_RGO composites. The 4f state of Pb in pristine MAPI contains two peaks at 142.818 eV and 137.943 eV corresponding to $4f_{5/2}$ and $4f_{7/2}$ states respectively. These peaks were shifted towards higher magnitude of binding energy by 0.34 eV in MAPI/S2_RGO composites as compared to the pristine MAPI suggesting facile transfer of photogenerated electrons towards the anchored RGO. Similar trends were observed in I3d state where peaks responsible for $3d_{3/2}$ and $3d_{5/2}$ states were shifted 0.32 eV towards higher binding energy after incorporation of RGO. The observed shifts in binding energy towards higher values for Pb and I refer to an effective interfacial charge transfer through the robust MAPI/RGO heterojunction which ultimately translated into improved photocatalytic performance.[35]

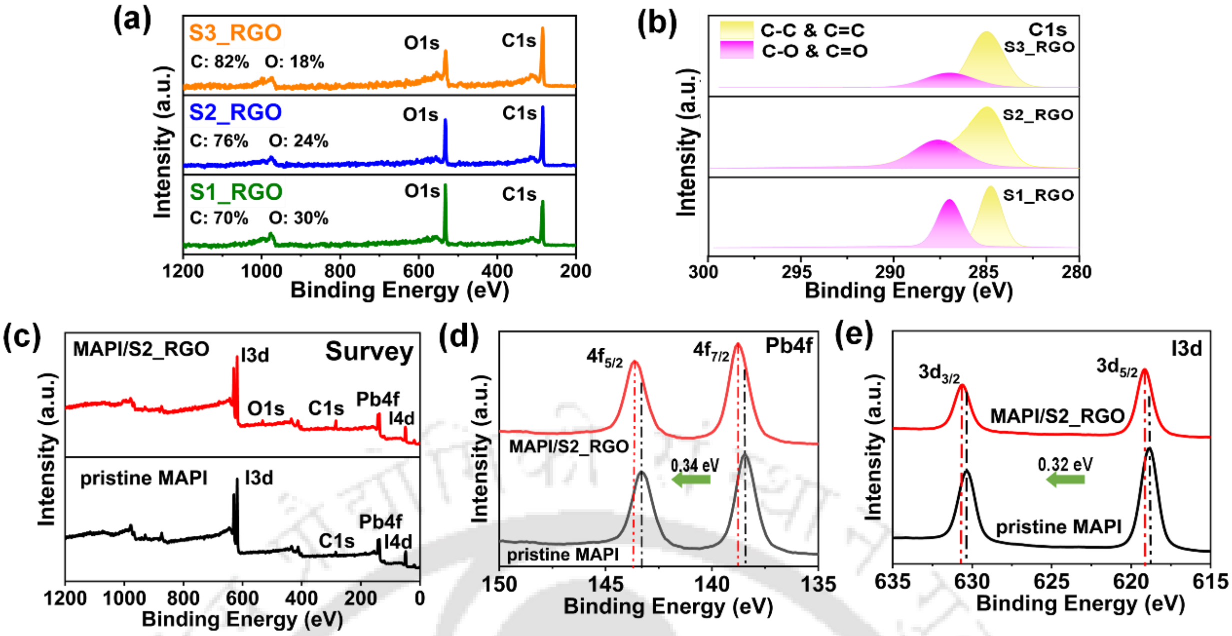

Figure 2.5: (a) XPS Survey scan (b) deconvoluted C1s XPS spectra of S1_RGO, S2_RGO, S3_RGO. (c) XPS survey of MAPI/S2_RGO. High resolution XPS spectrum of (d) Pb4f (e) I3d.

To explore the role of three variants of RGOs for charge transfer mechanism in MAPI/RGO composites, steady state photoluminescence (PL) study was carried out as illustrated in **Figure 2.6 a**. All MAPI/RGO composites registered photoluminescence emission at around 759 nm with different intensities owing to their varied degree of radiative charge recombination. A noteworthy decline in PL intensities were observed in all MAPI/RGO composites compared to pristine MAPI, which displayed the most elevated intensity of photoluminescence. Conversely, MAPI/S1_RGO and MAPI/S2_RGO exhibited the lowest PL intensities, that refers to most enriched charge separation in heterostructures.[36] In context of transient photocurrent (**Figure 2.6 b**), it was observed that MAPI/S2_RGO composites demonstrated the highest photocurrent, while the photocurrent gradually depreciated for MAPI/S1_RGO and MAPI/S3_RGO composites respectively. As anticipated, pristine MAPI exhibited the lowest photocurrent when subjected to identical electric bias. In terms of transient photocurrent, higher value indicates occurrence of effective and efficient charge migration in MAPI/RGO composites.[37]

These results were validated by electrochemical impedance spectroscopy (EIS) measurement as well. As shown in **Figure 2.6 c**, the MAPI/S2_RGO with smallest semicircle arc dictates the lowest interfacial charge transfer resistance resulting into expedite interfacial charge transfer.[38] For MAPI/S1_RGO and MAPI/S3_RGO composites, the interfacial charge transfer resistance gradually increases and is maximum for pristine MAPI. The aforementioned photoelectrochemical and electrochemical investigations collectively provide compelling evidence that S1_RGO and S2_RGO greatly facilitated the charge separation as well as rapid interfacial charge transfer from MAPI to RGO in composites, while the performance of MAPI/S1_RGO was slightly inferior. On the other hand, MAPI/S3_RGO demonstrated the lowest performance among all composites.

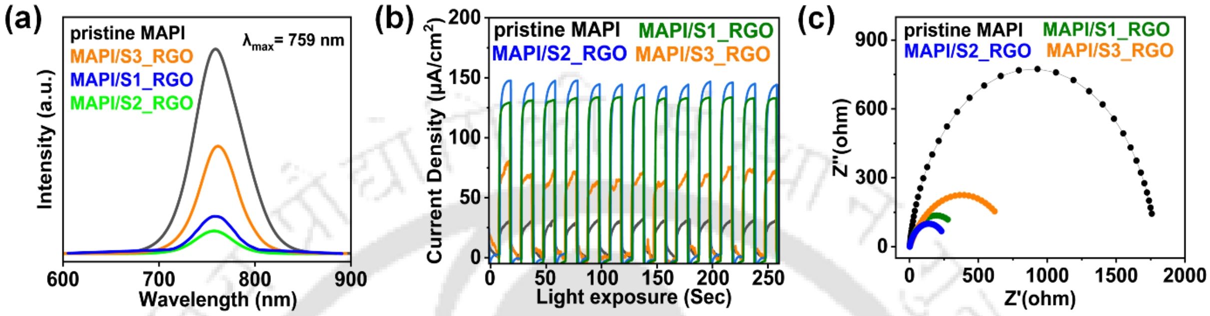

Figure 2.6: (a) Steady-state PL spectra, (b) transient photocurrent responses under visible light ($\lambda \geq 420$ nm) irradiation, (c) EIS Nyquist plots of pristine MAPI and MAPI/RGO composites.

For the purpose of photocatalytic H_2 generation reactions, the MAPI/RGO composites were fabricated by incorporating co-catalysts and precursors such as PbI_2 and MAI in a mixed solution of MAPI saturated aqueous HI/H_3PO_2, through the process of in-situ crystallization. In this MAPI-saturated HI/H_3PO_2 (5:1 v/v) solution, the photocatalytic H_2 evolution activity of the as-prepared samples were assessed under visible white light LED irradiation. The three most crucial components in this photocatalytic reaction are the photocatalyst, the light source and the reaction media. To confirm this, a series of controlled photocatalytic experiments were conducted, wherein each of these components was removed individually. Under these experimental conditions, no H_2 gas was detected in the absence of visible light irradiation, and the MAPI microcrystals were disintegrated in the absence of HI in the reaction medium. Nonetheless, the photocatalytic activities were confirmed through the gas chromatography under the influence of visible light on a photocatalyst, immersed in MAPI saturated HI/H_3PO_2 solution. The H_2 evolution rate for all the samples was compiled and presented as a function of the duration of light exposure in **Figure 2.7 a.** The H_2 evolution activity of pristine MAPI was found to be only 30 μmol g^{-1} h^{-1}. This lacklustre performance could be due to a smaller number of surface reaction sites on MAPI surfaces, leading to reduction in generation of photogenerated electrons and delayed transfer to the reaction media.[20]

Surprisingly, the H_2 evolution performance got noticeably improved with the introduction of RGO on MAPI microcrystals. The MAPI/S3_RGO composites exhibited a rate of H_2 evolution of 1176 μmol $g^{-1}h^{-1}$, lowest among all composites while MAPI/S2_RGO delivered the highest HER activity of 4493 μmol g^{-1} h^{-1} recorded among all the variants of MAPI/RGO composites. A performance comparison table (Table S1) has been added in the supplementary section which comprises all recent studies.

The observed result exceeds the value of pristine MAPI microcrystals by almost 150 folds. The declination in HER activities for MAPI/S3_RGO composites illustrated in **Figure 2.7 a** might be attributed to the misalignment of band edge positions between MAPI and RGO. It is worth noting that all composites, with a lower loading percentage (5 wt.%) of the co-catalyst (RGO), were able to generate mmol scale H_2 evolution. This occurrence could be elucidated by the process of in-situ crystallization (depicted in scheme 1), where the RGO clusters were deeply embedded on the MAPI surface (**Figure 2.4 a**). Consequently, the likelihood of segregation between MAPI and RGO decreases during the magnetic stirring for HER activity. Moreover, this aids in the formation of a strong heterojunction, resulting in the aforementioned improvement in HER activity. In terms of H_2 evolution activity, MAPI/RGO composites not only outperformed pristine MAPI but also exhibited superior HER performance when compared to Pt-deposited MAPI.[19] In addition, it is also worth mentioning that the MAPI/S2_RGO combination exhibited good stability in HER over prolonged duration (**Figure 2.7 b**). The photocatalytic H_2 evolution was carried out with MAPI/S2_RGO composites under white light LED for 100 hours. There was no considerable loss in HER activity for 10 consecutive cycles and each cycle was of 7 hours long with 1 hour gap for evacuation and purging inert N_2 gas. However, after a long irradiation of 80 hours, the HER activity significantly decreased throughout the course of the last two cycles. The decline in the measured activity might be attributed to the consumption of H_3PO_2 during the cyclic reaction processes, leading to the excessive generation of I_3^- ions that could impede the absorption of light by the MAPI composites.[39] High resolution XPS and TEM studies of MAPI/S2_RGO samples were done after 100 hours of HER activities. This indicate that no considerable degradation had been observed after 100 hours long HER activities (**Figure S2.7, S2.8**).

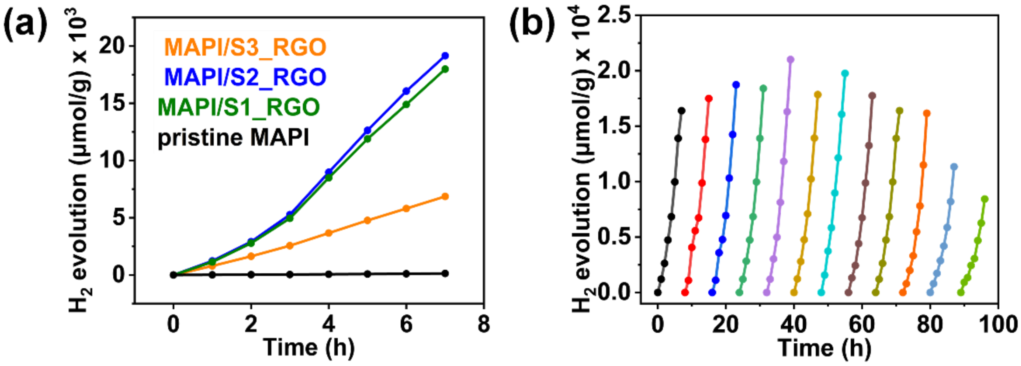

Figure 2.7: (a) Comparative study of H$_2$ evolution of all MAPI/RGO composites (5 wt.%) and (b) H$_2$ evolution activity of MAPI/S2_RGO composites over 100 hours long white light LED exposure.

A crucial technique, electrochemical Mott-Schottky analysis was employed to assess the conduction band minima (CBM) of three variants of RGOs. This investigation unveiled a positive slope in the RGOs, suggesting their classification as n-type semiconductors. The flat band potentials (E_{FB}) were estimated for three RGOs (**Figure S2.9**). In case of S1_RGO, the flat band potential (E_{FB}) was determined to be -0.32 V vs Ag/AgCl reference electrode, which is corresponds to -0.12 V relative to the Normal Hydrogen Electrode (NHE).[40] The conduction band minima (CBM) of the n-type semiconductor was assumed to be 0.1 V more negative than the flat band potential (vs NHE).[18, 41] Consequently, the calculated CBM for S1_RGO was -0.22 V with respect to NHE. With progression in degree of chemical reduction from S1_RGO to S3_RGO, the E_{FB} (vs Ag/AgCl) became more negative gradually. The estimated flat band potential (E_{FB}) for S2_RGO was -0.55 V vs Ag/AgCl, resulting in CBM value of -0.45 V vs NHE. The most extensively reduced variant, S3_RGO, exhibited an E_{FB} value of -0.9 V vs Ag/AgCl, corresponding to CBM value of -0.8 V vs NHE. The E_{FB} values of the RGOs clearly indicate a trend where, the flat band potential approaches more and more upward from $E(H^+/H_2)$ reference (0 V vs NHE) i.e. E_{FB} become more negative as the degree of chemical reduction of RGO increases.

The comprehension of the distinct photocatalytic and the photochemical properties can be readily attained through the examination and juxtaposition of the energy profile diagram of three composites, summarized in **Figure 2.8**. From the UPS data, the valence band maxima (VBM) of MAPI was found to be -5.45 eV relative to vacuum.[19] Following the incorporation of band gap energy (1.55 eV) with VBM, the resultant conduction band minima (CBM) of MAPI was calculated to be -3.9 eV against vacuum i.e., -0.6 V vs NHE. The H$_2$ electrode potential $E(H^+/H_2)$ was considered as -4.5 eV with respect to vacuum level.[18] For MAPI/S1_RGO and MAPI/S2_RGO, the conduction band minima (CBM) of RGO were positioned lower than the CBM of MAPI but higher than the redox potential of the hydrogen/hydrogen ion $E(H^+/H_2)$ which is 0 V vs NHE, this particular arrangement of energy bands presents an ideal scenario for efficient photogenerated charge transfer from MAPI to RGO and ultimately resulting into successful proton reduction under sunlight. Conversely, in the case of S3_RGO, the CBM was situated above the energy levels of MAPI, rendering it energetically unfeasible for photogenerated charge transfer between MAPI and S3_RGO co-catalyst. This unfavorable energy band alignment leads to the lowest rate of hydrogen evolution as well as negatively impacting other properties such as transient photocurrent and photoluminescence intensity. Though the CBM of S1_RGO and S2_RGO were situated in between the CBM of MAPI and $E(H^+/H_2)$, it was observed that the MAPI/S2_RGO composite exhibited slightly superior photocatalytic and photochemical properties in comparison to MAPI/S1_RGO, as dictated by the principles of thermodynamics. This could be explained by the fact that CBM of S2_RGO is positioned higher than of S1_RGO.[42-44]

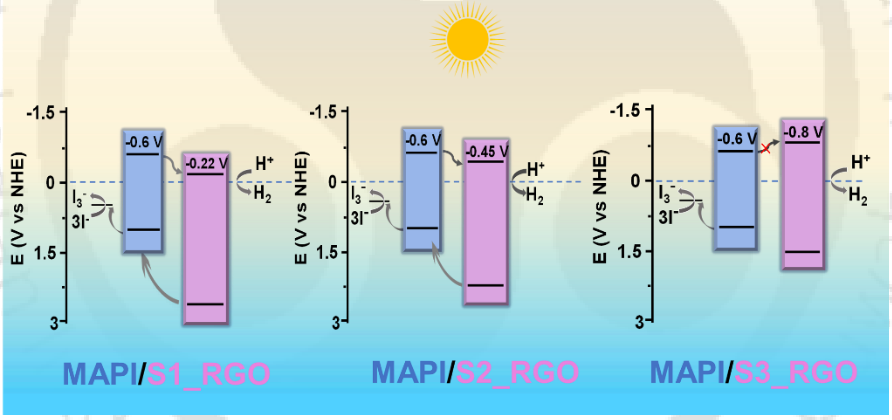

Figure 2.8: Schematic illustration of band alignment of MAPI/RGO composites and mechanism of H_2 evolution in aqueous HI.

2.4 Experimental section

Materials: Graphite powder, Na_2SO_3, lead iodide (99%), hydrogen iodide (57 wt% in H_2O) were purchased from Sigma-Aldrich. $KMnO_4$, $NaNO_3$, 30% H_2O_2 were obtained from Merck India. Methylammonium iodide was purchased from Great cell solar. Hypo phosphorus acid was obtained from Loba chemie. All other chemicals were used as received.

Preparation of MAPI powder and MAPI saturated solution: MAPI was synthesized by dissolving MAI and PbI_2 in molar ratio of 1:1 in HI/H_3PO_2 aqueous solution. Specifically, 15 g PbI_2 was dissolved in 50 ml of HI acid (57 wt% in water), then 5.15 g MAI was slowly added into the solution with vigorous stirring under 80°C. The saturated solution used here was prepared by adding 57 wt% of HI at 50 wt% H_3PO_2 in 5:1(v/v) ratio. The reaction solution with black precipitate was stirred and heated to 100°C for 1h for crystallization to attain the dynamic equilibrium, followed by cooling down to room temperature to obtain the saturated solution containing black MAPI precipitates at the bottom. The MAPI precipitates were separated out from saturated solution by centrifuge, the obtained saturated solution was stored for next photocatalytic measurements, while the precipitates were dried in a vacuum oven at 80°C to get pristine MAPI powder.

Synthesis of RGO from graphene: The synthesis was performed based on the reported modified Hummer's method[28] with slight modifications. Briefly 3g of graphite powder was added to 81 ml of conc. H_2SO_4 followed by 3 g $NaNO_3$ addition to the solution. Thereafter, 9 g of $KMnO_4$ was added in portions with continuous stirring. The solution was then subjected to 24 hours stirring. Ice cubes were then added carefully in the solution followed by addition of 30% H_2O_2 dropwise until the black colour turned yellow. For the reduction of GO into RGO, 50 mg, 100 mg and 200 mg of Na_2SO_3 were added for S1_RGO, S2_RGO and S3_RGO respectively until the yellow colour turned black. The solution was stirred for few hours followed by separation via centrifugation at 6000 rpm for 5 minutes. Several DI water washings were carried out to get pH neutral confirmed by litmus paper test and clear $BaCl_2$ solution. The obtained RGO was freeze dried to get a black coloured dry powder.

Fabrication of MAPI/RGO composites: MAPI/RGO composites were prepared by a novel *in-situ* crystallization procedure. Instead of manually mixing MAPI and RGO in MAPI saturated HI-H_3PO_2 (5:1 v/v) solution, 20 mg of 3 variants of RGOs (≈ 5 wt.% with respect to total MAPI formed) were added into the HI-H_3PO_2 solution containing PbI_2 (0.65 mmol/ml) followed by constant stirring at 75°C until a homogeneous dispersion was obtained. Then solid methylammonium Iodide (MAI) (0.65 mmol) was slowly added to the PbI_2/RGO solution. A black precipitate started to appear immediately upon MAI addition. The reaction mixture was then subjected to constant stirring and heating at 100°C for 3 hours followed by cooling down. The composites were separated using a centrifuge and washed with dry ethyl acetate for three times followed by vacuum drying at 85°C.

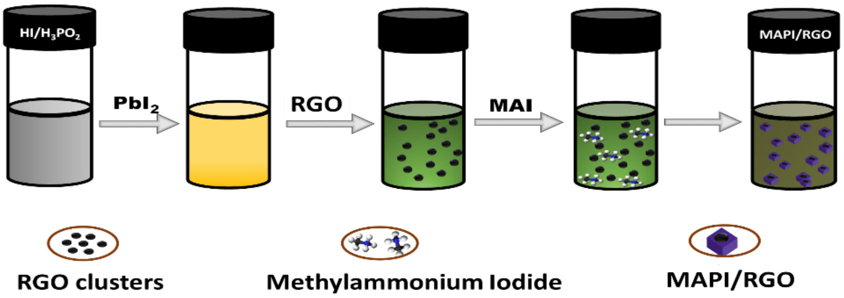

Figure 2.9: Synthesis of MAPI/RGO composites via in-situ crystallization.

Characterization

Powder X-ray diffractogram was obtained from Rigaku Micromax-007HF diffractometer equipped with Cu Kα1 irradiation (λ = 1.54184 Å) at scan rate of 5°/min. Morphology studies were conducted using ZEISS, SIGMA FESEM and microscope (TEM) (JEOL-JEM 2010 operated at 200 kV). X-ray photoelectron spectroscopy (XPS) measurement was executed using a PHI 5000 Versa Probe III automated photoelectron spectrometer (ULVAC-PHI, Japan) with an Al Kα X-ray beam (1486.7 eV) at 20 kV, 84 W for the analysis of the chemical compositions. Solid state UV-vis spectra were recorded on a PerkinElmer Lambda-750 UV-vis-near-IR spectrometer equipped with an integrating sphere and $BaSO_4$ powders were used as a reflectance standard. Photoluminescence spectra were determined by a Horiba Scientific FluoroMax-4 spectrofluorometer spectrometer. Energy-dispersive X-ray (EDX) spectroscopy (Sigma 300, Zeiss) was used for surface elemental analysis. CH Instruments 760D were used for Electrochemical measurements.

Photocatalytic measurement

The photocatalytic hydrogen evolution experiments were carried out in a glass vessel coupled with gas chromatograph (Agilent 7820A GC System). A typical process consists: (a) 50 mg of photocatalyst dispersed in 15 mL of MAPI saturated aqueous solution of HI/ H_3PO_2 under constant stirring at 25°C, (b) degassing the photocatalytic chamber for 30 min, (c) using online gas chromatography to confirm no H_2 was being generated in the reaction chamber in absence of light irradiation and (d) turning on the light source to start the photocatalytic HI splitting reaction with continuous monitoring of the hydrogen generation by gas chromatograph.

Photoelectrochemical measurement

The electrochemical impedance spectroscopy (EIS), Mott-Schottky curves and transient photocurrent response curves were performed on the electrochemical workstation (CH Instruments Ins.) in a three-electrode configuration with the assembled photoelectrodes (photocatalysts coated on 1 cm^2 of carbon paper) as the working electrode, the Ag/AgCl as the reference electrode and the Pt wire as the counter electrode. The EIS experiments were performed in MAPI saturated aqueous HI/H_3PO_2 solution under scan rate of 10 mV s^{-1}. Mott-Schottky curves were obtained using MAPI saturated aqueous HI/H_3PO_2 solution as electrolyte at 1000 Hz frequency.

Visible light source for photocatalytic measurements

The visible light source used here for the experiments is a 50 W with power density of 150 mW/cm^2 white LED bought from Ledvance Osram. The spectrum of this light source is 420 - 790 nm.

Table 2.1: A summary of the performance and experimental parameters of reported halide perovskite photocatalysts for H_2 evolution.

MHP Catalyst	Co-catalyst	Light source	Irradiation area (cm^2)	Activity	Reference cited in main Article
$MAPbI_3$	Pt	($\lambda \geq$ 475 nm) 100 mW/cm^2	0.25 cm^2	57 µmol g^{-1} h^{-1}	17
$MAPbBr_{3-x}I_x$	Pt	100 W, $\lambda \geq$420 nm) 100 mW/ cm^2	Π cm^2	651.2 µmol g^{-1} h^{-1}	28
$MAPbI_3$	RGO	120 mW/cm^2 $\lambda \geq$420 nm	18.1 cm^2	939 µmol g^{-1}h^{-1}	30
$MAPbI_3$	TiO_2/Pt	200 mW/cm^2 $\lambda \geq$420 nm	1.82 cm^2	1784 µmol g^{-1} h^{-1}	31

MAPbI$_3$	Ni$_3$C	λ ≥ 420 nm, 100 mW/cm^2	0.25 cm^2	2362 µmol g^{-1} h^{-1}	18
MAPbI$_3$	Black P	λ ≥ 420 nm, 100 mW/cm^2	0.25 cm^2	3742 µmol g^{-1} h^{-1}	29
BA$_2$MA$_3$Pb$_4$I$_{13}$	Pt	AM 1.5G, 100 mW/cm^2	Π cm^2	3948 µmol g^{-1} h^{-1}	26
MAPbI$_3$	RGO with C≈76% and O≈ 24%	λ ≥ 420 nm, 150 mW/cm^2	4.9 cm^2	4493 µmol g^{-1} h^{-1}	This work
MAPbI$_3$	Multishell TiO$_2$/Pt	λ ≥ 420 nm, 150 mW/cm^2	28.26 cm^2	6856 µmol h-^{1} g^{-1}	44
MAPbI$_3$	Carbonized polymer dot	λ ≥ 420 nm, 100 mW/cm^2	0.25 cm^2	11497 µmol g^{-1} h^{-1}	43
MAPbI$_3$	MoS$_2$	280 W, λ≥ 410 nm, 100 mW/cm^2	0.14 cm^2	30000 µmolg^{-1} h^{-1}	19

2.5 Conclusion

Role of oxygen content dependent RGOs in MAPI/RGO heterostructures has been investigated for photochemical and photoelectrochemical activities. This article also summarizes the fact that variation in extent of chemical reduction not only controls the atomic percentage of oxygen content, but also governs the varied bandgaps as well as band edge positions for three variants of RGOs. Among all these variations, S2_RGO with bandgap of 2.59 eV and oxygen content of 24% was identified as the best performing co-catalyst with highest HER. On contrary MAPI/S3_RGO registered lowest photoelectrochemical and HER activities where S_3/RGO is the most chemically reduced variant of RGO with lowest oxygen content (18%) with a bandgap of 2.33 eV. For MAPI/S1_RGO composites the performance were slightly lesser than MAPI/S2_RGO. To rationalize the occurrence of disparities in photoelectrochemical and photocatalytic activities of all three MAPI/RGO composites, we have proposed an electron transfer mechanism, where depending upon the relative CBM positions of MAPI and respective RGO, dissimilar photogenerated electron transfer took place.

As we move from S1_RGO towards S3_RGO, the position of the conduction band minima of RGOs gradually shifted in a more negative direction with respect to reference in the NHE. Ultimately for MAPI/S3_RGO, the CBM of S3_RGO was situated above the CBM of MAPI, resulting into lowest rate of H_2 evolution and other properties such as transient photocurrent and photoluminescence intensity. For MAPI/S1_RGO and MAPI/S2_RGO, the CBM of S1_RGO and S2_RGO were positioned lower than the CBM of MAPI but higher than the redox potential of the $E(H^+/H_2)$ which is best possible scenario for photogenerated electron transfer, still MAPI/S2_RGO performed slightly better due to thermodynamic reason. It is also noteworthy to mention that significantly lesser co-catalyst loading percentage were (5 wt. %) used for composites formation which could be possible due to robust heterostructures formed by in-situ crystallization process.

2.6 Reference

(1) Khaselev, O.; Turner, J. A. A Monolithic Photovoltaic-Photoelectrochemical Device for Hydrogen Production via Water Splitting. *Science* **1998**, *280*, 425–427.

(2) Yuan, Q.; Liu, D.; Zhang, N.; Ye, W.; Ju, H.; Shi, L.; Long, R.; Zhu, J.; Xiong, Y. Noble-metal-free Janus-like Structures by Cation Exchange for Z-scheme Photocatalytic Water Splitting under Broadband Light Irradiation. *Angew., Chem., Int. Ed.* **2017**, *56* (15), 4206–4210.

(3) Bowker, M. Sustainable Hydrogen Production by the Application of Ambient Temperature Photocatalysis. *Green Chem.* **2011**, *13*, 2235-2246.

(4) Liu, W.; Zuo, H.; Wang, J.; Xue, Q.; Ren, B.; Yang, F. The Production and Application of Hydrogen in Steel Industry. *Int. J. Hydrogen Energy* **2021**, *46*, 10548–10569.

(5) Stolten, D.; Emonts, B. Hydrogen Science and Engineering, 2 Volume Set: Materials, Processes, Systems, and Technology; John Wiley & Sons, 2016.

(6) Hermesmann, M.; Müller, T. E. Green, Turquoise, Blue, or Grey? Environmentally Friendly Hydrogen Production in Transforming Energy Systems. *Prog. Energy Combust. Sci.* **2022**, *90*, 100996.

(7) Rahman, M. Z.; Kibria, M. G.; Mullins, C. B. Metal-Free Photocatalysts for Hydrogen Evolution. *Chem. Soc. Rev.* **2020**, *49*, 1887–1931.

(8) Li, W.; Wang, F.; Zhang, Z.; Ma, X.; Min, S. Coupling of MAPbI$_3$ Microcrystals with Conductive Polyaniline for Efficient Visible-Light-Driven H$_2$ Evolution. *Sustain. Energy Fuels* **2022**, *6*, 76–80.

(9) Chen, X.; Shen, S.; Guo, L.; Mao, S. S. Semiconductor-Based Photocatalytic Hydrogen Generation. *Chem. Rev.* **2010**, *110*, 6503–6570.

(10) Garai, R.; Gupta, R. K.; Hossain, M.; Iyer, P. K. Surface Recrystallized Stable 2D–3D Graded Perovskite Solar Cells for Efficiency beyond 21%. *J. Mater. Chem. A* **2021**, *9*, 26069–26076.

(11) Sidhik, S.; Wang, Y.; De Siena, M.; Asadpour, R.; Torma, A. J.; Terlier, T.; Ho, K.; Li, W.; Puthirath, A. B.; Shuai, X.; Agrawal, A.; Traore, B.; Jones, M.; Giridharagopal, R.; Ajayan, P. M.; Strzalka, J.; Ginger, D. S.; Katan, C.; Alam, M. A.; Even, J.; Kanatzidis, M. G.; Mohite, A. D. Deterministic Fabrication of 3D/2D Perovskite Bilayer Stacks for Durable and Efficient Solar Cells. *Science* **2022**, *377*, 1425–1430.

(12) Garai, R.; Gupta, R. K.; Tanwar, A. S.; Hossain, M.; Iyer, P. K. Conjugated Polyelectrolyte-Passivated Stable Perovskite Solar Cells for Efficiency beyond 20%. *Chem. Mater.* **2021**, *33*, 5709–5717.

(13) Garai, R.; Afroz, M. A.; Gupta, R. K.; Iyer, P. K. Efficient Trap Passivation of MAPbI$_3$ via Multifunctional Anchoring for High-Performance and Stable Perovskite Solar Cells. *Adv. Sustainable Syst.* **2020**, *4* (8), 2000078, DOI: 10.1002/adsu.202000078.

(14) Zhang, Y.; Liu, Y.; Yang, Z.; Liu, S. (frank). High-Quality Perovskite MAPbI$_3$ Single Crystals for Broad-Spectrum and Rapid Response Integrate Photodetector. *J. Energy Chem.* **2018**, *27*, 722–727.

(15) Chen, B.; Baek, S.-W.; Hou, Y.; Aydin, E.; De Bastiani, M.; Scheffel, B.; Proppe, A.; Huang, Z.; Wei, M.; Wang, Y.-K.; Jung, E.-H.; Allen, T. G.; Van Kerschaver, E.; García de Arquer, F. P.; Saidaminov, M. I.; Hoogland, S.; De Wolf, S.; Sargent, E. H. Enhanced Optical Path and Electron Diffusion Length Enable High-Efficiency Perovskite Tandems. *Nat. Commun.* **2020**, *11*, 1257.

(16) Galkowski, K.; Mitioglu, A.; Miyata, A.; Plochocka, P.; Portugall, O.; Eperon, G. E.; Wang, J. T.-W.; Stergiopoulos, T.; Stranks, S. D.; Snaith, H. J.; Nicholas, R. J. Determination of the Exciton Binding Energy and Effective Masses for

Methylammonium and Formamidinium Lead Tri-Halide Perovskite Semiconductors. *Energy Environ. Sci.* **2016**, *9*, 962–970.

(17) Park, S.; Chang, W. J.; Lee, C. W.; Park, S.; Ahn, H.-Y.; Nam, K. T. Photocatalytic Hydrogen Generation from Hydriodic Acid Using Methylammonium Lead Iodide in Dynamic Equilibrium with Aqueous Solution. *Nat. Energy* **2016**, *2*, 16185.

(18) Zhao, Z.; Wu, J.; Zheng, Y.-Z.; Li, N.; Li, X.; Tao, X. Ni_3C-Decorated MAPbI3 as Visible-Light Photocatalyst for H_2 Evolution from HI Splitting. *ACS Catal.* **2019**, *9*, 8144–8152.

(19) Guan, W.; Li, Y.; Zhong, Q.; Liu, H.; Chen, J.; Hu, H.; Lv, K.; Gong, J.; Xu, Y.; Kang, Z.; Cao, M.; Zhang, Q. Fabricating $MAPbI_3/MoS_2$ Composites for Improved Photocatalytic Performance. *Nano Lett.* **2021**, *21*, 597–604.

(20) Li, W.; Wang, F.; Zhang, Z.; Min, S. $MAPbI_3$ Microcrystals Integrated with Ti_3C_2Tx MXene Nanosheets for Efficient Visible-Light Photocatalytic H_2 Evolution. *Chem. Commun.* **2021**, *57*, 7774–7777.

(21) Yao, Q.; Li, H.; Xue, J.; Jiang, S.; Zhang, Q.; Bao, J. Promoting Photocatalytic H2 Evolution through Retarded Charge Trapping and Recombination by Continuously Distributed Defects in Methylammonium Lead Iodide Perovskite. *Angew., Chem., Int. Ed.* **2023**, *62* (34), e202308140, DOI: 10.1002/anie.202308140.

(22) Zhao, X.; Chen, S.; Yin, H.; Jiang, S.; Zhao, K.; Kang, J.; Liu, P. F.; Jiang, L.; Zhu, Z.; Cui, D.; Liu, P.; Han, X.; Yang, H. G.; Zhao, H. Perovskite Microcrystals with Intercalated Monolayer MoS_2 Nanosheets as Advanced Photocatalyst for Solar-Powered Hydrogen Generation. *Matter* **2020**, *3*, 935–949.

(23) Xia, Z.; Liu, B.; Xiao, Y.; Hu, W.; Deng, M.; Lü, C. Integrating Hybrid Perovskite Nanocrystals into Metal–Organic Framework as Efficient S-Scheme Heterojunction Photocatalyst for Synergistically Boosting Controlled Radical Photopolymerization under 980 Nm NIR Light. *ACS Appl. Mater. Interfaces* **2023**, *15*, 57119–57133.

(24) Liu, J.; Zhang, H.; Wang, J.; Zong, X. Tuning the Dimensionality of Organic–Inorganic Hybrid Perovskites towards Improved Photocatalytic Hydrogen Production. *J. Mater. Chem. A* **2024**, *12*, 5740–5747.

(25) Wang, X.; Peng, Y.; Yang, S.; Yang, H. G.; Hou, Y. Recent Progress in Metal Halide Perovskite Photocatalysts for Hydrogen Evolution. *Mater. Chem. Front*. **2023**, *7*, 4635–4657.

(26) Fu, H.; Liu, X.; Fu, J.; Wu, Y.; Zhang, Q.; Wang, Z.; Liu, Y.; Zheng, Z.; Cheng, H.; Dai, Y.; Huang, B.; Wang, P. 2D/Quasi-2D Ruddlesden–Popper Perovskite: A High-Performance Photocatalyst for Hydrogen Evolution. *ACS Catal*. **2023**, *13*, 14716–14724.

(27) Liu, X.; Zhang, Q.; Zhao, S.; Wang, Z.; Liu, Y.; Zheng, Z.; Cheng, H.; Dai, Y.; Huang, B.; Wang, P. Integrating Mixed Halide Perovskite Photocatalytic HI Splitting and Electrocatalysis into a Loop for Efficient and Robust Pure Water Splitting. *Adv. Mater.* **2023**, *35* (19), 2208915, DOI: 10.1002/adma.202208915.

(28) Wu, Y.; Wang, P.; Guan, Z.; Liu, J.; Wang, Z.; Zheng, Z.; Jin, S.; Dai, Y.; Whangbo, M.-H.; Huang, B. Enhancing the Photocatalytic Hydrogen Evolution Activity of Mixed-Halide Perovskite CH3NH3PbBr3–xIx Achieved by Bandgap Funneling of Charge Carriers. *ACS Catal.* **2018**, *8*, 10349–10357.

(29) Li, R.; Li, X.; Wu, J.; Lv, X.; Zheng, Y.-Z.; Zhao, Z.; Ding, X.; Tao, X.; Chen, J.-F. Few-Layer Black Phosphorus-on-MAPbI$_3$ for Superb Visible-Light Photocatalytic Hydrogen Evolution from HI Splitting. *Appl. Catal. B* **2019**, *259*, 118075, DOI: 10.1016/j.apcatb.2019.118075.

(30) Wu, Y.; Wang, P.; Zhu, X.; Zhang, Q.; Wang, Z.; Liu, Y.; Zou, G.; Dai, Y.; Whangbo, M.-H.; Huang, B. Composite of $CH_3NH_3PbI_3$ with Reduced Graphene Oxide as a Highly Efficient and Stable Visible-light Photocatalyst for Hydrogen Evolution in Aqueous HI Solution. *Adv. Mater*. **2018**, *30* (7), 1704342, DOI: 10.1002/adma.201704342.

(31) Wang, X.; Wang, H.; Zhang, H.; Yu, W.; Wang, X.; Zhao, Y.; Zong, X.; Li, C. Dynamic Interaction between Methylammonium Lead Iodide and TiO_2 Nanocrystals Leads to Enhanced Photocatalytic H_2 Evolution from HI Splitting. *ACS Energy Lett.* **2018**, *3* (5), 1159–1164.

(32) Yu, P.; Wang, L.; Xie, Y.; Tian, C.; Sun, F.; Ma, J.; Tong, M.; Zhou, W.; Li, J.; Fu, H. High-Efficient, Stable Electrocatalytic Hydrogen Evolution in Acid Media by Amorphous Fe_xP Coating Fe2N Supported on Reduced Graphene Oxide. *Small* **2018**, *14* (35), 1801717, DOI: 10.1002/smll.201801717.

(33) Pan, J.; Wang, B.; Dong, Z.; Zhao, C.; Jiang, Z.; Song, C.; Wang, J.; Zheng, Y.; Li, C. The 2D RGO-NiS_2 Dual Co-Catalyst Synergistic Modified g-C_3N_4 Aerogel towards Enhanced Photocatalytic Hydrogen Production. *Int. J. Hydrogen Energy* **2019**, *44*, 19942–19952.

(34) Gupta, B.; Kumar, N.; Panda, K.; Kanan, V.; Joshi, S.; Visoly-Fisher, I. Role of Oxygen Functional Groups in Reduced Graphene Oxide for Lubrication. *Sci. Rep*. **2017**, *7*, 45030, DOI: 10.1038/srep45030.

(35) Yu, J.; Xu, X. Expediting H_2 Evolution over $MAPbI_3$ with a Nonnoble Metal Cocatalyst Mo_2 C under Visible Light. *Energy Mater. Adv*. **2022**, DOI: 10.34133/2022/9836095.

(36) Yang, L.; Yu, J.; Fu, Q.; Kong, L.; Xu, X. Mesoporous Single-Crystalline $SrNbO_2N$: Expediting Charge Transportation to Advance Solar Water Splitting. *Nano Energy* **2022**, *95*, 107059.

(37) Alam, S.; Sahu, T. K.; Qureshi, M. One-Dimensional Co(OH)F as a Noble Metal-Free Redox Mediator and Hole Extractor for Boosted Photoelectrochemical Water Oxidation in Worm-like Bismuth Vanadate. *ACS Sustain. Chem. Eng*. **2021**, *9*, 5155–5165.

(38) Pathak, A.; Chhoker, S.; Singh, P.; Sharma, H.; Kumar, R. Electrochemical Studies of Halide Perovskite and Its Correlation for Photocatalytic Applications. *Solid State Sci.* **2023**, *139*, 107159, DOI: 10.1016/j.solidstatesciences.2023.107159.

(39) Wang, F.; Liu, X.; Zhang, Z.; Min, S. A Noble-Metal-Free MoS_2 Nanosheet-Coupled $MAPbI_3$ Photocatalyst for Efficient and Stable Visible-Light-Driven Hydrogen Evolution. *Chem. Commun*. **2020**, *56*, 3281–3284.

(40) Li, S.; Yu, H.; Wang, Y.; Wang, S.; Zhang, L.; Zhu, P.; Gao, C.; Yu, J. Exploring a Ni-N4 Active Site-Based Conjugated Microporous Polymer Z-Scheme Heterojunction through Covalent Bonding for Visible Light-Driven Photocatalytic CO_2 Conversion in Pure Water. *Small* **2023**, e2305900.

(41) He, J.; Wang, J.; Chen, Y.; Zhang, J.; Duan, D.; Wang, Y.; Yan, Z. A Dye-Sensitized Pt@UiO-66(Zr) Metal-Organic Framework for Visible-Light Photocatalytic Hydrogen Production. *Chem. Commun*. **2014**, *50*, 7063–7066.

(42) Feng, D.; Cheng, Y.; He, J.; Zheng, L.; Shao, D.; Wang, W.; Wang, W.; Lu, F.; Dong, H.; Liu, H.; Zheng, R.; Liu, H. Enhanced Photocatalytic Activities of g-C$_3$N$_4$ with Large Specific Surface Area via a Facile One-Step Synthesis Process. *Carbon* **2017**, *125*, 454–463.

(43) Zhao, Y.; Zeng, Q.; Yu, Y.; Feng, T.; Zhao, Y.; Wang, Z.; Li, Y.; Liu, C.; Liu, J.; Wei, H.; Zhu, S.; Kang, Z.; Zhang, H.; Yang, B. Enhanced Charge Separation and Photocatalytic Hydrogen Evolution in Carbonized-Polymer-Dot-Coupled Lead Halide Perovskites. *Mater. Horiz.* **2020,** *7*, 2719–2725.

(44) Han, W.; Wei, Y.; Wan, J.; Nakagawa, N.; Wang, D. Hollow Multishell-Structured TiO$_2$/MAPbI$_3$ Composite Improves Charge Utilization for Visible-Light Photocatalytic Hydrogen Evolution. *Inorg. Chem*. **2022**, *61*, 5397–5404.

2.7 Supporting Information

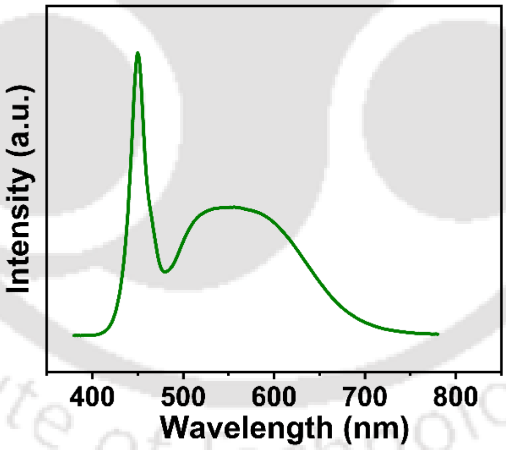

Figure S2.1: Electroluminescence of light source.

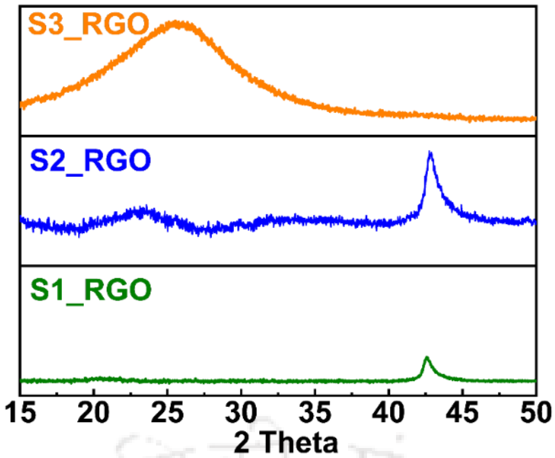

Figure S2.2: XRD of 3 variants of RGOs.

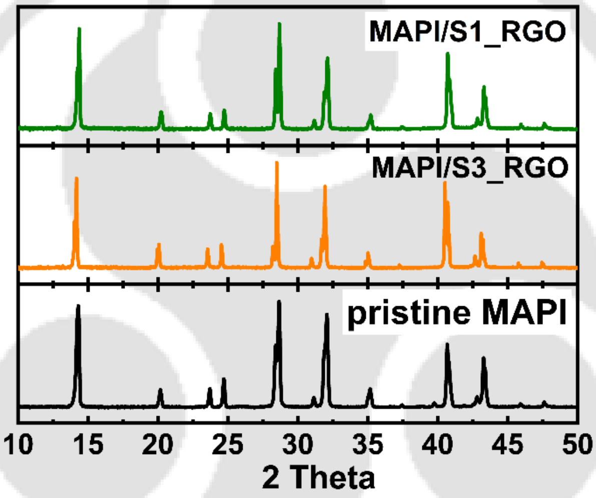

Figure S2.3: XRD study of MAPI/RGO composites.

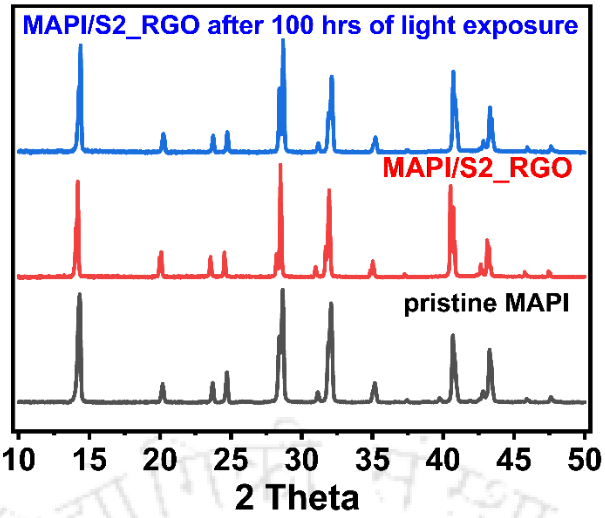

Figure S2.4: Stability study of MAPI/RGO.

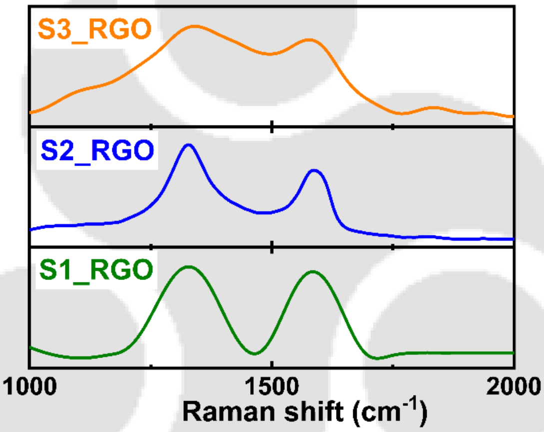

Figure S2.5: Raman spectra of 3 RGOs.

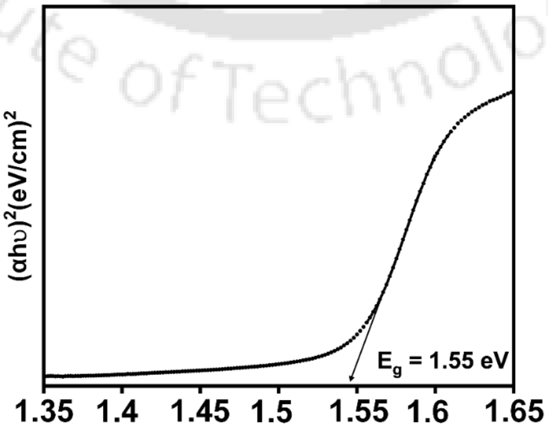

Figure S2.6: Band gap of pristine MAPI calculated from Tauc plot.

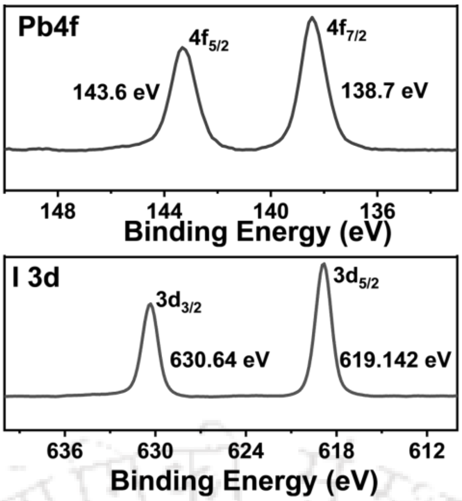

Figure S2.7: High resolution XPS of MAPI/S2_RGO after 100 hours of hydrogen evolution.

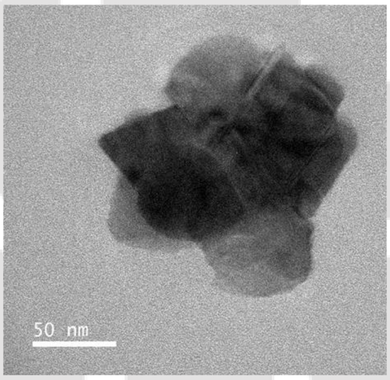

Figure S2.8: TEM image of MAPI/S2_RGO after 100 hours of hydrogen evolution.

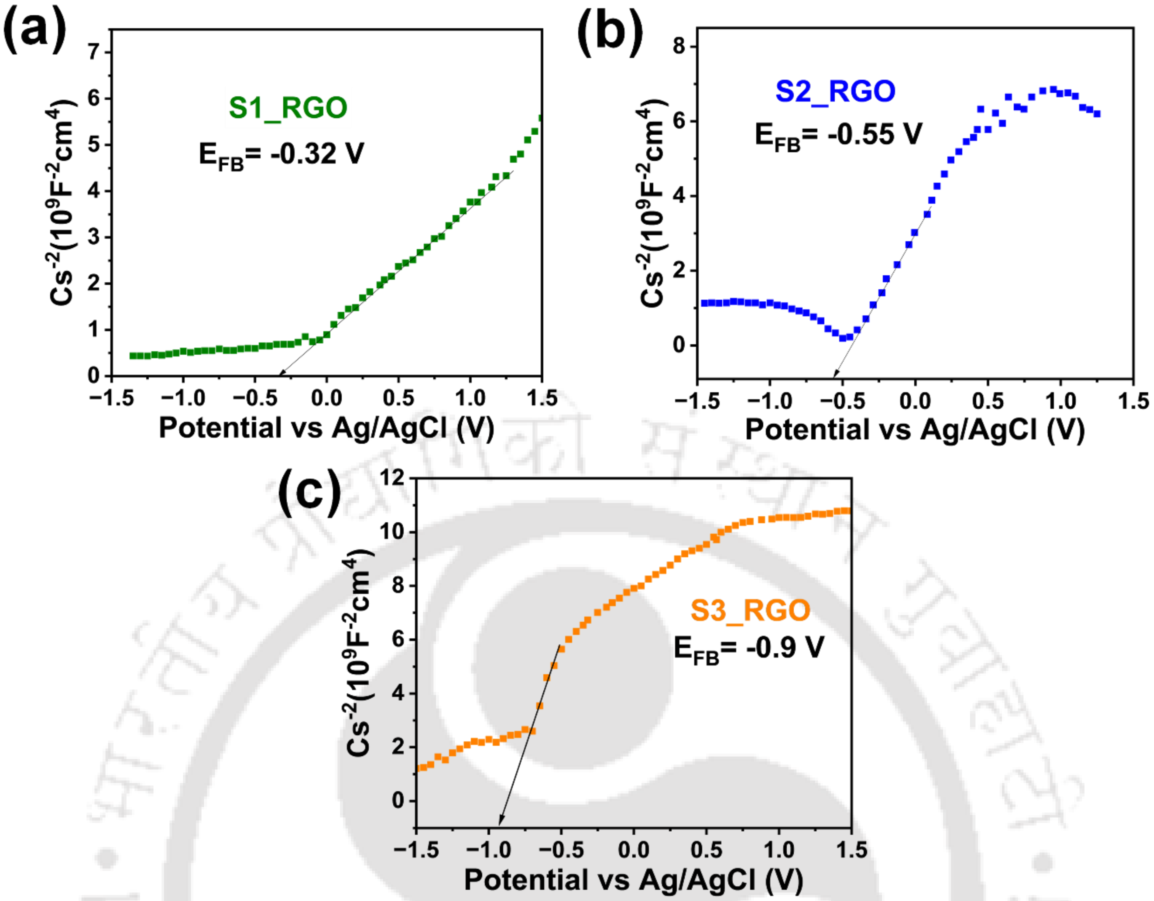

Figure S2.9: Mott-Schottky analysis of 3 RGOs taken at 1000 Hz.

[This page was left empty intentionally]

CHAPTER 3

Solvent assisted shape dependent $MAPbI_3$/polyfluorene heterostructures with larger surface area for improved photocatalytic H_2 evolution

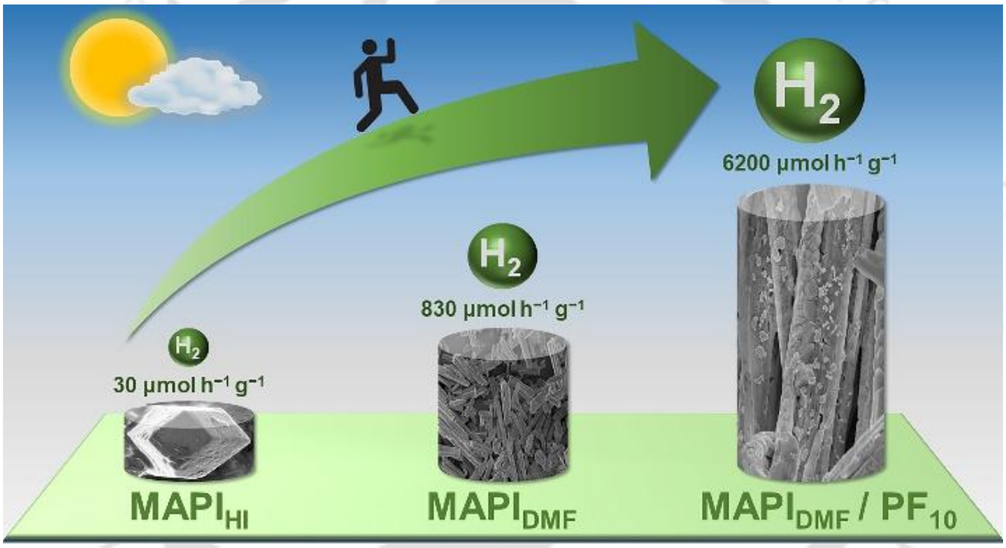

Article: Pal, T.; Bhowmik, S.; Tanwar, A. S.; Suhail, A.; Peela, N. R.; Sastri, C. V.; Iyer, P. K. Solvent Assisted Shape Dependent $MAPbI_3$/Polyfluorene Heterostructures with a Larger Surface Area for Improved Photocatalytic H_2 Evolution. *Energy Adv.* **2024**, *3*, 2965–2971.

Keywords. Solvent controlled, morphology, surface area, MAPI, halide perovskite, polyfluorene co-catalyst, photocatalytic H_2 evolution.

3.1 Abstract

Although lead based $MAPbI_3$ has been used as a material for photocatalytic hydrogen evolution but conventionally synthesized $MAPbI_3$ in HI solution suffers from very low HER activity with hydrogen evolution rate of 30 μmol h^{-1} g^{-1}. Several efforts have been made to boost the HER performance by tagging a co-catalyst. But no such significant approach was made to improve the HER activities of pristine $MAPbI_3$. In this work the shape and morphology of $MAPbI_3$ have been modified by a simple solvent altercation route. This led towards substantial transformation in shape and morphology affecting various facets of photocatalytic and photochemical performance. DMF assisted pristine $MAPbI_3$ exhibited an HER activity of 830 μmol h^{-1} g^{-1}, almost 28 folds better than typical HI based $MAPbI_3$. This work highlights on how solvent transition from HI to DMF can influence the shape and surface morphologies which impact the photocatalytic and photoelectrochemical performances of pristine $MAPbI_3$. To further enhance the HER activities of DMF assisted $MAPbI_3$, as-synthesized Polyfluorene co-catalyst was integrated on $MAPbI_3$ Surface. Under optimized condition the hydrogen evolution of $MAPbI_3$/polyfluorene composites can reach up to 6200 μmol h^{-1} g^{-1}

3.2 Introduction

The generation of solar driven green hydrogen (H_2) fuel has been put forward as a potential solution to address the ever-increasing crisis of global energy demand and environmental pollution concerns [1–3]. The utilization of diversified semiconductor photocatalysts for photocatalytic H_2 evolution has garnered significant attention as a sustainable and environmentally-friendly method for converting solar energy into H_2.[4–6] When considering the utilization of solar energy, an efficient photocatalyst should have an appropriate bandgap and conduction band minima in order to effectively capture a wide range of sunlight wavelengths and transfer the photogenerated charges to form H_2 fuel. Hybrid organic-inorganic perovskites ($MAPbI_3$), possesses a remarkable) optical bandgap of 1.5 eV with absorption coefficient in range of 10^4-10^5 cm^{-1}. These properties enable it to effectively absorb visible light within a wavelength range of approximately 400 to 800 nm.[7,8] Furthermore, $MAPbI_3$ (MAPI) demonstrates exceptional characteristics, including charge transport and a lengthy charge diffusion length of approximately 25 µm in $MAPbI_3$. As a result, it has significantly enhanced PCE of $MAPbI_3$ based solar cells, achieving over 20%.[9–12] $MAPbI_3$ possesses these attractive characteristics that allow it to emerge as a promising contender for photocatalytic HER. However, it's inherent instability in aqueous solutions presents a formidable obstacle when it comes to its application in photocatalysis. Recently, researchers led by Park and co-workers have successfully tackled this challenge by skilfully establishing a delicate equilibrium between the solvation and crystallization of $MAPbI_3$ in a saturated aqueous HI solution. As a result, they were able to achieve photocatalytic H_2 evolution through HI splitting. This breakthrough opens up new avenues for harnessing the potential of $MAPbI_3$ in photocatalytic processes.[13] However, when compared to traditional semiconductors, the observed rate of hydrogen evolution reaction (HER) of $MAPbI_3$ in an aqueous solution of HI is relatively low. This is likely due to the significant recombination of photogenerated charges within the microcrystals of $MAPbI_3$. Recent studies have demonstrated that the incorporation of electron transporters, such as Pt, TiO_2, MoS_2, CoP, carbonized polymer dot, black P, NiCoB combined with the $MAPbI_3$ photocatalyst, can enhance the efficiency of charge transportation by quickly extracting the photogenerated electrons from $MAPbI_3$.[14-20] These co-catalysts facilitate the reduction of protons present in aqueous HI solution to generate H_2. As a result, the rates of HER in $MAPbI_3$-based composites got significantly improved compared to $MAPbI_3$ alone. These findings offer valuable insights into the modulation of charge transportation for enhancing the photocatalytic performance of hybrid perovskite nanocrystals in hydrogen evolution reactions.

In recent years several efforts were made to enhance the HER activities of $MAPbI_3$ by tagging a co-catalyst as previously discussed. However, there has been limited studies focusing on the enhancement of the hydrogen evolution rates of pristine $MAPbI_3$.[21-24] For an efficient photocatalyst their characteristics like surface area, morphology, and particle dimensions, are crucial parameters that exert a notable impact on the efficiency of the hydrogen evolution reaction (HER). [25- 27] In a chemical reaction; parameters like reaction temperature, reaction time, concentration of reactants, solvent polarity play a crucial role to determine the morphology of resulting product.[28] In this study we have investigated how variation in solvents from polar protic to polar aprotic can alter the surface area and surface morphology. In this study, keeping reactant concentration constant, we have fabricated $MAPbI_3$ (MAPI) using two distinct methods, wherein the variation in the solvent medium results in two different morphologies that lead to discrepancies in the efficiency of photocatalytic and photoelectrochemical processes. The cuboid morphology of MAPI was assisted by the polar protic solvent HI, contrasts with the rodlike shape of MAPI facilitated by the polar aprotic solvent DMF. The rod-shaped MAPI produced with DMF (referred to as $MAPI_{DMF}$) exhibited superior performances in both photocatalytic and photoelectrochemical activities compared to the cuboid-shaped MAPI synthesized with HI (referred to as $MAPI_{HI}$).

To improve the performance of $MAPI_{DMF}$ in a more effective way, a polyfluorene based polymer has been incorporated with $MAPI_{DMF}$ as a co-catalyst via *in-situ* fabrication. ($MAPI_{DMF}/PF_{10}$) composites were prepared with polyfluorene of 10 weight percentages with respect to MAPI. Conjugated polymeric materials can easily absorb visible light irradiation as they possess extended and delocalized π-systems, leading to their application in organic photonics and organic electronics and as well as photocatalytic hydrogen evolution. The π-conjugated polyfluorene core functions as an antenna system that efficiently channels the electrons produced by the absorbed solar radiation originating from the photo absorber (MAPI) and subsequently transports them within the solution. $MAPI_{DMF}/PF_{10}$ exhibited maximum hydrogen evolution of 6200 $\mu mol\ h^{-1}\ g^{-1}$. The as-prepared composites were fully characterized through UV-Visible spectroscopy, XRD, FESEM, Brunauer, Emmett, and Teller (BET) surface area analysis, steady state photoluminescence, three electrodes electrochemical and photoelectrochemical techniques. Among all three samples $MAPI_{DMF}/PF_{10}$ had performed the best while $MAPI_{HI}$ exhibited the lowest values.

3.3 Results and discussion

The as-prepared MAPI$_{HI}$ and MAPI$_{DMF}$ powders were analyzed by XRD as shown in **Figure 3.1a**. The as-prepared MAPI$_{HI}$, and MAPI$_{DMF}$ powders have indistinguishable XRD patterns with the standard ones, confirming the successful formation of single-phase product.[29] This indicates even after solvent altercation; the perovskite crystal structure remains intact. Even after the incorporation of polyfluorene co-catalyst, for MAPI$_{DMF}$/PF$_{10}$ no change in XRD pattern were observed. Even after 80 hours of white light irradiation inside aqueous HI solution, XRD of MAPI$_{DMF}$/PF$_{10}$ composites retained its crystal structure, evident from XRD patterns (**Figure S3.1**).

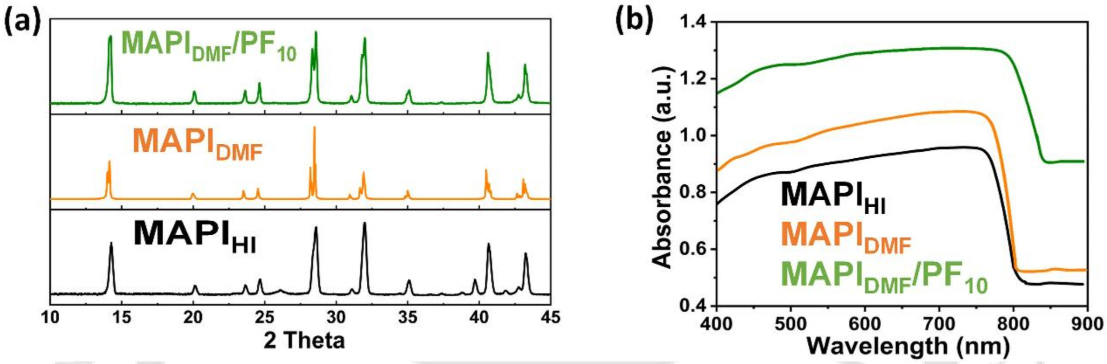

Figure 3.1: (a) XRD diffractogram, (b) UV-Visible spectra of pristine MAPI and composites.

The sunlight absorption properties within visible range were further studied by the UV-vis spectroscopy for pristine MAPI$_{HI}$, MAPI$_{DMF}$, and MAPI$_{DMF}$/PF$_{10}$ composites. As shown in the **Figure 3.1b,** MAPI$_{DMF}$ has higher molar absorbance as compared to MAPI$_{HI.}$ Additionally, the absorption tail was extended beyond 800 nm for MAPI$_{DMF}$ as compared to MAPI$_{HI}$. This observation suggests that the transition from HI to DMF solvent has led to a noteworthy enhancement in the light absorption properties and spectral range of MAPI. Upon the addition of a polyfluorene co-catalyst, there was a noticeable enhancement in light absorption. The light absorption range was further extended up to 1000 nm as well. It is worth noting that about half of the solar irradiation received is in the infrared region. The elongated absorption tail plays a crucial role in improving the efficiency of solar-to-hydrogen conversion.[30]

To understand the effect of solvent on morphology in great details, field emission SEM was employed. Pristine MAPI is highly crystalline in nature. **Figure 3.2a**, **b** portrayed the fact that drastic change in morphology were observed by altercation of reaction medium from HI to DMF. HI assisted MAPI (MAPI$_{HI}$) had a morphology corresponding to cuboid structure and smooth surface whereas MAPI prepared in DMF reaction medium had microrod shaped morphology. This substantial transformation in shape and morphology affects various facets of photocatalytic and photochemical performances.[31, 32] Moreover, the incorporation of polyfluorene as a co-catalyst with MAPI$_{DMF}$ resulted in the formation of microstructures where small clusters of polyfluorene moieties were uniformly dispersed and firmly embedded on the surface of MAPI, indicating a strong integration between MAPI and polyfluorene (**Figure 3.2c**). The robust heterojunction was a result of in-situ crystallization technique that was utilized for the synthesis. Energy dispersive X-ray spectroscopy were conducted to observe the distribution of elements on all over the MAPI surface. Elemental mapping of the MAPI$_{DMF}$/polyfluorene photocatalyst composite (**Figure 3.2d-g**) depict that the Pb, I and N atoms (contributed by MAPI) were observed to be uniformly distributed throughout the crystal.[30] Transmission Electron Microscopy (TEM) was utilized to study the heterojunction of polyfluorene with perovskite phase in detail. The MAPI$_{DMF}$/PF$_{10}$ heterostructures exhibited the typical rod like morphology of the perovskite phase (high density contrast due to presence of Pb) and the granular morphology of the PF polymer (low density contrast globular shape) anchored on the perovskite microrod, similar to the SEM observation (**Figure S3.2**).

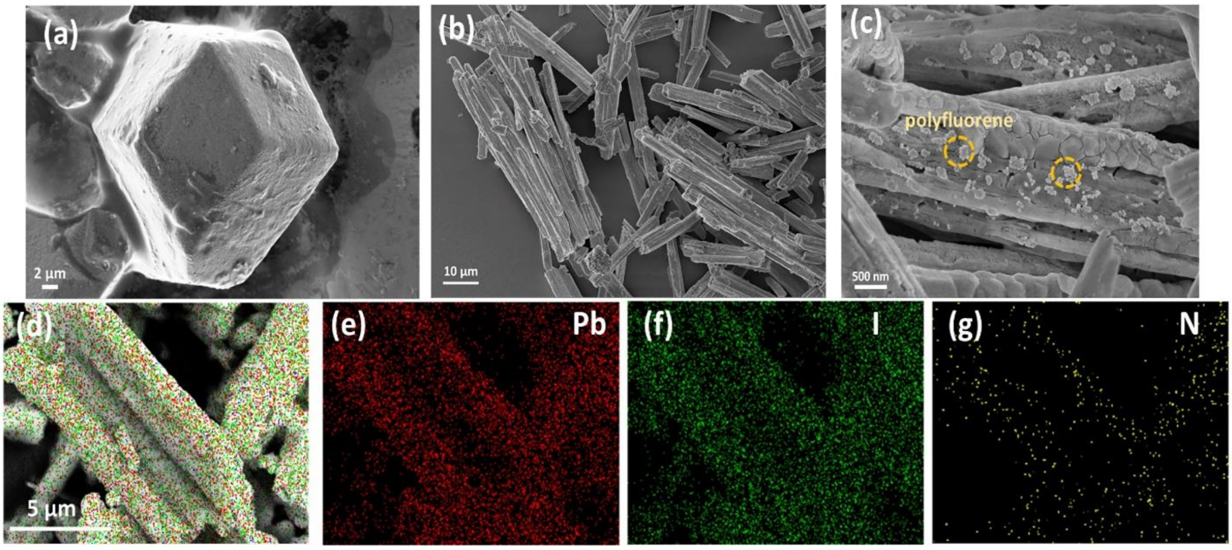

Figure 3.2: FESEM images of (a) MAPI$_{HI}$, (b) MAPI$_{DMF}$, (c) MAPI$_{DMF}$/PF$_{10}$. EDX elemental mapping of (d) all elements, (e) Pb, (f) I, (g) N.

The rate of hydrogen evolution reaction is regulated by the specific surface area. The quantity of photons striking the photocatalyst surface is positively correlated with the activity of HER, indicating that the reaction occurs on the surface of the photocatalyst.[33-35] **Figure 3.3a**, depicts adsorption–desorption isotherms of both MAPI$_{HI}$ and MAPI$_{DMF}$. The adsorption desorption isotherms of both samples were of type II (BDDT classification).[36] The isotherm pertaining to MAPI$_{DMF}$ shifted towards greater magnitude of absorbed quantity compare to the MAPI$_{HI}$. The hysteresis loop for MAPI$_{DMF}$ was spread all over the region of relative pressure whereas for MAPI$_{HI}$ the hysteresis loop shifted towards lower relative pressure. BET analysis of the samples showed a surface area of 1.333 m^2/g and 7.875 m^2/g for MAPI$_{HI}$ and MAPI$_{DMF}$ microcrystals respectively.

The average pore size of MAPI$_{HI}$ and MAPI$_{DMF}$ were evaluated as 7.115 nm and 3.421 nm respectively depicted in **Figure 3.3b**, indicating both samples were mesoporous in nature. In case of the MAPI$_{HI}$ sample, there is also a notable expansion of the nanopores. The pore size distribution curve of the MAPI$_{DMF}$ sample exhibits a considerable breadth with presence of an additional peak ranging from 6 nm to 11 nm as evident from visual inspection. This phenomenon suggests a higher pore abundance in the MAPI$_{DMF}$, leading to a larger pore volume of 0.011 cm^3 g^{-1} in comparison to the MAPI$_{HI}$ (0.002 cm^3 g^{-1}). **Table 3.1** summarizes the physical characteristics of the photocatalysts. In essence, the BET specific surface areas display a steady increase from 1.333 m^2/g to 7.875 m^2/g upon changing the solvent from HI to DMF, thereby directly influencing the photocatalytic and photochemical properties.

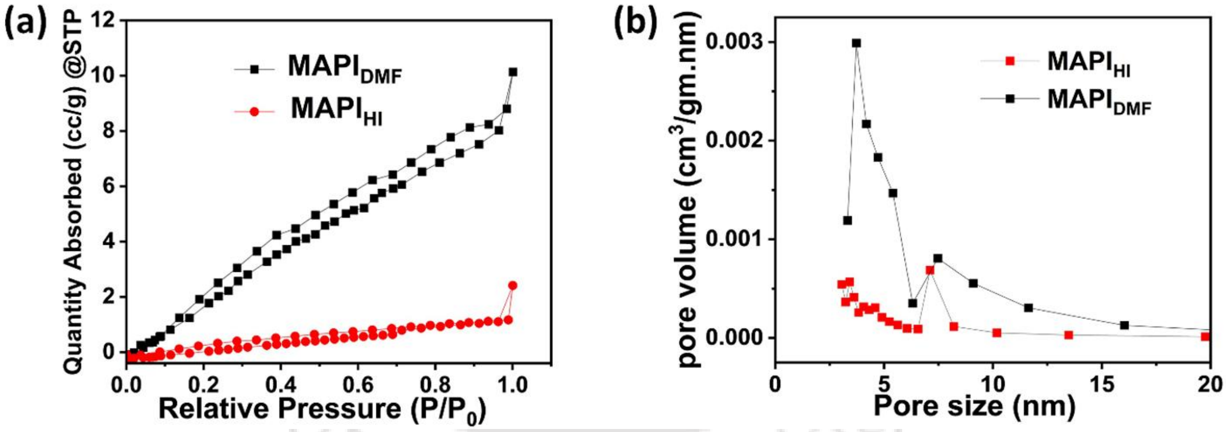

Figure 3.3 (a) Surface area and (b) pore size distribution of MAPI$_{DMF}$, and MAPI$_{HI}$.

Table 3.1. Surface area, pore size, pore volume and HER activities of $MAPI_{HI}$ and $MAPI_{DMF}$.

Sample	S_{BET} (m^2/g)	Pore size (nm)	Pore volume (cm^3/g)	HER activity
$MAPI_{HI}$	1.333 m^2/g	7.115 nm	0.002 cm^3 /g	30 µmol h^{-1} g^{-1}
$MAPI_{DMF}$	7.875 m^2/g	3.421 nm	0.011 cm^3/g	830 µmol h^{-1} g^{-1}

To explore the interplay between MAPI and polyfluorene co-catalyst, XPS technique was employed for $MAPI_{DMF}/PF_{10}$ composites. **Figure 3.4a** depicts the survey scan of $MAPI_{DMF}$ sample which revealed the existence of Pb, I, N, C elements. Specifically, for 4f Pb state in the pristine $MAPI_{DMF}$ exhibited distinct peaks at 143.32 eV and 138.44 eV, corresponding to the Pb $4f_{5/2}$ and $4f_{7/2}$ states, respectively. Conversely, the I 3d state of pristine $MAPI_{DMF}$ displayed two peaks at 630.31 eV and 618.81 eV, attributed to the $I3d_{3/2}$ and $I3d_{5/2}$ states. Upon introduction of polyfluorene co-catalyst on $MAPI_{DMF}$ surface, a notable shift towards higher binding energy was observed for both Pb4f and I3d states, as illustrated in **Figure 3.4b, c**. These findings consistently imply a synergy between MAPI and polyfluorene co-catalysts, indicating an efficient electron transfer from $MAPI_{DMF}$ to polyfluorene.[28]

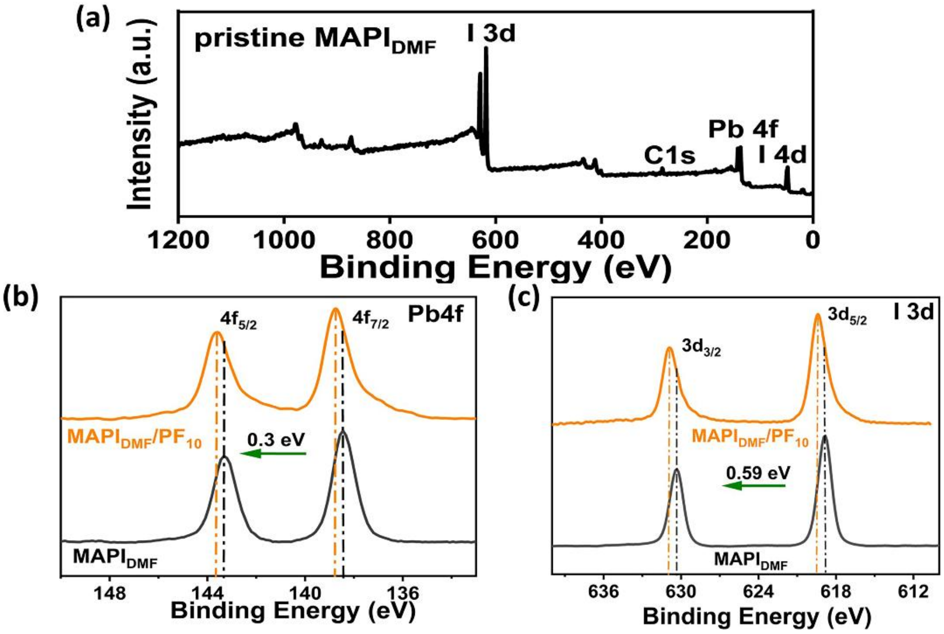

Figure 3.4: (a) XPS survey scan of $MAPI_{DMF,}$ high resolution XPS of (b) Pb and (c) I.

The photocatalytic activities of as-prepared pristine $MAPI_{HI}$, $MAPI_{DMF}$ and $MAPI_{DMF}/PF_{10}$ composites were confirmed through the gas chromatography under visible light where photocatalyst powders were immersed in a solution of HI and phosphorous acid (H_3PO_2)

saturated with methylammonium lead iodide (MAPI). Cube shaped HI assisted MAPI ($MAPI_{HI}$) exhibited a minuscule amount of H_2 evolution (30 μmol h^{-1} g^{-1}) owing to lack of active photoactive reaction sites and rapid photogenerated electrons recombination on pristine $MAPI_{HI}$ surface.[15] Surprisingly, DMF assisted MAPI ($MAPI_{DMF}$) registered HER of 830 μmol h^{-1} g^{-1}. The boosted HER activity of $MAPI_{DMF}$ upon altercation of solvent system from HI to DMF might be attributed to larger surface area possessed by rod shaped $MAPI_{DMF}$. As all photocatalytic reactions take place on catalyst (MAPI) surface, greater surface area leads to greater number of reaction sites and greater number of photons will be absorbed on $MAPI_{DMF}$ surfaces, owing to almost 28 times HER activity of $MAPI_{DMF}$.

To further enhance the performance of photocatalyst, polyfluorene co-catalyst (10 wt.%) was integrated on $MAPI_{DMF}$ surface. $MAPI_{DMF}$/polyfluorene composites were prepared by in-situ fabrication which create an intimate heterojunction between $MAPI_{DMF}$ and polyfluorene co-catalyst particles. The hydrogen evolution rate for all the samples were compiled and presented as a function of the duration of light exposure in **Figure 3.5a.** The hydrogen evolution reaction activity for HI splitting was significantly boosted upon incorporation of co-catalysts. While $MAPI_{DMF}$ exhibited HER of 830 μmol h^{-1} g^{-1}, $MAPI_{DMF}/PF_{10}$ composites exhibited maximum HER rate of 6200 μmol h^{-1} g^{-1}. After loading of 10 wt.% of polyfluorene on $MAPI_{DMF}$, hydrogen evolution rates accelerated by 7 times from previous one. Further increments in co-catalyst loading percentage did not affect the photocatalytic activity.

It is noteworthy to mention that, *in-situ* fabrication also facilitated the enhanced photocatalytic activity of $MAPI_{DMF}/PF_{10}$ composites. In this process the co-catalysts were deeply embedded on MAPI surfaces. Such kind of intimate integration form a strong heterojunction which decreases the likelihood of MAPI and polyfluorene separation while magnetic stirring during HER activity. The $MAPI_{DMF}$/polyfluorene composites not only exhibited superior performances than pristine MAPI, it also outperformed Pt deposited MAPI in terms of HER activity.[13] In terms of photocatalytic stability, $MAPI_{DMF}$/polyfluorene composites exhibited stability for prolonged time. Photocatalytic hydrogen evolution reactions were performed for $MAPI_{DMF}/PF_{10}$ for 80 hours under visible light irradiation depicted in **Figure 3.5b**. No considerable change in hydrogen evolution rate were observed for 56 hours. Polyfluorene, because of its long hydrophobic moiety it protects MAPI from structural degradation in water environment. In last 3 cycles a significant decline in H_2 evolution rate were observed might be due to depletion of H_3PO_2 concentration. Such declination in H_3PO_2 concentration, hinder the I_3^- to I^- conversion resulting excess generation of I_3^- ions that could inhibit the absorption of light by the MAPI composites also hindering efficient hole extraction.[38]

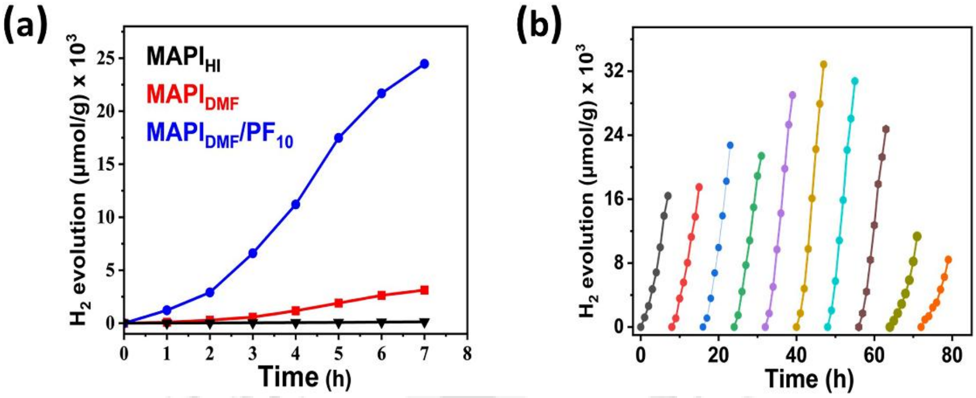

Figure 3.5. (a) Comparative HER activities of all samples. (b) 80 hours long stability study of MAPI$_{DMF}$/PF$_{10}$.

Intensity of photoluminescence strongly co-relates with electron-hole radiative recombination. A higher photoluminescence intensity indicates a greater extent of radiative recombination and consequently, a lower degree of charge separation and reduced photocatalytic activity. As depicted in **Figure 3.6a,** all samples registered photoluminescence emission at around 759 nm with different intensities owing to their varied degree of radiative charge recombination. It is noteworthy to mention that MAPI synthesized in two different solvents displayed distinct PL intensities of dissimilar manner. Notably, MAPI$_{HI}$ demonstrated the highest photoluminescence intensity, whereas MAPI$_{DMF}$ showed significantly lower levels. The enlargement of a photocatalyst's surface area can directly influence the rate of electron-hole recombination within the material. As indicated by the BET surface area analysis, the surface area of MAPI$_{DMF}$ is 7 times greater than that of MAPI$_{HI}$. This increased surface area of MAPI$_{DMF}$ may result in a lower likelihood of radiative charge recombination, leading to improved charge separation and enhanced photocatalytic performance.[37] To further enhance the efficiency of MAPI$_{DMF}$, heterostructures of MAPI/polyfluorene (MAPI$_{DMF}$/PF$_{10}$) were fabricated with 10 weight percent of polyfluorene on the surfaces of MAPI$_{DMF}$. Among all the photocatalysts, MAPI$_{DMF}$/PF$_{10}$ exhibited the lowest PL intensity indicating the most efficient charge separation and alternate charge migration pathway different from radiative recombination.

To explore role of polyfluorene co-catalysts embedded on MAPI$_{DMF}$ surface, we performed a series of Photoelectrochemical measurements. The photoelectrochemical study is commonly utilized to provide compelling evidence for the charge extraction in the photocatalyst composites.

Figure 3.6b, presents the cathodic polarization curves (I–V curves) of pristine $MAPI_{HI}$, $MAPI_{DMF}$ and $MAPI_{DMF}/PF_{10}$. These results indicate the occurrence of the hydrogen evolution reaction for all the catalysts. Furthermore, the $MAPI_{DMF}/PF_{10}$ composites showed a smaller overpotential compare to $MAPI_{HI}$ and $MAPI_{DMF}$, which suggested that polyfluorene could reduce the overpotential resulting more favourable electrocatalytic HER kinetics of $MAPI_{DMF}/PF_{10}$. This observation explains the accelerated rate of photocatalytic reductive hydrogen evolution reaction. This may be due to polyfluorene, which provide better charge separation and charge transport for photocatalysis.[38]

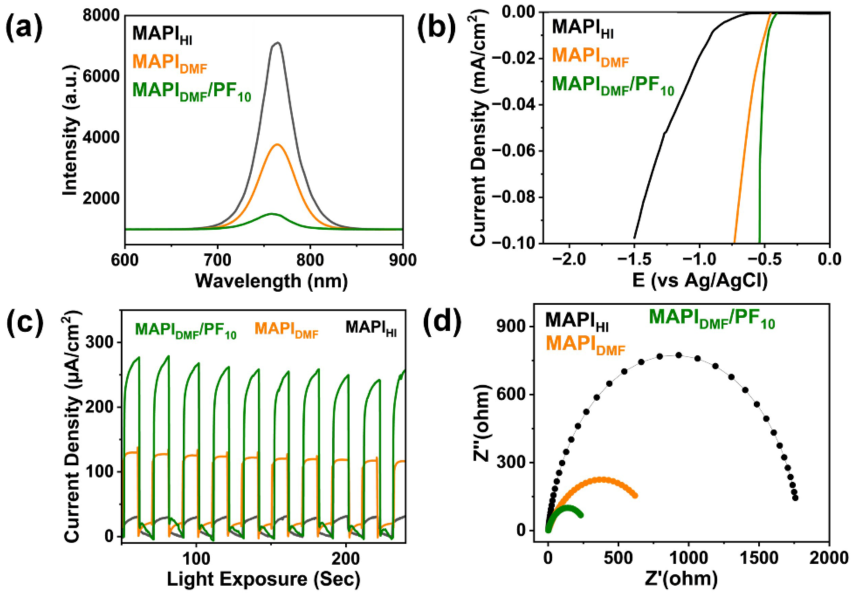

Figure 3.6. (a) Steady state PL, (b) Polarization curve, (c) transient photocurrent, (d) EIS Nyquist plot of $MAPI_{HI}$, $MAPI_{DMF}$ and $MAPI_{DMF}/PF_{10}$.

The photo-current responses for the pristine $MAPI_{HI}$, pristine $MAPI_{DMF}$, $MAPI_{DMF}/PF_{10}$ under several 10 sec on/off illumination cycles were performed and presented in **Figure** 3.**6c.** Unambiguously, in the case of turned-on condition, the photocurrent intensity was observed to remain almost unchanged and while promptly reducing to zero when the light turns off, signifying a swift photocurrent response to light on−off condition. $MAPI_{DMF}$ exhibited the higher photocurrent compared to $MAPI_{HI}$. While $MAPI_{HI}$ had the lowest value as expected. $MAPI_{DMF}/PF_{10}$ heterostructures exhibited the highest photocurrent under same electric bias. In terms of transient photocurrent, higher value indicates occurrence of efficient charge migration in $MAPI_{DMF}/PF_{10}$ composites.[39] These results were well validated by electrochemical impedance spectroscopy (EIS) measurement as shown in **Figure 3.6d**, $MAPI_{DMF}/PF_{10}$ with smallest semicircle arc dictates the lowest interfacial charge transfer resistance resulting into expedited interfacial charge transfer.[40] For pristine MAPI, the interfacial charge transfer resistance gradually increases and it is maximum for pristine $MAPI_{HI}$.

To investigate the electron transfer pathway in the $MAPI_{DMF}/PF_{10}$ composite, an initial investigation was conducted on MAPI using Ultraviolet Photoelectron Spectroscopy (UPS) analysis. The valance band maxima of $MAPI_{DMF}$ was determined to be -5.45 eV from UPS, while the bandgap was calculated to be 1.55 eV using Tauc plot. The conduction band minima was estimated as -3.9 eV (**Figure S3.3, S3.4**). In order to determine the LUMO of polyfluorene, a cyclic voltammetry experiment was carried out, which revealed a reduction potential ($E_{red, onset}$) of -0.46 V for the Polyfluorene co-catalyst as shown in **Figure 3.7a**. Subsequently, the LUMO of polyfluorene was determined to be -3.98 eV. The optical bandgap was calculated as 2.48eV from absorption onset of polyfluorene (**Figure S3.5**). Regarding the band structure of the overall composite, a type II heterojunction was proposed at the interface of polyfluorene and $MAPI_{DMF}$, as illustrated in **Figure 3.7b**, showcasing an ideal scenario for photocatalytic HER process. For H_2 evolution according to “band matching” theory, the CBM energy level of $MAPI_{DMF}$ was found to be more positive than that of polyfluorene, enabling the migration of photo-generated electrons from MAPI to polyfluorene. This phenomenon accelerates separation and transport of photogenerated electrons for the reduction of protons in reaction medium to generate H_2.[41, 42] Consequently, the electrons can be effectively extracted leading to a significant enhancement in the photocatalytic HER activity of the $MAPI_{DMF}/PF_{10}$ heterostructures.

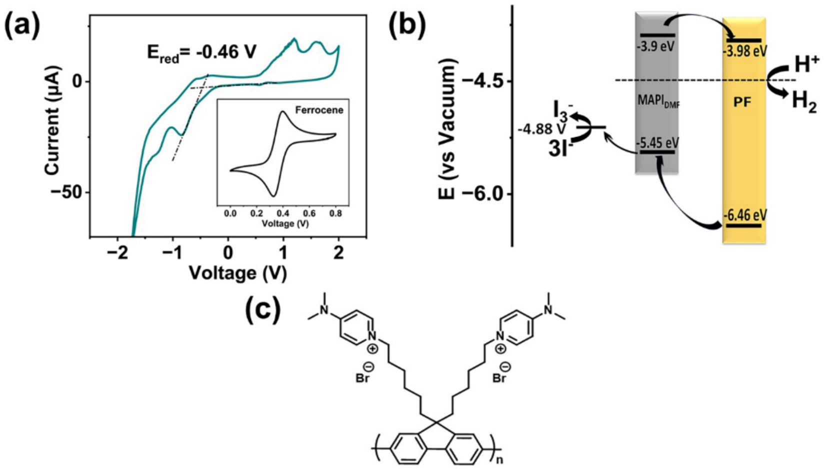

Figure 3.7: (a) Energy profile diagram of $MAPI_{DMF}$ and PF. (b) CV diagram of PF. (c) Molecular structure of Polyfluorene (PF) polymer.

3.4 Experimental Section

Materials:

Lead Iodide (PbI_2, 99%), Hydriodic Acid (57 wt% HI in H_2O), Fluorene (99%), 1,6-Dibromohexane (99%), 4-(Dimethylamino) pyridine (99%), were purchased from Sigma-Aldrich. Ferric Chloride Anhydrous (99%) was obtained from Merck, India. Methylammonium Iodide was purchased from Greatcell Solar, Australia. Hypophosphorus Acid (H_3PO_2, 50% in H_2O) was obtained from Loba Chemie, India. All chemicals were used as received.

Preparation of $MAPI_{HI}$ powder and MAPI saturated solution:

MAPI was synthesized by dissolving MAI and PbI_2 in molar ratio of 1:1 in HI/H_3PO_2 aqueous solution. Specifically, 15 g PbI_2 was dissolved in 50 mL of HI acid (57 wt% in water), then 5.15 g MAI was slowly added into the solution with vigorous stirring under 80°C. The saturated solution used here was prepared by adding 57 wt% of HI at 50 wt% H_3PO_2 in 5:1(v/v) ratio. The reaction solution with black precipitate was stirred and heated to 100°C for 1h for crystallization to attain the dynamic equilibrium, followed by cooling down to room temperature to obtain the saturated solution containing black MAPI precipitates at the bottom. The MAPI precipitates were separated out from saturated solution by centrifuge, the obtained saturated solution was stored for next photocatalytic measurements, while the precipitates were dried in a vacuum oven at 80°C to get pristine MAPI powder.

Preparation of MAPI$_{DMF}$: MAPI$_{DMF}$ was prepared by dissolving PbI$_2$ and MAI in a weight ratio of 3:1 in anhydrous DMF solvent followed by vigorous magnetic stirring at 70°C until a clean bright yellow solution was prepared. Anhydrous toluene was added dropwise in the solution. White precipitate will start to appear, toluene was added till complete precipitate appeared with constant stirring at 90°C for 3 hours. The reaction mixture was centrifuged with dry ethyl acetate and the precipitate was collected after 3 washes. The precipitate was dried in vacuum oven at 80°C for 12 hours and stored inside the glove box for further use.

Fabrication of MAPI$_{DMF}$/PF$_{10}$: PbI$_2$ and MAI were dissolved in a weight ratio of 3:1 in anhydrous DMF solvent followed by vigorous magnetic stirring at 70°C until a clean bright yellow solution was prepared. 10 weight % of polyfluorene was added in the solution and stirred at 70°C for 15 minutes. Anhydrous toluene was added dropwise in the solution. White precipitate will start to appear, toluene was added till complete precipitate appeared with constant stirring at 90°C for 3 hours. The reaction mixture was centrifuged with dry ethyl acetate and the precipitate was collected after 3 washes. The precipitate was dried in vacuum oven at 80°C for 12 hours and stored inside the glove box for further use.

Synthesis of PF: In a 10 mL round bottom flask, the precursor polymer (70 mg), which we had reported earlier (ACS Sens. 2018, 3, 8, 1451–1461), was solubilized in dimethylformamide (2 ml) and then added 4-Dimethylaminopyridine (DMAP) (0.3474 g). The reaction mixture was stirred for 4 days at 80°C in an inert nitrogen gas atmosphere. Later it was cooled to room temperature and poured into diethyl ether to get precipitates. The precipitates were collected and washed multiple times with dichloromethane (DCM) followed by drying at room temperature to get a brown-colored polymer (PF) (Yield = 90%). 1H NMR (600 MHz, δ, DMSO-d6): 8.24 (b), 7.95 (b), 7.87 (b), 7.82 (b), 7.46 (b), 7.36 (b), 6.97 (b), 4.05 (b), 3.15 (b), (b), 2.11 (b), 1.53 (b), 1.01 (b), 0.61 (b).

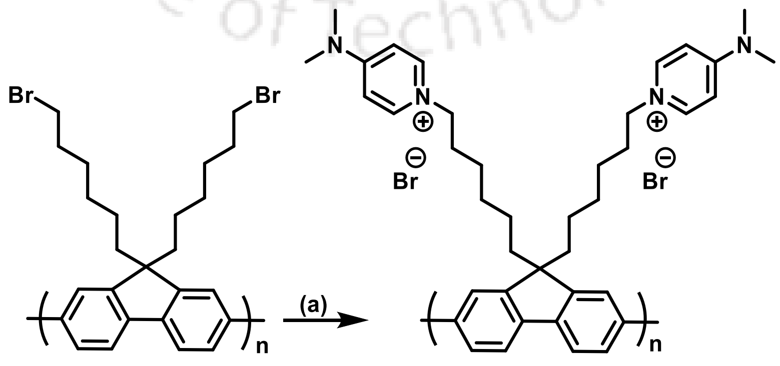

Figure 3.8. Synthesis of PF. (a) 4-Dimethylaminopyridine (DMAP), DMF, 70°C, 24 h.

Characterization

Same instrumentation used as chapter 2.

Photocatalytic measurement.

Same instrumentation used as chapter 2.

Photoelectrochemical measurement:

Same instrumentation used as chapter 2.

Table 3.2: Photophysical and electrochemical properties of polyfluorene.

Sample	λ_{abs} (nm)	λ_{abs} (nm)	λ_{onset} (nm)	Optical gap $=1240/\lambda_{onset}$ (eV)	$E_{red,onset}$ (V)	LUMO/HOMO (V)
PF	308 nm	439 nm	500 nm	2.48 eV	-0.46 V	-3.98 V/-6.46 V

Visible light source for photocatalytic measurements: The visible light source used here for the experiments is a 50 W with power density of 150 mW/cm^2 white LED bought from Ledvance Osram. The spectrum of this light source is 420 nm -790 nm.

3.5 Conclusion

Role of solvent assisted morphology dependent MAPI has been investigated for photocatalytic and photoelectrochemical activities. This article summaries the fact that altercation in reaction medium from HI to DMF not only alter the surface morphology from cuboid to rod shape, it also influences various aspects of photocatalytic and photoelectrochemical activities. $MAPI_{DMF}$ exhibited superior performances in terms of HER activities by 28 times Compared to $MAPI_{HI}$. The superior HER performances of $MAPI_{DMF}$ were supported by quenched photoluminescence intensity, higher photocurrent, lower charge transfer resistance. The improved photocatalytic and photoelectrochemical activities might be attributed to larger surface area possessed by rod shape $MAPI_{DMF}$. A greater surface area provides more reaction sites, enabling the absorption of a higher number of photons resulting accelerated H_2 evolution. A stable $MAPbI_3$/polyfluorene composite was successfully prepared by an *in-situ* fabrication. The incorporation of polyfluorene on $MAPI_{DMF}$ surfaces not only broadens the light absorption range but also enhances charge segregation and transport at the $MAPI_{DMF}/PF_{10}$ interface, leading to improved photocatalytic and photoelectrochemical activities. Under optimized conditions, $MAPI_{DMF}/PF_{10}$ exhibited a maximum HER activity of 6200 μmol h^{-1} g^{-1}. The enhanced HER activity of $MAPI_{DMF}/PF_{10}$ may be attributed to the efficient interfacial charge transfer from $MAPI_{DMF}$ to the polyfluorene co-catalyst owing to proper alignment of CBM of $MAPI_{DMF}$ and the LUMO of polyfluorene. This present work shows the immense possibilities of utilizing rationally designed metal free organic conjugated polymers for semiconductor photocatalysis applications, provided the physicochemical stability and band alignment criteria are well met.

3.6 Reference

(1) Yoon, T. P.; Ischay, M. A.; Du, J. Visible Light Photocatalysis as a Greener Approach to Photochemical Synthesis. *Nat. Chem.* **2010**, *2*, 527–532.

(2) Quarton, C. J.; Tlili, O.; Welder, L.; Mansilla, C.; Blanco, H.; Heinrichs, H.; Leaver, J.; Samsatli, N. J.; Lucchese, P.; Robinius, M.; Samsatli, S. The Curious Case of the Conflicting Roles of Hydrogen in Global Energy Scenarios. *Sustain. Energy Fuels* **2020**, *4*, 80–95.

(3) Tong, H.; Ouyang, S.; Bi, Y.; Umezawa, N.; Oshikiri, M.; Ye, J. Nano-photocatalytic Materials: Possibilities and Challenges. *Adv. Mater.* **2012**, *24*, 229–251.

(4) Kudo, A.; Miseki, Y. Heterogeneous Photocatalyst Materials for Water Splitting. *Chem. Soc. Rev.* **2009**, *38*, 253–278.

(5) Ismail, A. A.; Bahnemann, D. W. Photochemical Splitting of Water for Hydrogen Production by Photocatalysis: A Review. *Sol. Energy Mater. Sol. Cells* **2014**, *128*, 85–101.

(6) Burschka, J.; Pellet, N.; Moon, S.-J.; Humphry-Baker, R.; Gao, P.; Nazeeruddin, M. K.; Grätzel, M. Sequential Deposition as a Route to High-Performance Perovskite-Sensitized Solar Cells. *Nature* **2013**, *499*, 316–319.

(7) Eames, C.; Frost, J. M.; Barnes, P. R. F.; O'Regan, B. C.; Walsh, A.; Islam, M. S. Ionic Transport in Hybrid Lead Iodide Perovskite Solar Cells. *Nat. Commun.* **2015**, *6*, 1–8.

(8) Xing, G.; Mathews, N.; Sun, S.; Lim, S. S.; Lam, Y. M.; Grätzel, M.; Mhaisalkar, S.; Sum, T. C. Long-Range Balanced Electron- and Hole-Transport Lengths in Organic-Inorganic $CH_3NH_3PbI_3$. *Science* **2013**, *342*, 344–347.

(9) Garai, R.; Gupta, R. K.; Hossain, M.; Iyer, P. K. Surface Recrystallized Stable 2D–3D Graded Perovskite Solar Cells for Efficiency beyond 21%. *J. Mater. Chem. A* **2021**, *9*, 26069–26076.

(10) Kojima, A.; Teshima, K.; Shirai, Y.; Miyasaka, T. Organometal Halide Perovskites as Visible-Light Sensitizers for Photovoltaic Cells. *J. Am. Chem. Soc.* **2009**, *131*, 6050–6051.

(11) Liu, M.; Johnston, M. B.; Snaith, H. J. Efficient Planar Heterojunction Perovskite Solar Cells by Vapour Deposition. *Nature* **2013**, *501*, 395–398.

(12) Garai, R.; Gupta, R. K.; Tanwar, A. S.; Hossain, M.; Iyer, P. K. Conjugated Polyelectrolyte-Passivated Stable Perovskite Solar Cells for Efficiency beyond 20%. *Chem. Mater.* **2021**, *33*, 5709–5717.

(13) Park, S.; Chang, W. J.; Lee, C. W.; Park, S.; Ahn, H.-Y.; Nam, K. T. Photocatalytic Hydrogen Generation from Hydriodic Acid Using Methylammonium Lead Iodide in Dynamic Equilibrium with Aqueous Solution. *Nat. Energy* **2016**, *2*, 1–8.

(14) Han, W.; Wei, Y.; Wan, J.; Nakagawa, N.; Wang, D. Hollow Multishell-Structured TiO_2/$MAPbI_3$ Composite Improves Charge Utilization for Visible-Light Photocatalytic Hydrogen Evolution. *Inorg. Chem.* **2022**, *61*, 5397–5404.

(15) Guan, W.; Li, Y.; Zhong, Q.; Liu, H.; Chen, J.; Hu, H.; Lv, K.; Gong, J.; Xu, Y.; Kang, Z.; Cao, M.; Zhang, Q. Fabricating $MAPbI_3$/MoS_2 Composites for Improved Photocatalytic Performance. *Nano Lett.* **2021**, *21*, 597–604.

(16) Cai, C.; Teng, Y.; Wu, J.-H.; Li, J.-Y.; Chen, H.-Y.; Chen, J.-H.; Kuang, D.-B. In Situ Photosynthesis of an $MAPbI_3$/CoP Hybrid Heterojunction for Efficient Photocatalytic Hydrogen Evolution. *Adv. Funct. Mater.* **2020**, *30*. DOI: 10.1002/adfm.202001478.

(17) Zhao, Y.; Zeng, Q.; Yu, Y.; Feng, T.; Zhao, Y.; Wang, Z.; Li, Y.; Liu, C.; Liu, J.; Wei, H.; Zhu, S.; Kang, Z.; Zhang, H.; Yang, B. Enhanced Charge Separation and

Photocatalytic Hydrogen Evolution in Carbonized-Polymer-Dot-Coupled Lead Halide Perovskites. *Mater. Horiz.* **2020**, *7*, 2719–2725.

(18) Li, R.; Li, X.; Wu, J.; Lv, X.; Zheng, Y.-Z.; Zhao, Z.; Ding, X.; Tao, X.; Chen, J.-F. Few-Layer Black Phosphorus-on-$MAPbI_3$ for Superb Visible-Light Photocatalytic Hydrogen Evolution from HI Splitting. *Appl. Catal. B* **2019**, *259*, 118075, DOI: 10.1016/j.apcatb.2019.118075.

(19) Jiang, L.; Guo, Y.; Qi, S.; Zhang, K.; Chen, J.; Lou, Y.; Zhao, Y. Amorphous NiCoB-Coupled $MAPbI_3$ for Efficient Photocatalytic Hydrogen Evolution. *Dalton Trans.* **2021**, *50*, 17960–17966.

(20) Wu, Y.; Wang, P.; Zhu, X.; Zhang, Q.; Wang, Z.; Liu, Y.; Zou, G.; Dai, Y.; Whangbo, M.-H.; Huang, B. Composite of $CH_3NH_3PbI_3$ with Reduced Graphene Oxide as a Highly Efficient and Stable Visible-Light Photocatalyst for Hydrogen Evolution in Aqueous HI Solution. *Adv. Mater.* **2018**, *30*. https://doi.org/10.1002/adma.201704342.

(21) Yao, Q.; Li, H.; Xue, J.; Jiang, S.; Zhang, Q.; Bao, J. Promoting Photocatalytic H2 Evolution through Retarded Charge Trapping and Recombination by Continuously Distributed Defects in Methylammonium Lead Iodide Perovskite. *Angew. Chem. Int. Ed Engl.* **2023**, *62*, e202308140. https://doi.org/10.1002/anie.202308140.

(22) Yao, Q.; Li, H.; Xue, J.; Jiang, S.; Zhang, Q.; Bao, J. Promoting Photocatalytic H2 Evolution through Retarded Charge Trapping and Recombination by Continuously Distributed Defects in Methylammonium Lead Iodide Perovskite. *Angew. Chem. Int. Ed Engl.* **2023**, *62*, e202308140. https://doi.org/10.1002/anie.202308140.

(23) Fu, H.; Liu, X.; Fu, J.; Wu, Y.; Zhang, Q.; Wang, Z.; Liu, Y.; Zheng, Z.; Cheng, H.; Dai, Y.; Huang, B.; Wang, P. 2D/Quasi-2D Ruddlesden–Popper Perovskite: A High-Performance Photocatalyst for Hydrogen Evolution. *ACS Catal.* **2023**, *13* , 14716–14724.

(24) Liu, J.; Zhang, H.; Wang, J.; Zong, X. Tuning the Dimensionality of Organic-Inorganic Hybrid Perovskites towards Improved Photocatalytic Hydrogen Production. *J. Mater. Chem. A* **2024**, *12*, 5740–5747.

(25) Yu, J.; Yu, Y.; Zhou, P.; Xiao, W.; Cheng, B. Morphology-Dependent Photocatalytic H_2-Production Activity of CdS. *Appl. Catal. B* **2014**, *156–157*, 184–191.

(26) Vaquero, F.; Navarro, R. M.; Fierro, J. L. G. Influence of the Solvent on the Structure, Morphology and Performance for H_2 Evolution of CdS Photocatalysts Prepared by Solvothermal Method. *Appl. Catal. B* **2017**, *203*, 753–767.

(27) Liu, Z.; Zhuang, Y.; Dong, L.; Mu, H.; Li, D.; Zhang, F.; Xu, H.; Xie, H. Enhancement Mechanism of Photocatalytic Hydrogen Production Activity of CeO_2/CdS by Morphology Regulation. *ACS Appl. Energy Mater.* **2023**, *6*, 7722–7736.

(28) Yu, J.; Xu, X. Expediting H_2 Evolution over $MAPbI_3$ with a Nonnoble Metal Cocatalyst Mo_2C under Visible Light. *Energy Mater. Adv.* **2022**, DOI: DOI: 10.34133/2022/9836095.

(29) Jin, Z.; Li, T.; Zhang, L.; Wang, X.; Wang, G.; Hao, X. Construction of a Tandem S-Scheme GDY/CuI/CdS-R Heterostructure Based on Morphology-Regulated Graphdiyne (g-C_nH_{2n-2}) for Enhanced Photocatalytic Hydrogen Evolution. *J. Mater. Chem. A* **2022**, *10,* 1976–1991.

(30) Yukta; Parikh, N.; Chavan, R. D.; Yadav, P.; Nazeeruddin, M. K.; Satapathi, S. Highly Efficient and Stable 2D Dion Jacobson/3D Perovskite Heterojunction Solar Cells. *ACS Appl. Mater. Interfaces* **2022**, *14*, 29744–29753.

(31) Wang, M.; Zhang, G.; Guan, Z.; Yang, J.; Li, Q. Spatially Separating Redox Centers and Photothermal Effect Synergistically Boosting the Photocatalytic Hydrogen Evolution of $ZnIn_2S_4$ Nanosheets. *Small* **2021**, *17,* DOI: 10.1002/smll.202006952.

(32) Cao, S.; Jiang, J.; Zhu, B.; Yu, J. Shape-Dependent Photocatalytic Hydrogen Evolution Activity over a Pt Nanoparticle Coupled g-C_3N_4 Photocatalyst. *Phys. Chem. Chem. Phys.* **2016**, *18*, 19457–19463.

(33) Chen, P.; Chen, L.; Ge, S.; Zhang, W.; Wu, M.; Xing, P.; Rotamond, T. B.; Lin, H.; Wu, Y.; He, Y. Microwave Heating Preparation of Phosphorus Doped G-C_3N_4 and Its Enhanced Performance for Photocatalytic H_2 Evolution in the Help of Ag_3PO_4 Nanoparticles. *Int. J. Hydrogen Energy* **2020**, *45*, 14354–14367.

(34) Sun, S.; Li, H.; Xu, Z. J. Impact of Surface Area in Evaluation of Catalyst Activity. *Joule* **2018**, *2*, 1024–1027.

(35) Feng, D.; Cheng, Y.; He, J.; Zheng, L.; Shao, D.; Wang, W.; Wang, W.; Lu, F.; Dong, H.; Liu, H.; Zheng, R.; Liu, H. Enhanced Photocatalytic Activities of G-C_3N_4 with Large Specific Surface Area via a Facile One-Step Synthesis Process. *Carbon* **2017**, *125*, 454–463.

(36) Camacho-Escobar, L.; Palma-Goyes, R. E.; Ortiz-Landeros, J.; Romero-Ibarra, I.; Gamba-Vásquez, O. A.; Vazquez-Arenas, J. Unraveling the Structural and Composition Properties Associated with the Enhancement of the Photocatalytic Activity under Visible Light of Ag_2O/$BiFeO_3$-Ag Synthesized by Microwave-Assisted Hydrothermal Method. *Appl. Surf. Sci.* **2020**, *521*, 146357, DOI: 10.1016/j.apsusc.2020.146357.

(37) Sachs, M.; Pastor, E.; Kafizas, A.; Durrant, J. R. Evaluation of Surface State Mediated Charge Recombination in Anatase and Rutile TiO_2. *J. Phys. Chem. Lett.* **2016**, *7*, 3742–3746.

(38) Liu, Q.; Shi, J.; Hu, J.; Asiri, A. M.; Luo, Y.; Sun, X. $CoSe_2$ Nanowires Array as a 3D Electrode for Highly Efficient Electrochemical Hydrogen Evolution. *ACS Appl. Mater. Interfaces* **2015**, *7*, 3877–3881.

(39) Zhu, M.; Fujitsuka, M.; Zeng, L.; Liu, M.; Majima, T. Dual Function of Graphene Oxide for Assisted Exfoliation of Black Phosphorus and Electron Shuttle in Promoting Visible and Near-Infrared Photocatalytic H_2 Evolution. *Appl. Catal. B* **2019**, *256*, 117864, DOI: 10.1016/j.apcatb.2019.117864.

(40) Zhao, X.; Chen, S.; Yin, H.; Jiang, S.; Zhao, K.; Kang, J.; Liu, P. F.; Jiang, L.; Zhu, Z.; Cui, D.; Liu, P.; Han, X.; Yang, H. G.; Zhao, H. Perovskite Microcrystals with Intercalated Monolayer MoS_2 Nanosheets as Advanced Photocatalyst for Solar-Powered Hydrogen Generation. *Matter* **2020**, *3*, 935–949.

(41) He, K.; Xie, J.; Liu, Z.-Q.; Li, N.; Chen, X.; Hu, J.; Li, X. Multi-Functional Ni_3C Cocatalyst/g-C_3N_4 Nanoheterojunctions for Robust Photocatalytic H_2 Evolution under Visible Light. *J. Mater. Chem. A* **2018**, *6*, 13110–13122.

(42) Gopikrishna, P.; Das, D.; Adil, L. R.; Iyer, P. K. Saturated and Stable White Electroluminescence from Linear Single Polymer Systems Based on Polyfluorene and Mono-Substituted Dibenzofulvene Derivatives. *J. Phys. Chem. C* **2017**, *121*, 18137–18143.

3.7 Supporting Information

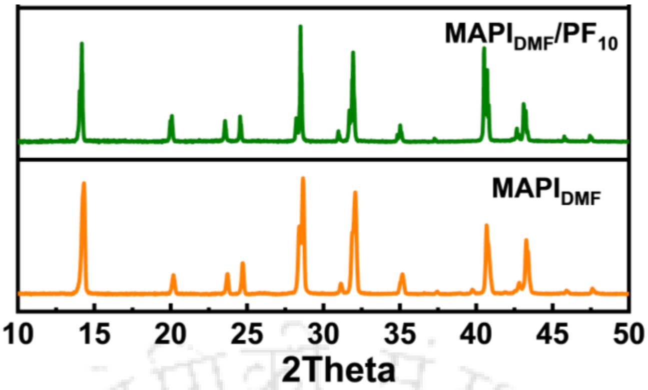

Figure S3.1: XRD study of MAPI$_{DMF}$ and MAPI$_{DMF}$/PF$_{10}$ after 80 hours of HER activities.

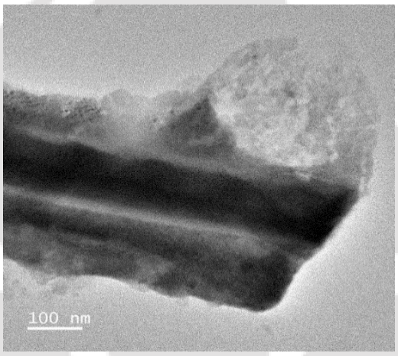

Figure S3.2: TEM image of MAPI$_{DMF}$/PF$_{10}$.

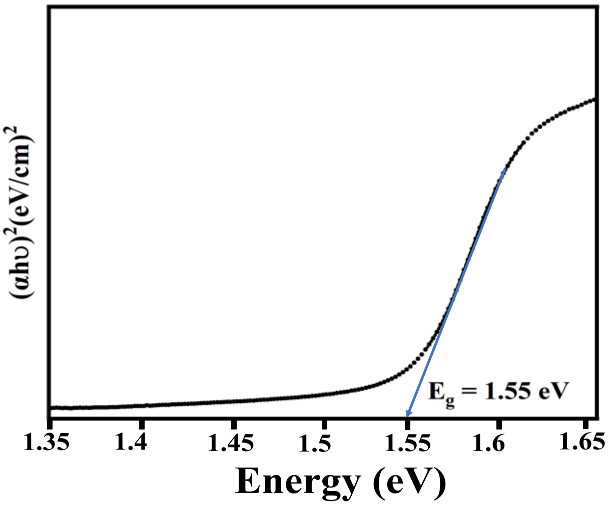

Figure S3.3: Band gap of pristine MAPI$_{DMF}$ calculated from Tauc plot.

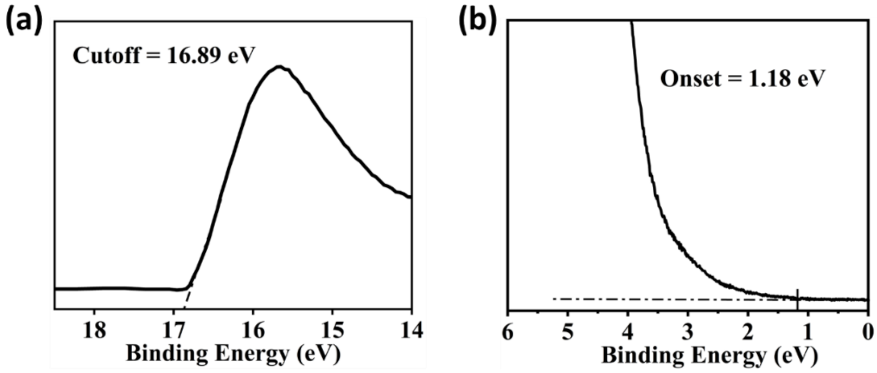

Figure S3.4: UPS spectra of $MAPI_{DMF}$.

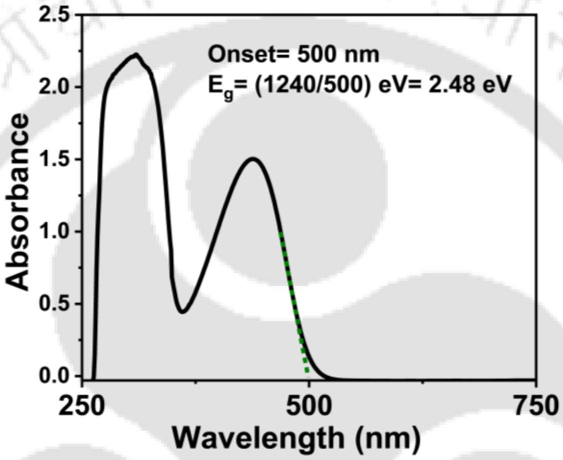

Figure S3.5: UV-Visible spectra of polyfluorene taken in DMF.

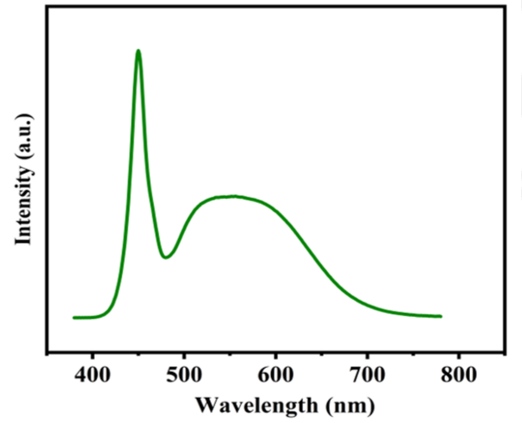

Figure S3.6: Electroluminescence of white LED light source.

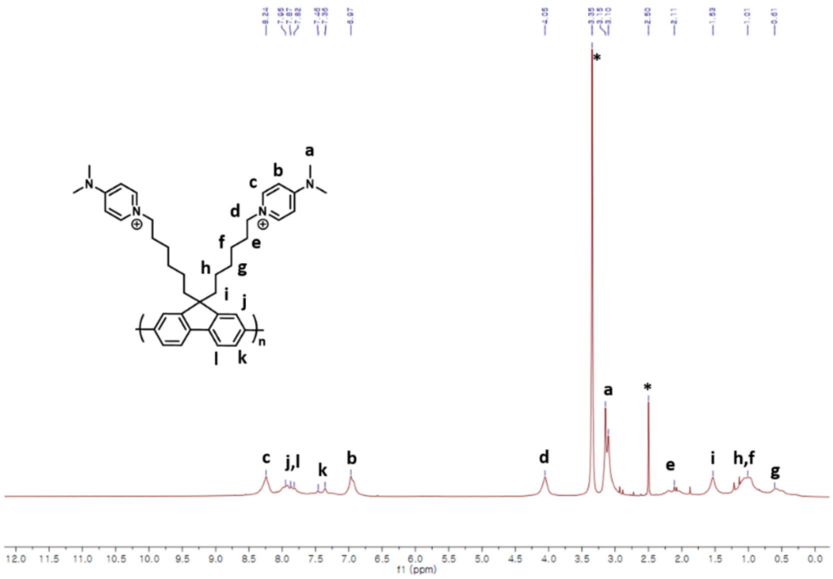

Figure S3.6 : 1H NMR spectra of PF.

[This page was left empty intentionally]

CHAPTER 4

Transformation from type-I to type-II $MA_3Bi_2I_9$ based heterostructure photocatalyst via energy band engineering

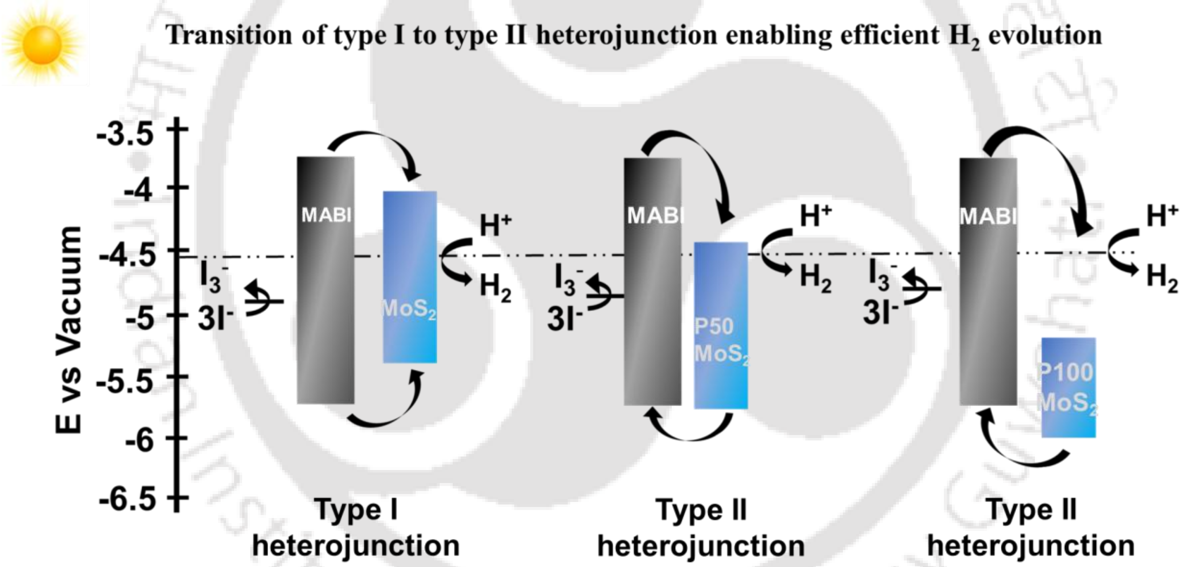

Keyeords - MoS_2/ $MA_3Bi_2I_9$ heterostructures, Phosphorus doping effect, Energy band engineering, transformation type I to type II heterojunction.

4.1 Abstract.

The photocatalytic dissociation of HI utilizing halide perovskites offers an environmentally benign and economically viable approach for hydrogen production at ambient temperature conditions. Lead-halide perovskites have shown encouraging efficacy in the domain of photocatalytic hydrogen generation. A lead-free Bi based hybrid perovskite, specifically $MA_3Bi_2I_9$ (MABI), has been successfully synthesized in a heterostructure configuration, wherein $MA_3Bi_2I_9$ (MABI) perovskite was in-situ grown around MoS_2 co-catalyst. This research underscores that for MoS_2/MABI heterostructures, doping of phosphorus not only modified the energy levels it also altered the band gap of MoS_2. The shifted energy levels of MoS_2 relative to MABI resulted into unique energy bands arrangements for 3 composites. A transition of heterojunction from type I to type II was observed with phosphorus doped MoS_2 containing composites. Among all 3 composites, P50_MoS_2/MABI possessed advantageous band alignment, which facilitates efficient photogenerated charge separation and transport. Under optimal reaction parameters, the hydrogen evolution rate can attain 1576 µmol $g^{-1}h^{-1}$ for P50_MoS_2/MABI composites.

4.2 Introduction

To meet the need for clean and renewable energy, H_2 stand as a potential candidate against the fossil fuels as well as mitigating the environment deterioration. Amongst the various strategies adopted for H_2 generation, photocatalysis stands as a most promising approach to mitigate the problem of energy crisis.[1-3] The photocatalytic solar energy conversion process till date is realized with various oxide-based materials like TiO_2, $CaTiO_3$ etc.[4-6] However, the last few years have witnessed the tremendous utilization of lead halide-based perovskite for H_2 solar to electricity generation.[7-9] The halide-based perovskite was widely explored for photovoltaic and optoelectronic application due to their efficient light absorption property, large extinction coefficient, high carrier mobility, larger carrier lifetime, tunable band gap and low exciton binding energy.[10-12] These properties also make them a suitable candidate for photocatalysis for solar H_2 generation.[13-15] The research growth of halide perovskite has increased since Nam and coworkers used methyl ammonium lead iodide as a photocatalyst for H_2 generation in 2016 by HI splitting.[16] They observed that methyl ammonium lead iodide was stable in a saturated HI solution and under visible light irradiation, splits HI producing H_2 by maintaining a dynamic equilibrium by the $MAPbI_3$ dissolution and reprecipitation in saturated aqueous solution.[17, 18]

Despite of good photocatalytic activity by the lead-based halide perovskite, the high toxicity of lead and material instability limits its utility for large scale application.[19] Therefore, there is a need to explore stable and lead-free perovskite material.[20] One alternative is the substitution of Pb by Sn since it belongs to the same group, but the intrinsic instability of Sn^{2+} against air and moisture readily oxidizes Sn^{2+} to Sn^{4+} state degrading the material. Recent study highlights bismuth-based perovskite as a substitution to the lead-based perovskite as Bi^{3+} is isoelectronic with Pb^{2+} with comparable electronegativity, similar ionic radii.[21-23] These are extremely stable in ambient condition unlike Pb and Sn based perovskite materials. A class of Bismuth based perovskite of general formula $A_3Bi_2X_9$ where A is monovalent cation (Cs^+ or MA^+) and X is halide anion (Cl^-, Br^-, I^-) is recent used as photoactive material both in photovoltaic application and photocatalytic HER. [24, 25] Of it, $MA_3Bi_2I_9$ (MABI) is the much less investigated material. Its structure is consisting of a metal halide octahedra layers with void between the two layers filled by MA^+ cations and the octahedral $(Bi_2I_9)^{3-}$ clusters in $MA_3Bi_2I_9$ is surrounded by MA^+ cations. In 2019, Zhao et. al reported a heterojunction of MABI as a photocatalyst and Pt metal as cocatalyst (MABI/Pt) for HI splitting.[26] A heterojunction structure prevents the carriers recombination and favours the efficient charge transfer by forming a Schottky barrier.[27]

However, the use of expensive Pt metal as cocatalyst is a big hindrance for practical application. Exploring the inorganic cocatalyst is another means for efficient charge carrier separation and transfer for enhanced H_2 generation.[28] A non-noble material, Molybdenum disulfide MoS_2, a transition metal dichalcogenide is well explored cocatalyst to enhance the photocatalytic activity of a photocatalyst and serve as the active sites to lower the overpotential of the HER improving the H_2 evolution rate.[29] Its high activity, good resistivity as well as stability against strong acid and economically inexpensive against noble Pt metal makes it promising cocatalyst material for photocatalytic HER.

In this work, we have delineated a series of composites composed of $MA_3Bi_2I_9$ and variants of MoS_2, which together establish heterostructures aimed at enhancing photocatalytic H_2 evolution in HI solution upon exposure to visible light irradiation. Through UPS analysis it was discerned that phosphorus doping instigates a downward trend in the VBM. As the phosphorus doping concentration increases, the VBM is observed to shift into a considerably deeper negative energy domain. This doping not only modifies the band alignment of MoS_2 but also alters the band gaps of the three MoS_2 variants. The relative positions of the CBM and VBM of both the MABI and MoS_2 constituents within the composites engender three distinct scenarios. The doping has induced a transition from a type I heterostructure observed in MoS_2/MABI to a type II heterojunction noted in the other two doped variants of composites. This heterojunction transition has significantly influenced the photocatalytic hydrogen evolution reaction (HER) activities, resulting in varied HER performance across the three composites.

The electronic band engineering attributed to change in elemental composition, could impact on charge transfer characteristics in photocatalytic HER activities. Even though all heterostructures exhibited improved HER activity as compared to pristine MABI, the highest photocatalytic H_2 generation rates were delivered by P50_MoS_2/MABI composites. Pristine MABI showed HER activity of 15 μmol g^{-1} h^{-1} under visible white light LED, whereas for P50_MoS_2/MABI composites, the registered maximum HER activity was 1576 μmol g^{-1} h^{-1}, which is 100 times higher than pristine MABI.

4.3 Result & discussion

The powder X-ray diffraction (PXRD) analysis of $MA_3Bi_2I_9$ (MABI) revealed diffraction peaks at angles of 12.46°, 12.79°, 14.40°, 17.02°, 24.56°, 25.31°, 25.76°, 26.95°, 29.06°, 31.64°, 32.31°, and 39.13°; these peaks can be attributed to the (100), (101), (103), (105), (006), (202), (203), (216), and (208) crystallographic planes, respectively, as illustrated in **Figure 4.1a**. The XRD pattern obtained for $MA_3Bi_2I_9$ was found to be in remarkable concordance with previously reported data.[26] The crystallinity, phase characteristics, and compositional analysis of the synthesized MoS_2 nanostructures and all P doped MoS_2 variants (P50_MoS_2, P100_MoS_2) were initially assessed through PXRD analysis. The comparative PXRD patterns for the P doped MoS_2 and the pristine MoS_2 are displayed in **Figure 4.1b**. Three prominent peaks at 15.52°, 32.12°, and 57°, corresponding to the (002), (100), and (110) planes of MoS_2, were identified, aligning with prior literature.[30] Due to the high crystallinity of MABI, no discernible broad peaks characteristic of the amorphous MoS_2 cocatalyst were detected in the diffractogram of the MoS_2/MABI composites, as shown in **Figure 4.1a**. The stability of perovskite-like materials is a significant concern; hence, the ambient stability of the synthesized MABI was evaluated. MABI was subjected to aerobic conditions for a duration of 50 hours, after which the PXRD pattern was re-recorded. The PXRD pattern obtained from the light-exposed MABI is presented in **Figure S4.2**. The results indicated negligible changes in the PXRD pattern, suggesting that MABI possesses exceptional stability even after 55 hours of photocatalytic hydrogen generation.

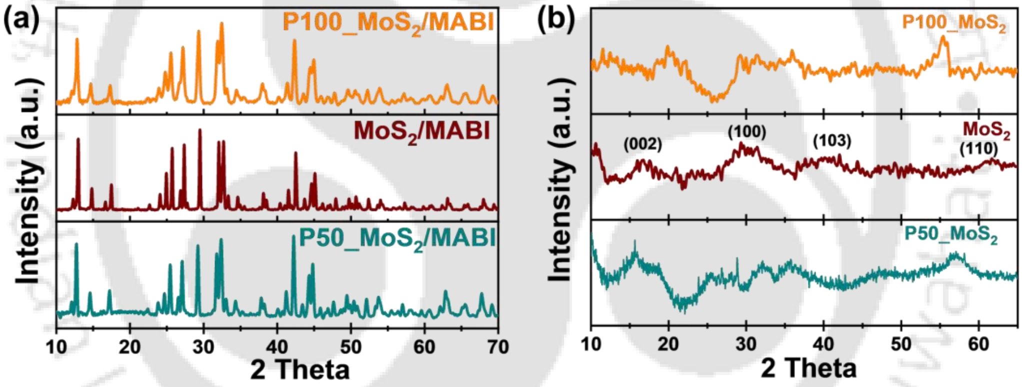

Figure 4.1: XRD patterns of (a) three MoS_2/MABI composites, (b) 3 variants of MoS_2

The light absorption characteristics of the synthesized MABI and its various MoS_2/MABI composites were analyzed utilizing UV-vis absorption spectroscopy. The resulting MABI powder demonstrated a significant absorbance within the visible light spectrum and a broad absorption range spanning 500–600 nm, as depicted in **Figure 4.2**. The Tauc plot (shown in **Figure S4.3**) indicated that MABI possesses a band gap of 1.98 eV, which aligns remarkably well with findings from prior investigations.[31] This favorable band gap of MABI motivates further investigation into its potential as a photocatalyst for H_2 generation applications. In this regard, MoS_2 and phosphorus doped MoS_2 were combined with MABI to achieve enhanced H_2 evolution performance. The solid-state UV-visible spectra of all samples (MABI, MoS_2/MABI, P50_MoS_2/MABI, P100_MoS_2/MABI) demonstrated that the incorporation of MoS_2 onto the MABI substrate significantly broadened the absorption spectrum of solar radiation. Moreover, P doped MoS_2 further extended the absorption range to 750 nm. Consequently, the P doped MoS_2/MABI heterostructures are anticipated to absorb a wide spectrum of sunlight.[15] The band gaps of MoS_2, P50_MoS_2, and P100_MoS_2 were determined to be 1.39 eV, 1.28 eV, and 1.07 eV, respectively, as illustrated in **Figure S4.4**.

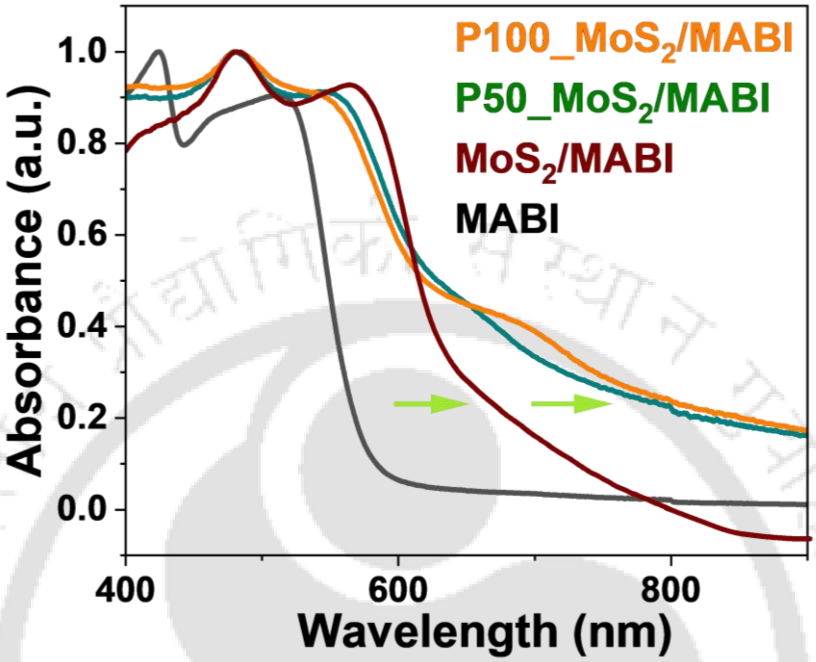

Figure 4.2: Solid state UV-visible spectra of MABI and its three composites.

To elucidate the morphology and structural characteristics of MABI and its composites, as well as the interactions between MABI and MoS_2 within the MoS_2/MABI heterostructures, FESEM and FETEM analyses were conducted. **Figures 4.3a, b** exhibited the FESEM images of pristine MABI and MoS_2/MABI composites, respectively. The pristine MABI microcrystals exhibited a high degree of crystallinity, characterized by hexagonal shape and smooth surface morphology.[32] Furthermore, following the integration of MoS_2 with MABI, a microstructure emerged where diminutive MoS_2 clusters were observed to be securely attached to the MABI surface, indicating a close integration of MABI and MoS_2. This robust heterojunction may be attributed to the growth of MABI microcrystal structures around the MoS_2 clusters. Energy Dispersive X-ray Spectroscopy (EDX) was employed to analyze the elemental distribution within the composites. The elemental mapping of the MoS_2/MABI photocatalyst composite (**Figure 4.3 d, e, f** and **g**) reveals the presence of I, Bi atoms (contributed by MABI) and Mo, S (contributed by MoS_2). Which were uniformly dispersed throughout the crystal structure.

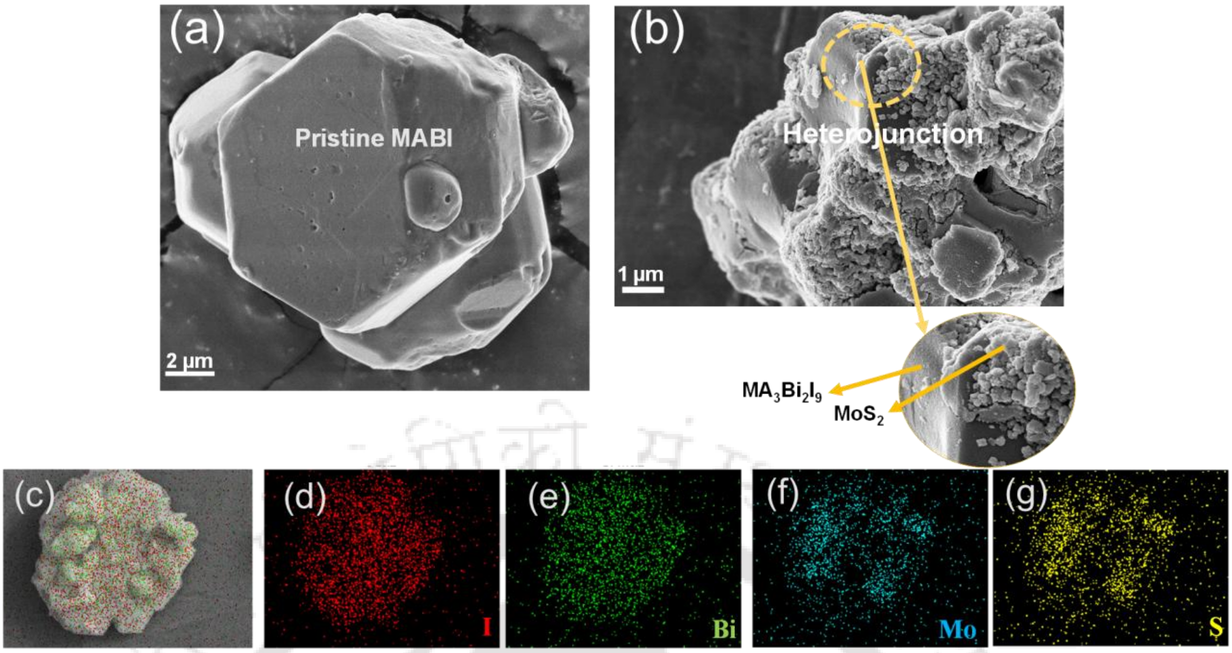

Figure 4.3: FESEM top view images of (**a**) pristine MABI and (**b**) MoS_2/MABI composite. EDX elemental mapping of (**c**) all elements, (**d**) I, (**e**) Bi, (**f**) Mo, (**g**) S for pristine MABI.

TEM and HRTEM analysis of MoS_2/MABI heterostructures provides valuable insights into their crystal structural characteristics, which were essential for understanding and optimizing their performance in HER activities. TEM analysis of MoS_2/MABI heterostructures typically shows distinct regions of both MABI and MoS_2.[33] Where MABI microcrystal exhibited hexagonal crystal structure while MoS_2 generally have layered structures, depicted in **Figure 4.4a**.

High-resolution TEM image of composites (**Figure 4.4b**) revealed the crystal lattice of both MABI and MoS_2 components. It also showed the mixing of two interfaces between these two materials which is of particular interest, as it plays a crucial role in the heterostructure's properties.[34] The d-spacing of MABI and MoS_2 were calculated as 0.23 nm and 0.29 nm respectively.

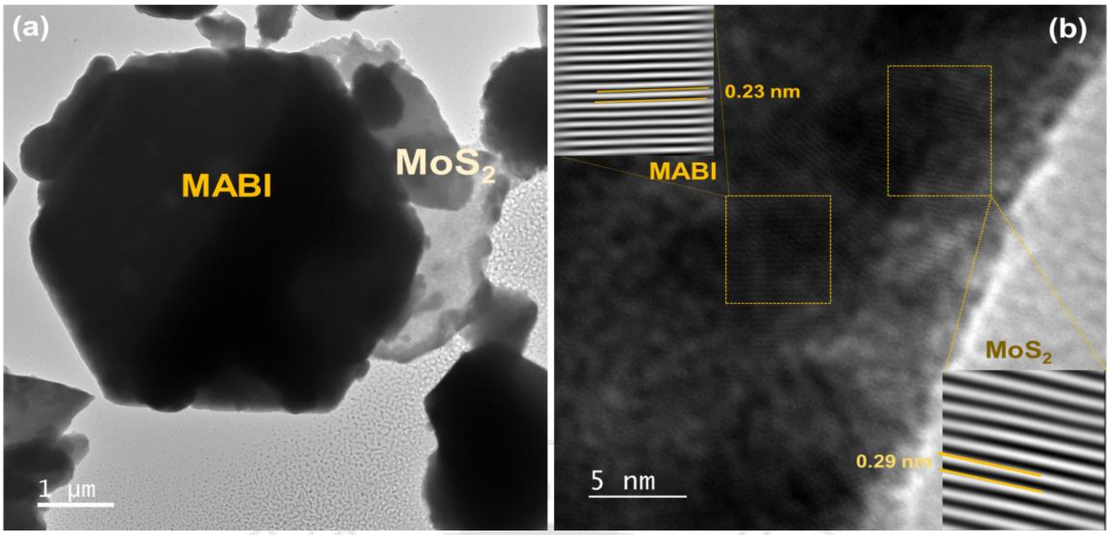

Figure 4.4: (a) TEM and **(b)** HRTEM images of P50_MoS_2/MABI composites. Inset of (B) shows the magnified images of MABI and P50_MoS_2.

The X-ray photoelectron spectroscopy (XPS) analysis was utilized for a more comprehensive examination. The XPS survey spectrum of the synthesized P50_MoS_2/MABI illustrated in **Figure 4.5a**, reveals the existence of C, N, Bi, I, Mo, S, P elements. The high-resolution XPS spectrum of I3d was depicted in **Figure 4.5c**, which reveals two peaks at 630.36 eV and 618.732 eV for pristine MABI, corresponding to the I3$d_{3/2}$ and I3$d_{5/2}$ states of I^- ions, respectively. These peaks associated with the 3$d_{3/2}$ and 3$d_{5/2}$ states exhibited a shift of 0.23 eV towards higher binding energy following the integration of P50_MoS_2 in P50_MoS_2/MABI composites.

The high-resolution XPS spectrum of Bi4f was shown in **Figure 4.5d**. This spectrum presented two peaks at binding energy of 156.5 eV and 161.88 eV for pristine MABI, attributed to two doublets of +3 oxidation states, assigned as Bi4$f_{7/2}$ and Bi4$f_{5/2}$ respectively. A shift towards higher binding energy by 0.31 eV was observed in the P50_MoS_2/MABI composites compared to the pristine MABI, indicating an efficient transfer of photogenerated electrons to the anchored P50_MoS_2.[35]

For P50_MoS_2/MABI composites, the Mo 3d peaks appeared at 229.32 and 232.28 eV, as depicted in **Figure 4.5e**. Which were attributed to the doublet of Mo 3$d_{5/2}$ and Mo 3$d_{3/2}$, respectively for Mo^{4+}. Also sulfur atoms-related 2s peak was observed at 226.38 eV. for S^{2-}. In addition, a peak at 235.48 eV corresponds to the Mo^{6+} of MoO_3. For P50_MoS_2/MABI composites, Mo3d state demonstrated a red shift of approximately 0.65 eV when compared to pristine P50_MoS_2, as illustrated in **Figure 4.5e**. These findings consistently imply that P50_MoS_2 present in composites was accepting photoelectrons, which leads to a decrease in the binding energy of the Mo3d state. The observed shifts in binding energy towards higher values for Bi and I, and lower values for Mo, indicate an efficient interfacial charge transfer from MABI to P50_MoS_2 through a robust heterojunction, ultimately enhancing the photocatalytic performance of P50_MoS_2/MABI.[36] The high resolution XPS of phosphorus present in P50_MoS_2/MABI composites were also displayed in **Figure S4.6**, depicting presence of $P2p_{1/2}$ and $P2p_{3/2}$ doublets.

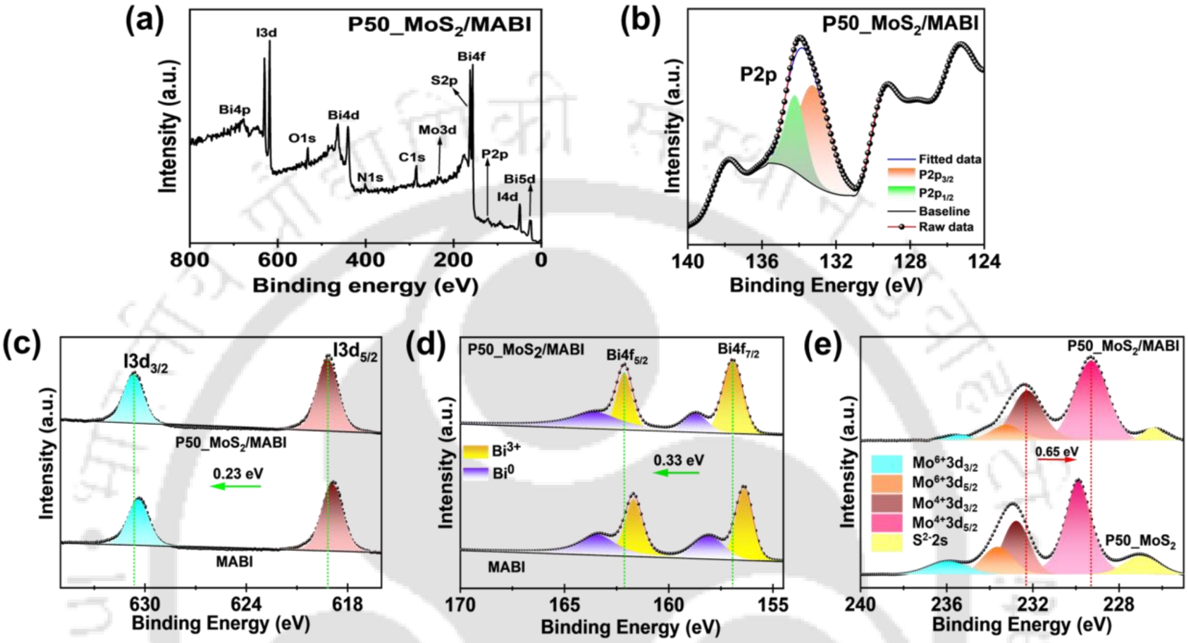

Figure 4.5: XPS survey scan of (a) P50_MoS_2/MABI. High resolution deconvoluted XPS spectra of (b) P2p, (c) I3d, (d) Bi4f and (e) Mo3d for composites and the pristine components.

To investigate the role of MoS_2 as a co-catalyst within the charge transfer mechanism of MoS_2/MABI composites, time-resolved photoluminescence investigation was undertaken, as illustrated in **Figure 4.6a**. The MABI compound and three distinct variants of MoS_2/MABI composites displayed decay phenomena at approximately 630 nm, characterized by diverse patterns that reflect their unique rates of charge recombination. The aggregate recombination rate is represented by the sum of both radiative and non-radiative recombination rates. The lifetimes corresponding to these decay processes exhibited a significant correlation with the recombination dynamics of electron-hole pairs. The pristine MABI demonstrated an average lifetime of 8.2 ns. As depicted in **Figure 4.6a**, the photoluminescence decay of MABI markedly accelerated in the presence of the three MoS_2 variants, necessitating the application of a two-exponential function to fit the PL kinetics. The mean lifetimes for all three MoS_2/MABI composites were notably diminished, indicating an expedited charge transfer mechanism within the heterostructures. Consequently, MoS_2 can efficiently facilitate the extraction of photogenerated electrons from MABI due to the favorable alignment of energy levels.[36] Among the three heterostructures analyzed, the P50_MoS_2/MABI and P100_MoS_2/MABI composites exhibited marginally higher lifetimes in comparison to the MoS_2/MABI configuration. Specifically, P50_MoS_2/MABI and P100_MoS_2/MABI recorded lifetimes of 3.7 ns and 4.2 ns, respectively. In contrast, the MoS_2/MABI composite demonstrated the lowest recorded lifetime of 2.91 ns. The TRPL decay parameters were included in tabular form (**Table 4.1**). To elucidate the observed discrepancies in lifetime data among the three composites, the band alignments between the MABI and MoS_2 constituents were scrutinized. The P50_MoS_2/MABI and P100_MoS_2/MABI composites were classified as type II heterostructures, whereas the MoS_2/MABI composite was categorized as a type I heterostructure. Type I heterostructures facilitate the confinement of both electrons and holes within the same component, typically the layer exhibiting a narrower bandgap. Although this configuration promotes radiative recombination owing to the enhanced spatial overlap of charge carriers, it generally results in reduced lifetimes as electrons and holes remain in close proximity. Such phenomena impose constraints on photocatalytic processes, where effective charge separation is paramount. Conversely, type II heterostructures enable the preferential accumulation of electrons and holes in distinct components. This spatial segregation of charge carriers across the interface substantially mitigates recombination, leading to extended time-resolved photoluminescence lifetimes. An extended lifetime correlates with a reduction in the recombination of photoelectrons and holes, thereby increasing the probability of successful charge separation and migration, ultimately diminishing photocatalytic activity.[37]

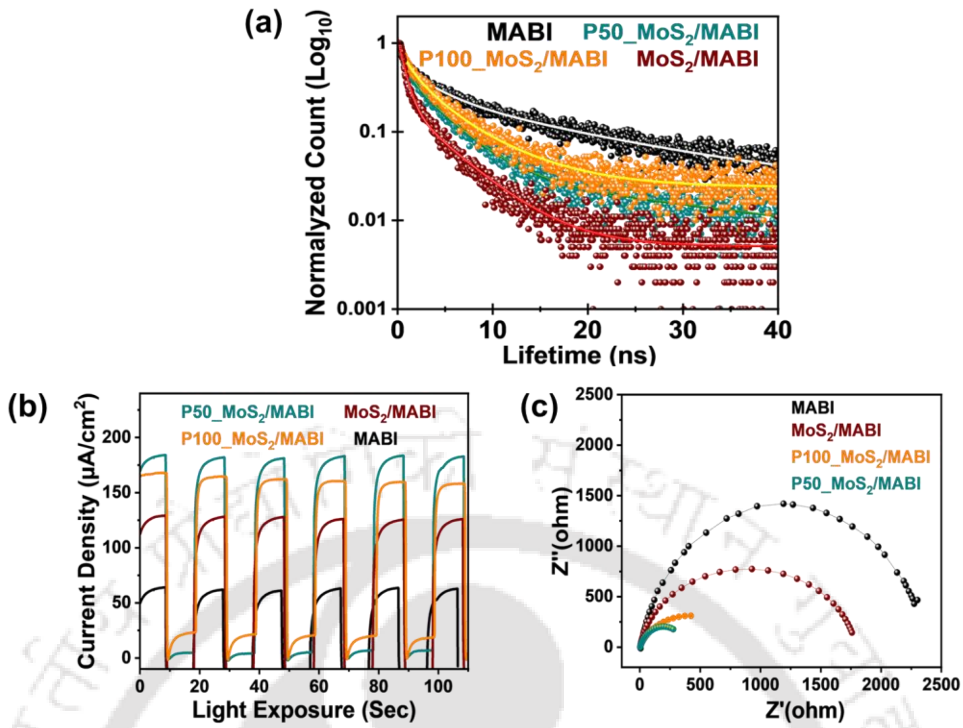

Figure 4.6: (a) Time resolved photoluminescence decay at 630 nm (**b**) transient photocurrent responses under visible light (λ ≥ 420 nm) irradiation, and (**c**) EIS Nyquist plots of pristine MABI and MoS_2/MABI composites.

The photoelectrochemical (PEC) evaluation was employed to furnish substantial evidence regarding charge separation and transfer within the composites. The photo-current responses for the unmodified MABI and its various composites were recorded over multiple 10-second illumination intervals and were depicted in **Figure 4.6b**. Clearly, under the illumination condition, the photocurrent intensity was noted to remain relatively stable, while it rapidly diminished to zero upon cessation of light, indicating a swift photocurrent response to the on-off light conditions. It was noted that the P50_MoS_2/MABI composites exhibited the highest photocurrent, whereas the photocurrent progressively declined for the MoS_2/MABI and P100_MoS_2/MABI composites, respectively. As expected, the pristine MABI displayed the lowest photocurrent when subjected to the same electrical bias. In the realm of transient photocurrent, a higher value signifies effective and efficient charge mobility within the composites, which frequently correlates with the superior hydrogen evolution rate among all tested samples.[38] These findings were corroborated by electrochemical impedance spectroscopy (EIS) measurements, as illustrated in **Figure 4.6c**. The P50_MoS_2/MABI composite, exhibiting the smallest semicircle arc, signifies the lowest interfacial charge transfer resistance, thereby facilitating expedited charge transfer at the interface. In contrast, the interfacial charge transfer resistance for the other MABI composites progressively increased, peaking for the pristine MABI.[39] This indicates that charge migration was most arduous for the pristine MABI, consequently resulting in the lowest photocurrent. This observation elucidates that under certain scenario P doped MoS_2 based heterostructures displayed superior photo-electrochemical properties which ultimately translated into accelerated photocatalytic reductive hydrogen evolution reaction rates. Which might be attributed due to improved charge separation and transport for photocatalytic processes.[40]

In the context of photocatalytic hydrogen generation reactions, the MoS_2/MABI composites were synthesized through the incorporation of cocatalysts and precursors, notably BiI_3 and MAI, within a mixed solution of MABI-saturated aqueous HI/H_3PO_2, utilizing the method of in situ crystallization. The photocatalytic hydrogen evolution efficiency of the synthesized samples was evaluated under visible white light LED irradiation in the MABI-saturated HI/H_3PO_2 (5:1 v/v) solution. The three fundamental elements in this photocatalytic process are the photocatalyst, the illumination source, and the reaction medium. To validate this assertion, a sequence of controlled photocatalytic experiments was performed, during which each component was systematically omitted. Under these controlled conditions, no hydrogen gas was observed in the absence of visible light irradiation, and the MABI microcrystals underwent disintegration when HI was absent from the reaction medium. Nevertheless, the photocatalytic activities were verified via gas chromatography, with the visible light acting upon a photocatalyst immersed in the MABI-saturated HI/H_3PO_2 solution. The hydrogen evolution rates for all samples were compiled and illustrated as a function of light exposure duration in **Figure 4.7a**. Hydrogen evolution activity of pristine MABI was determined to be a mere 15 $\mu mol\ g^{-1}\ h^{-1}$. This subpar performance may be attributed to a limited number of surface reaction sites present on MABI surfaces, resulting in a diminished generation of photogenerated electrons and a delayed transfer to the reaction medium.[41]

Unexpectedly, the hydrogen evolution reaction (HER) performance exhibited a significant enhancement upon the incorporation of MoS_2 co-catalyst with MABI microcrystals. The P100_MoS_2/MABI composites demonstrated an H_2 evolution rate of 250 $\mu mol\ g^{-1}h^{-1}$, representing the lowest performance among all composite materials, whereas the P50_MoS_2/MABI composites showcased the highest HER activity, achieving 1576 $\mu mol\ g^{-1}h^{-1}$, the most notable performance across the various composite formulations. A comparative performance summary table (**Table 4.2**) has been included in the Supporting Information.

This observed performance surpasses that of the pristine MABI microcrystals by nearly 100 times. This phenomenon can be elucidated through the in-situ crystallization process. wherein MoS_2 clusters are effectively integrated on the MABI surface (**Figure 4.3b and 4.4b**) resulting in probability of segregation between MABI and MoS_2 diminishes during magnetic stirring. Furthermore, this interaction fosters the formation of a robust heterojunction, contributing to the aforementioned enhancement of HER performance.

In terms of hydrogen evolution activity, the MoS_2/MABI composites not only surpassed pristine MABI but also displayed superior HER performance relative to MABI samples decorated with Pt.[26] Additionally, it is pertinent to note that the best performing P50_MoS_2/MABI composites exhibited commendable stability in HER activities over an extended duration (**Figure 4.7b**). The photocatalytic hydrogen evolution was conducted utilizing P50_MoS_2/MABI composites under white LED illumination for a period of 56 hours. There was no significant decline in HER activity over 8 consecutive cycles, each spanning 5 hours with a 1-hour interval for the evacuation and purging of inert nitrogen gas. However, following prolonged irradiation of 56 hours, a substantial decline in HER activity was observed during the final cycle. This reduction in measured activity may be attributed to an excessive accumulation of I^{3-}. However, XPS and TEM analysis of the P50_MoS_2/MABI samples were performed after 56 hours of HER activity, no significant degradation were observed following this duration (**Figure S4.7, S4.8**).

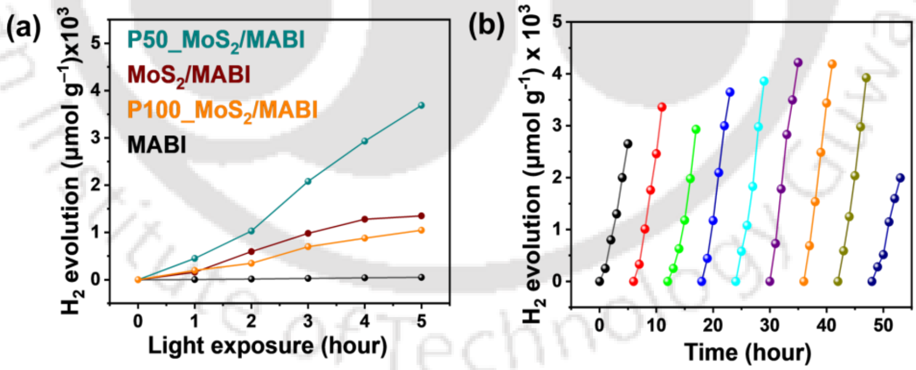

Figure 4.7. (a) Comparative study of H_2 evolution of all MoS_2/MABI composites (10 wt. %) and (b) H_2 evolution activity of P50_MoS_2/MABI composites over 55 h long white light LED exposure.

A crucial technique, UPS analysis, was employed to assess the VBM of three variants of MoS_2 as well MABI. This investigation revealed MABI has its VBM position at -5.74 eV. Whereas the VBM of pristine MoS_2 was positioned at -5.43 eV (**Figure S4.9**, **S4.10**). The obtained band gap of MABI and pristine MoS_2 were 1.98 eV and 1.39 eV respectively. Hence the CBM of MABI and MoS_2 were calculated as -3.76 eV and -4.04 eV. Notably upon doping of P, the VBM of doped MoS_2 got reduced significantly for both P50_MoS_2 and P100_MoS_2. The VBM of P50_MoS_2, obtained from UPS analysis was -5.76 eV (**Figure S4.11**). For P100_MoS_2, the VBM was calculated as -6.27 Ev (**Figure S4.12)**. Hence it is clearly evident that doping of phosphorus showed a downward trend for VBM. The band gap of both the P50_MoS_2 and P100_MoS_2 obtained from tauc plot followed a declining trend compare to MoS_2. The calculated band gap of both P50_MoS_2 and P100_MoS_2 were 1.28 eV and 1.07 eV respectively. Summing up both the data of VBM and band gap, the obtained CBM of P50_MoS_2 and P100_MoS_2 were -4.48 eV and -5.2 eV respectively.

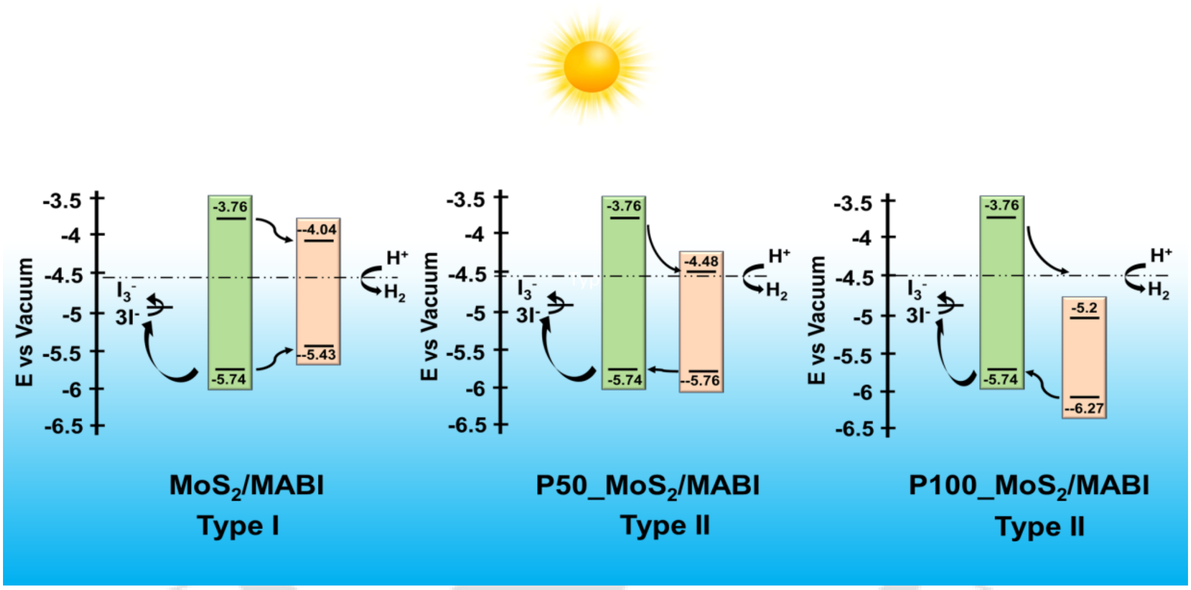

Figure 4.8: Schematic Illustration of Band Alignment of three variants of MoS_2/MABI Composites and Mechanism of H_2 evolution in Aqueous HI.

As delineated in **Figure 4.8** for MoS_2/MABI, the VBM of pristine MoS_2 was situated considerably above that of MABI, while the CBM resides below than that of MABI. This alignment of band positions exemplifies a classical type I heterostructure, wherein both the CBM and VBM of the pristine MoS_2 component were encompassed within the respective CBM and VBM of the MABI component. Consequently, both photogenerated electrons and holes were confined within the individual MoS_2 component of the composites. Such an arrangement enhances the probability of radiative recombination in MABI composites, potentially resulting in lower average TRPL lifetime and lower photocurrent leading towards reduced HER activities. In contrast, for the P-doped variant of MoS_2, a downward shift towards deeper negative energy region were observed as depicted in **Figure 4.8**. This downward shift created a favorable scenario for a type II heterojunction, where the CBM and VBM of MoS_2 were positioned below or in close proximity to those of MABI, yielding spatial separation of electrons and holes in P50_MoS_2/ MABI and P100_MoS_2/MABI composites. Photogenerated electrons were predominantly localized in the conduction band of the MoS_2 component, while holes were situated in the valence band of MABI. This spatial separation facilitates extended TRPL lifetimes and was beneficial for the transfer of photogenerated charges. The TRPL lifetime, photocurrent, and charge transfer resistance data further corroborate this observation.[42]

For two of the composites (MoS_2/MABI, P50_MoS_2/MABI) the CBM of MoS_2 components were situated above and in close proximity to the redox potential $E(H^+/H_2)$, which is -4.55 eV relative to vacuum or 0 V relative to NHE.[18] This specific configuration of energy bands were extremely crucial for co-catalyst mediated efficient proton reduction where MoS_2 and P50_MoS_2 could efficiently transferred the photoelectrons towards protons present in reaction medium. Conversely, the CBM of P100_MoS_2 was found to be positioned much deeper relative to $E(H^+/H_2)$. Though the relative energy bands alignment between MABI and P100_MoS_2 created a type II heterojunction which might be favourable for effective charge extraction from MABI towards P100_MoS_2, but this particular aforementioned band position of P100_MoS_2, was very detrimental for HER activities. The role of co-catalyst was to extract the photoelectron form MABI and transfer it towards the protons present in reaction medium hence P100_MoS_2 fails to serve as a co-catalyst. Despite of efficient charge separation and transfer, P100_MoS_2 could not facilitates the proton reduction, as its CBM was situated significantly below to $E(H^+/H_2)$.

The understanding of the distinct photocatalytic and photoelectrochemical characteristics can be elucidated through the analysis and comparison of the energy profile diagrams corresponding to the three composites, as depicted in **Figure 4.8.** As previously noted, among the three composites MoS_2/MABI, P50_MoS_2/MABI, and P100_MoS_2/MABI; the P-doped composites exhibited a type II heterostructure. For initial two composites, the MoS_2 component was instrumental in facilitating proton reduction. This observation clearly indicates that P50_MoS_2/MABI fulfils two of the most critical criteria for being an effective photocatalyst. In contrast, the other two composites fall short in one of these essential characteristics, adversely impacting their photocatalytic performance. Consequently, both MoS_2/MABI and P100_MoS_2/MABI exhibited HER activities within a comparable range. While P50_MoS_2/MABI have demonstrated the best HER performance as depicted in **Figure 7a**. Among the remaining two composites, although P100_MoS_2/MABI composites showcased superior TRPL lifetime and photocurrent but MoS_2/MABI with type I heterostructure have exhibited marginally superior HER performance.

4.4 Experimental section

Materials:

Ammonium molybdate tetrahydrate, Sodium hypophosphite monohydrate, Bismuth iodide, hydrogen iodide (57 wt% in H_2O), thiourea, anhydrous DMSO, anhydrous toluene were purchased from Sigma-Aldrich. Methylammonium iodide was purchased from Great cell solar. All chemicals were used as received.

Preparation of amorphous MoS_2 and P doped MoS_2

In a conventional synthesis procedure, 20 mL of ethylene diamine was solubilized in 10 mL of distilled water. Subsequently, 1 mmol of $(NH_4)_6Mo_7O_{24}\cdot 4H_2O$ was incorporated while stirring. Following complete dissolution, 4 mmol of thiourea was introduced and the mixture was agitated for a duration of 30 minutes. As a phosphorus precursor, varying amounts of $NaH_2PO_2\cdot H_2O$ (specifically, 50 mg and 100 mg) were incorporated into the precursor solution. The resultant solution was then transferred into a 50 mL Teflon-lined stainless-steel autoclave and subjected to heating at 200 °C for a period of 12 hours, after which it was allowed to cool to ambient temperature spontaneously. The resultant black precipitate was isolated via centrifugation and subjected to multiple washings with deionized water and ethanol to eliminate any residual ions, followed by drying at 50 °C for 6 hours in preparation for subsequent characterization. Three distinct variants of MoS_2 were synthesized, denoted as MoS_2, 50_MoS_2, and 100_MoS_2.

Preparation of MoS_2/MABI composites powder:

MABI was synthesized by dissolving MAI and BiI_3 in molar ratio of 3:2. Specifically, 1176.38 mg BiI_3 was dissolved in 5 ml of anhydrous DMSO at 80°C, then 476.88 mg MAI was slowly added into the solution with vigorous stirring. A saturated bright orange solution was formed used for further preparation. 165 mg of 3 variants of MoS_2 (≈ 10 wt.% with respect to total MABI formed) were added separately into three different solutions. Under stirring condition, anhydrous toluene was added dropwise in the solution. Black precipitate would start to appear. Addition of anhydrous toluene was continued till the complete precipitation appeared with constant stirring at 90°C for 3 hours. The reaction mixture was centrifuged with dry ethyl acetate and the precipitate was collected after 3 washes. The precipitate was dried in vacuum oven at 80°C for 12 hours and stored inside the glove box for further use.

Visible light source for photocatalytic measurements

The visible light source used here for the experiments is a 50 W with power density of 150 mW/cm^2 white LED bought from Ledvance Osram. The spectrum of this light source is 420 - 790 nm.

Table 4.1: Table for parameters of TRPL decays.

	A_1	**t_1 (ns)**	**A_2**	**t_2 (ns)**	**Average lifetime (Tav)**
MABI	0.49569	0.86823	0.40312	9.05049	8.187 ns
P50_MoS_2/MABI	0.5647	0.8355	0.432	4.45275	3.740 ns
P100_MoS_2/MABI	0.5647	0.83559	0.432	4.45275	4.2 ns

Table 4.2: performance and experimental parameters of reported halide perovskite photocatalysts for H_2 evolution.

Material	Light source	H_2 production [μmol $g^{-1}h^{-1}$]	References
$MA_3Bi_2I_9$	300 W Xe-lamp with a 400 nm cutoff filter	12.9	1
$MA_3Bi_2I_9$/Pt	300 W Xe-lamp with a 400 nm cutoff filter	169.21	1
P50_MoS_2/$MA_3Bi_2I_9$	50 W white LED with power density of 150 mW/cm^2	1176	This work

4.5 Conclusion

The influence of phosphorus doping on the band gap and energy levels have been meticulously analyzed. This study elucidates that the band gap of MoS_2 declines from 1.39 eV for pristine MoS_2 to 1.28 eV for P50_MoS_2, and it further diminished to 1.07 eV for P100_MoS_2 upon doping with P. Concurrently, the VBM energy level of all the MoS_2 variants experienced a downward shift. Consequently, P50_MoS_2/MABI and P100_MoS_2/MABI composites have established a type II heterojunction, whereas MoS_2/MABI results in a type I heterojunction. It is noteworthy that type II heterojunctions are typically more favorable for the separation and migration of photogenerated charges when compared to type I heterostructures, P50_MoS_2/MABI demonstrated superior photocatalytic and photoelectrochemical efficiencies relative to the others.

Even though P100_MoS_2/MABI possessed type II heterojunction still it exhibited the least reaction rates among three composites. The relative energy band positions of P100_MoS_2 and MABI might be attributed to the diminished HER activity. The CBM of P100_MoS_2 was located at significantly deeper energy level compared to $E(H^+/H_2)$, inhibiting its function as a photoelectron carrier, thereby resulting in the compromised photocatalytic HER activities of P100_MoS_2/MABI composites.

4.6 Reference

(1) Shaner, M. R.; Atwater, H. A.; Lewis, N. S.; McFarland, E. W. A Comparative Technoeconomic Analysis of Renewable Hydrogen Production Using Solar Energy. *Energy Environ. Sci.* **2016**, *9*, 2354–2371.

(2) Hassan, Q.; Abdulateef, A. M.; Hafedh, S. A.; Al-samari, A.; Abdulateef, J.; Sameen, A. Z.; Salman, H. M.; Al-Jiboory, A. K.; Wieteska, S.; Jaszczur, M. Renewable Energy-to-Green Hydrogen: A Review of Main Resources Routes, Processes and Evaluation. *Int. J. Hydrogen Energy* **2023**, *48*, 17383–17408.

(3) Ueckerdt, F.; Bauer, C.; Dirnaichner, A.; Everall, J.; Sacchi, R.; Luderer, G. Potential and Risks of Hydrogen-Based e-Fuels in Climate Change Mitigation. *Nat. Clim. Chang.* **2021**, *11*, 384–393.

(4) Li, F.; Liu, G.; Liu, F.; Yang, S. A WO3-TiO_2 Nanorod/$CaCO_3$ Photocatalyst with Degradation-Regeneration Double Sites for NO_2-Inhibited and Durable Photocatalytic NO. *Chemosphere* **2023**, *324*, 138277. DOI: 10.1016/j.chemosphere.2023.138277.

(5) Wang, J.; Sun, S.; Pan, L.; Xu, Z.; Ding, H.; Li, W. Preparation and Properties of $CaCO_3$-Supported Nano-TiO_2 Composite with Improved Photocatalytic Performance. *Materials* **2019**, *12*, 3369. DOI: 10.3390/ma12203369.

(6) Demina, P. A.; Voronin, D. V.; Lengert, E. V.; Abramova, A. M.; Atkin, V. S.; Nabatov, B. V.; Semenov, A. P.; Shchukin, D. G.; Bukreeva, T. V. Freezing-Induced Loading of TiO2 into Porous Vaterite Microparticles: Preparation of $CaCO_3$/TiO_2 Composites as Templates to Assemble UV-Responsive Microcapsules for Wastewater Treatment. *ACS Omega* **2020**, *5*, 4115–4124.

(7) Yukta; Chavan, R. D.; Mahapatra, A.; Prochowicz, D.; Yadav, P.; Iyer, P. K.; Satapathi, S. Improved Efficiency and Stability in 1,5-Diaminonaphthalene Iodide-Passivated 2D/3D Perovskite Solar Cells. *ACS Appl. Mater. Interfaces* **2023**, *15*, 53351–53361.

(8) Baishya, H.; Adhikari, R. D.; Patel, M. J.; Yadav, D.; Sarmah, T.; Alam, M.; Kalita, M.; Iyer, P. K. Defect Mediated Losses and Degradation of Perovskite Solar Cells: Origin, Impacts and Reliable Characterization Techniques. *J. Energy Chem.* **2024**, *94*, 217–253.

(9) Das Adhikari, R.; Baishya, H.; Patel, M. J.; Yadav, D.; Iyer, P. K. Bi-Directional Modification to Quench Detrimental Redox Reactions and Minimize Interfacial Energy Offset for NiO_X/Perovskite-Based Solar Cells. *Small* **2024**, *20*, e2404588. DOI: 10.1002/smll.202404588.

(10) Kamminga, M. E.; de Wijs, G. A.; Havenith, R. W. A.; Blake, G. R.; Palstra, T. T. M. The Role of Connectivity on Electronic Properties of Lead Iodide Perovskite-Derived Compounds. *Inorg. Chem.* **2017**, *56*, 8408–8414.

(11) Tailor, N. K.; Mishra, S.; Sharma, T.; De, A. K.; Satapathi, S. Cation-Dependent Hot Carrier Cooling in the Lead-Free Bismuth Halide $A_3Bi_2I_9$ (A = FA, MA, and Cs) Perovskite. *J. Phys. Chem. C Nanomater. Interfaces* **2021**, *125*, 9891–9898.

(12) Roknuzzaman, M.; Zhang, C.; Ostrikov, K. K.; Du, A.; Wang, H.; Wang, L.; Tesfamichael, T. Electronic and Optical Properties of Lead-Free Hybrid Double Perovskites

for Photovoltaic and Optoelectronic Applications. *Sci. Rep.* **2019**, *9*, 718. DOI: 10.1038/s41598-018-37132-2.

(13) Chen, S.; Yin, H.; Liu, P.; Wang, Y.; Zhao, H. Stabilization and Performance Enhancement Strategies for Halide Perovskite Photocatalysts. *Adv. Mater.* **2023**, *35*, e2203836. DOI: 10.1002/adma.202203836.

(14) Pal, T.; Bhowmik, S.; Suhail, A.; Sharma, S.; Peela, N. R.; Sastri, C. V.; Iyer, P. K. Composites of Reduced Graphene Oxide and $MAPbI_3$ Crystals for Photocatalytic Hydrogen Generation. *ACS Appl. Nano Mater.* **2024**, *7*, 12163–12170.

(15) Pal, T.; Bhowmik, S.; Tanwar, A. S.; Suhail, A.; Peela, N. R.; Sastri, C. V.; Iyer, P. K. Solvent Assisted Shape Dependent $MAPbI_3$/Polyfluorene Heterostructures with a Larger Surface Area for Improved Photocatalytic H_2 Evolution. *Energy Adv.* **2024**, *3*, 2965–2971.

(16) Park, S.; Chang, W. J.; Lee, C. W.; Park, S.; Ahn, H.-Y.; Nam, K. T. Photocatalytic Hydrogen Generation from Hydriodic Acid Using Methylammonium Lead Iodide in Dynamic Equilibrium with Aqueous Solution. *Nat. Energy* **2016**, *2*, 16185. DOI: 10.1038/nenergy.2016.185.

(17) Zhao, X.; Chen, S.; Yin, H.; Jiang, S.; Zhao, K.; Kang, J.; Liu, P. F.; Jiang, L.; Zhu, Z.; Cui, D.; Liu, P.; Han, X.; Yang, H. G.; Zhao, H. Perovskite Microcrystals with Intercalated Monolayer MoS_2 Nanosheets as Advanced Photocatalyst for Solar-Powered Hydrogen Generation. *Matter* **2020**, *3*, 935–949.

(18) Guan, W.; Li, Y.; Zhong, Q.; Liu, H.; Chen, J.; Hu, H.; Lv, K.; Gong, J.; Xu, Y.; Kang, Z.; Cao, M.; Zhang, Q. Fabricating $MAPbI_3/MoS_2$ Composites for Improved Photocatalytic Performance. *Nano Lett.* **2021**, *21*, 597–604.

(19) Wani, A. L.; Ara, A.; Usmani, J. A. Lead Toxicity: A Review. *Interdiscip. Toxicol.* **2015**, *8*, 55–64.

(20) Tang, Y.; Mak, C. H.; Zhang, J.; Jia, G.; Cheng, K.-C.; Song, H.; Yuan, M.; Zhao, S.; Kai, J.-J.; Colmenares, J. C.; Hsu, H.-Y. Unravelling the Interfacial Dynamics of Bandgap Funneling in Bismuth-Based Halide Perovskites. Adv. Mater. 2023, 35, e2207835. DOI: 10.1002/adma.202207835.

(21) Mondal, A.; Gupta, S. Bismuth (Bi^{3+}) Based Lead-Free Halide Perovskitoid for Light Driven Applications: A Potential Low-Toxic Alternative for Lead (Pb^{2+}). *Mater. Lett.* **2024**, *366*, 136572. DOI: 10.1016/j.matlet.2024.136572.

(22) Park, J. G.; Park, S. W.; Hong, K. H. High-throughput Screening of Perovskite Inspired Bismuth Halide Materials: Toward Lead-free Photovoltaic Cells and Light-emitting Diodes. *Nanotechnology* **2022**, *33*. DOI: 10.1088/1361-6528/ac88db.

(23) Soykan, C.; Gocmez, H. The Physical Properties of Bismuth Replacement in Lead Halogen Perovskite Solar Cells: $CH_3NH_3Pb_{1-x}Bi_xI_3$ Compounds by Ab-Initio Calculations. *Results Phys.* **2019**, *13*, 102278. DOI: 10.1016/j.rinp.2019.102278.

(24) Feng, J.; Mak, C. H.; Jia, G.; Han, B.; Shen, H.-H.; Santoso, S. P.; Kai, J.-J.; Yuan, M.; Song, H.; Colmenares, J. C.; Hsu, H.-Y. Unlocking Interfacial Interactions of in Situ Grown

Multidimensional Bismuth-based Perovskite Heterostructures for Photocatalytic Hydrogen Evolution. *Adv. Energy Mater.* **2024**, *14*. DOI: 10.1002/aenm.202402785.

(25) Miodyńska, M.; Klimczuk, T.; Lisowski, W.; Zaleska-Medynska, A. Bi-Based Halide Perovskites: Stability and Opportunities in the Photocatalytic Approach for Hydrogen Evolution. *Catal. Commun.* **2023**, *177*, 106656. DOI: 10.1016/j.catcom.2023.106656.

(26) Guo, Y.; Liu, G.; Li, Z.; Lou, Y.; Chen, J.; Zhao, Y. Stable Lead-Free $(CH_3NH_3)_3Bi_2I_9$ Perovskite for Photocatalytic Hydrogen Generation. *ACS Sustain. Chem. Eng.* **2019**, *7*, 15080–15085. DOI: 10.1021/acssuschemeng.9b03761.

(27) Purohit, S.; Yadav, K. L.; Satapathi, S. Metal Halide Perovskite Heterojunction for Photocatalytic Hydrogen Generation: Progress and Future Opportunities. *Adv. Mater. Interfaces* **2022**, *9*, 2200058. DOI: 10.1002/admi.202200058.

(28) Ran, J.; Zhang, J.; Yu, J.; Jaroniec, M.; Qiao, S. Z. Earth-Abundant Cocatalysts for Semiconductor-Based Photocatalytic Water Splitting. *Chem. Soc. Rev.* **2014**, *43*, 7787–7812.

(29) Alfa, I.; Hafeez, H. Y.; Mohammed, J.; Abdu, S.; Suleiman, A. B.; Ndikilar, C. E. A Recent Progress and Advancement on MoS_2-Based Photocatalysts for Efficient Solar Fuel (Hydrogen) Generation via Photocatalytic Water Splitting. *Int. J. Hydrogen Energy* **2024**, *71*, 1006–1025.

(30) Nethravathi, C.; Prabhu, J.; Lakshmipriya, S.; Rajamathi, M. Magnetic Co-Doped MoS_2 Nanosheets for Efficient Catalysis of Nitroarene Reduction. *ACS Omega* **2017**, 2, 5891–5897.

(31) Ahmad, K.; Raza, W.; Kumar, P.; Khan, M. Q.; Alsalme, A.; Kim, H. Mechanochemical Synthesis of Lead-Free Perovskite-like $MA_3Bi_2I_9$ for Photo-Catalytic Hydrogen Production. Chemistry **2023**, *29*, e202300250. DOI: 10.1002/chem.202300250.

(32) Tang, Y.; Mak, C. H.; Liu, R.; Wang, Z.; Ji, L.; Song, H.; Tan, C.; Barrière, F.; Hsu, H.-Y. In Situ Formation of Bismuth-based Perovskite Heterostructures for High-performance Cocatalyst-free Photocatalytic Hydrogen Evolution. *Adv. Funct. Mater.* **2020**, *30*, 2006919. DOI: 10.1002/adfm.202006919.

(33) Zhang, M.; Lei, L.; Zheng, X. Zero-Dimensional Lead-Free Perovskite Single Crystals for the Sensitive Detection of Visible Light and X-Rays. *Chemistry* **2025**, *31*, e202404004. DOI: 10.1002/chem.202404004.

(34) Wu, Y.; Wang, P.; Zhu, X.; Zhang, Q.; Wang, Z.; Liu, Y.; Zou, G.; Dai, Y.; Whangbo, M.-H.; Huang, B. Composite of CH_3 NH_3 PbI_3 with Reduced Graphene Oxide as a Highly Efficient and Stable Visible-Light Photocatalyst for Hydrogen Evolution in Aqueous HI Solution. *Adv. Mater.* **2018**, *30*. DOI: 10.1002/adma.201704342.

(35) Yu, J. X.; Xu, X. X. Expediting H_2 Evolution over $MAPbI_3$ with a Nonnoble Metal Cocatalyst Mo_2C under Visible Light. *Energy Mater. Adv.* **2022**, *2022*. DOI: 10.34133/2022/9836095.

(36) Wang, H.; Wang, X.; Chen, R.; Zhang, H.; Wang, X.; Wang, J.; Zhang, J.; Mu, L.; Wu, K.; Fan, F.; Zong, X.; Li, C. Promoting Photocatalytic H_2 Evolution on Organic–Inorganic Hybrid Perovskite Nanocrystals by Simultaneous Dual-Charge Transportation Modulation. *ACS Energy Lett.* **2019**, *4* (1), 40–47.

(37) Moon, H. S.; Hsiao, K.-C.; Wu, M.-C.; Yun, Y.; Hsu, Y.-J.; Yong, K. Spatial Separation of Cocatalysts on Z-Scheme Organic/Inorganic Heterostructure Hollow Spheres for Enhanced Photocatalytic H_2 Evolution and in-Depth Analysis of the Charge-Transfer Mechanism. *Adv. Mater.* **2023**, *35* (4), e2200172. DOI: 10.1002/adma.202200172.

(38) You, S.; Wang, H.; Bi, S.; Zhou, J.; Qin, L.; Qiu, X.; Zhao, Z.; Xu, Y.; Zhang, Y.; Shi, X.; Zhou, H.; Tang, Z. A Biopolymer Heparin Sodium Interlayer Anchoring TiO_2 and $MAPbI_3$ Enhances Trap Passivation and Device Stability in Perovskite Solar Cells. *Adv. Mater.* **2018**, *30*, e1706924. DOI: 10.1002/adma.201706924.

(39) Xie, R.; Fang, K.; Liu, Y.; Chen, W.; Fan, J.; Wang, X.; Ren, Y.; Song, Y. Z-Scheme In_2O_3/WO_3 Heterogeneous Photocatalysts with Enhanced Visible-Light-Driven Photocatalytic Activity toward Degradation of Organic Dyes. *J. Mater. Sci.* **2020,** *55*, 11919–11937.

(40) Chakraborty, S.; Kalita, D.; Agarwal, S.; Vashishth, S.; Mathew, N.; Maity, S.; Goud, D.; Rao, A.; Peter, S. C.; Singh, A. K.; Eswaramoorthy, M. Tuning the Electrocatalytic Activity of Pd Nanocatalyst toward Hydrogen Evolution and Carbon Dioxide Reduction Reactions by Nickel Incorporation. *Chem. Mater.* **2024**, *36*, 6547–6557.

(41) Li, W.; Wang, F.; Zhang, Z.; Min, S. $MAPbI_3$ Microcrystals Integrated with Ti3C2Tx MXene Nanosheets for Efficient Visible-Light Photocatalytic H_2 Evolution. *Chem. Commun.* **2021**, *57*, 7774–7777.

(42) Meng, X.; Wang, S.; Zhang, C.; Dong, C.; Li, R.; Li, B.; Wang, Q.; Ding, Y. Boosting Hydrogen Evolution Performance of a CdS-Based Photocatalyst: In Situ Transition from Type I to Type II Heterojunction during Photocatalysis. *ACS Catal.* **2022**, *12*, 10115–10126.

4.7 Supporting Information

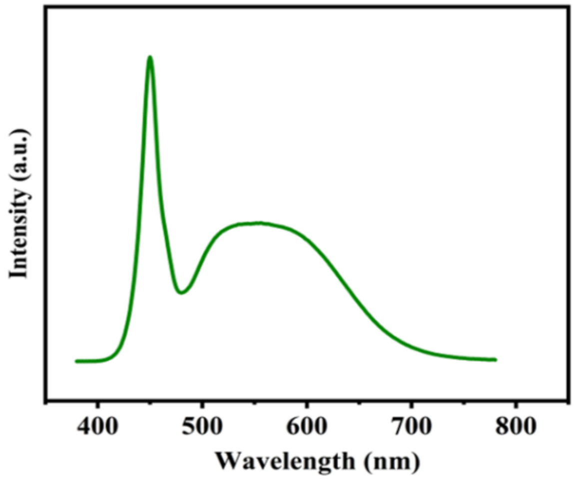

Figure S4.1: Electroluminescence of LED light source.

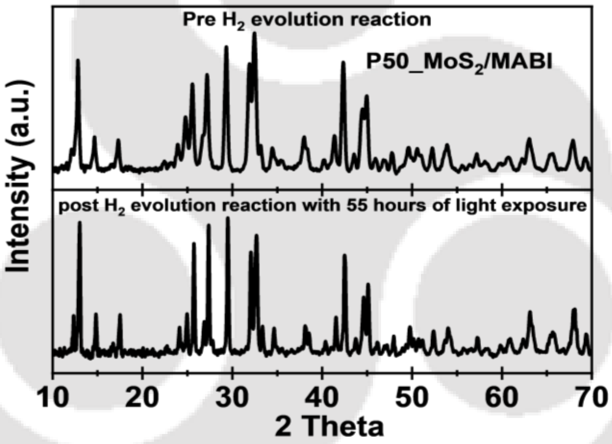

Figure S4.2: Stability study of P50_MoS_2/MABI composites through XRD.

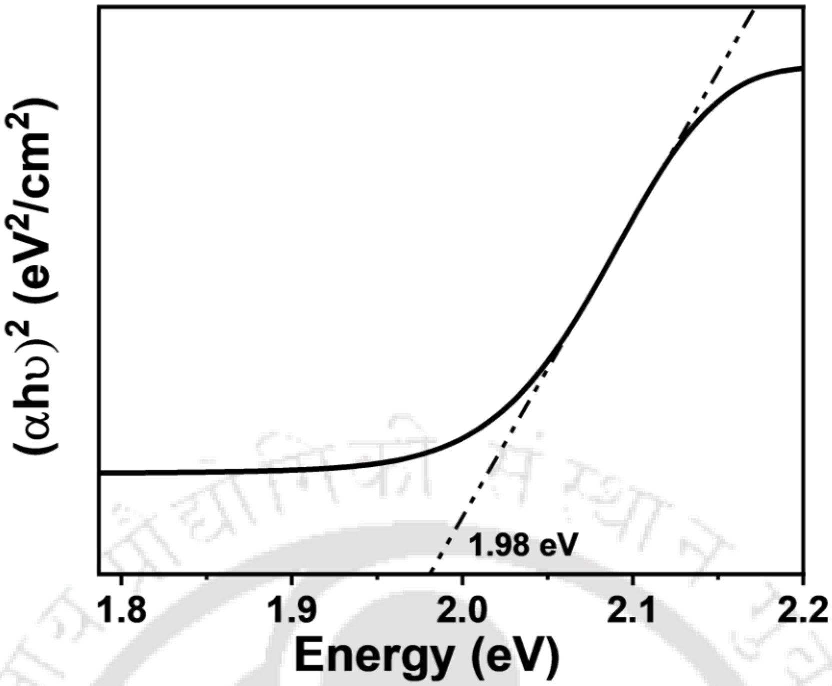

Figure S4.3: Band gap of MABI.

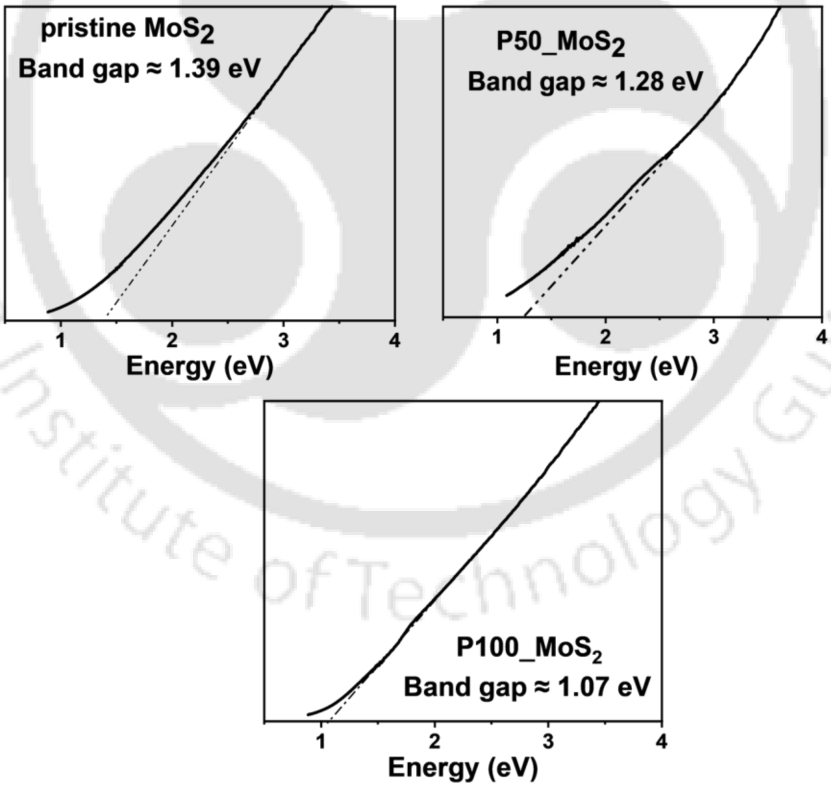

Figure S4.4: Band gap of 3 variants of MoS_2.

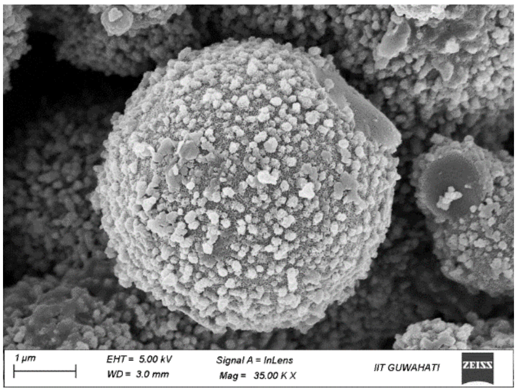

Figure S4.5: FESEM image of amorphous MoS_2.

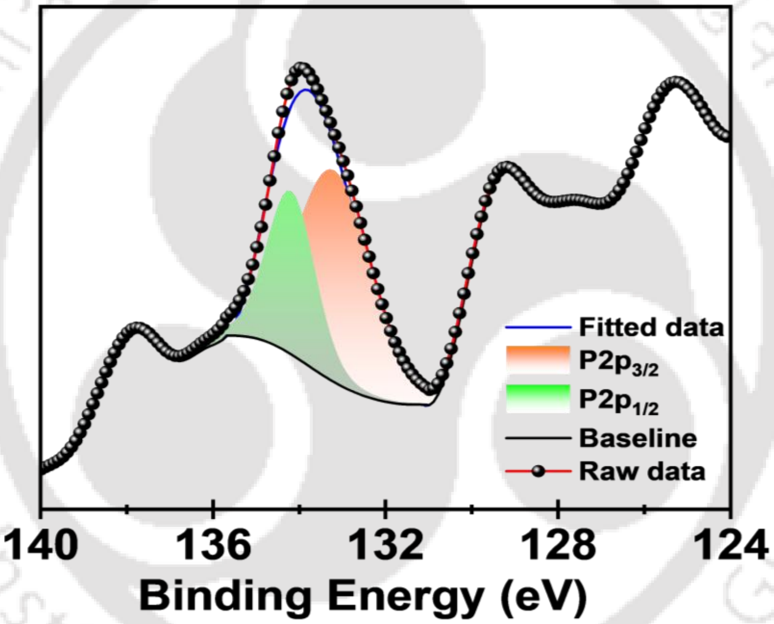

Figure S4.6: XPS of P2p for P50_MoS_2/MABI.

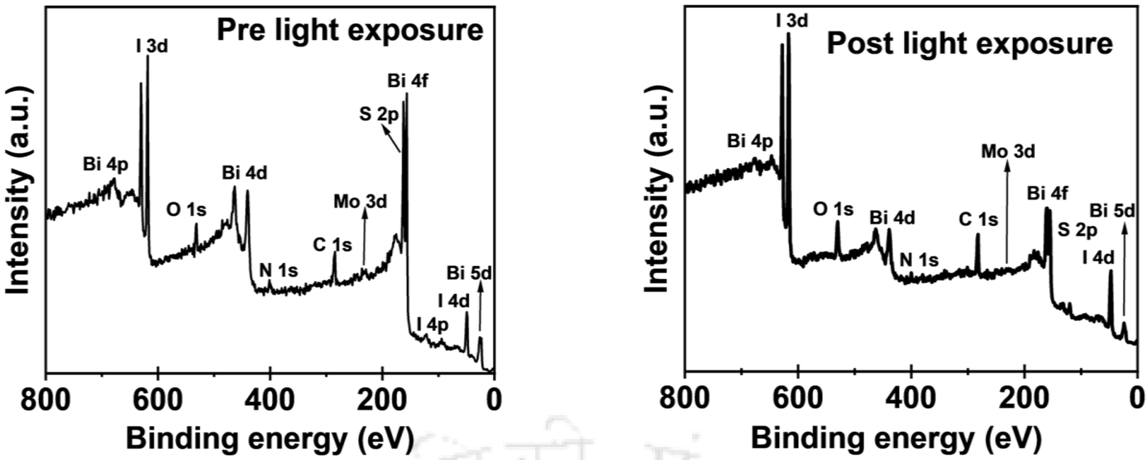

Figure S4.7: XPS **of** P50_MoS_2/MABI, post hydrogen evolution reaction.

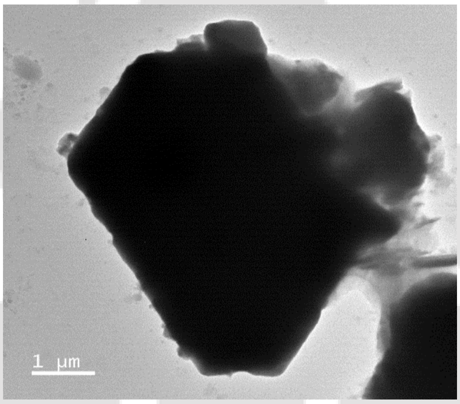

Figure S4.8: TEM image of P50_MoS_2/MABI, post hydrogen evolution reaction.

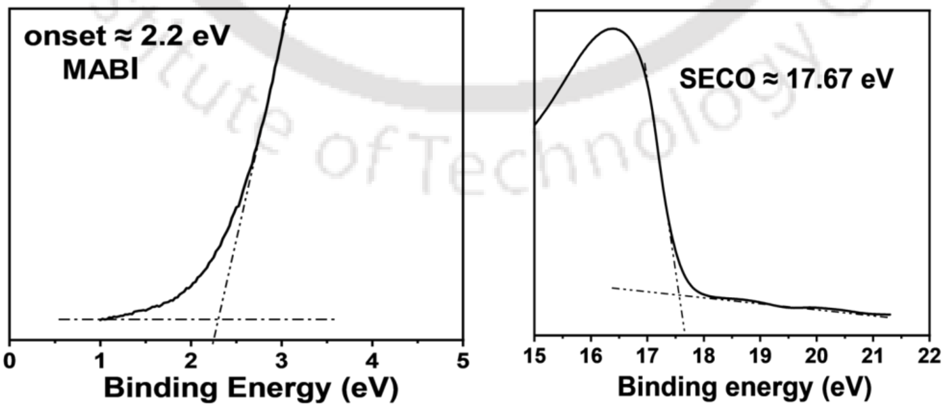

Figure S4.9: UPS analysis of MABI.

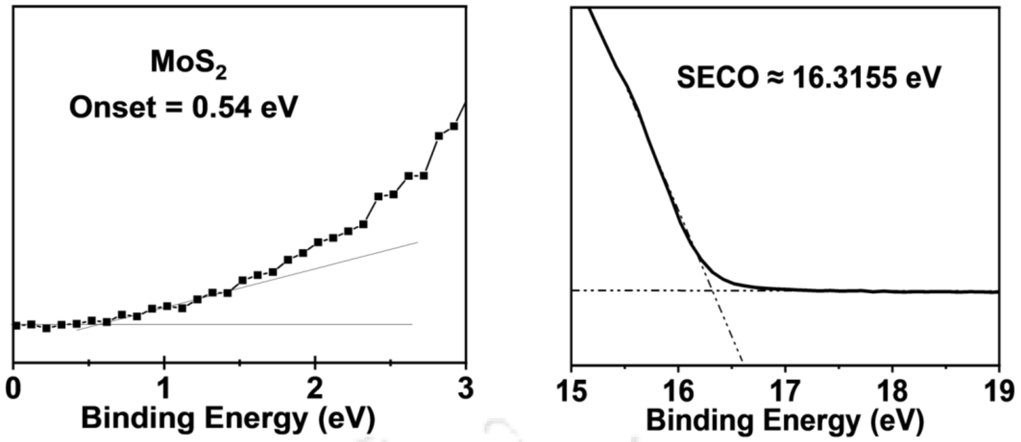

Figure S4.10: UPS analysis of MoS_2.

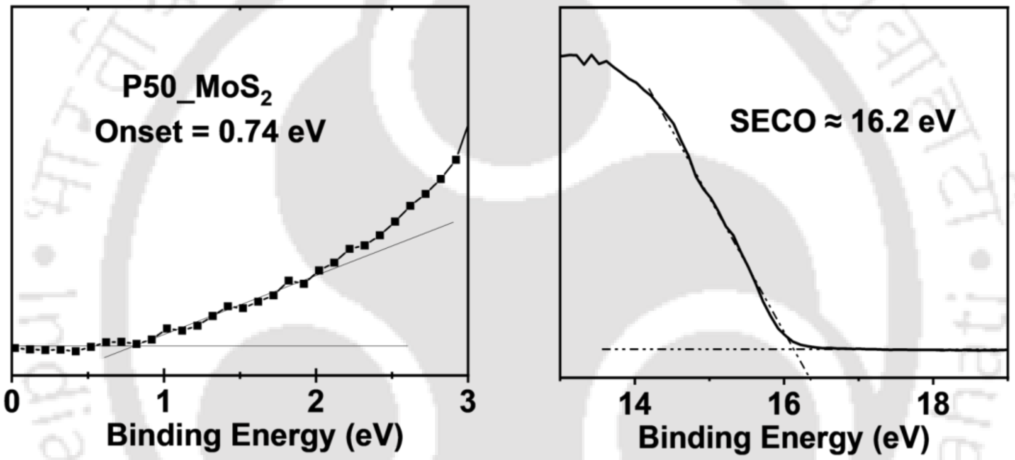

Figure S4.11: UPS analysis of P50_MoS_2.

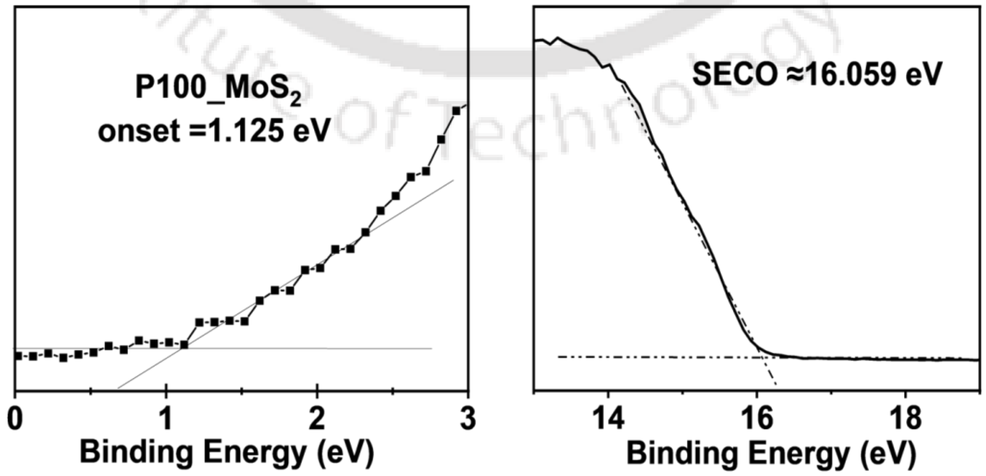

Figure S4.12: UPS analysis of P100_ MoS_2.

[This page was left empty intentionally]

CHAPTER 5

Molecularly Doped Porphyrin Covalent Heterojunction Carbon Nitride Instigating Cocatalyst-Free Solar Energy Harvesting via Water Splitting

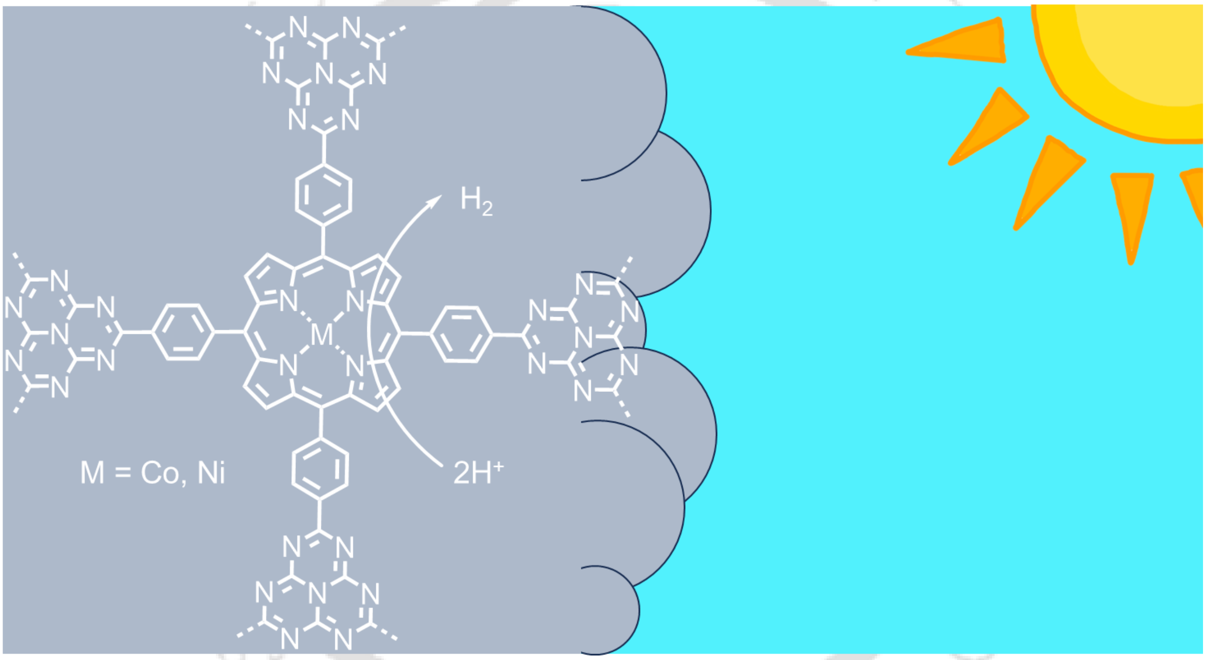

5.1 Abstract:

Graphitic carbon nitride (g-C_3N_4) is a promising metal-free semiconductor for photocatalytic solar energy conversion, yet its practical application is hindered by high charge recombination rates, limited visible light absorption, and lack of catalytic centers. Molecular doping offers an effective strategy to address these limitations by incorporating functional molecular fragments within the carbon nitride framework, enhancing charge separation and electronic properties without the interfacial losses typical of heterojunctions. In this work, we report the rational design of a integrated porphyrin-carbon nitride covalent heterojunction catalyst via a molecular doping approach. A meso-Tetrakis(4-cyanophenyl)porphyrin derivative is functionalized to form polymerizable 2,4-diamino-1,3,5-triazine (DAT) domains, enabling copolymerization with melamine. The resulting porphyrin-doped carbon nitride exhibits extended light absorption, suppressed radiative recombination, and intrinsic catalytic centers. Post-synthetic metalation with Ni or Co yields active, cocatalyst-free photocatalysts for efficient solar-driven water splitting. This strategy demonstrates a versatile platform for constructing multifunctional, molecular heterojunction carbon nitride materials tailored for solar energy applications. Under photocatalytic conditions using visible light, the Ni and Co based porphyrin modified CNs show HER rate of 4100 $\mu mol \cdot g^{-1} h^{-1}$ & 4560 $\mu mol \cdot g^{-1} h^{-1}$ respectively.

5.2 Introduction

Recently graphitic carbon nitride (g-C_3N_4 or g-CN) has garnered praiseworthy reputation as a low cost, metal free, environmentally benign semiconductor material, suitable for several applications including solar energy harvesting using artificial photosynthesis or solar cells.[1-3] Artificial photosynthesis requires semiconductor materials that can absorb sunlight preferentially in the visible region and create charge pairs which can in turn be utilized to perform specific chemical reactions.[4, 5] Despite of several advantages compared to some all-inorganic semiconductors like TiO_2, ZnO, CdS *etc.*, pristine carbon nitride suffers from mainly efficiency issues attributed to several facts like, pristine heptazine based CN has a notoriously high extent of optical recombination in the form of fluorescence and poor carrier dynamics overall. By far the high propensity of radiative recombination directly affects the catalytic efficiency the most. Some other factors like lack of reaction centers in the framework and poor optical absorption of pristine CN at wavelengths above 450 nm further impedes real life implementation of carbon nitride for photocatalytic applications.[1, 2] However, luckily, as carbon nitride is an organic derived polymeric material, it is far easier to modulate its structural fragments as compared to inorganic materials, where limited possibilities are available.[3] Elemental doping is a method that has been extensively employed to improve carrier dynamics of carbon nitrides.[6] But molecular doping has proven its effectivity in this aspect more prominently, utilizing and strategically tweaking the very polymeric property of CN. Molecular doping is a method where whole molecules or molecular fragments can be attached in the CN framework, providing a universal and effective platform for precisely modulating electronic effects in the material.[7] It also enables introducing donor-acceptor type electronic push-pull effects, leading towards efficient charge separation or utilizing conducting π-bridge fragments within the framework to increase overall carrier dynamics.[8] In contrast to the more commonly utilized methods of heterojunction formation, molecular doping gives rise to homojunction or covalent molecular heterojunction materials, which greatly eliminates the interfacial charge transfer losses, without compromising the positive synergistic effects arising from the tuning of local electronic structures.[7, 8] In order to attach molecular fragments into the carbon nitride framework, strategically designed monomers need to be synthesized which contain polymerizable domains compatible to be copolymerized with melamine or dicyandiamide.[9] The attached fragments can be of bridging type, dangling/pendant type or fused ring type depending on the nature of fragment used.[10] Typical polymerizable domains are 2,4-diamino-1,3,5-triazine (DAT); 2,4-diaminopyrimidine (DAP) and pyrimidine nucleobases and their derivatives (substituted uracils etc.) but not limited to. [11-13] Polymerizing molecular materials containing those abovementioned domains leads to copolymerization of the moiety with melamine or dicyandiamide to form substituted heptazines (fused/ carbon rich/ non-stoichiometric) causing molecular doping in the framework.

Porphyrins are highly sought after molecular fragments in various subdomains of catalysis including photocatalysis for solar energy harvesting. They are robust macrocyclic structures bearing a metal center bound to the ligand core which is often highly catalytically active and selective towards electron transfer reactions.[14] Also, their inherent intense light harvesting capability, photoactivity and high thermal stability is extremely beneficial when utilizing them with a material like carbon nitride, which demands for high temperature processibility. The strategy of incorporating a whole porphyrin core into the carbon nitride framework entails a rational designing of a polymerizable porphyrin monomer. Incorporation of a porphyrin inside the carbon nitride framework not only improves its light absorption due to chromophoric effects, but also provides a catalytic center for interfacial reactions like proton reduction to occur. Concisely, this strategy single handedly serves multiple purposes of (a) increasing the light absorption range, (b) suppressing the radiative recombination significantly and (c) providing a self-catalytic site to circumvent the need of an externally attached hydrogen evolution co-catalysts, which are often platinum group metals. Attachment of porphyrins to various classes of semiconductor materials has already been widely researched, however, the strategies quite often result in a porphyrin-semiconductor heterojunction.[15-18] For fabricating carbon nitride-porphyrin molecular heterojunctions, strategies like Schiff-condensation[19] and amide-condensation[20] between the $-NH_2$ group of carbon nitride and >C=O or -COOH side groups of porphyrins have been explored, respectively. Despite the anchoring of porphyrins onto the carbon nitride moiety, these types of covalent bonding often fail to provide a strong planar delocalization electronically, due to the flexible nature of the linkage. Fusing the porphyrin moiety in the carbon nitride framework *via* π-conjugation strategy can effectively circumvent the abovementioned issue.[21-23] Nevertheless, fabricating porphyrin based covalent molecular heterojunction catalysts having a π-conjugated connectivity requires very specific designing strategies which narrow down the choice of molecular attachment domains.

As discussed earlier, DATs can be considered as key intermediate monomers for the synthesis of molecularly doped carbon nitrides via a copolymerization route.[9] Thus, strategically designing DATs with desired molecular fragments can truly open up a facile pathway towards molecular doping of CN frameworks. To begin with the designing of the polymerizable porphyrin, a classic reaction of alkyl/aryl nitriles was revisited, which undergo cyclization reaction with dicyandiamide under basic conditions to form substituted DATs.[11] The present work employs meso-Tetrakis(4-cyanophenyl)porphyrin as a simple porphyrin fragment to build up a covalently bound carbon nitride-porphyrin molecular heterojunction catalyst. Porphyrins are thermally stable molecules inherently, and formation of DAT substitutions further increase it to an even higher degree, reducing the chances of their thermal degradation during polymerization and conserving material homogeneity. The cyanophenyl porphyrin undergoes DAT formation when reacted with excess dicyandiamide in NMP using a KOH catalyst. Then the DAT substituted porphyrin can form a supramolecular assembly with melamine, which upon high temperature copolymerization, forms the covalent heterojunction carbon nitride. Post metalation of this material with Ni or Co ions produces a metalloporphyrin-CN derivative as the active water splitting semiconductor. It is noteworthy to mention that the DAT substituted porphyrin has been utilized itself as a photoactive H-bonded organic framework (HOF) for photocatalytic removal of U(VI) from water,[24, 25] and as a molecular dopant in carbon nitride for photocatalytic H_2 evolution[21] and CO_2 reduction applications.[22, 23] However, the works utilize precious co-catalysts like Pt,[21] and the synthesis of the porphyrin fused carbon nitride employs urea as the precursor,[21-23] which often leads to very porous, slightly amorphous carbon nitrides compared to melamine derived ones. Our work employs melamine as the main precursor to increase the overall crystallinity of the CN photocatalyst and also exploits the DAT porphyrin's capability to form an H-bonded supramolecular assembly with melamine, as a key step in synthesis, for better homogeneity.[26, 27] Moreover, we also observe that, upon post-metalation, the metalated porphyrin sites not only act as chromophoric centres, augmenting the photo-properties of the material, but also, act as self-catalytic sites for HER to occur, avoiding the use of precious co-catalysts. Under photocatalytic conditions using visible light, the Ni and Co based porphyrin modified CNs show HER rate of 4150 $\mu mol \cdot g^{-1} h^{-1}$ & 4600 $\mu mol \cdot g^{-1} h^{-1}$ respectively.

5.3 Results & Discussions

The detailed synthetic procedure of the photocatalysts have been described thoroughly in the experimental section (5.4). The DAT substituted porphyrin undergoes a supramolecular assembly formation with melamine in Water-DMF at elevated temperature. The assembly when polymerized at 550 °C results in a porphyrin grafted carbon nitride with molecular homojunction bonding mode. The porphyrin inclusion on the carbon nitride framework resulted in a darker colored (greyish) carbon nitride as compared to the pale-yellow pristine g-C_3N_4 as observed in (**Figure S5.1**). The schematic representation of the formation of both pristine (g-CN) and porphyrin doped (g-CN_Por) carbon nitrides is depicted in **Figure 5.1**. The metalation of the porphyrin core was carried out *via* post-metalation strategy, to ensure the metalation of only those porphyrin centers which survived during the high temperature polymerization. The post metalation of g-CN_Por with Co^{2+} and Ni^{2+} yielded g-CN_Por_Co and g-CN_Por_Ni respectively.

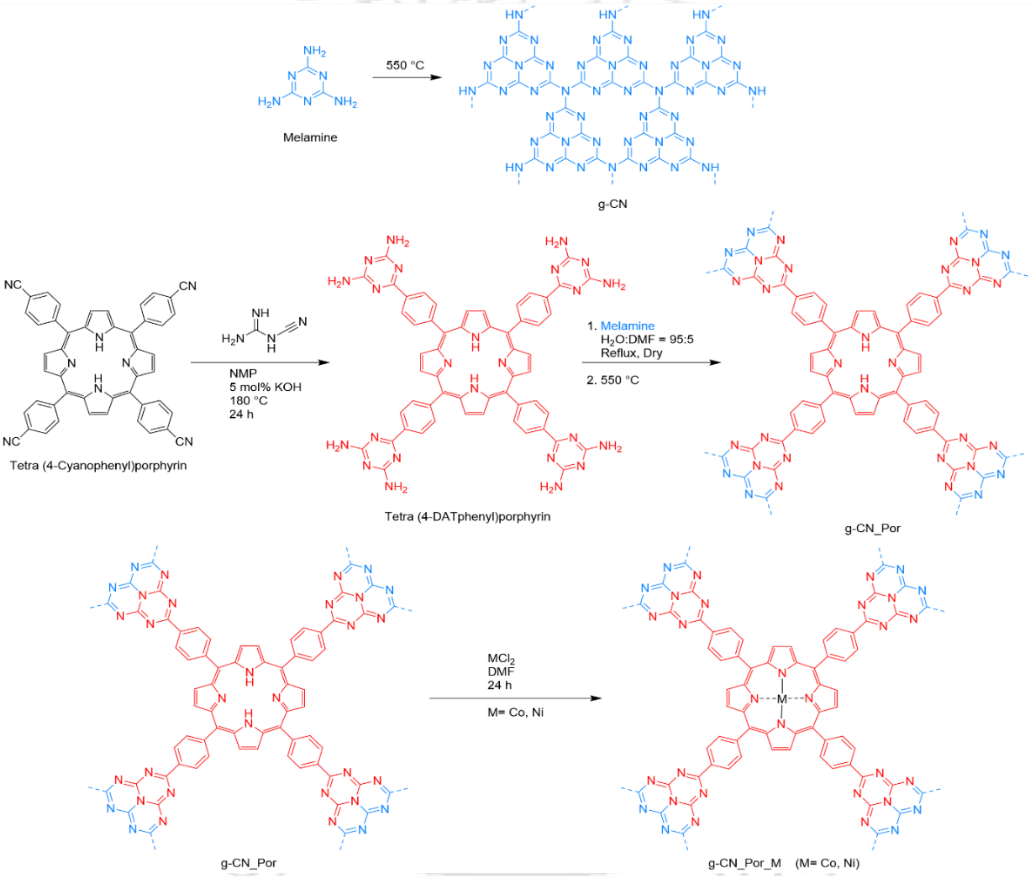

Figure 5.1: Design strategy and synthesis

To start with, both SEM and TEM imaging was performed to understand whether the inclusion of the porphyrin moiety had any effect on the overall the morphology of the basic carbon nitride structure. (**Figure 5.2a-d**) & (**Figure S5.2a-h**) represent the scanning electron micrographs of all the carbon nitride materials. The surface morphology study *via* SEM unveils that, all the carbon nitride materials show a very similar, irregular and agglomerated assembly of crumpled graphenic sheets, a very common trait of 2D carbon materials.[28] The low loading of the porphyrin precursor as a dopant did not show any significant change in the surface morphology of g-CN_Por *vs.* g-CN, as the DAT porphyrin probably has the same polymerization pathway and kinetics like its matrix melamine and the deliberate use of a preformed supramolecular assembly further ensured homogeneity in the polymerization environment. As post-metalation is a simple metal ion-ligand interaction only, it also didn't alter the overall morphology further. (**Figure 5.2e-h**) & (**Figure S5.3a-h**) represent the high-resolution transmission electron micrographs and transmission electron micrographs of all the carbon nitride materials respectively. The fine microstructure determination *via* TEM and HRTEM unveils that, all the CN materials maintained the basic morphology of layered sheetlike structures common to that of 2D graphemic carbon materials.[29] g-CN and g-CN_Por didn't show any significant structural differences whatsoever, further supporting the claim of negligible effect on polymerization dynamics of low loading of the porphyrin dopant. However, to visualize the dispersed metallic sites for the metalated samples g-CN_Por_Co and g-CN_Por_Ni, very high-resolution images both in bright field and HAADF conditions could not be recorded due to the material's fast degrading response under high influx of electron beam.

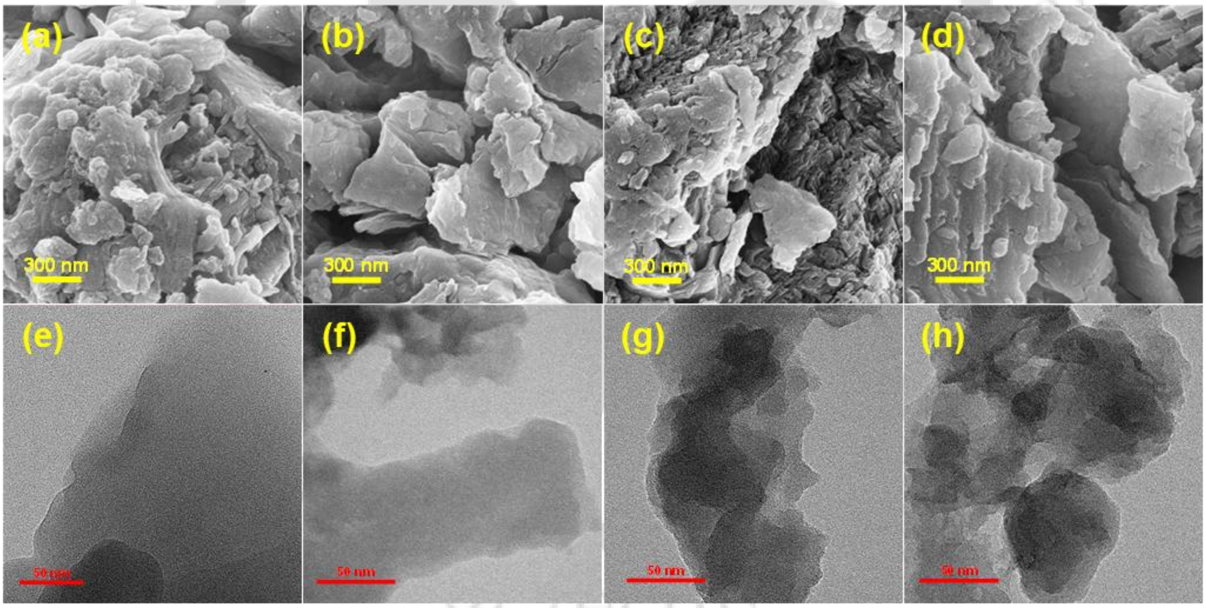

Figure 5.2: (a) SEM, (e) HRTEM of g-CN; (b) SEM, (f) HRTEM of g-CN_Por; (c) SEM, (g) HRTEM of g-CN_Por_Co & (d) SEM, (h) HRTEM of g-CN_Por_Ni.

Elemental mapping was also performed along with the SEM study to visualize the presence of different elements in the samples. (**Figure S5.4 b-c**) and (**Figure 5.3b-c** and **5.3f-g**) shows the presence of both C and N channels in g-CN_Por, g-CN_Por_Co and g-CN_Por_Ni respectively. While **(Figure 5.3d & 5.3h)** represent the presence of Co and Ni channels, further confirming the metalation performed. (**Figures S5.4a** and **Figure 5.3a & 5.3e**) represent mapping overlay on the field of view.

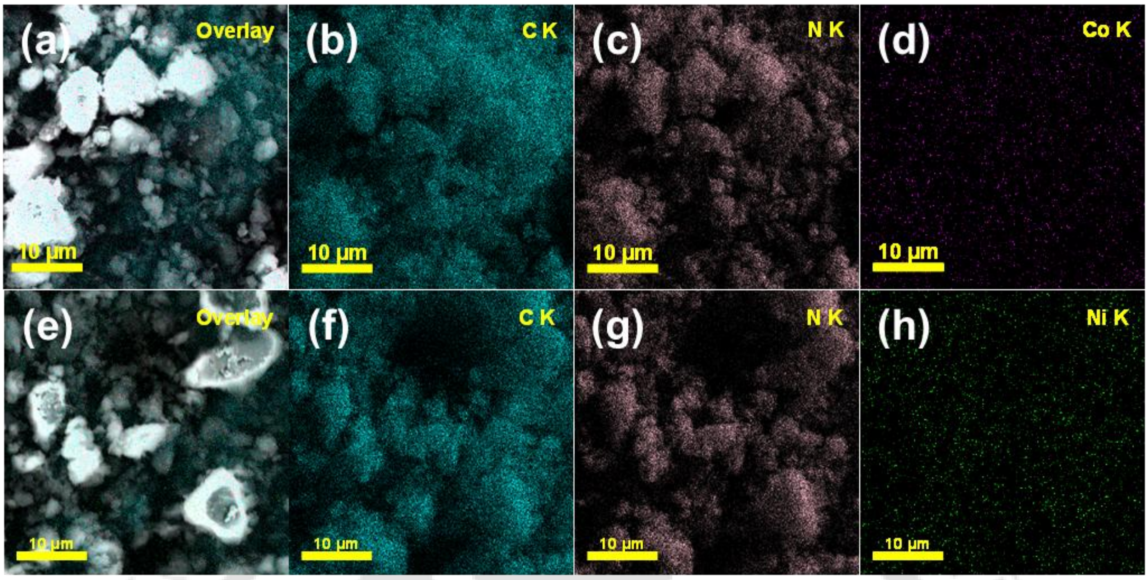

Figure 5.3: EDX mapping of (a-d) g-CN_Por_Co & (e-h) g-CN_Por_Ni. (a) Overlay, (b) C K channel, (c) N K channel & (d) Co K channel of g-CN_Por_Co. (e) Overlay, (f) C K channel, (g) N K channel & (h) Ni K channel of g-CN_Por_Ni.

UV-Vis Diffused Reflectance Spectroscopy was performed to understand the optical properties of the different CN materials. As seen in (**Figure 5.4a**) the optical absorbance cutoff for g-CN could be observed at 450 nm with distinct absorbance features at about 400 nm and 300 nm regions corresponding to the n→π* and π→π* transitions respectively which is quite usual for pristine forms of g-C_3N_4.[30] On the other hand, g-CN_Por, g-CN_Por_Co and g-CN_Por_Ni showed a collectively similar spectral absorbance behaviour but contrasting g-CN.

The spectral features corresponding to n→π* and π→π* transitions were preserved, but apparently the absorption edge could be observed to be blue shifted. However, upon closer inspection through bandgap calculations using Tauc plot *via* Kubelka-Munk transformations, actually a very slight reduction in bandgap was observed for all the porphyrin doped CN materials as compared to pristine CN. g-CN_Por, g-CN_Por_Co & g-CN_Por_Ni showed bandgap values of 2.73 eV, 2.72 eV & 2.72 eV respectively, while g-CN showed 2.75 eV (**Figure S5.5 a-e**). Getting back to the absorbance plot in (**Figure 5.3a**) with this insight shows that, the apparent blue shift feature is a relative spectral absorbance redistribution across the varying wavelengths in the 400-450 nm region, whereas, the band edge actually tilted slightly towards the higher wavelength region resulting into an effective reduction in bandgap. The reduction in bandgap could be attributed to a more effective delocalization in the newly formed porphyrin modified heptazine framework.[31] Also, it is noteworthy that, a tail absorption region with low optical density could be observed in all porphyrin modified CN materials, which could be arising due to the formation of new surface/sub-band/defect states, as inclusion of the porphyrin moiety distorts the electronic energy levels of the heptazine conjugated structure (Cite). It is also worth mentioning that, the porphyrin Q bands could not be resolved in the spectra, due to a very low amount of loading of the porphyrin.

Powder X-Ray Diffraction study was performed to identify, whether the inclusion of the porphyrin led to any crystallographic changes in the parent CN framework (**Figure 5.4b**). The presence of two typical peaks at 13.2° and 27.6° corresponding to the (1 0 0) and (0 0 2) planes of the carbon nitride materials were observed across all the samples, which implies that, the slight molecular doping of the porphyrin moiety into the heptazine framework did not alter the crystallographic identity of the overall carbon nitride framework.[32]

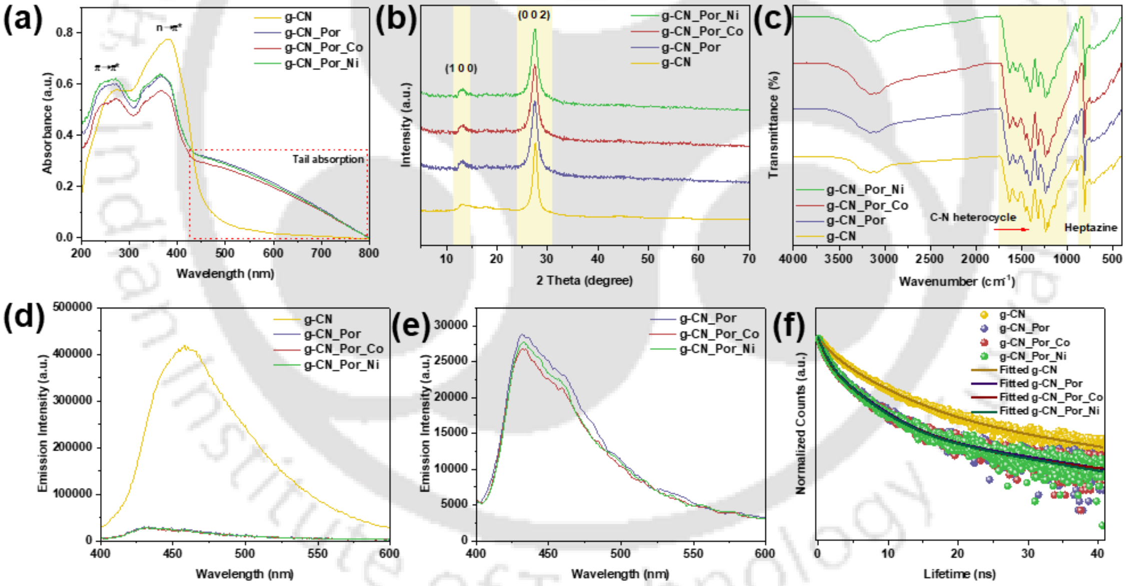

Figure 5.4. (a) UV-Vis DRS, (b) PXRD, (c) FT-IR, (d-e) Steady State Photoluminescence, (f) Time Resolved Photoluminescence Spectra of all CN materials.

FT-IR spectroscopy was performed to unveil the bonding and chemical structure aspects of the formed CN materials. As seen in (**Figure 5.4c**) all the materials exhibited the presence of vibrational signatures corresponding to CN heterocycles between 1200-1700 cm^{-1} and the breathing mode of the tri-s-triazine/heptazine moiety at ~806 cm^{-1}. The combined uncondensed $-NH_2$ & adsorbed -OH vibrations can also be observed at 3200-3400 cm^{-1} region.[33] This implies that despite of molecular doping, the new framework still holds all the vibrational signatures of the parent carbon nitride and does not produce any new form of CN structure. However, it is to be noted that, due to very mild dopant loading and also the commonly merging regions of vibrations of the porphyrin with the melem structure, the vibrational signatures of the porphyrin moiety could not be separately resolved, including the typical -CH stretching vibrations at nearly 3100 cm^{-1} region for g-CN_Por. For the metalated samples g-CN_Por_Co and g-CN_Por_Ni the presence of Metal-N bonds also could not be resolved due to similar dilution reasons.

To explore the function of porphyrin within the charge transfer mechanism of g-CN_Por covalent heterojunction, a Steady State Photoluminescence (SSPL) analysis was performed, as illustrated in (**Figure 5.4d & e**). Both g-CN and three variants of covalent heterojunctions had exhibited photoluminescent emissions broadly at 440-460 nm from 360 nm excitation, with varying intensities that indicate their distinct levels of radiative charge recombination. The intensity of photoluminescence demonstrates a significant relationship with the radiative recombination of electron-hole pairs. A heightened emission intensity is indicative of an increased radiative recombination of photoelectrons and holes, thereby reducing the probability of successful charge separation, migration, and consequently diminishing photocatalytic efficiency. Remarkably, the pristine g-CN exhibited the highest photoluminescence intensity, while the covalent attachment of porphyrin moieties resulted in a notable decrease in photoluminescence intensity relative to pristine g-CN (**Figure 5.4d**).[34] Additional reductions in photoluminescence intensity were observed upon metalation (Ni^{2+} & Co^{2+}) at the porphyrin core. Among the three covalent heterojunctions, g-CN_por_Co displayed the lowest intensity, signifying the most effective charge separation (**Figure 5.4e**). However, it is to be remembered that, due to scattering and several other factors, final conclusions cannot be drawn from the gradual decrement of SSPL intensity within that short range from (**Figure 5.4e**). To draw the final conclusions on the series of PL behaviour, the help of Time Resolved Photoluminescence has to be taken.

The Time Resolved Photoluminescence spectra were also obtained using a 375 nm laser to elucidate the dynamic charge behaviors (**Figure 5.4f**), which can be suitably represented by a three-exponential decay model. The lifetimes associated with the TRPL decay processes exhibited a profound correlation with the recombination dynamics of electron-hole pairs. The pristine g-CN revealed an average lifetime of 7.6 ns. As illustrated in **Figure 5.4f**, the photoluminescence decay of g-CN was markedly augmented in the presence of porphyrin moieties, with g-CN_Por demonstrating a reduced average lifetime of 6.99 ns. The mean lifetimes for all three g-CN_Por covalent heterojunctions were significantly diminished, thereby illustrating an expedited charge transfer mechanism within the covalent heterostructures facilitated by the covalent linkage. The observed decrease in average lifetime (**Table 5.1**) indicates that the singlet exciton dissociation was enhanced in g-CN_Por, attributable to the improved charge transfer kinetics.[34] The incorporation of transition metal ions (Ni^{2+}, Co^{2+}) further diminished the average lifetime, potentially due to more efficient charge separation and migration. For g-CN_Por_Co and g-CN_Por_Ni, the calculated average lifetimes were 4.16 ns and 5.10 ns, respectively. Among the three covalent heterojunctions examined, g-CN_por_Co demonstrated the lowest recorded lifetime. The parameters pertaining to the TRPL decay were summarized in tabular form (**Table 5.1**). It is to be remembered that the lifetimes τ_1, τ_2, & τ_3 don't mean anything physically, however their collective behavior reflected through τ_{av} signifies a direct physical attribute related to effectual charge transfer. Lesser average lifetime is a director of the presence of an alternative charge transfer pathway, thus implying more effective charge separation, extraction and migration.

Table 5.1. TRPL lifetimes of CN materials.

Sample	A_1	τ_1 (ns)	A_2	τ_2 (ns)	A_3	τ_3 (ns)	τ_{av} (ns)
g-CN	0.47158	1.55133	0.5083	4.8647	0.05521	18.53956	7.6
g-CN_Por	0.68726	0.92831	0.34644	3.66001	0.01802	24.97175	6.99
g-CN_Por_Co	0.6376	0.81143	0.36289	3.18215	0.0339	11.49824	4.16
g-CN_Por_Ni	0.67432	0.85935	0.36394	3.35762	0.02308	16.88216	5.10

To investigate the surface chemical composition of the synthesized catalysts in deeper detail, X-Ray Photoelectron Spectroscopy (XPS) was utilized. The global survey XPS spectra of g-CN and g-CN_Por exhibited C and N as main elements with slight presence of O as chemisorbed water as surface hydroxyl (**Figure S5.6a-b**). High resolution XPS spectra of C1s and N1s channels were recorded and deconvoluted to have three main components. For g-CN C1s spectra the peak at 284.87 eV corresponded to adventitious C, whereas, peaks at 286.38 eV & 288.28 eV corresponded to $C-(N)_3$ & N=C-N linkages. N1s spectra for g-CN also reveals three components at 398.78 eV, 399.78 eV and 401.18 eV C=N-C, $N-(C)_3$ and $C-NH_2$ functionalities.[35] On the other hand, C1s spectra of g-CN_Por also showed three similar components at 284.68 eV, 286.18 eV & 287.93 eV corresponding to adventitious C and C=C backbone of the porphyrin, $C-(N)_3$, and N=C-N linkages respectively. The N1s spectrum of g-

CN_Por was deconvoluted to three similar regions located at 398.43 eV, 399.98 eV & 401.08 eV corresponding to C=N-C, N-$(C)_3$ & C-NH_2 linkages (**Figure S5.6c-f**). The C1s spectrum of g-CN_Por_Co showed synthetic components located at 284.78 eV, 286.31 eV & 288.18 eV respectively corresponding to adventitious C and C=C backbone of the porphyrin, C-$(N)_3$, and N=C-N linkages, whereas for g-CN_Por_Ni the same peaks were located at 284.68 eV, 286.28 eV & 288.13 eV. N1s spectra of g-CN_Por_Co was synthetically deconvoluted with three components located at 398.68 eV, 400.23 eV & 401.28 eV corresponding to C=N-C, N-$(C)_3$ & C-NH_2 linkages, whereas for g-CN_Por_Ni the same peaks were located at 398.62 eV, 400.18 eV & 401.29 eV (**Figure 5.5a-b & d-e**).

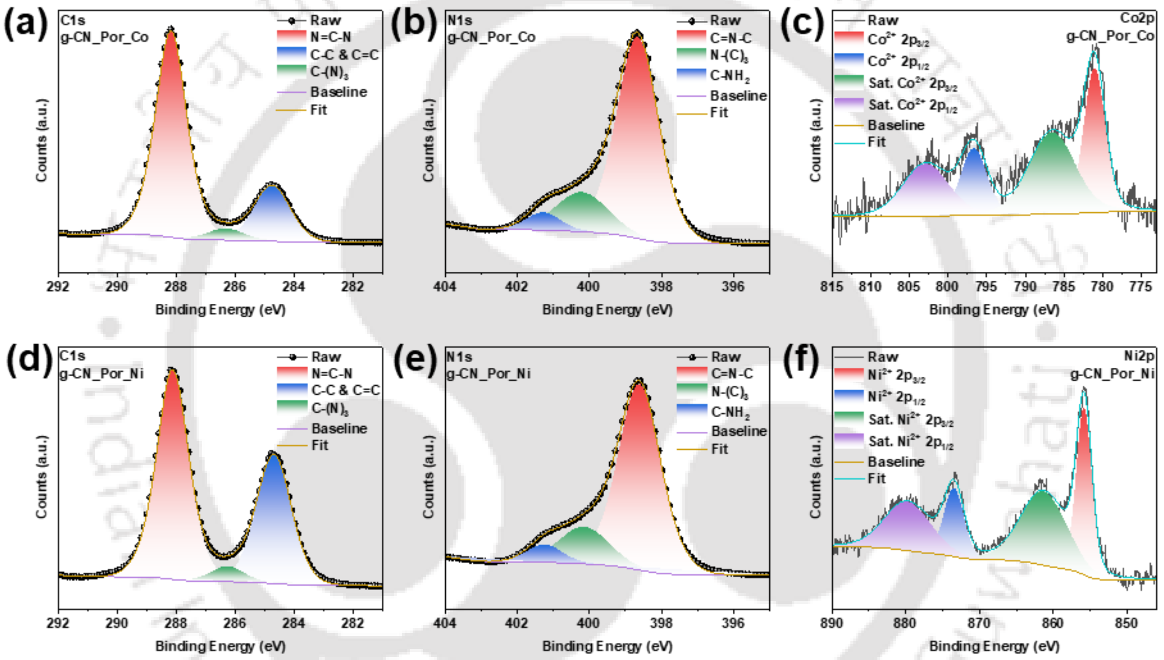

Figure 5.5: (a) C1s (b) N1s, (c) Co2p high resolution XPS of g-CN_Por_Co. (d) C1s, (e) N1s, (f) Ni2p high resolution XPS of g-CN_Por_Ni.

The global Survey XPS spectra for g-CN_Por_Co and g-CN_Por_Ni showed four main elements each, in which C, N and O were common as discussed before, along with the metal peaks of Co and Ni respectively (**Figure S5.7a-b**). g-CN_Por_Co and g-CN_Por_Ni showed four synthetic peaks in Co2p and Ni 2p channels respectively corresponding to the $2p_{3/2}$ and $2p_{1/2}$ regions of their respective metals associated with their corresponding satellite peaks. The main peaks corresponding to $2p_{3/2}$ & $2p_{1/2}$ regions were best fitted with only one component each, which indicated the presence of singularly valent metal centre, in this present case the bivalent metal centre (Co^{2+} & Ni^{2+}). The peaks at 781.07 eV & 796.63 eV for g-CN_Por_Co corresponded to Co $2p_{3/2}$ and $2p_{1/2}$ regions in Co^{2+}-N_4 coordination, typical of a metal porphyrin coordination atmosphere (**Figure 5.5c**). For g-CN_Por_Ni, the peaks at 855.88 eV & 873.48eV corresponded to Ni $2p_{3/2}$ & $2p_{1/2}$ regions in a similar Ni^{2+}-N_4 coordination atmosphere, which is again indicative of a typical metal porphyrin centre (**Figure 5.5f).**

The photoelectrochemical (PEC) assessment was conducted to provide compelling evidence concerning the mechanisms of charge separation and transfer within the g-CN_Por covalent heterojunctions. The photo-current responses for the unmodified g-CN alongside all three covalent heterojunctions were systematically recorded over several 10-second illumination intervals and are presented in **Figure 5.6a**. Notably, under illuminated conditions, the photocurrent intensity was observed to maintain a relatively stable photocurrent, while it swiftly declined upon the cessation of light, thereby indicating a rapid photocurrent response to the alternating light conditions. It was observed that the g-CN_Por_Co had presented the highest photocurrent, whereas the photocurrent value exhibited a progressive reduction in the g-CN_Por_Ni and g-CN_Por heterostructures, respectively. As anticipated, the pristine g-CN displayed the lowest photocurrent when subjected to the identical electrical bias. In the context of transient photocurrent, an elevated value is indicative of effective and efficient charge mobility within the heterostructure, which frequently correlates with a superior hydrogen evolution rate among all samples tested. These findings were substantiated by electrochemical impedance spectroscopy (EIS) measurements, as depicted in **Figure 5.6b**. The g-CN_Por_Co composite, characterized by the smallest semicircle arc, signifies the lowest interfacial charge transfer resistance, thereby facilitating expedited charge transfer at the interface. Conversely, the interfacial charge transfer resistance for the other heterostructures progressively escalated, culminating in peak for the pristine g-CN. This observation suggests that charge migration was most challenging for the pristine g-CN, consequently resulting in the lowest photocurrent.[36]

These PEC experiments further reinforced the conclusions drawn from SSPL and TRPL investigations. This observation elucidates that the covalent integration of porphyrin moieties onto g-CN significantly accelerated both charge separation and charge transfer, which were further enhanced with the incorporation of transition metal ions (Ni^{2+}, Co^{2+}), ultimately translating into accelerated rates of photocatalytic reductive hydrogen evolution reactions.

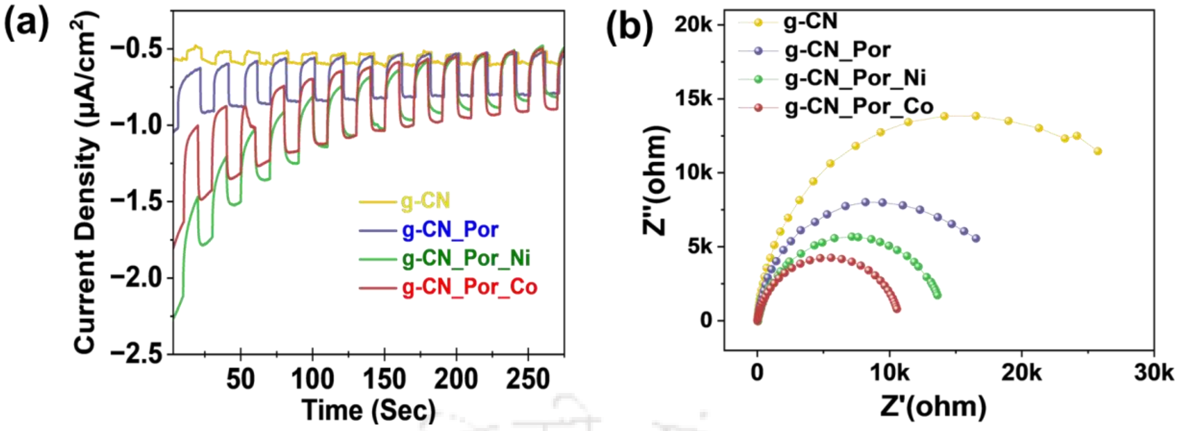

Figure 5.6: (a) Photocurrent and (b) EIS spectra of all CN samples.

Porphyrin-grafted g-CN_Por, has come to the forefront as an exceptionally promising class of photocatalytic materials specifically tailored for facilitating the hydrogen evolution reaction, which is of paramount importance in the realm of sustainable energy. The ideal conditions under which this reaction is optimized can be articulated as follows: specifically, a precise amount of 25 mg of the photocatalysts is meticulously dispersed in a total volume of 50 mL of deionized water through the application of ultrasonic agitation, ensuring that the particles are evenly distributed within the aqueous medium. Furthermore, triethanolamine serves the crucial role of a sacrificial agent within this experimental setup, thereby contributing to the overall efficiency of the photocatalytic process. The resultant suspension, after preparation, is subjected to irradiation with a 300 W xenon lamp, which is notably equipped with a 420 nm cutoff filter to ensure that only the desired wavelengths of light are utilized in the reaction. These meticulously defined optimal conditions will then serve as the foundational parameters for subsequent discussions and analyses regarding the performance assessment of the various photocatalysts involved in this study. In a systematic investigation of the photocatalytic hydrogen evolution reaction (HER) activities of different materials, namely g-CN, g-CN_Por, g-CN_Por_Co & g-CN_Por_Ni, assessments were conducted under visible light irradiation, with the hydrogen production rates for all samples being compiled and represented graphically as a function of the duration of exposure to light, as illustrated in **Figure 5.7** The hydrogen production rates achieved by the g-CN were found to be relatively modest, measuring at only 1.35 $\mu mol \cdot h^{-1}$ when utilizing 25 mg of catalysts, respectively, indicative of rather low photocatalytic efficiency. This underwhelming performance can plausibly be ascribed to a variety of factors, including but not limited to the limited availability of surface reaction sites that facilitate the necessary interactions for hydrogen evolution, as well as the pronounced tendency for radiative recombination of charge carriers, which leads to a significant reduction in the number of photogenerated electrons and consequently results in a sluggish transfer process to the surrounding reaction medium.

However, when g-CN is synergistically covalently anchored with modified porphyrin, there is a remakable enhancement in the photocatalytic hydrogen production activity of the resulting material, known as g-CN_Por, which strongly suggests the critical importance of such covalent integration in enhancing photocatalytic performance. The hydrogen production rate of this hybrid material is observed to be approximately 3383 $\mu mol \cdot g^{-1}h^{-1}$ which is an astounding 3300 times higher than that of g-CN, underscoring the effective augmentation of photocatalytic activity through this innovative hybridization approach.[37] This synergistic effect is primarily attributed to the superior visible-light absorption capabilities exhibited by the porphyrin component, in conjunction with the robust semiconducting characteristics inherent to g-CN, which collectively contribute to significant enhancements in the overall photocatalytic activity observed in the experimental results. Metalated organic molecules onto g-CN represents a highly effective and sophisticated approach that can significantly enhance the photocatalytic activities associated with hydrogen evolution reactions. By introducing metal ions it activated the catalytic centre which helped in optimizing charge dynamics, as well as expanding the range of light absorption capabilities. The strategic incorporation of non-novel metals such as Ni and Co at the catalytic center has demonstrably amplified the efficiency of photocatalytic hydrogen evolution processes, showcasing their essential role in advancing this field of study. Furthermore, the addition of these metal ions has resulted in a pronounced enhancement of the electronic properties, specifically through the establishment of a robust π electron cloud that exerts a substantial pulling force from the g-CN substrate towards the catalytic center, thereby facilitating improved charge transfer mechanisms. For instance, the g-CN_Por_Ni has exhibited remarkable hydrogen evolution activities quantified at an impressive rate of 4150 $\mu mol \cdot g^{-1}h^{-1}$, thereby highlighting its potent photocatalytic efficiency. In a similar vein, the g-CN_Por_Co has achieved the highest hydrogen evolution rate, recorded at an extraordinary 4600 $\mu mol \cdot g^{-1}h^{-1}$, thereby underscoring the significant impact of metalation.

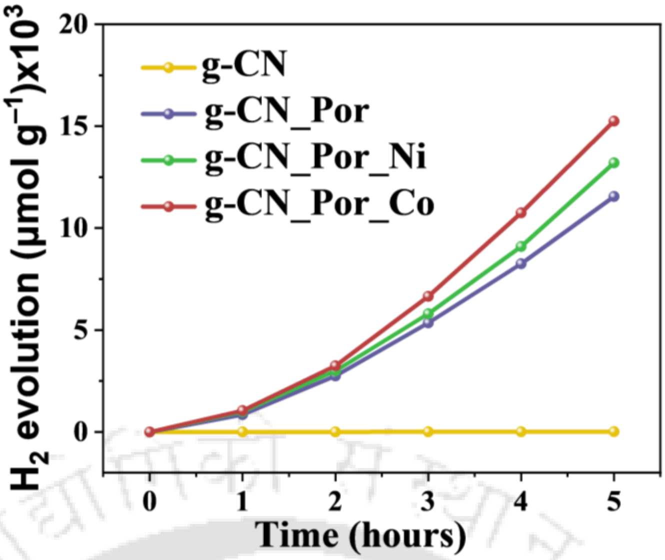

Figure 5.7: H_2 evolution activities of 4 CN samples.

In order to gain a more profound comprehension of the photocatalytic activities exhibited by the catalysts, additional experiments were conducted to evaluate the band potentials of the two catalysts. The Mott−Schottky plots corresponding to the two catalysts (g-CN, g-CN_Por) were illustrated in **Figures 5.8 a, b**. Each catalyst demonstrated positive slopes, indicating the characteristics of n-type semiconductors.[38] The flat band potential was estimated to be -1.11 eV and -1.14 eV for g-CN and g-CN_Por, respectively, with reference to the (Ag/AgCl, KCl saturated) electrode. These values were subsequently recalculated to determine the flat band potential relative to the NHE using the equation ($E_{NHE} = E_{Ag/AgCl\ (KCl\ saturated)} + 0.199$ V).[39] The resultant values were -0.911 eV and -0.941 eV relative to NHE for g-CN and g-CN_Por. The VB XPS (the initial component of XPS) provided data regarding the energy difference between the valence band maximum (VBM) and the Fermi level energy (E_f) for the two catalysts,[40] which were found to be 2.28 eV and 2.2 eV for g-CN and g-CN_Por respectively (**Figure S5.8**). For n-type semiconductors, the flat band potential (E_F) is regarded as equivalent to the Fermi energy level (E_f). [41,42] Therefore, the VBM for g-CN and g-CN_Por were calculated to be 1.37 eV and 1.26 eV, respectively against NHE. Considering the bandgap for 2 materials which were 2.75 eV and 2.73 eV, the calculated CBM would be -1.38 eV and-1.47 eV for g-CN and g-CN_Por respectively.

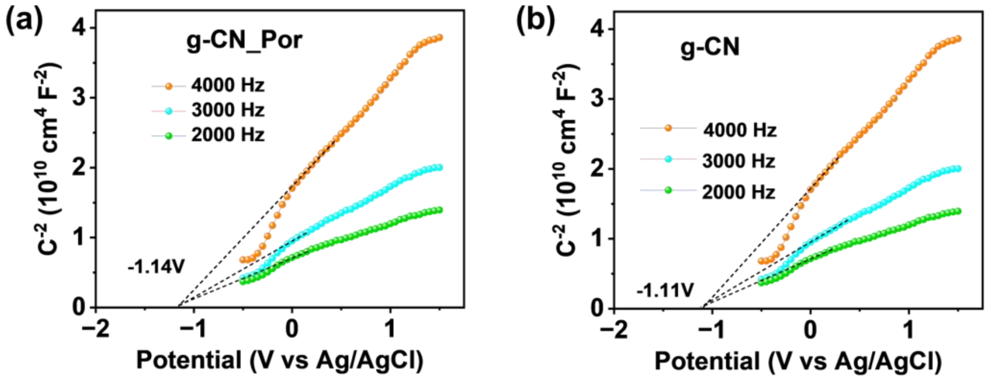

Figure 5.7: The Mott−Schottky plots of (a) g-CN_Por and (b) g-CN samples.

5.4 Experimental Section

Materials

Melamine A.R., Diacyandiamide A.R. were purchased from Research lab Fine Chem Industries, Mumbai, India. Acetic acid glacial A.R. was purchased from Rankem (Avantor), Mumbai, India. 4-Formyl benzonitrile (4-Cyanobenzaldehyde) was purchased from BLDPharm, India. Pyrrole was purchased from Tokyo Chemical Industries (TCI), India. Methanol, DMF and NMP were purchased from Merck, India. 2-Methoxyethanol A.R. & Potassium Hydroxide (KOH) A.R. was purchased from Avra Chemicals, Hyderabad, India. $NiCl_2.6H_2O$ and $CoCl_2.6H_2O$ of ultrapure grade were purchased from Alfa Aesar (Thermo Scientific). All chemicals were used as received except pyrrole, which was distilled freshly prior synthesis due to poor storage properties.

Synthesis of Tetrakis(4-Cyanophenyl)porphyrin:

This compound was synthesized using the classical Addler-Longo method with slight modifications. In a 1 L 3 neck round bottom flask, 600 mL of glacial acetic acid was taken. To the flask, 13.113 g of 4-Cyanobenzaldehyde (4-Formyl benzonitrile) was added along with a magnetic stir bar of appropriate size. The solution of the aldehyde in the acetic acid was then heated to 100 °C in an oil bath with stirring. 6.709 g of freshly distilled pyrrole was weighed out in a beaker and was diluted in 20 mL of glacial acetic acid. The pyrrole in acetic acid solution was rapidly added in the hot aldehyde solution in the flask and a slow stream of pure O_2 gas was purged for 10 minutes alongside rapid stirring. The solution started to rapidly darken starting from a cherry red color through deep purple which appeared black due to high concentrations. The purging was stopped and the reaction mixture was heated at reflux for 4 hours with a condenser attached. Upon completion of 4 hours the solution was cooled to room temperature and the precipitated impure porphyrin was filtered in a Büchner funnel. The impure porphyrin was purified using Soxhlet extraction using anhydrous methanol as a solvent until the methanol extract was virtually colorless (4-cyanophenyl porphyrin is very less soluble in methanol but impurities are). Finally, the extracted clean porphyrin was collected and passed through a short plug of neutralized silica gel (neutralized with triethylamine) and eluted with hot chloroform. The whole extraction can easily take 8-10 L of chloroform based on this scale. The purple solution was evaporated under a rotavapor and the shiny purple solid was collected. The collected solid is practically pure for most of the purposes. Yield: ~7g (39%). Both ^{1}H NMR and FTIR spectra matched literature.[43]

Synthesis of Tetrakis(4-DATphenyl)porphyrin:

The DAT substituted porphyrin, also known as Tetrakis[4-(3,5-diaminotriazino)phenyl]porphyrin, was synthesized using a reported procedure with slight modifications. N-Methylpyrrolidone (NMP) was used as a solvent for this reaction owing to the limited solubility of the cyanoporphyrin in classical reaction solvent 2-Methoxyethanol (Methyl cellosolve). Original work by Dahal and Goldberg used DMSO as a solvent[2] however, we found NMP equally good maybe arguably better, in terms of final separation and purification. 714 mg (1 mmol) of previously synthesized 4-cyanophenyl porphyrin was dissolved in 80 mL of hot (150 °C) NMP with rapid magnetic stirring. To this solution 841 mg (10 mmol) of dicyandiamide was added. The solution was stirred while hot and to it, 112 mg (2 mmol) KOH dissolved in 5 mL 2-Methoxyethanol was added dropwise in a span of 10 minutes. The solution slowly attained a dark green color followed by restoration of the purple color once again. The solution was kept at 200 °C for next 48 hours and then cooled to room temperature. The cold solution was then added into 500 mL of ice-cold water, the DAT porphyrin crashed out as a purple amorphous precipitate. The precipitate was collected using filtration in a Büchner funnel and dried in a vacuum oven for 24 hours at 150 °C. Yield: nearly quantitative. Both UV and NMR spectra matches with literature.[44]

Synthesis of g-CN:

20 g Melamine was loaded in a 100 ml corundum crucible with lid in a muffle furnace and was heated to 550 °C for 4 hours at a ramp of 4 °C/min. The cooling was naturally done inside the furnace and the crucible was only taken off when it reached room temperature. The atmosphere of the furnace was natural air, however, the lid on the crucible ensured that the polymerization took place under self-generated pyrolytic atmosphere of melamine. The g-CN was obtained as a pale-yellow clump weighing 9.6 g (48%). The clumps were ground in an agate mortar pestle and washed with boiling hot Milli-Q® water to remove unreacted melamine and oligomers. The powder was dried in a hot air oven at 120 °C before use.

Synthesis of g-CN_Por:

6 g Melamine was taken in an agate mortar pestle and to that 120 mg (2 wt%) of Tetrakis(4-DATphenyl)porphyrin was added. The mixture was mixed and ground thoroughly for 20 minutes and was taken in a 100 ml round bottom flask. 57 ml Milli-Q® water added to it along with a stir bar. Then 3 ml DMF was added to it, totaling the volume to 60 ml (95:5 for H_2O:DMF). The DMF serves to increase the wettability of both melamine and the porphyrin in water, decreasing the chances of clumping. The mixture was then stirred vigorously and heated in an oil bath at reflux (with condenser)

for 12 hours. After the reflux, the condenser was removed and the solvent was allowed to be evaporated till dryness. The oil temperature was increased to 165 °C to allow DMF to evaporate. After the drying was complete the powder and chunks were removed from the flask and again ground in an agate mortar pestle. The light purple white powder obtained this way is the H-bonded supramolecular assembly of melamine with the DAT porphyrin. This precursor powder was then loaded in a 30 ml corundum crucible with lid, and heated in a muffle furnace in a similar setup used for g-CN. The heating protocol used was as follows. The ramp was always set to 4 °C/min. The initial heating was done at 300 °C for 1 hour, followed by at 500 °C for 3 hours and lastly at 550 °C for 1 hour. Cooling was natural. Rest of the cleaning protocol was same as g-CN. The choice of sequential heating was to ensure homogenous polymerization. The initial heating at 300 °C ensures the start of polymerization of the melamine and DAT groups thus locking the porphyrin in the melamine matrix. This allows oligomerization which increases thermal stability of the dopant lessening the chances of charring. The 500 °C step is the main polymerization temperature and the 550 °C step ensures the graphitic phase formation. While performing the same protocol at direct heating mode to 550 °C we obtained an inhomogeneous colored material, with poorer performance, thus sequential heating was chosen to ensure homogeneity. A greyish powder was obtained weighing 3 g (~49%).

Metalation of g-CN_Por (Synthesis of g-CN_Por_Co and g-CN_Por_Ni):

500 mg g-CN_Por powder was taken in two glass vials each (15 ml borosilicate glass). To that 50 mg each (large excess) $CoCl_2.6H_2O$ or $NiCl_2.6H_2O$ were added followed by 10 ml each DMF. Stir bars were added in the vials. After capping, the vials were heated on a hotplate stirrer for 24 hours with stirring at 100 °C. After the heating was over, the mixtures were taken in two 15 ml conical centrifuge tubes with the aid of a little bit of methanol. Centrifugation cleaning was repeated for 12 times with 6 times of Milli-Q® water and methanol each. After that drying was performed in a hot air oven at 120 °C.

5.5 Conclusion

In conclusion, the chemical functionalization of $g-C_3N_4$ via a covalent methodology employing cyano porphyrin has been demonstrated to serve as a significant tactic for augmenting and introducing novel properties to $g-C_3N_4$, thereby facilitating charge separation and enhancing visible light absorption in the tail region. This advancement enables the attainment of improved HER activities from ascorbic acid aqueous solutions. The covalent grafting of porphyrin moieties onto the g-CN sheet has provided coordination sites for transition metals such as Ni^{2+} and Co^{2+}. The Metal co-ordinated por_g-CN could further enhance the H_2 evolution rates. The presence of metalated porphyrin moieties on g-CN has been shown to alter the kinetics of photogenerated charge migration, as evidenced by photocurrent and impedance studies.

Porphyrin-anchored g-CN has demonstrated hydrogen evolution of 383 μmol·g^{-1}h^{-1}, which represents 284 times that of pristine g-CN. Notably, the maximum hydrogen evolution recorded was 4200 μmol·g^{-1}h^{-1}, achieved by Co_por_g-CN. This accelerated HER performance was attained through covalent linkage, where the migration of photogenerated charge transfer was considerably more feasible in comparison to conventional heterostructures. In instances involving g-CN with two-component heterostructures, the components were affixed through either electrostatic interactions or weak van der Waals forces. During hydrogen production under stirring conditions, there existed a substantial likelihood of segregation of these loosely bound components, thereby compromising the integrity of the g-CN heterostructures, which is highly detrimental to HER activities. Between the Ni and Co metalated photocatalysts, Co_por_g-CN exhibited a slight upper hand in terms of HER activities. This superiority can be elucidated through the mechanism of hydrogen generation. In the case of transition metal-coordinated photocatalysts, prior to the formation of molecular hydrogen, metal hydride bonds are established. The rupture of these metal hydride bonds generates hydride ions (H^-), which subsequently capture protons from the reaction medium, leading to the generation of H_2. The cleavage of the metal hydride bond is regarded as the rate-determining step (RDS) that governs the rate of hydrogen evolution. The displacement of the H^- ion, which initiates the formation of molecular H_2, is considerably more facile for Co_por_g-CN.

5.6 Reference

1. Goettmann, F.; Fischer, A.; Antonietti, M.; Thomas, A. Metal-Free Catalysis of Sustainable Friedel-Crafts Reactions: Direct Activation of Benzene by Carbon Nitrides to Avoid the Use of Metal Chlorides and Halogenated Compounds. *Chem Commun* **2006**, (43), 4530-4532. DOI: 10.1039/b608532f.
2. Wang, X. C.; Maeda, K.; Thomas, A.; Takanabe, K.; Xin, G.; Carlsson, J. M.; Domen, K.; Antonietti, M. A Metal-Free Polymeric Photocatalyst for Hydrogen Production from Water Under Visible Light. *Nat Mater* **2009**, *8* (1), 76-80. DOI: 10.1038/Nmat2317.
3. Bhowmik, S.; Phukan, S. J.; Sah, N. K.; Roy, M.; Garai, S.; Iyer, P. K. Review of Graphitic Carbon Nitride and Its Composite Catalysts for Selective Reduction of CO_2. *Acs Appl Nano Mater* **2021**, *4* (12), 12845-12890. DOI: 10.1021/acsanm.1c02896.
4. Fujishima, A.; Honda, K. Electrochemical Photolysis of Water at a Semiconductor Electrode. *Nature* **1972**, *238* (5358), 37-38. DOI: 10.1038/238037a0.
5. Tachibana, Y.; Vayssieres, L.; Durrant, J. R. Artificial Photosynthesis for Solar Water-Splitting. *Nat Photonics* **2012**, *6* (8), 511-518. DOI: 10.1038/nphoton.2012.175.

6. Fu, J. W.; Liu, K.; Jiang, K. X.; Li, H. J. W.; An, P. D.; Li, W. Z.; Zhang, N.; Li, H. M.; Xu, X. W.; Zhou, H. Q.; et al. Graphitic Carbon Nitride with Dopant Induced Charge Localization for Enhanced Photoreduction of CO_2 to CH_4. *Adv Sci* **2019**, *6* (18). DOI: 10.1002/advs.201900796.
7. Zhang, J. S.; Chen, X. F.; Takanabe, K.; Maeda, K.; Domen, K.; Epping, J. D.; Fu, X. Z.; Antonietti, M.; Wang, X. C. Synthesis of a Carbon Nitride Structure for Visible-Light Catalysis by Copolymerization. *Angew Chem Int Edit* **2010**, *49* (2), 441-444. DOI: 10.1002/anie.200903886.
8. Zhang, J. S.; Zhang, G. G.; Chen, X. F.; Lin, S.; Möhlmann, L.; Dolega, G.; Lipner, G.; Antonietti, M.; Blechert, S.; Wang, X. C. Co-Monomer Control of Carbon Nitride Semiconductors to Optimize Hydrogen Evolution with Visible Light. *Angew Chem Int Edit* **2012**, *51* (13), 3183-3187. DOI: 10.1002/anie.201106656.
9. Bojdys, M. J.; Wohlgemuth, S. A.; Thomas, A.; Antonietti, M. Ionothermal Route to Layered Two-Dimensional Polymer-Frameworks Based on Heptazine Linkers. *Macromolecules* **2010**, *43* (16), 6639-6645. DOI: 10.1021/ma101008c.
10. Zhou, T. Y.; Che, G. B.; Liu, C. B.; Ding, L.; Teng, H. H. Recent Advances on Small Molecule Doped Carbon Nitride Photocatalysts: Application in Environmental Water Remediation and Clean Energy Production. *Arab J Chem* **2024**, *17* (6). DOI: 10.1016/j.arabjc.2024.105808.
11. Duong, A.; Rajak, S.; Tremblay, A. A.; Maris, T.; Wuest, J. D. Molecular Organization in Crystals of Bis(diaminotriazinyl)-Substituted Derivatives of Benzene, Pyridine, and Pyrazine. *Cryst Growth Des* **2019**, *19* (2), 1299-1307. DOI: 10.1021/acs.cgd.8b01694.
12. Rajak, S.; Vu, N. N.; Kaur, P.; Duong, A.; Nguyen-Tri, P. Recent Progress on the Design and Development of Diaminotriazine Based Molecular Catalysts for Light-Driven Hydrogen Production. *Coordin Chem Rev* **2022**, *456*. DOI: 10.1016/j.ccr.2021.214375.
13. Wang, Y. Y.; Zhao, S.; Zhang, Y. W.; Chen, W. X.; Yuan, S. H.; Zhou, Y. M.; Huang, Z. W. Synthesis of Graphitic Carbon Nitride with Large Specific Surface Area via Copolymerizing with Nucleobases for Photocatalytic Hydrogen Generation. *Appl Surf Sci* **2019**, *463*, 1-8. DOI: 10.1016/j.apsusc.2018.08.215.
14. Tebo, A.; Herrero, C.; Aukauloo, A. Porphyrins and Metalloporphrins as Components in Artificial Photosynthesis Research. In *Handbook of Porphyrin Science*, Kadish, K. M., Smith, K. M., Guilard, R. Eds.; Vol. 34; World Scientific, 2014; pp 195-237.
15. Liu, S.; Zhou, S. T.; Hu, C.; Duan, M.; Song, M. G.; Huang, F. L.; Cai, J. G. Coupling Graphitic Carbon Nitrides with Tetracarboxyphenyl Porphyrin Molecules through Π–Π Stacking for Efficient Photocatalysis. *J Mater Sci-Mater El* **2020**, *31*, 10677-10688. DOI: 10.1007/s10854-020-03617-y.
16. Das, B.; Pala, L. P. R.; Mohanta, M. K.; Devi, M.; Chakraborty, D.; Peela, N. R.; Qureshi, M.; Dhar, S. S. Organic-Inorganic Hybrid Photocatalyst Consisting of a Highly Conjugated Metal

Complex and Graphitic Carbon Nitride for Efficient Hydrogen Evolution and Cr(Vi) Reduction. *J Mater Chem A* **2022**, *10*, 23691-23703.

17. Da Silva, E. S.; Moura, N. M. M.; Neves, M. G. P. M. S.; Coutinho, A.; Prieto, M.; Silva, C. G.; Faria, J. L. Novel Hybrids of Graphitic Carbon Nitride Sensitized with Free-Base Mesotetrakis(Carboxyphenyl) Porphyrins for Efficient Visible Light Photocatalytic Hydrogen Production. *Appl Catal B-Environ* **2018**, *221*, 56-69.
18. Zhang, J.; Wang, A. J.; Zhao, W.; Li, C.; Chen, X. D.; Wang, Y.; Zhu, W. H.; Zhong, Q. Influence of Metal-Porphyrins on the Photocatalysis of Graphitic Carbon Nitride. *Dyes Pigments* **2018**, *153*, 241-247.
19. Zhao, G. X.; Pang, H.; Liu, G. G.; Li, P.; Liu, H. M.; Zhang, H. B.; Shi, L.; Ye, J. H. Co-Porphyrin/Carbon Nitride Hybrids for Improved Photocatalytic CO_2 Reduction Under Visible Light. *Appl Catal B-Environ* **2017**, *200*, 141-149.
20. Ma, Z. Y.; Zeng, C.; Hu, L. L.; Zhao, Q.; Yang, Q.; Niu, J. F.; Yao, B. H.; He, Y. Q. A High-Performance Photocatalyst of Zntcpp Sensitized Porous Graphitic Carbon Nitride for Antibiotic Degradation Under Visible Light Irradiation. *Appl Surf Sci* **2019**, *484*, 489-500.
21. Tian, S. F.; Chen, S. D.; Ren, X. T.; Cao, R. H.; Hu, H. Y.; Bai, F. Bottom-Up Fabrication of Graphitic Carbon Nitride Nanosheets Modified with Porphyrin via Covalent Bonding for Photocatalytic H_2 Evolution. *Nano Res* **2019**, *12*, 3109-3115.
22. Tian, S. F.; Chen, S. D.; Ren, X. T.; Hu, Y. Q.; Hu, H. Y.; Sun, J. J.; Bai, F. An Efficient Visible-Light Photocatalyst for CO_2 Reduction Fabricated by Cobalt Porphyrin and Graphitic Carbon Nitride via Covalent Bonding. *Nano Res* **2020**, *13*, 2665-2672.
23. Hayat, A.; Sohail, M.; Taha, T. A.; Alenad, A. M.; Uddin, I.; Hayat, A.; Ali, T.; Shah, R. H.; Irfan, A.; Khan, W. U.; et al. A Superficial Intramolecular Alignment of Carbon Nitride through Conjugated Monomer for Optimized Photocatalytic CO_2 Reduction. *Catalysts* **2023**, *13*. DOI: 10.3390/catal13020309.
24. Wu, P.; Yin, X. Y.; Zhao, Y. F.; Li, F. Z.; Yang, Y. Y.; Liu, N.; Liao, J. L.; Lan, T. Porphyrin-Based Hydrogen-Bonded Organic Framework for Visible Light Driven Photocatalytic Removal of U(VI) From Real Low-Level Radioactive Wastewater. *J Hazard Mater* **2023**, *459*. DOI: 10.1016/j.jhazmat.2023.132179.
25. Wu, P.; Zhao, Y. F.; Yin, X. Y.; Cao, H.; Li, F. Z.; Yang, J. J.; Yang, Y. Y.; Liu, N.; Liao, J. L.; Lan, T. Enhanced Photocatalytic Removal of U(VI) from Real Radioactive Wastewater by Modulating the Surface Charge Microenvironment in Porphyrin-Based Hydrogen-Bonded Organic Framework. *Acs Appl Mater Inter* **2024**, *16*, 33657-33668. DOI: 10.1021/acsami.4c06992.
26. Chamorro-Posada, P.; Dante, R. C.; Vazquez-Cabo, J.; Dante, D. G.; Martin-Ramos, P.; Rubin-Lopez, O.; Sanchez-Arevalo, F. M. From Urea To Melamine Cyanurate: Study of a Class of

Thermal Condensation Routes for the Preparation of Graphitic Carbon Nitride. *J Solid State Chem* **2022**, *310*. DOI: 10.1016/j.jssc.2022.123071.

27. Zheng, Y.; Zhang, Z. S.; Li, C. H. A Comparison of Graphitic Carbon Nitrides Synthesized from Different Precursors through Pyrolysis. *J Photoch Photobio A* **2017**, *332*, 32-44. DOI: 10.1016/j.jphotochem.2016.08.005.
28. Saeed, M.; Munir, M.; Intisar, A.; Waseem, A. Facile Synthesis of a Novel Ni-WO3@g-C3N4 Nanocomposite for Efficient Oxidative Desulfurization of Both Model and Real Fuel. *ACS Omega* **2022**, *7* , 15809–15820.
29. Hassan, F.; Backer, S. N.; Almanassra, I. W.; Ali Atieh, M.; Elbahri, M.; Shanableh, A. Solar-Matched S-Scheme ZnO/g-C_3N_4 for Visible Light-Driven Paracetamol Degradation. *Sci. Rep.* **2024**, *14*, 12220. DOI: 10.1038/s41598-024-60306-0.
30. Xu, Z.; Nie, J.; Mao, G.; Guo, J.; Wu, C. Engineering Dual Carbon and Nitrogen Vacancies in G-C3N4 for Enhanced Photodegradation of Tetracycline Hydrochloride. *Langmuir* **2024**, *40*, 23051–23059.
31. Zhao, Y.; Qin, H.; Wang, Z.; Wang, H.; He, Y.; Tian, Q.; Luo, Q.; Xu, P. Facile Synthesis of Cadmium-Doped Graphite Carbon Nitride for Photocatalytic Degradation of Tetracycline under Visible Light Irradiation. *Environ. Sci. Pollut. Res. Int.* **2022**, *29*, 74062–74080.
32. Mehtab, A.; Alshehri, S. M.; Ahmad, T. Photocatalytic and Photoelectrocatalytic Water Splitting by Porous G-C_3N_4 Nanosheets for Hydrogen Generation. *ACS Appl. Nano Mater.* **2022**. DOI: 10.1021/acsanm.2c02460.
33. Zhang, C.; Liu, J.; Huang, X.; Chen, D.; Xu, S. Multistage Polymerization Design for G-C3N4 Nanosheets with Enhanced Photocatalytic Activity by Modifying the Polymerization Process of Melamine. *ACS Omega* **2019**, *4*, 17148–17159.
34. Li, C.; Wu, H.; Du, Y.; Xi, S.; Dong, H.; Wang, S.; Wang, Y. Mesoporous 3D/2D NiCoP/g-C_3N_4 Heterostructure with Dual Co–N and Ni–N Bonding States for Boosting Photocatalytic H_2 Production Activity and Stability. *ACS Sustain. Chem. Eng.* **2020**, *8*, 12934–12943.
35. Chen, L.; Yang, S.; Qi, W.; Zhang, Q.; Zhu, J.; Zhao, P. Supramolecular Self-Assembly of Nitrogen-Deficient Ag/g-C3N4 Nanofiber Films with Enhanced Charge Transfer Dynamics for Efficient Visible-Light Photocatalytic Activity. *ACS Appl. Mater. Interfaces* **2021**, *13*, 49993–50004.
36. Xia, P.; Zhu, B.; Cheng, B.; Yu, J.; Xu, J. 2D/2D g-C3N4/MnO2 Nanocomposite as a Direct Z-Scheme Photocatalyst for Enhanced Photocatalytic Activity. *ACS Sustain. Chem. Eng.* **2018**, *6*, 965–973.
37. Wang, H.; Jiang, J.; Yu, L.; Peng, J.; Song, Z.; Xiong, Z.; Li, N.; Xiang, K.; Zou, J.; Hsu, J.-P.; Zhai, T. Tailoring Advanced N-Defective and S-Doped g-C3 N4 for Photocatalytic H2 Evolution. *Small* **2023**, *19*, e2301116. DOI: 10.1002/smll.202301116.

38. Han, Z.; Zhao, Y.; Gao, G.; Zhang, W.; Qu, Y.; Zhu, H.; Zhu, P.; Wang, G. Erbium Single Atom Composite Photocatalysts for Reduction of CO_2 under Visible Light: CO2 Molecular Activation and 4f Levels as an Electron Transport Bridge. *Small* **2021**, *17*, 2102089.
39. Wang, H.; Zhang, X.; Xie, J.; Zhang, J.; Ma, P.; Pan, B.; Xie, Y. Structural Distortion in Graphitic-C_3N_4 Realizing an Efficient Photoreactivity. *Nanoscale* **2015**, *7*, 5152–5156.
40. Liu, Y.; Zou, R.; Chen, Z.; Tu, W.; Xia, R.; Iwuoha, E. I.; Peng, X. Engineering a Hydrophobic−Hydrophilic Diphase in a Bi_2WO_6-C_3N_4 Heterojunction for Solar-Powered CO_2 Reduction. *ACS Catal.* **2024**, *14*, 138−147.
41. Gao, E.; Wang, W.; Shang, M.; Xu, J. Synthesis and enhanced photocatalytic performance of graphene-Bi_2WO_6 composite. *Phys. Chem. Chem. Phys.* **2011**, *13*, 2887−2893.
42. Bai, Y.; Ye, L.; Wang, L.; Shi, X.; Wang, P.; Bai, W.; Wong, P. K. g-C_3N_4/$Bi_4O_5I_2$ heterojunction with I_3^-/I^- redox mediator for enhanced photocatalytic CO2 conversion. *Appl. Catal., B* **2016**, *194*, 98−104.
43. Lindsey, J. S.; Schreiman, I. C.; Hsu, H. C.; Kearney, P. C.; Marguerettaz, A. M. Rothemund and Adler-Longo Reactions Revisited: Synthesis of Tetraphenylporphyrins under Equilibrium Conditions. *J. Org. Chem.* **1987**, *52*, 827–836.
44. Dahal, S.; Goldberg, I. Solid-state supramolecular chemistry of porphyrins. Hydrogen-bonded networks and porous crystals of *meso*-tetra[4-(3,5-diaminotriazino)phenyl]porphyrin. *J. Phys. Org. Chem.* **2000**, *13*, 382-387.

5.7 Supporting Information

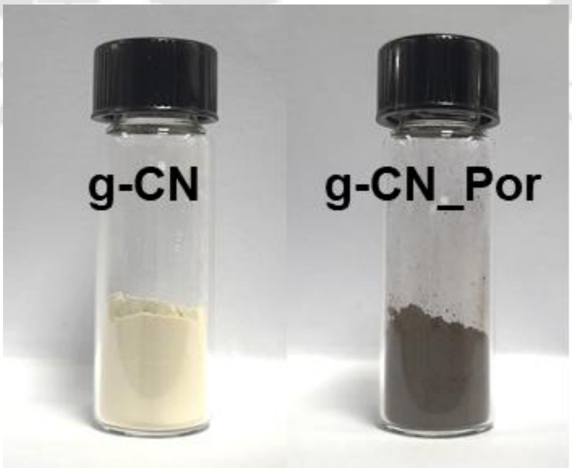

Figure S5.1: Digital photographs of pristine (L) and porphyrin doped (R) carbon nitrides as synthesized.

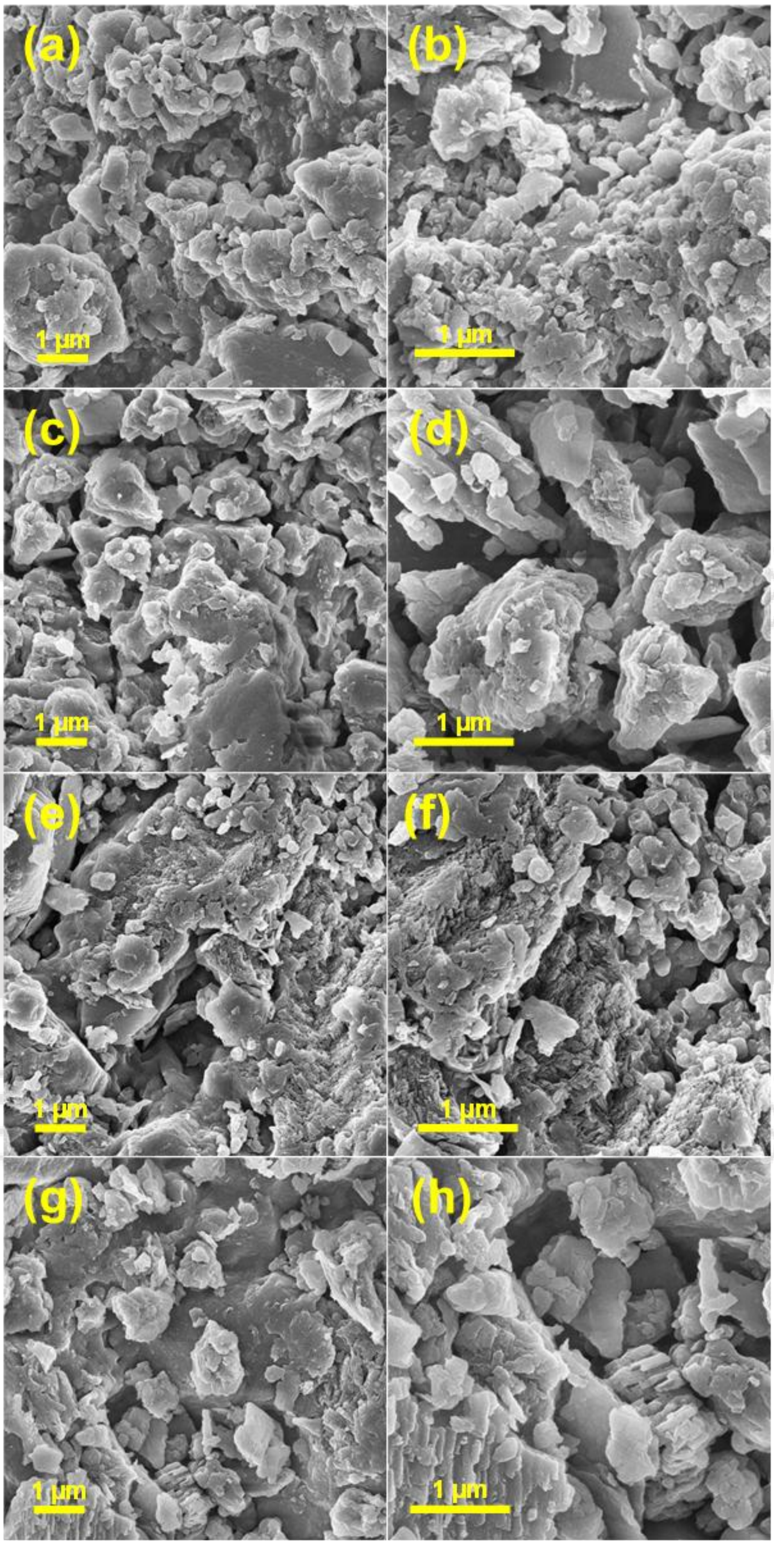

Figure S5.2: SEM micrographs of (a), (b) g-CN; (c), (d) g-CN_Por; (e), (f) g-CN_Por_Co & (g), (h) g-CN_Por_Ni.

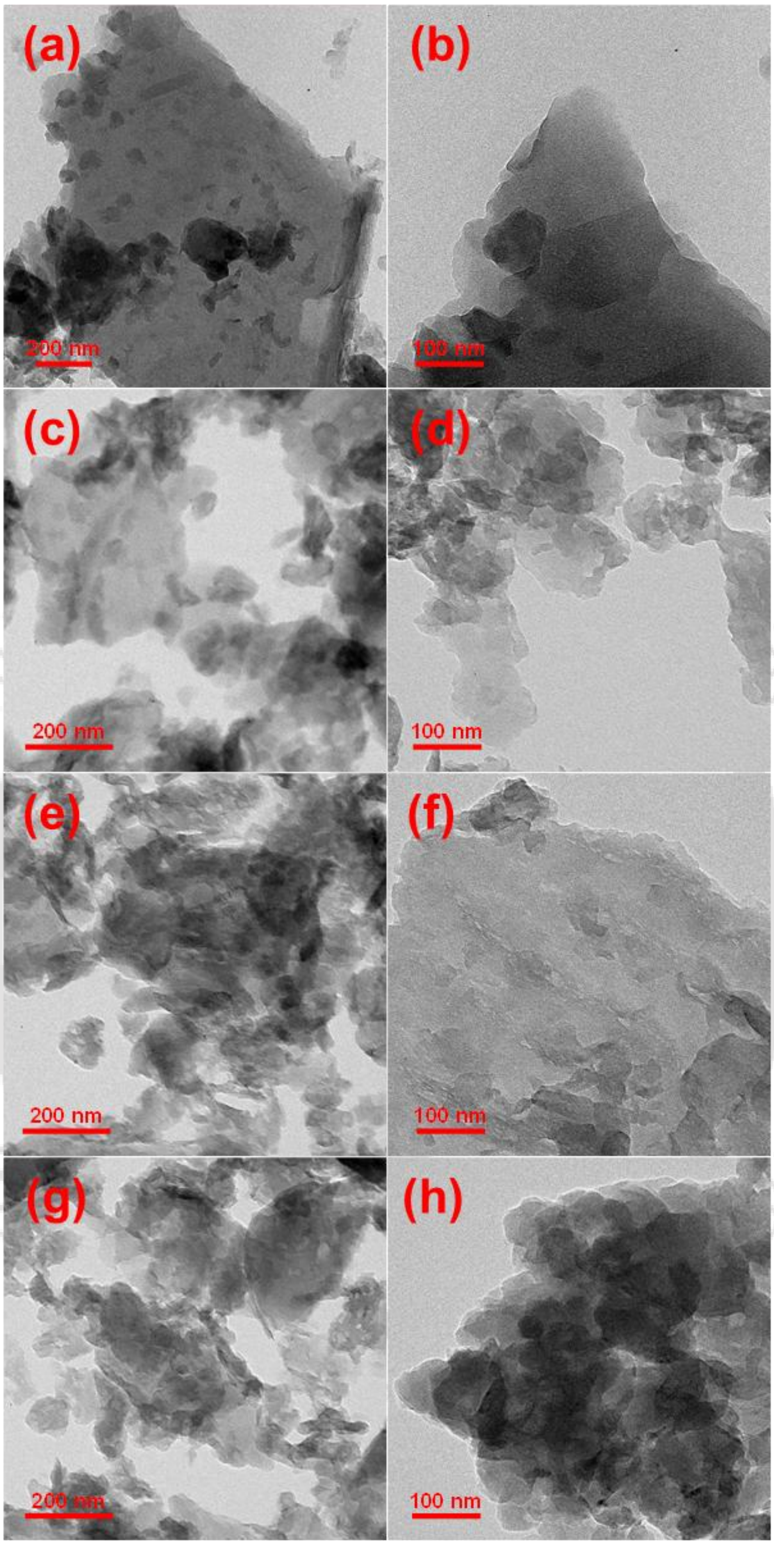

Figure S5.3: TEM micrographs of (a), (b) g-CN; (c), (d) g-CN_Por; (e), (f) g-CN_Por_Co & (g), (h) g-CN_Por_Ni.

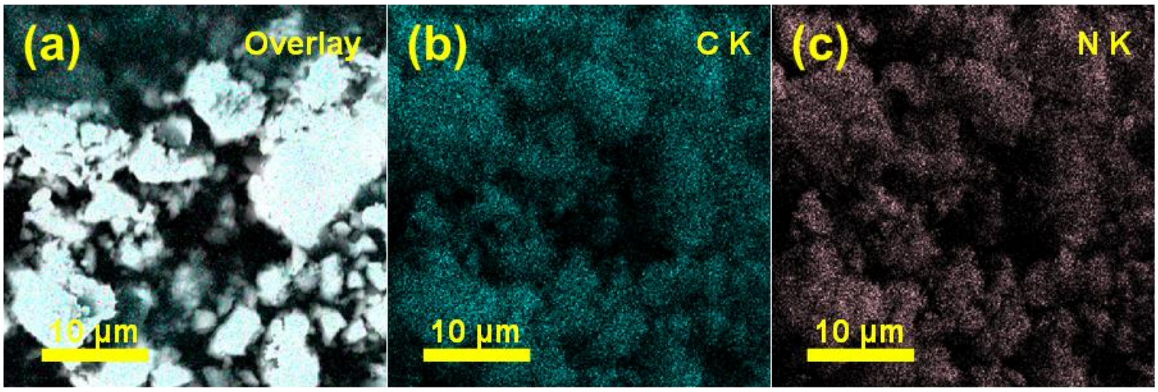

Figure S5.4: EDX mapping of g-CN_Por, (a) Overlay, (b) C K channel, (c) N K channel.

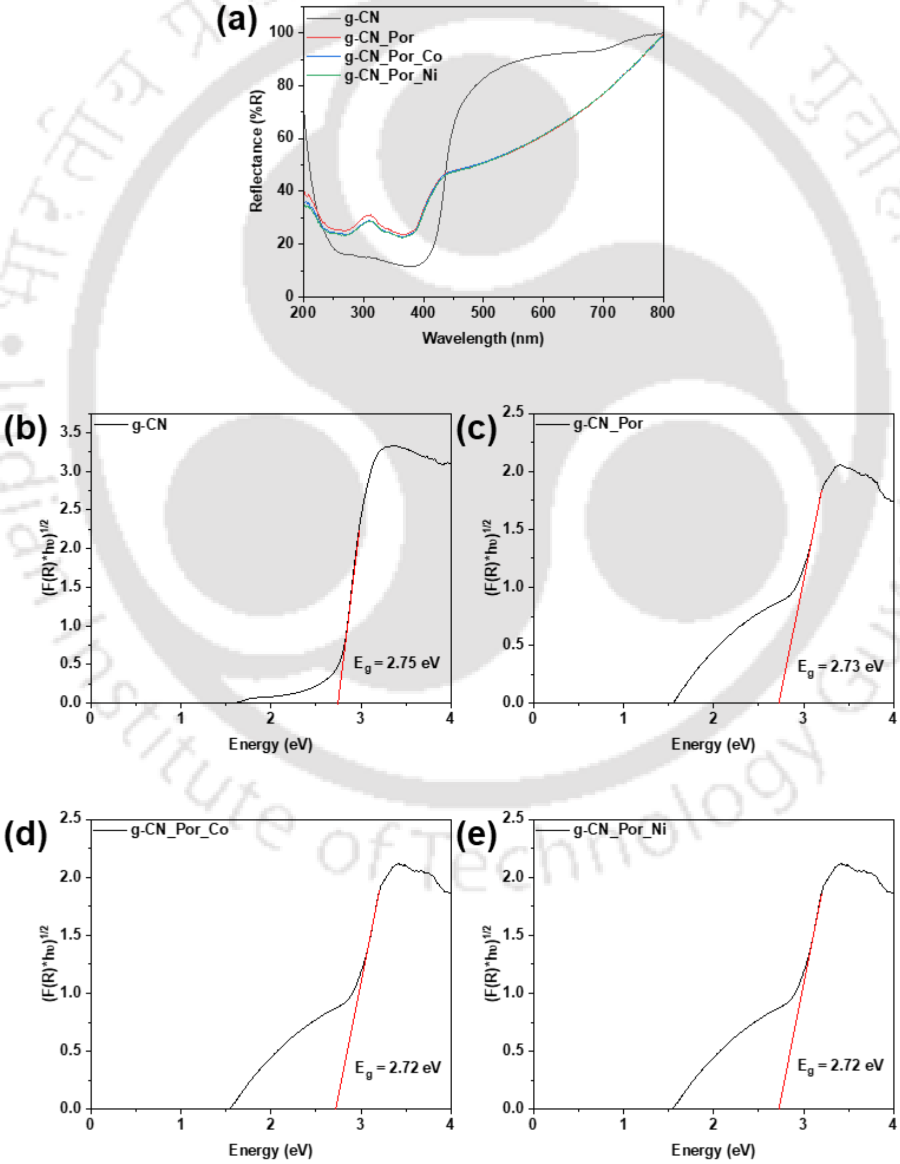

Figure S5.5: (a) Reflectance plot of all CN materials. (b-e) Tauc plot of g-CN, g-CN_Por, g_CN_Por_Co & g-CN_Por_Ni respectively.

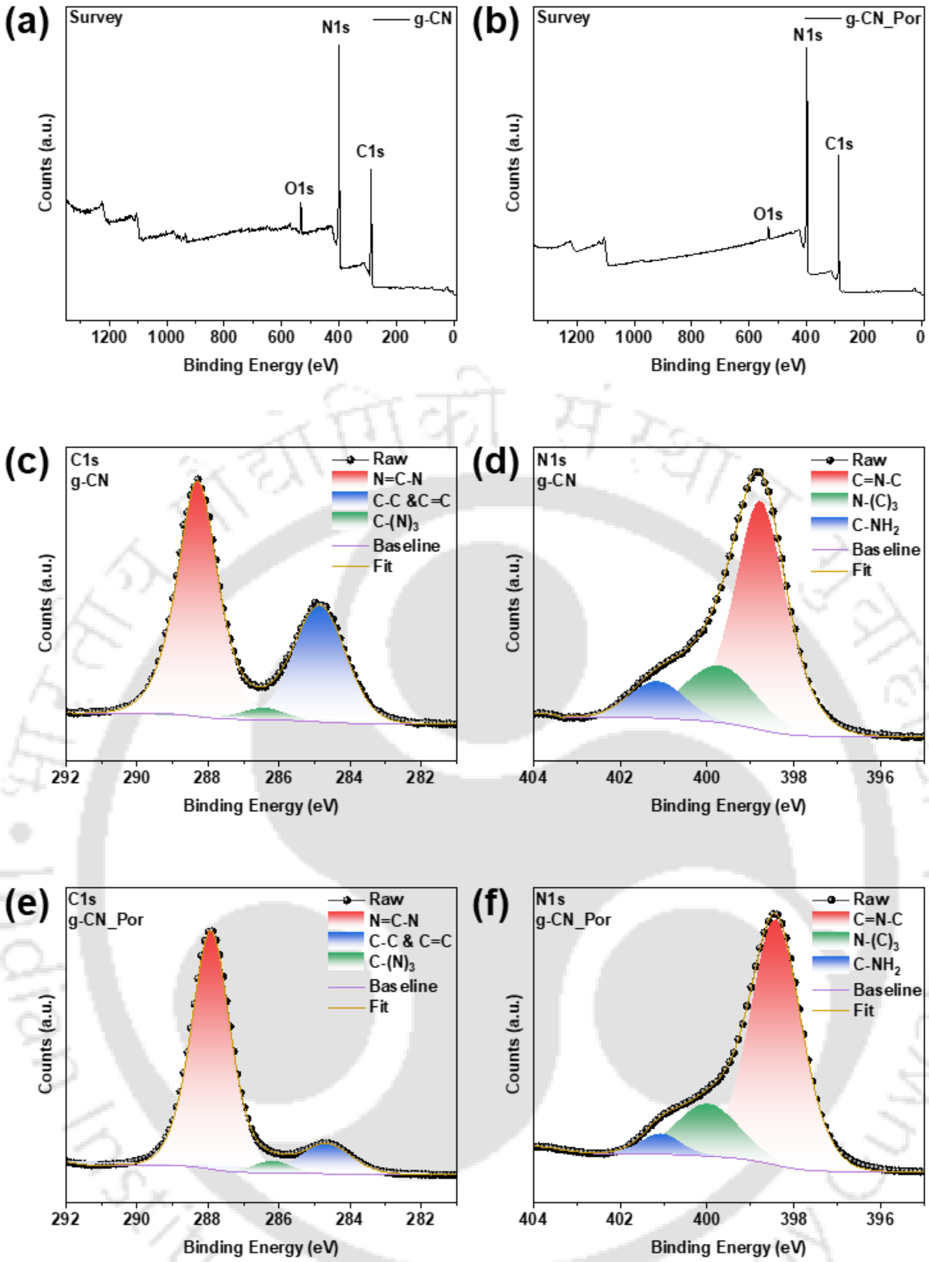

Figure S5.6: (a) Survey XPS of g-CN, (b) Survey XPS of g-CN_Por, (c) C1s High resolution XPS of g-CN, (d) N1s High resolution XPS of g-CN, (e) C1s High resolution XPS of g-CN_Por & (f) N1s High resolution XPS of g-CN_Por.

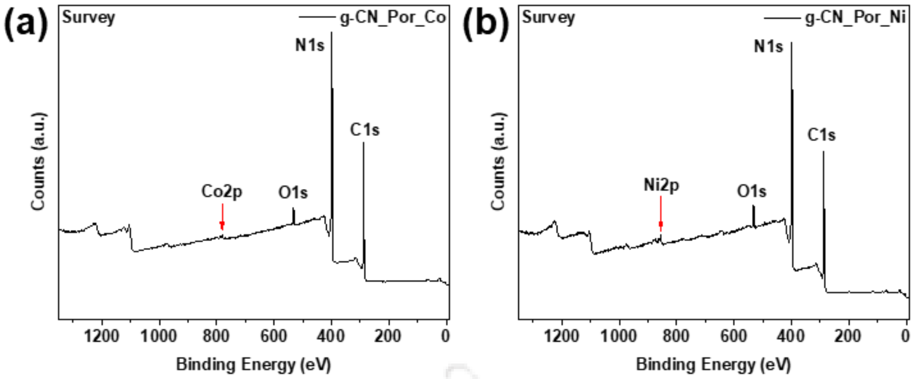

Figure S5.7: (a) Survey XPS of g-CN_Por_Co & (b) Survey XPS of g-CN_Por_Ni.

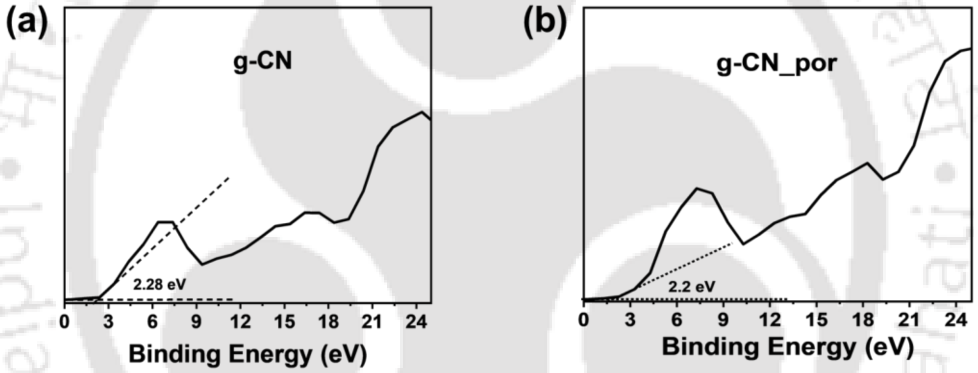

Figure S5.8: VB XPS of (a) g-CN and (b) g-CN_Por.

List of publications

(1) **Pal, T**.; Bhowmik, S.; Suhail, A.; Sharma, S.; Peela, N. R.; Sastri, C. V.; Iyer, P. K. Composites of Reduced Graphene Oxide and $MAPbI_3$ Crystals for Photocatalytic Hydrogen Generation. *ACS Appl. Nano Mater.* **2024**, *7*, 12163–12170.

(2) **Pal, T**.; Bhowmik, S.; Tanwar, A. S.; Suhail, A.; Peela, N. R.; Sastri, C. V.; Iyer, P. K. Solvent Assisted Shape Dependent $MAPbI_3$/Polyfluorene Heterostructures with a Larger Surface Area for Improved Photocatalytic H_2 Evolution. *Energy Adv.* **2024**, *3*, 2965–2971.

(3) **Pal, T.;** Bhowmik, S.; Suhail, A.; Peela, N. R.; Sastri, C. V.; Iyer, P. K. Transformation from type-I to type-II $MA_3Bi_2I_9$ based heterostructure photocatalyst via energy band engineering. (under review)

(4) **Pal, T**.; Bhowmik, S.; Suhail, A.; Peela, N. R.; Sastri, C. V.; Iyer, P. K. Molecularly Doped Porphyrin-Carbon Nitride Covalent Heterojunction Instigating Cocatalyst-Free Solar Energy Harvesting via Water Splitting. (under preparation).